

DISSERTATION

TROPICAL CYCLONE KINETIC ENERGY AND STRUCTURE EVOLUTION IN
THE HWRFX MODEL

Submitted by

Katherine S. Maclay

Department of Atmospheric Science

In partial fulfillment of the requirements

For the Degree of Doctor of Philosophy

Colorado State University

Fort Collins, Colorado

Fall 2011

Doctoral Committee:

Advisor: Thomas Vonder Haar

Co-Advisor: Mark DeMaria

Wayne Schubert

Russ Schumacher

David Krueger

ABSTRACT

TROPICAL CYCLONE KINETIC ENERGY AND STRUCTURE EVOLUTION IN THE HWRFx MODEL

Tropical cyclones exhibit significant variability in their structure, especially in terms of size and asymmetric structures. The variations can influence subsequent evolution in the storm as well as its environmental impacts and play an important role in forecasting. This study uses the Hurricane Weather Research and Forecasting Experimental System (HWRFx) to investigate the horizontal and vertical structure of tropical cyclones. Five real data HWRFx model simulations from the 2005 Atlantic tropical cyclone season (two of Hurricanes Emily and Wilma, and one of Hurricane Katrina) are used.

Horizontal structure is investigated via several methods: the decomposition of the integrated kinetic energy field into wavenumber space, composite analysis of the wind fields, and azimuthal wavenumber decomposition of the tangential wind field. Additionally, a spatial and temporal decomposition of the vorticity field to study the vortex Rossby wave contribution to storm asymmetries with an emphasis on azimuthal wavenumber-2 features is completed. Spectral decomposition shows that the average low level kinetic energy in azimuthal wavenumbers 0, 1 and 2 are 92%, 6%, and 1.5% of the total kinetic energy. The kinetic energy in higher wavenumbers is much smaller. Analysis also shows that the low level kinetic energy wavenumber 1 and 2 components

can vary between 0.3-36.3% and 0.1-14.1% of the total kinetic energy, respectively. The asymmetries associated with storm motion, environmental shear, and the relative orientation of these vectors are examined. A composite analysis shows a dominant wavenumber-1 asymmetry associated with the storm motion and shear vectors. For storm motion the asymmetry is located in the right front quadrant relative to the motion vector with a magnitude exceeding 2.5 m/s, and for shear the asymmetry is located 90° left of the shear vector with a magnitude exceeding 5 m/s. The locations of these wavenumber-1 asymmetries are consistent with the findings of previous studies. Further composite analysis of the asymmetries associated with the relative orientation of the storm motion and shear vectors reveals that when the vectors are aligned versus opposed the wavenumber-1 asymmetries have roughly equivalent magnitude but very different azimuthal location (when aligned the maximum is located in the left front quadrant relative to the storm motion, and when opposed is located nearly 90° to the right of the storm motion). The magnitude of the wavenumber-2 asymmetries is much larger when the storm motion and shear vectors are aligned (exceeding 2.5 m/s) than when they are opposed (~0.5 m/s). The results indicate that shear induced asymmetries extend more deeply through the troposphere than storm motion induced asymmetries. Furthermore, the vortex Rossby wave analysis provides compelling evidence to support their existence and their contribution to the wavenumber-2 asymmetries in the simulated storms.

The vertical structure is studied in terms of the relationship between the size of the radius of maximum wind and its slope, and whether the radius of maximum wind is well approximated by a constant absolute angular momentum surface. The impacts of environmental shear on these relationships are specifically examined. While there is

some evidence to suggest that moderate shear can have a constructive influence on the storm, the relationships between the radius of maximum wind and its slope, and the slopes of the radius of maximum wind and the constant absolute angular momentum surface deteriorate quickly with increasing shear.

The vertical warm core structure of the tropical cyclones is investigated in terms of the height and magnitude of the primary and any possible secondary warm core features (as measured in terms of the temperature anomalies). The purpose of this analysis is to determine the general warm core structure and establish if there are any significant trends with respect to storm evolution, environmental shear, or storm intensity change. It is determined that there is often a dual warm core structure with a primary warm anomaly located in the 5-10 km height region with a magnitude generally between 5-10 K and a secondary warm anomaly located either below 5 km or in the 16-19 km region of lesser magnitude. The height and magnitude of the primary warm core is not found to be linked to the environmental shear and is weakly correlated to the 6 h averaged intensity change.

Finally, the cold pool structure of the storms is briefly examined. The simulated storms exhibit persistent cold pockets at low levels that are likely related to evaporation of rain. An investigation of whether these cold pockets are enhanced in association with extratropical transition processes reveals a notable decrease in the low level cold anomalies for the simulation experiencing extratropical transition.

ACKNOWLEDGEMENTS

I would like to thank my advisors Thomas Vonder Haar and Mark DeMaria for all the support and guidance they provided me during my time as a doctoral candidate. I would also like to thank my committee members Wayne Schubert, David Krueger, and Russ Schumacher for their comments and reviews of this work. Additionally, a special thanks to my former committee member Taka Ito for his time and effort.

There were quite a number of people who provided me assistance along the way in one capacity or another. For the folks at HRD, Frank Marks, Sundararaman Gopalakrishnan, Thiago Quirino, and Kevin Yeh, who provided me access to the HWRFx model simulations and their extremely useful post-processing diagnostics tools, my sincere thanks! From EMC, Vijay Tallapragada and Naomi Surgi provided access to HWRF data in the early stages of my work. My thanks to the following people from CIRA: John Knaff, Jack Dostalek, Andrea Schumacher, Deb Molenar, and Rob Viola, and the following people from the CSU Atmospheric Science Department: Brian McNoldy and Kate Musgrave. Finally, my deepest thanks to my family and friends for all of their love and encouragement along the way!

Funding for this research was sponsored by CIRA activities and participation in the HFIP (Hurricane Forecast Improvement Project) under NOAA grant number NA090AR4320074.

TABLE OF CONTENTS

Abstract	ii
Acknowledgements	v
Chapter 1 – Introduction	1
1.1 Background on Tropical Cyclone Structure	3
1.2 Hypotheses and Outline	11
Chapter 2 – Model Data and Storm/Simulation Overviews	14
2.1 The HWRFx Model	14
2.2 Storm Background and Simulation Overviews	16
2.2.1 Hurricane Emily.....	16
2.2.2 Hurricane Katrina.....	23
2.2.3 Hurricane Wilma.....	28
2.3 Intensity and Kinetic Energy	36
2.4 Tangential Wind Structure	43
Chapter 3 – Methodology	49
3.1 Fourier Analysis (Wavenumber Decomposition)	49
3.2 Shear, Storm Motion, and Directional Difference	57
Chapter 4 – Horizontal Structure	69
4.1 Integrated Kinetic Energy Wavenumber Decomposition and Analysis	70
4.2 Composite Wind Field Analysis and Decomposition	78
4.3 Vortex Rossby Wave Analysis	92
4.4 Summary and Discussion of Results	97

Chapter 5 – Vertical Structure	108
5.1 Vertical Structure of the RMW and AAM	108
5.1.1 Slope of the RMW and Intensity.....	117
5.1.2 Slope of the RMW and Size of the RMW.....	121
5.1.3 RMW and Absolute Angular Momentum Surface.....	130
5.2 Warm Core Structure	135
5.2.1 Discussion of Warm Core Results.....	151
5.2.2 Cold Pool Analysis.....	153
Chapter 6 – Conclusions	157
6.1 Summary and Conclusions	157
6.2 Future Work	163
References	165

CHAPTER 1 – INTRODUCTION

Tropical cyclones are annually occurring severe atmospheric phenomena with far reaching societal impacts. As suggested by their name, they are of tropical origin typically forming between 10-30° latitude north/south. Their paths often take them far into the subtropics and midlatitudes through the course of their lifetime. Those that have land interactions can wreak devastation from extreme winds and flooding from storm surge and/or torrential rains. For this reason, it is important to gain a thorough understanding of how they evolve in terms of track, intensity and all aspects of their dynamic and thermodynamic three dimensional structures in varying synoptic environments in order to better forecast and prepare for them. In terms of track and intensity forecasting, substantial effort has been put into improvement of their accuracy, but this is less so for forecasting size and structure. Case in point, the National Hurricane Center (NHC) carries out annual evaluations of the official tropical cyclone forecasts from the season including verification of the forecast track and intensity. However, while the NHC also forecasts the extent of the 34, 50, and 64 knot winds in each quadrant of the storm, they do not perform verification of these parameters because they are not considered sufficiently reliable, and ground truth is often lacking. This is especially unfortunate because tropical cyclone size and wind field structure is by no means the same from one storm to the next. Figure 1.1 provides an example of two hurricanes with dramatically different size and structure. Hurricane Dean 2007 is the example of a

smaller storm, and at the time of the image the storm intensity is 130 knots (kt), the radius of maximum wind (RMW) is 20 nautical miles (nmi), and the maximum extent of the hurricane force (64 kt) winds is 50 nmi. Hurricane Ike 2008 was a very large storm, and at the time of the image its intensity is 90 kt, the RMW is 50 nmi, and the maximum extent of the hurricane force winds is 105 nmi. The size of a storm can have a significant effect on its impacts. Simply put, for two storms of equal intensity the larger storm will have a greater extent of damaging winds and flooding rains, and a greater magnitude of storm surge. In addition to the storm size, structural forecasting is further complicated by asymmetries. As suggested by the infrared imagery in Figure 1.1, both of the example storms exhibit some structural asymmetries. This study focuses on the asymmetric horizontal wind structure, and the vertical axisymmetric structure in terms of the radius of maximum wind (RMW), absolute angular momentum (AAM), and finally the warm core vertical structure.

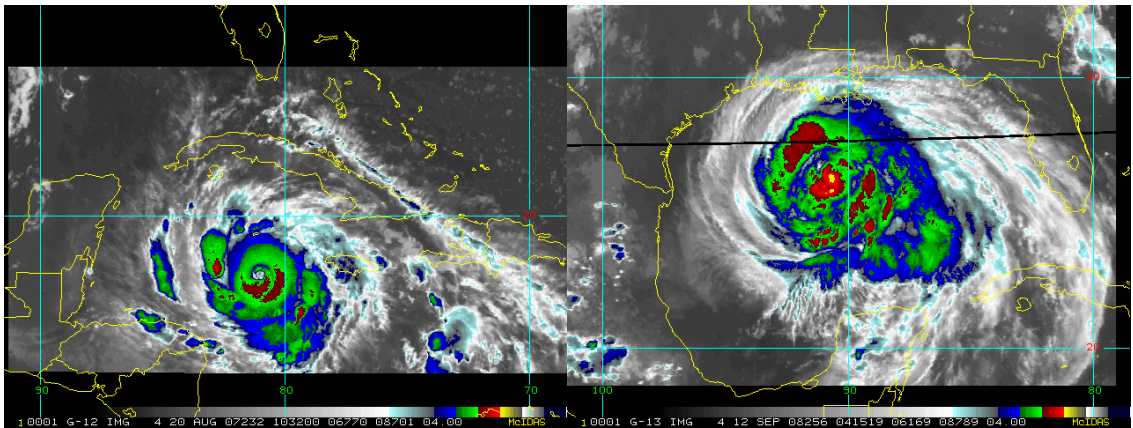


Figure 1.1: GOES infrared satellite imagery of Hurricane Dean 2007 (left) and Hurricane Ike 2008 (right). H. Dean: intensity ~130 kt, RMW ~20 nmi, maximum extent of 64 kt wind ~50 nmi; H. Ike: intensity ~90 kt, RMW ~50 nmi, maximum extent of 64 kt wind ~105 nmi.

1.1 Background on Tropical Cyclone Structure

The low level tropical cyclone structure is a fairly broad topic covering aspects such as the horizontal and vertical wind field, convective features (i.e., rainbands and convective asymmetries), and thermal core features. These structures all exhibit high variability throughout the evolution of a storm, and have been the subject of much study. The purpose of the study presented here is to improve upon the scientific community's current understanding of tropical cyclone structural evolution. This leads to the question: what is the current understanding of tropical cyclone structure?

The tropical cyclone wind field can be generally described as consisting primarily of a largely axisymmetric component and a more varying asymmetric component, where the magnitude of the symmetric part is larger than the asymmetric part (Shapiro 1996; Pendergrass and Willoughby 2009). Studies have shown that there are some common features that show up in the storm asymmetries. Many storms exhibit distinct wavenumber-1 asymmetries in their wind and convective structures. These asymmetries have been shown to be related to a number of factors.

One well known cause of the asymmetric wind is the kinematic effect of the storm translation, or motion. The storm motion velocity has a positive additive effect to the storm circulation velocities on the right side relative to the storm motion vector, and a negative additive effect to the storm circulation velocities on the left side. So for a symmetric hurricane, the winds to the right of the storm motion vector will be stronger than those to the left. Studies have further analyzed this and how it relates to increased boundary layer frictional asymmetry that can then cause more asymmetries in the

boundary layer winds, inflow and convergence, and convection (e.g., Shapiro 1983; Kepert 2001; Kepert and Wang 2001; Corbosiero and Molinari 2002 & 2003).

A number of observational studies have investigated convective and rainfall asymmetries in vertically sheared storms (Corbosiero and Molinari 2002 & 2003; Chen et al. 2006; Ueno 2007; Cecil 2007). The findings were that convective activity and rainfall rates within the inner-core are typically enhanced downshear to downshear left. The convective asymmetry maxima can be shown to be related to tangential wind asymmetry maxima. Firstly, enhanced convection is associated with enhanced vertical motion, and where there is increased vertical motion one will find an increase in the convergent inflow at low levels. Schwendike and Kepert (2008), looking at the boundary layer wind structure in Hurricanes Danielle (1998) and Isabel (2003), found that the tangential wind maxima occurs approximately 90° azimuthally downstream from the location of the maximum inflow. Ueno (2008), studying a real data simulation of Typhoon Chaba (2004), also found this relationship, and furthermore found evidence that a sheared environment can lead to enhanced inflow in the left front quadrant relative to the shear and a tangential wind maximum in the left rear quadrant.

The recent studies of Ueno and Kunii (2009) and Ueno and Bessho (2011) investigated the azimuthal location of wavenumber-1 tangential wind asymmetries taking into account both the storm motion and the shear and the orientations of the two vectors relative to each other. When the two vectors are opposed then the maximum tangential wind occurs to the right of the storm motion vector. When the two vectors are approximately aligned (the shear is in the same direction as the storm motion), and if the shear is large enough, then the tangential wind asymmetry maxima shifts to the left of the

storm motion. They also saw evidence of a wavenumber-2 asymmetry in the tangential wind field for the scenario where the storm motion and shear vectors approximately align. The Ueno and Kunii (2009) study used assimilated observational data from the western Pacific typhoon seasons of 2004-2007. The Ueno and Bessho (2011) study used surface wind data from the NASA Quick Scatterometer (QuikSCAT) ocean surface vector wind retrievals and JMA (Japan Meteorological Agency) global analysis data for storms from the 2004-2007 typhoon seasons to investigate the influence of shear on asymmetries in the surface wind field.

Topographic effects and land interactions can also cause asymmetries in the wind field structure of tropical cyclones. One need only observe satellite imagery of any number of storms that have passed by or over land. Chang (1982) studied the orographic effects of an idealized island mountain range on a moving tropical cyclone using a numerical simulation with a primitive equation model and noted asymmetries, especially at the surface, of the tropical cyclone wind field as the storm approaches and interacts with the topography. Bender et al. (1987) completed a numerical analysis of the effect of island terrain on TCs for three real island scenarios: the Greater Antilles in the Caribbean, the northern Philippines, and Taiwan. They found that island interactions can affect the basic TC flow and wind field and cause changes in the storms track and intensity. Furthermore, the storm can become less vertically coherent and a reduction in the moisture supply from dry air entrainment can both lead to storm decay. The overall storm structure in terms of the location of the warm core, area of intense precipitation, upper and lower circulation centers, and surface pressure center can all become displaced from one another during passage over island terrain. Farfan and Zehnder (2001) studied

the landfall of tropical cyclone Nora (1997) in northwest Mexico via a modeling study with the Pennsylvania State University-National Center for Atmospheric Research Mesoscale Model version 5 (MM5), which increased disorganization in the storm convection as it approached the Baja peninsula. Yang et al. (2008) studied a simulation of Typhoon Nari's (2001) interactions with Taiwan, noting significant asymmetries in the tangential and radial winds as the storm moved over Taiwan. Both of the two previous studies mention that the topographic interactions induce a secondary circulation that may affect the storm vortex. So, tropical cyclones that interact with land with mountainous terrain can be affected through a disruption to the low level circulation that is forced over the terrain, resulting in asymmetries. Also, TCs depend on the warm, moist ocean surface as a source of energy. So a storm that has a portion of its circulation pass over land can experience a reduction in the surface flux of energy into the storm which can contribute to asymmetries in the storm structure (Kepert 2006). The magnitude of the effect and consequent asymmetries is highly dependent on the amount of topographic/land interaction (i.e., length of time, amount of land, type of land, etc).

Another possible mechanism for structural asymmetries in TCs is internal dynamically driven vortex Rossby waves. The presence of vortex Rossby waves, sometimes referred to as potential vorticity (PV) waves, in tropical cyclones and their role in structural asymmetries has been discussed in a number of studies. Guinn and Schubert (1993), using a simple f-plane shallow water model, discussed their role in hurricane spiral bands and suggested that vortex Rossby waves act to restore symmetry to a hurricane vortex. A number of studies have expanded on the theory of vortex Rossby waves and discussed their involvement in storm asymmetries such as spiral bands,

mesovortices, and elliptical eyes, and their role in intensity changes (Montgomery and Kallenbach 1997; Kuo et al. 1999; Reasor et al. 2000; Wang 2001 & 2002; Braun 2002). A few studies even present observational data that suggests a possible presence of vortex Rossby waves. Specifically, the Kuo et al. (1999) study is motivated by observation of an elliptic eye in Typhoon Herb (1996), and the Reasor et al. (2000) study uses dual-Doppler radar of Hurricane Olivia (1994) that shows evidence of an azimuthal wavenumber-2 vortex Rossby wave mode propagating around the eyewall. The theory of vortex Rossby waves, such as their propagation speed and direction and where best to look for them, will be covered more thoroughly later.

Extratropical transition is also a way by which the structure of a tropical cyclone can become quite asymmetric. Jones et al. (2006) gives detailed information about the various aspects of tropical cyclone extratropical transition. As a storm begins the process of extratropical transition, which occurs as it moves poleward (with increasing speed as it is influenced by the midlatitude westerly currents), it is moving into an environment that, generally, is increasingly baroclinic and vertically sheared with decreasing sea surface temperatures and an increasing Coriolis parameter. All of these features influence the storm structure, which becomes increasingly asymmetric and the circulation broadens considerably.

In addition to the asymmetric structure, the symmetric component also has considerable variability. Maclay et al. (2008) demonstrated that integrated kinetic energy can be used as an approximate measure of the size of a storm's wind field. Powell and Reinhold (2007) also discuss the advantages of using integrated kinetic energy as a metric for storm destructive potential. The TC wind field size is especially important in

determining the destructive potential of a storm both in terms of the wind damage, and, perhaps more significantly (AMS 1993), in the possible storm surge.

The vertical structure of tropical cyclones is also an important topic because the slope and warm core structure can influence the convection and intensity changes in the storm. Stern and Nolan (2009) investigated the vertical structure of the tangential wind in tropical cyclones and specifically focused on a few general concepts, namely, 1) The outward slope of the RMW decreases with increasing intensity (a theory proposed by Shea and Gray 1973); 2) The outward slope of the RMW increases with increasing RMW; and 3) The RWM is approximately a constant absolute angular momentum surface. The study used three-dimensional Doppler wind fields from seven storms, and they determined that while there really is not a relationship between the slope of the RMW and storm intensity, the other two hypotheses are more robust and seemed to verify. Other observationally based studies, such as the Marks et al. (1992) study of Hurricane Norbert and the Franklin et al. (1993) analysis of Hurricane Gloria, have also shown evidence that the slope of the RMW closely compares to a constant absolute angular momentum surface.

The height of the warm core is another aspect of TC structure. Tropical cyclones are warm core systems meaning that the warmest temperatures occur near the radial center. Generally the warm core is defined by the temperature anomaly (the deviations from a defined environmental temperature profile) and the height where the temperature anomalies are greatest. There has been relatively little research done to fully analyze the warm core structure of tropical cyclones. Stern and Nolan (2011) provide a good review of previous studies that have included some measurement or analysis of tropical cyclone

warm core height. Some observationally based studies have presented a snapshot of the warm core structure for specific storms. La Seur and Hawkins (1963) determined a warm core height around 11 km for Hurricane Cleo (1958). Hawkins and Rubsam also found a warm core height of approximately 11 km in Hurricane Hilda (1964). Hawkins and Imbembo (1976) investigated Hurricane Inez (1966) and found a dual warm core structure with one thicker (in the vertical sense) warm core located around 10 km and a second located around 4 km. Halverson et al. (2006) did a study of Hurricane Erin (2001) and determined a warm core height positioned roughly at 6 km. Knaff et al. (2004) used the Advanced Microwave Sounding Unit (AMSU) temperature retrievals to measure the height of tropical cyclone warm cores and found an average warm core height of approximately 12 km. Furthermore, they determined that the height of the warm core decreases with increasing shear. However, Stern and Nolan (2011) cast doubt on the robustness of the relationship between warm core height and shear magnitude, as well as question whether the AMSU instrument is even capable of accurately measuring the true warm core structure of the storm given its horizontal resolution (at best, 50 km). Taking into account the instrument's horizontal resolution, the 12 km height of the maximum warm core might be a result of the inability to adequately measure the warm core in the lower levels because that typically has a smaller horizontal scale due to eyewall slope.

A few modeling studies of tropical cyclones have also documented the warm core structure of tropical cyclones. Kurihara (1975) used an axisymmetric numerical model to simulate a tropical cyclone and showed a warm core located around 250 hPa (approximately 10.5 km). Rotunno and Emanuel (1987) also used an axisymmetric

numerical model and, for various configurations, show dual warm core structures with a primary warm core height located around 7 km, 6 km, and 11 km and then a secondary warm core heights around 16 km, 18 km, and 17 km, respectively. Liu et al. (1997 & 1999) studied a simulation of Hurricane Andrew (1992) finding warm core heights in the 5 km and 7 km range. Stern and Nolan (2011) used the high resolution Weather Research and Forecasting Model (WRF) to run idealized simulations of a tropical cyclone with the specific purpose of studying the warm core structure. In their simulations they found a primary warm core generally around 4-8 km and a secondary warm core located around 13-14 km. Researchers have implied a relationship between the height of the warm core and storm intensity and/or shear, but a direct and robust relationship has not been established.

Tropical cyclone studies are generally either observationally based or modeling based. There are advantages and disadvantages to both. The clear benefit of an observational study is that it is directly analyzing the real atmospheric phenomena. So, in a sense it is more pure. However, observationally based studies are greatly limited by the data that is available. This is not a limitation for modeling based studies. Model data allows for far more in depth analysis of a storm than could be done with any real storm. Gridded, three dimensional, simultaneous measurements every hour throughout the lifetime of a storm is never going to be feasible for a real storm. However, this is what one gets when using a model. The obvious problem with using a model is that it is not real, but models are ever improving in recreating atmospheric phenomena. While a model will never perfectly recreate the atmospheric phenomena, they get ever closer, and in using a model to study the atmosphere one learns about the atmosphere and learns how

to improve the model. In light of this, this will be a modeling based study, using an experimental version of the Hurricane WRF model (HWRFx) developed by the Hurricane Research Division.

1.2 Hypotheses and Outline

The overall objective of this study is to provide further insight into the structural evolution of tropical cyclones using simulated storms initialized with real data. Table 1.1 shows a summary of the basic research questions. With respect to the asymmetric structures in the horizontal fields, the wavenumber amplitudes of kinetic energy components can provide an estimation of the significance of asymmetric structure for storms through their evolution. The direction of the shear and motion vectors relative to each other have been hypothesized, with supporting evidence, to play an important part in the structure of TC wind field asymmetries (Ueno and Bessho, 2011), and a goal of this work is to determine if these relationships are evident in high-resolution real-data storm simulations. An additional goal is to determine if there is any evidence to support the existence of vortex Rossby waves contributing to the asymmetries. The asymmetries related to environmental shear and motion should vary on a synoptic timescale, while those related to vortex Rossby waves have a faster timescale. It is hypothesized that the slowly varying asymmetries are the dominant features in TC wind fields.

This study will also investigate TC vertical structure with the purpose of illuminating the role of the magnitude of the shear in the vertical structure, the question being: does the relationship between the size of the RMW and the slope of the RMW hold up and is the RMW approximately a constant absolute angular momentum surface in

low, medium and high shear scenarios? Finally, this research will take a detailed look into the vertical warm core structure in the simulated storms to determine what the general structure is, how it evolves over time, and if the height and magnitude of the warm core is related to storm intensity change and/or shear. A brief look into the cold pool structure will also be performed to determine if there are any salient features, particularly with respect to a storm undergoing extratropical transition.

Table 1.1: Summary of the basic research questions

TOPIC		QUESTION
Horizontal Asymmetric Structure	Wind Field Structure	Effects of storm motion on asymmetries?
		Effects of shear on asymmetries?
		Effects of the orientation of the shear vector to the storm motion vector on asymmetries?
		How do the above relationships change with height?
	Vorticity Field Structure	Is there evidence of a vortex Rossby wave contribution to the asymmetries and if so is it a significant contribution?
Vertical Structure in a Sheared Environment (low/medium/high)	Tangential Winds	How does the relationship between the slope of the RMW and the RMW change when stratifying by shear?
		Is the slope of the RMW still well approximated by a constant angular momentum surface in sheared storms?
	Warm Core	What is the general structure in terms of height and magnitude?
		How does it change through the evolution of a storm?
		Is the height related to storm intensity change and/or shear?
	Cold Pool	Are there any significant cold pool features?

The HWRFx model data is described in Chapter 2 along with overviews of the real storm and the real data simulations of the storms. Five simulations from three storms

will be considered (Hurricanes Emily, Katrina, and Wilma from the 2005 Atlantic hurricane season). These simulations were chosen based on the availability of the HWRFx output files for cases that included a wide range of storm motion and environmental shear. This includes comparisons of the storm tracks, and intensity and kinetic energy evolutions. Chapter 3 describes the details of the analysis methods used in each part of the study. This includes details of the calculation of the simulated storm motion and shear vectors, and the spatial and temporal Fourier wavenumber decomposition. In Chapter 4 the integrated kinetic energy wavenumber decomposition results are presented, and the results of the study of the wind field asymmetries relative to the storm motion, shear and the directional difference (DD) between the two vectors along with a discussion of how they relate to previous studies are described. Chapter 4 also includes an analysis of whether there is any evidence to support that vortex Rossby waves are contributing to the wavenumber-2 spatial asymmetries. In Chapter 5 the vertical structure of the simulated storms is analyzed by examining the slopes of the RWM and constant AAM surfaces, and the results are compared to earlier studies with an emphasis on the role of environmental shear. Chapter 5 concludes with a study of the height of the warm core in the simulations and how these results relate to the current understanding of TC vertical warm core structure. Finally, Chapter 6 summarizes the results found in the study, discusses their implications, and describes future work ideas.

CHAPTER 2 – MODEL DATA AND STORM/SIMULATION OVERVIEWS

2.1 The HWRFx Model

The Hurricane Weather Research and Forecasting Experimental System (HWRFx) is an experimental version of the National Center for Environmental Prediction's (NCEP's) HWRF model (Gopalakrishnan et al. 2010). It was developed at the NOAA Office of Oceanic and Atmospheric Research (OAR) for the purpose of studying hurricane intensity change at high resolution. The scientific documentation for the original HWRF model, which is also a good reference for the HWRFx model, is available from Gopalakrishnan et al. (2011). The HWRFx is a non-hydrostatic forecast model. The non-hydrostatic model formulation is of unique design, where hydrostatic equations are adjusted to take into account non-hydrostatic motions. The methodology for this aspect is described fully in Janjic et al. (2001), and Janjic (2003). The model uses a multiple grid system with a 27 km parent domain and a 9 km moving nest (henceforth, 27:9 km), which matches that of the operational HWRF model (use by the National Hurricane Center) through the 2011 hurricane season. It has 42 vertical levels in a hybrid pressure-sigma coordinate system.

In terms of model initialization and parameterization, the HWRFx model uses GFDL initial conditions, where the GFDL initial conditions are formed using an axisymmetric version of the GFDL hurricane model (Yeh et al. 2011). The short wave radiation parameterization is provided by the Dudhia scheme (Dudhia 1989). The long

wave radiation parameterization uses the techniques of Mlawer et al. (1997). The Ferrier scheme is used for the microphysics (Ferrier et al. 2002). Convection parameterization in the HWRFx is from the simplified Arakawa-Schubert scheme (Hong and Pan 1998), and the planetary boundary layer parameterization is provided by the methods of Hong and Pan (1996). The surface layer scheme is from Moon et al. (2007), and the ‘Noah’ land-surface model provides the lower boundary forcing over land (Ek et al. 2003). The ocean sea surface temperatures are initialized from the GFS analysis at 1° resolution and kept constant through each forecast run. Note: the HWRFx physical parameterizations differ from HWRF model for the short and long wave radiation schemes, and for the land and ocean schemes (Yeh et al. 2011). Additionally, the operational HWRF model uses a different vortex initialization which is described in the model’s scientific documentation (Gopalakrishnan et al. 2011).

The HWRFx version used in this study is without ocean coupling, but is of real data simulations from three Atlantic storms from 2005: two separate simulations each of Hurricane’s Emily and Wilma, and one simulation of Hurricane Katrina. All of the diagnostics and calculations are performed with only the inner nested grid. The model data has been interpolated from a latitude-longitude grid to a cylindrical grid, with radial grid spacing of 2 km and azimuthal grid spacing of 1° on a radial domain extending to 250 km from the storm center. The storm center in the HWRFx model is defined as the location of the minimum dynamic pressure, and this is approximately coincident with the center point of the nested grid. The uncertainty is a result of the method used to keep the nested domain at the defined center of the storm. The logic is that if the storm center moves more than 27 km (or 3 nested grid points) then the nested domain is moved so as

to maintain a storm centered grid. So, the actual storm center and the center of the nested grid are not necessarily exactly synchronized at every time step. This will be important to keep in mind for some of the study results. Also, for the diagnostic analyses the vertical coordinates have been interpolated from the original hybrid pressure-sigma coordinates to height coordinates.

2.2 Storm Background and Simulation Overviews

As previously mentioned, simulations from three storms were chosen from the 2005 Atlantic tropical cyclone season for this study. There are a total of five separate simulations: two from Hurricane Emily, two from Hurricane Wilma and one from Hurricane Katrina. These storms were chosen from the available simulations to cover a broader spectrum of TC evolution and environmental conditions. To illustrate this, a brief synopsis of each of the actual storms is given followed by track, intensity, and kinetic energy comparisons between the real and simulated storms.

2.2.1 Hurricane Emily

The information for the following synopsis of Hurricane Emily has been supplied by the NHC Tropical Cyclone Report by Franklin and Brown (2006). Figure 2.1 shows the best track positions and Figure 2.2 shows the best track intensity of the storm through its lifetime. The tropical depression that became Hurricane Emily formed July 11th approximately 1075 nmi (nautical miles) east of the southern Windward Islands. The depression moved westward through a fairly dry area under moderate easterly shear. It then formed into a tropical storm at 0000UTC July 12th about 800 nmi east of the southern Windward Islands. At this time the storm translational speed picked up to 17 kt

due to a low level increase in the easterlies. This low level surge also brought a drier environment and created westerly shear over the storm core. These features inhibited convection within the storm. On July 13th the convection was still disorganized and there were little to no changes evident in the flight-level winds. However, visual estimates of the state of the sea surface indicated that the surface winds were increasing. Based on aircraft data, the circulation center seemed to have reformed to the northeast of its previous position sometime around 0000UTC July 14th, and strengthened the storm to hurricane intensity. At this time the storm was approximately 85 nmi to the east-southeast of Grenada. The convection formed a more symmetric shape in the storm and as the storm passed over Grenada at 0700UTC July 14th its maximum winds reached 75 kt.

Having entered the Caribbean Sea, Emily turned west-northwest, and it would keep this heading throughout the next week as a mid-level high pressure built westward to the north of the storm. The storm intensified while crossing the Caribbean Sea and reached a maximum intensity of 115 kt (Category 4) with a minimum central pressure of 952 hPa early on July 15th. At 1200UTC aircraft reconnaissance data reported concentric eyewalls of 8 and 25 nmi diameter. By 1800UTC the storm had weakened considerably to a Category 2. It then reintensified through July 16th as it passed south of Jamaica reaching 140 kt (Category 5) by 0000UTC July 17th. A slow weakening began after this, although there was no clear external synoptic forcing contribution nor was there evidence of any concentric eyewalls. Emily passed over Cozumel as a 115 kt, Category 4 storm and made landfall on the Yucatan Peninsula at 0630UTC July 18th. After traveling across the Yucatan, it entered the Gulf of Mexico around 1200UTC of the same day, still at

hurricane strength. Once back over warm waters, it reintensified reaching 80 kt by 1200UTC July 19th. It had a larger wind field after passing over the Yucatan, but with the reintensification to 110 kt, it developed a sharp wind maximum. As it neared the Mexican coast land based radar as well as aircraft reconnaissance captured evidence of a distinct concentric eyewall, with the strongest flight-level winds occurring in the outer ring. The storm made landfall at 1200UTC July 20th near San Fernando, Mexico as a 110 kt Category 3 storm. Once over land, Emily weakened and dissipated over the Sierra Madre Oriental mountain range.

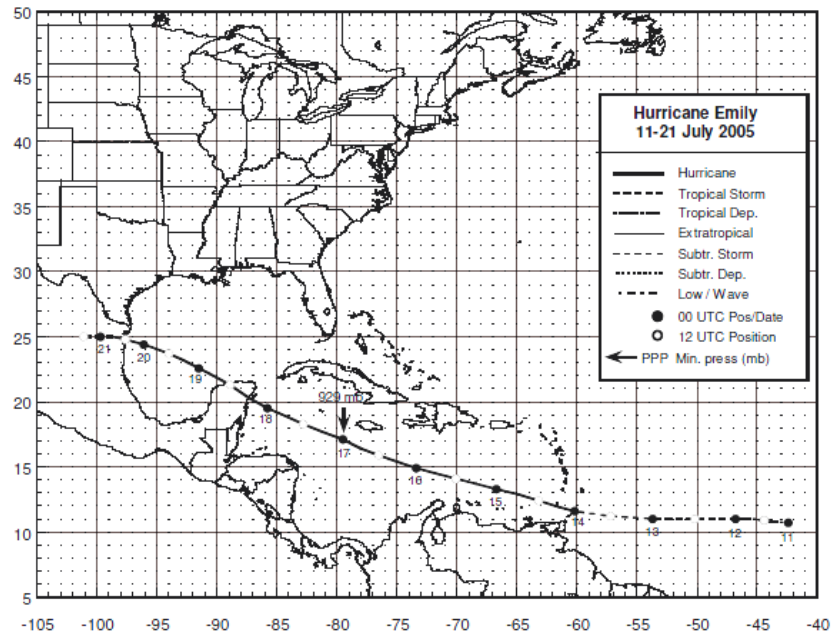


Figure 2.1: Best track positions for Hurricane Emily, 11-21 July 2005 (Franklin and Brown 2006)

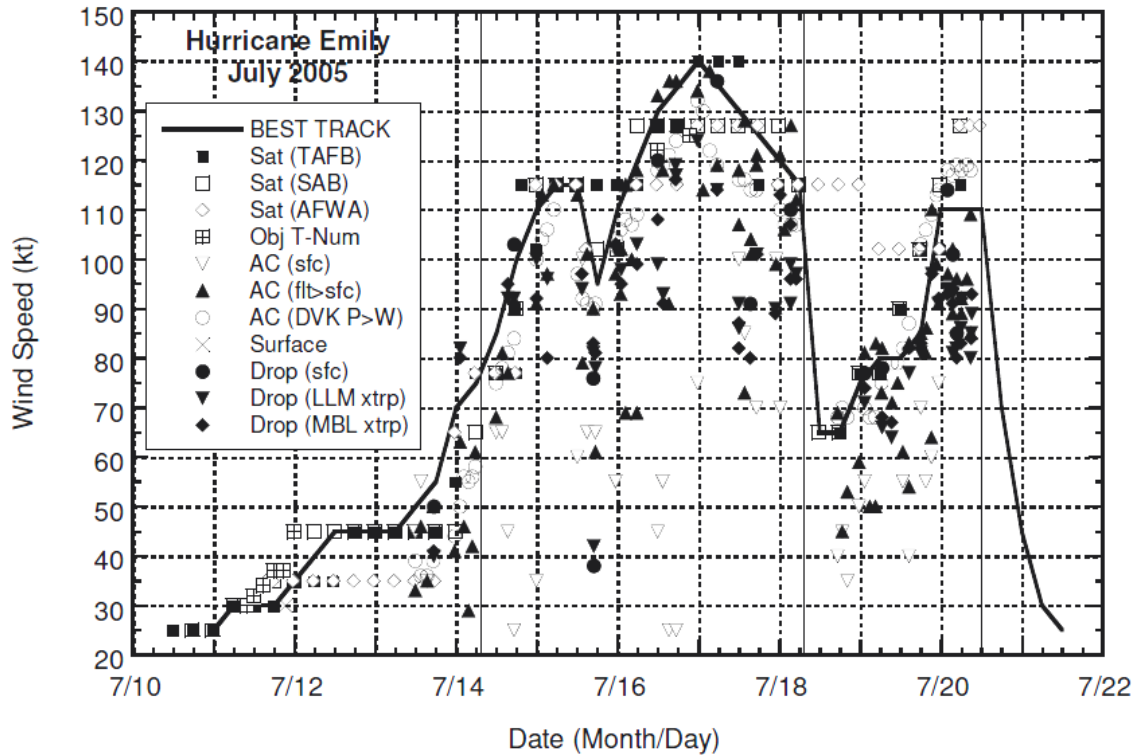


Figure 2.2: Best track intensity along with wind observations of Hurricane Emily, 11-21 July 2005 (Franklin and Brown 2006)

Two model simulations were chosen for this storm. The first is initialized July 13th at 00Z and the second July 15th at 00Z. The first simulation begins when the storm is not yet to hurricane strength and is still east of the Caribbean, and the second simulation begins when the storm is far more organized, at hurricane strength and within the Caribbean Sea. Figures 2.3 and 2.4 show the HWRFx simulation tracks of the storm along with the matching best track positions from the actual storm. The model did a fair job with the tracks, although the first simulation track is consistently too far north-northeast, taking the storm to the north of the island of Jamaica. The second simulation track is closer to the actual storm track, although it, too, takes the storm a little too far north-northeast, skimming the island of Jamaica and the tip of the Yucatan peninsula.

The landfall position in Mexico for the second simulation is fairly consistent with the actual landfall.

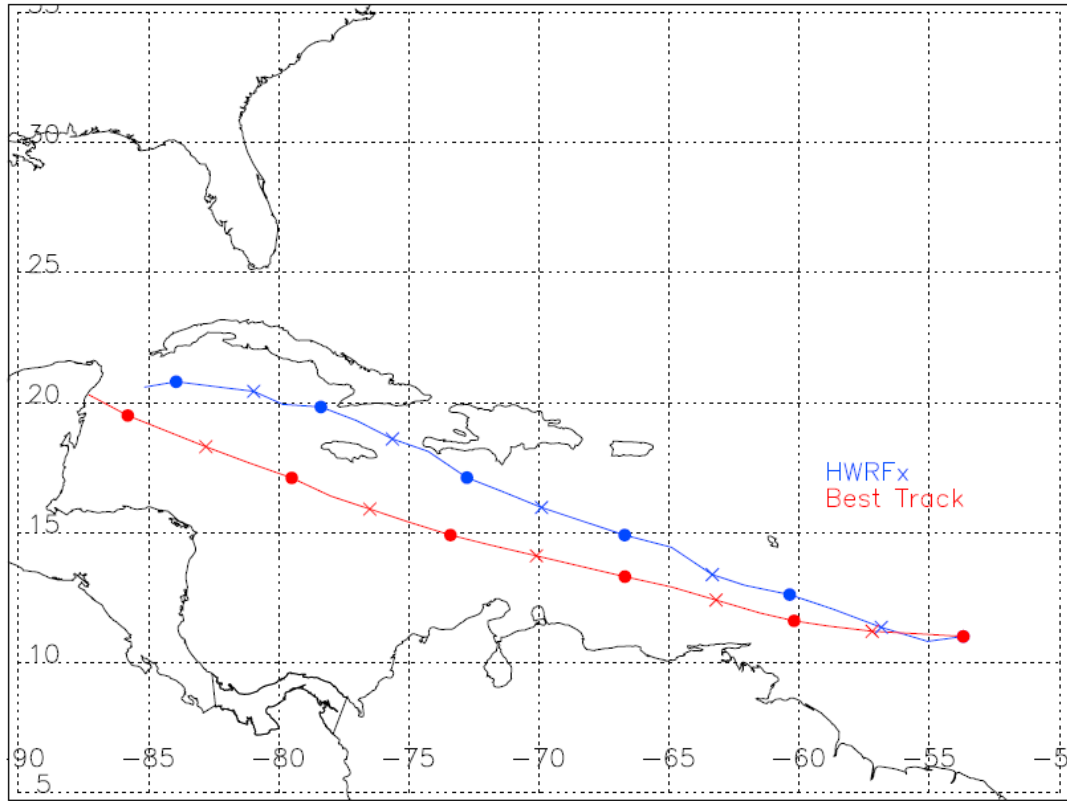


Figure 2.3: Track positions for the 13 July 2005 HWRFX simulation (blue) of Hurricane Emily along with the matching best track positions (red) of the actual storm. The solid dots indicate the 00Z positions, and the 'X' marks indicate the 12Z positions.

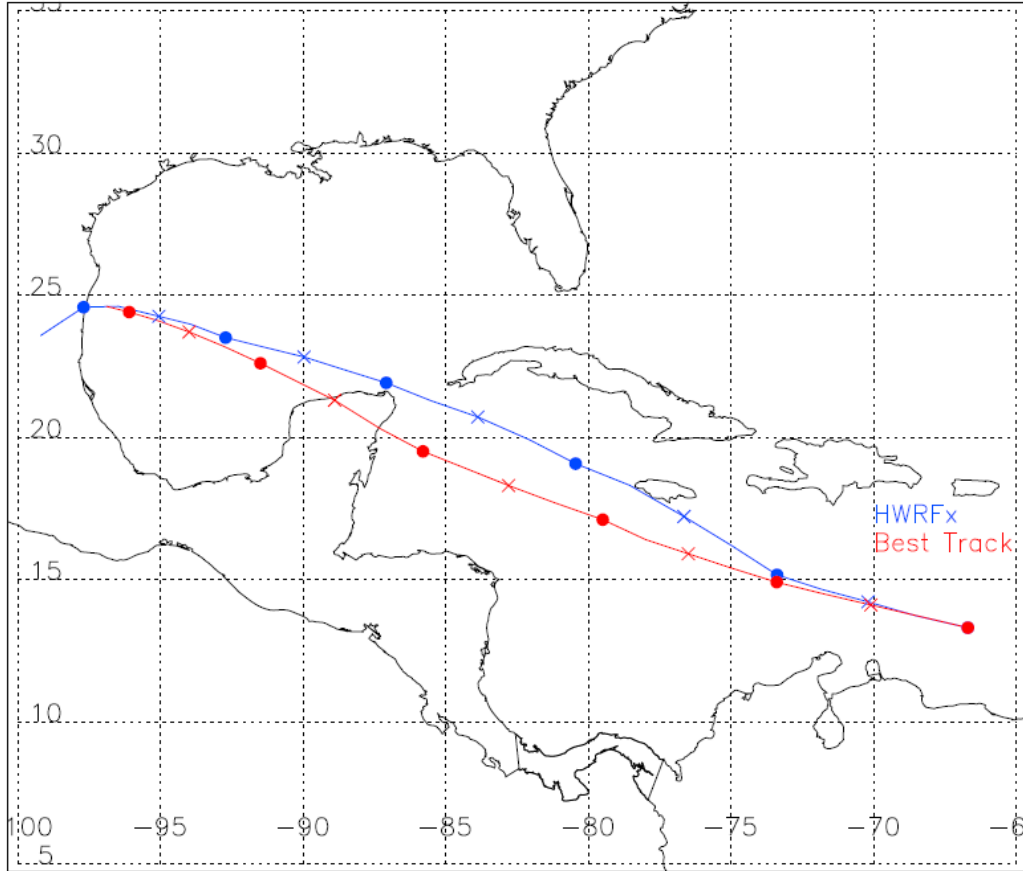


Figure 2.4: Track positions for the 15 July 2005 HWRFx simulation (blue) of Hurricane Emily along with the matching best track positions (red) of the actual storm. The solid dots indicate the 00Z positions, and the ‘X’ marks indicate the 12Z positions.

The model intensities and the best track intensities for each simulation of Hurricane Emily are shown in Figures 2.5 and 2.6. The model intensities are simply the magnitude of the maximum 10 m wind in the nested domain at each forecast time. For the 13 July 2005 simulation of Hurricane Emily (Figure 2.5) the model over intensifies the storm initially, but then levels off when the actual storm experiences two periods of intensification, the second of which brings the storm to its peak intensity of over 70 m/s (Category 5). The simulated storm reaches no such intensity peaking at a little over 50 m/s (barely a Category 3).

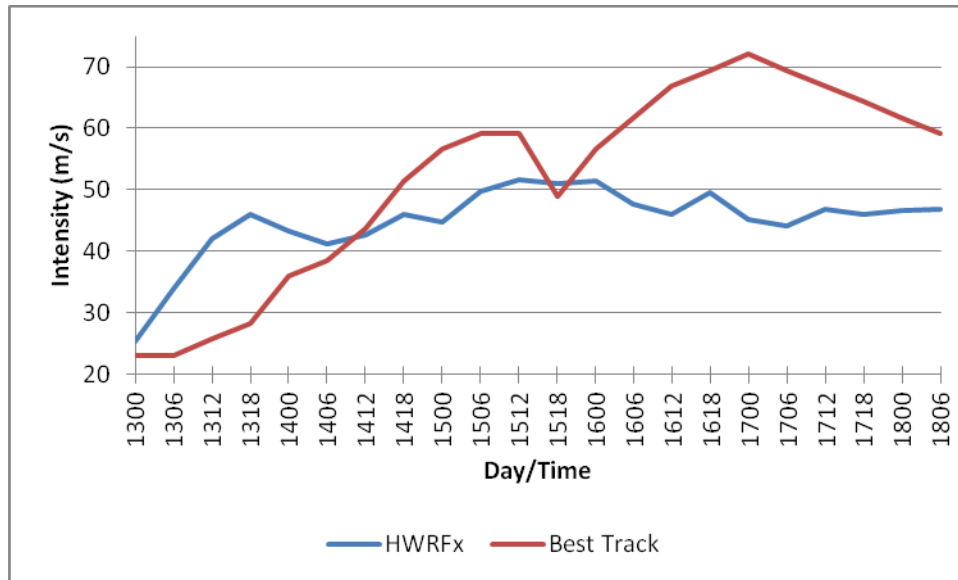


Figure 2.5: Surface intensity comparison between the 13 July 2005 HWRfX simulation of Hurricane Emily (blue) and the NHC best track intensity (red).

The 15 July 2005 simulation (Figure 2.6) is hampered by a poor initialization as evident by its more than 5 m/s weaker initial intensity. Aside from this, the model does not capture the rapid intensification that the actual storm experienced. There is no big drop in the simulation intensity, but that is because the model storm did not pass over the Yucatan as the actual storm did. However, the model storm does intensify the storm during its passage over the Gulf of Mexico much like the actual, although more moderately so.

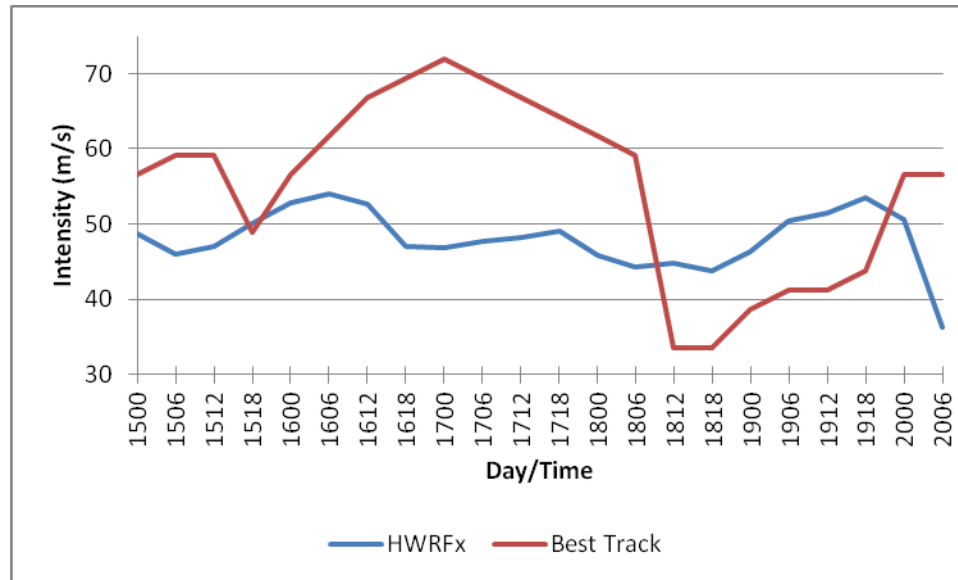


Figure 2.6: Surface intensity comparison between the 15 July 2005 HWRFX simulation of Hurricane Emily (blue) and the NHC best track intensity (red).

2.2.2 Hurricane Katrina

The information for the following synopsis of Hurricane Katrina has been supplied by the NHC Tropical Cyclone Report by Knabb et al. (2006). Figure 2.7 shows the best track positions and Figure 2.8 shows the best track intensity of the storm through its lifetime. What would eventually become Hurricane Katrina formed into a tropical depression (TD12) around 1800UTC August 23rd approximately 175 nmi southeast of Nassau. It formed from a combination of the mid-tropospheric remnants of tropical depression 10, a tropical wave originated off of Africa, and the interactions of these features with an upper level trough that had begun to weaken. The system became better organized over the Bahamas the evening of August 23rd, and deep convection increase overnight in the eastern portion of the cyclone began forming a well-defined band early August 24th. Based on aircraft reconnaissance data, the system was upgraded to a tropical storm at 1200UTC August 24th when it was centered over the central Bahamas. A weakness in the low-tropospheric subtropical ridge allowed the storm to take a more

northwesterly path. As the storm developed an inner-core and deepened, it came under the influence of a strengthening middle to upper level tropospheric ridge located over the northern Gulf of Mexico and the southern United States. This ridge turned the storm to a more westward path toward southern Florida on August 25th. An intense blow up of deep convection over the low-level center caused the storm to further strengthen and it reached hurricane strength around 2100UTC August 25th, just two hours before its center made landfall on the southeast coast of Florida as a 75 kt, Category 3 hurricane. The ridge mentioned earlier provided a west southwesterly steering flow during this time. A well-defined eye could be seen in WSR-88D Doppler radar directly before the storm made landfall in Florida, and this eye feature then proceeded to become more clearly defined as the storm traversed the southern Florida peninsula. The storm spent only six hours over land and much of this time was spent over the Everglades, the warm, moist environment of which may have been an important contributing factor in the unusual developments of the storm's eye feature. The land passage did, however, weaken the system to tropical storm strength (60 kt) and it entered into the Gulf of Mexico at 0500UTC August 26th. Once again over water, it quickly reintensified to hurricane strength (65 kt). At this time a very large upper-level anticyclone taking up much of the Gulf of Mexico provided the storm with a low shear environment and efficient upper-level outflow. Katrina then began a rapid intensification (an increase of more than 30 kt in 24 h) going from 65 to 95 kt by 0600UTC August 27th. An eye could be clearly seen on satellite imagery earlier on this day and the storm reached 100 kt by 1200UTC August 27th. The inner eyewall then broke down and a new outer eyewall formed, during which the storm intensity remained at 100 kt. The wind field expanded substantially nearly doubling in size with tropical

storm force winds extending out to 140 nmi from the center of the storm by the end of the day. The ridge started shifting eastward, and a mid-latitude trough growing over the north central United States provided a westward steering current August 27th and a turn toward the northwest on August 28th as the storm moved around the western edge of the retreating edge. The new eyewall contracted to a well-defined ring by 0000UTC August 28th. A second rapid intensification began and Katrina intensified from a Category 3 to a 5 in less than 12 h reaching 145 kt by 1200UTC August 28th. By 1800UTC the storm reached its peak intensity of 150 kt approximately 170 nmi southeast of the mouth of the Mississippi river. The wind field continued to expand with hurricane force winds eventually extending out to 90 nmi from the center of the storm and tropical storm force winds extending out 200 nmi. The eyewall began to erode on the southern side late on August 28th while a second outer ring of convection came together. The storm turned northward around the ridge (now over Florida) August 29th and made landfall near Buras, Louisiana at 1110UTC August 29th at 110 kt (Category 3) and then continued northward making its final landfall near the Louisiana/Mississippi border at 105 kt intensity. Internal structure changes appear to be the cause for rapid weakening that occurred in the last 18 h before landfall, however, the tropical storm and hurricane force winds extended out just as far as when the storm was at its most intense. The storm quickly dissipated after landfall, weakening to Category 1 intensity by 1800UTC August 29th.

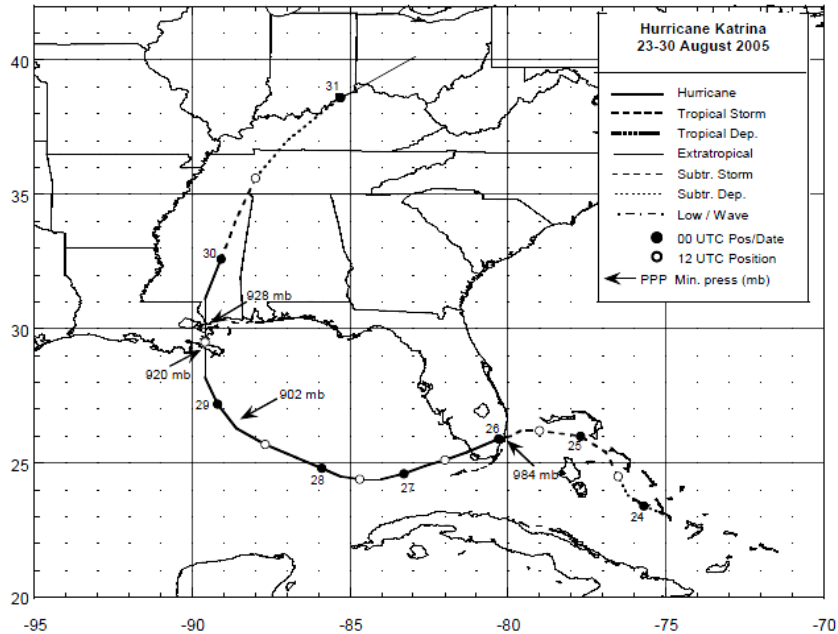


Figure 2.7: Best track positions for Hurricane Katrina, 23-30 August 2005 (Knabb et al. 2006)

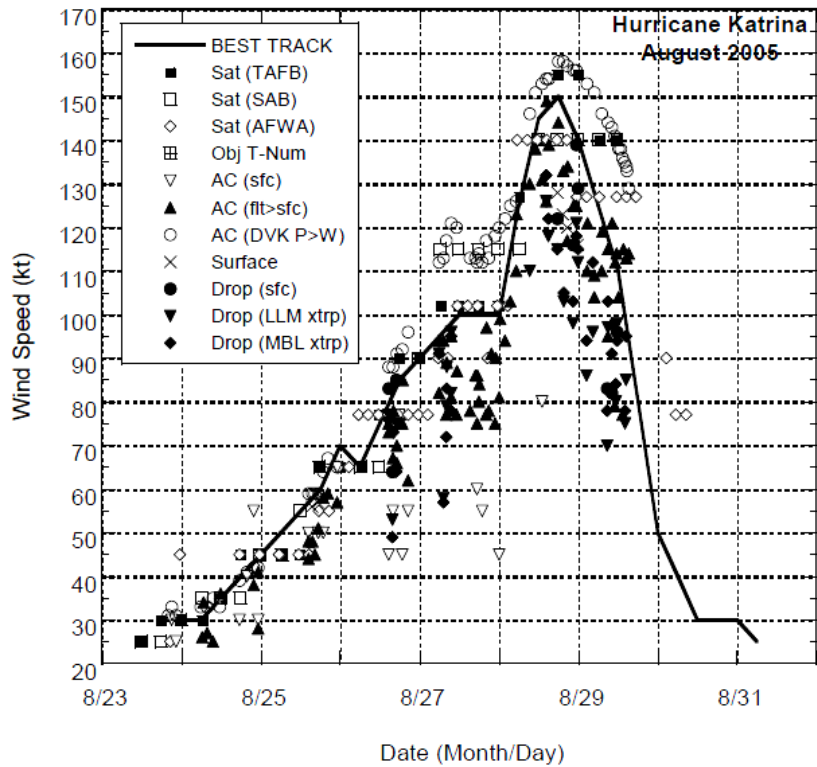


Figure 2.8: Best track intensity along with wind observations of Hurricane Katrina, 23-30 August 2005 (Knabb et al. 2006)

One model simulation is used for Hurricane Katrina, and it is initialized at August 26th at 00Z when the storm was just over the southern tip of Florida and moving into the Gulf of Mexico. The track of the HWRFx simulation along with the matching best track positions of the actual storm is shown in Figure 2.9. The simulation track compares quite well to the actual track. It was off-track mostly in that it's track went too far westward and made landfall about one degree longitude too far west in Louisiana.

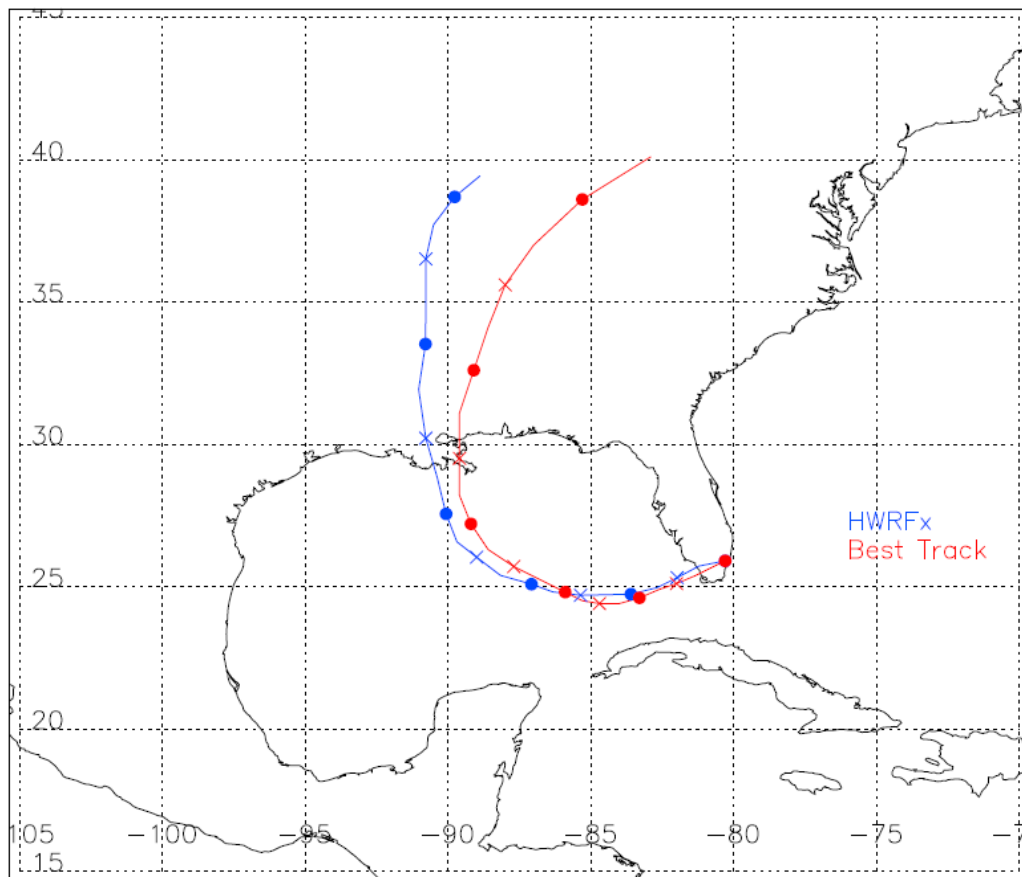


Figure 2.9: Track positions for the 26 August 2005 HWRFx simulation (blue) of Hurricane Katrina along with the matching best track positions (red) of the actual storm. The solid dots indicate the 00Z positions, and the 'X' marks indicate the 12Z positions.

The model simulation intensities and the best track intensities for the simulation of Hurricane Katrina are shown in Figure 2.10. The model did a fairly good job with the intensification and weakening of the storm, however it did not capture the impressive

rapid intensification that the actual storm went through to reach its peak intensity as a Category 5 storm. The simulated storm only reached peak intensity at a bit over 60 m/s as a Category 4 storm. Overall, it was a comparatively good intensity forecast.

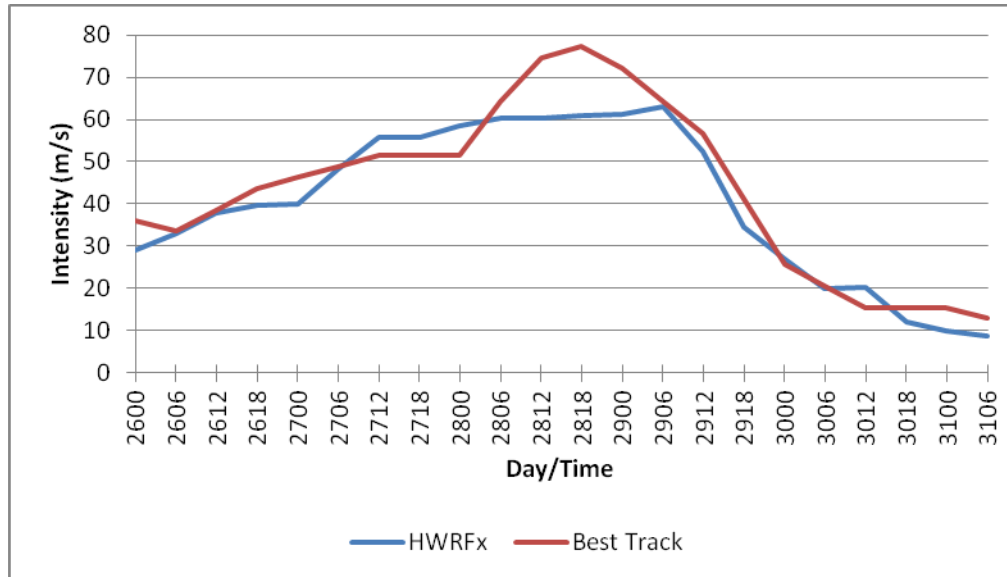


Figure 2.10: Surface intensity comparison between the 26 August 2005 HWRfX simulation of Hurricane Katrina (blue) and the NHC best track intensity (red).

2.2.3 Hurricane Wilma

The information for the following synopsis of Hurricane Wilma has been supplied by the NHC Tropical Cyclone Report by Pasch et al. (2006). Figure 2.11 shows the best track positions and Figure 2.12 shows the best track intensity of the storm through its lifetime. During the second week of October 2005 a large low-tropospheric circulation and a broad area of convective activity developed in the Caribbean. From this a concentrated area of disturbed weather and a surface low pressure formed near Jamaica. By 1800UTC October 14th this organized into a tropical depression centered around 190 nmi east southeast of Grand Cayman. There was a weak steering flow during the next few days, so the depression experienced slow and erratic movement during this time,

however, the system slowly strengthened. It was upgraded to tropical storm Wilma at 0600UTC October 17th. The next day the storm turned towards a more west northwesterly path and strengthened to a hurricane. Later on October 18th the storm began an explosive intensification which carried through into the next day. By 0600UTC October 19th Wilma had reached 150 kt, a Category 5 hurricane. This is a previously unheard of intensification within 24 h for the Atlantic basin. The storm reached its peak intensity of 160 kt by 1200UTC October 19th, and during this time aircraft reconnaissance data showed that the storm's eye had contracted to around 2 nmi diameter with a minimum central pressure of 882 hPa (also a record for the Atlantic). The Category 5 intensity was sustained until October 20th when the winds dropped to 130 kt and the tiny eye was replaced by a much larger 40 nmi diameter one. The storm's eye remained this large or larger for the remaining duration of its lifetime. By October 21st a mid-level ridge to the northeast grew and a series of shortwave troughs in the westerlies started to break down the high pressure over the Gulf of Mexico. This enabled the storm to take a more northwest and north-northwest motion towards the Yucatan Peninsula. It made landfall on Cozumel at 2145UTC October 21st at 130 kt (Category 4) and it was likely only slightly weaker when it crossed the coast of the Yucatan 5 h later. The mid-tropospheric high to the north dissipated and the storm slowly moved northward crossing the extreme northeast portion of the Yucatan Peninsula, and the storm emerged into the Gulf of Mexico at approximately 0000UTC October 23rd at 85 kt intensity. A strong mid-tropospheric trough moving east from the central United States provided a strong southwesterly steering current which moved the storm more quickly to the northeast towards southern Florida. The upper-level flow increased over the storm as did the

vertical deep shear, which was up to 25 kt by early October 24th. Despite this strong shear the storm continued to strengthen over the southeast Gulf of Mexico and the intensity was up to 110 kt as the storm approached Florida. It made landfall in southwest Florida near Cape Romano at 1030UTC October 24th as a 105 kt Category 3 storm. From there Wilma continued to pick up translational speed, and moved across southern Florida at 20 to 25 kt, crossing the state in about 4.5 h. During this time the maximum winds dropped to 95 kt (Category 2). There was a strong cold front from a mid-tropospheric trough which moved across to the west of the storm, but the cold, drier air associated with it were not able to penetrate the storm's core, and Wilma again reintensified reaching 110 kt by 0000UTC October 25th. The storm finally gave in to unfavorable environmental conditions as it quickly moved (at 40-45 kt) to the northeast over the Western Atlantic transitioning into an extratropical cyclone and was eventually dissolved within another extratropical cyclone over Nova Scotia.

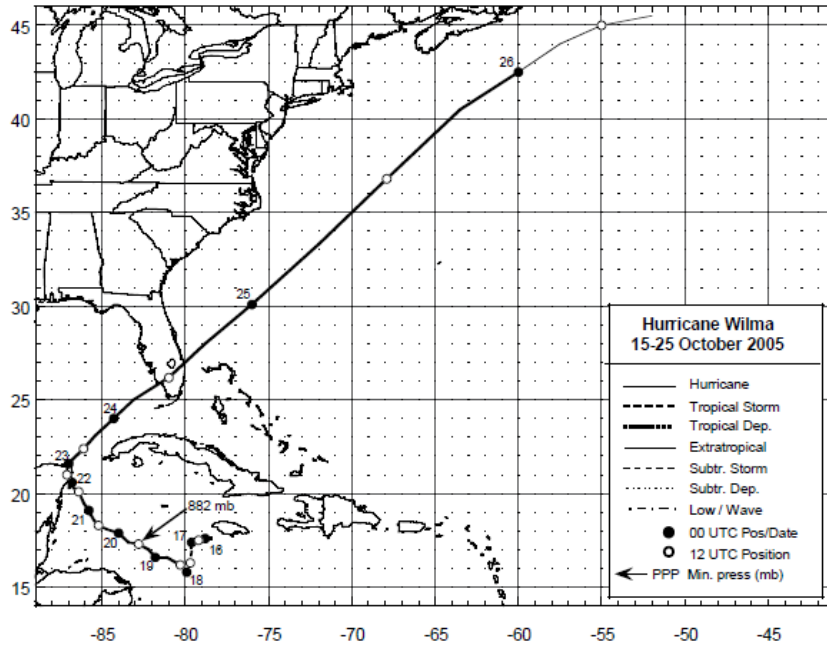


Figure 2.11: Best track positions for Hurricane Wilma, 15-25 October 2005 (Pasch et al. 2006)

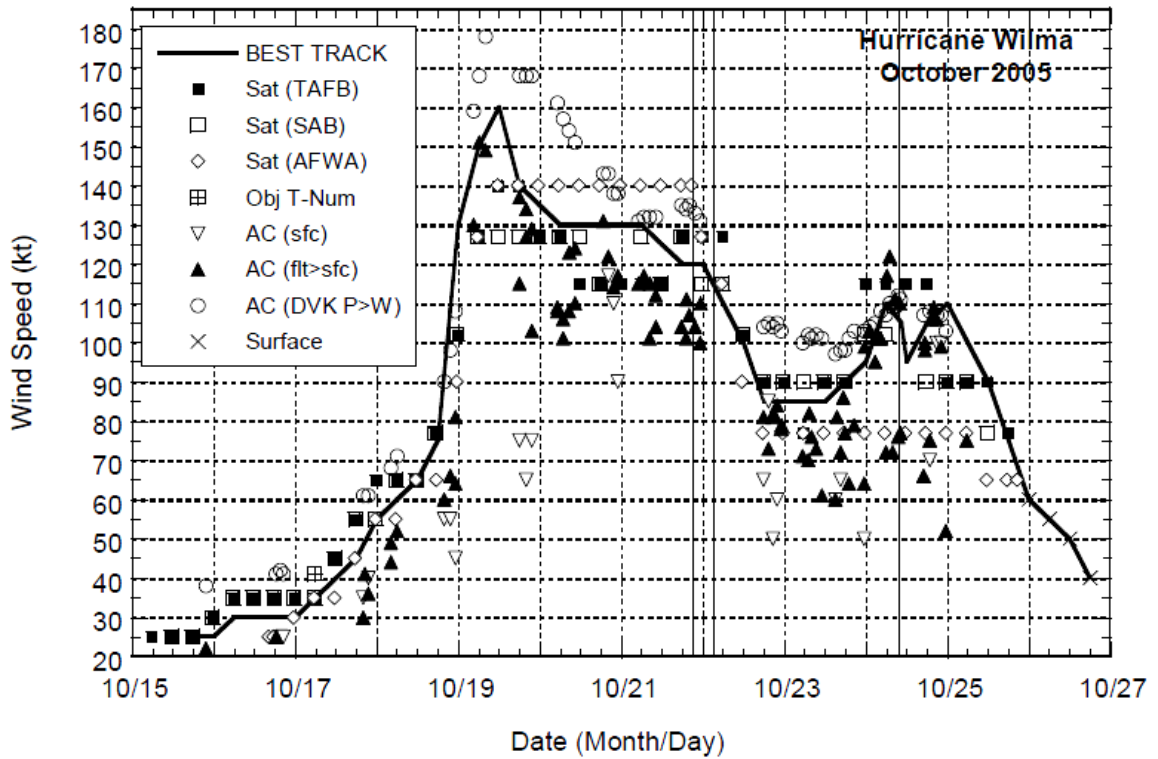


Figure 2.12: Best track intensity along with wind observations of Hurricane Wilma, 15-25 October 2005 (Pasch et al. 2006)

Two simulations are used of Hurricane Wilma. One covers the first part of the storm evolution in the Caribbean and into the Gulf of Mexico (initialization on October 18th at 00Z), and the second covers the later part of the storm evolution beginning in the Gulf of Mexico and then continuing in the Atlantic through extratropical transition (initialization on October 22nd at 00Z). The first simulation track along with the matching best track positions of the actual storm is shown in Figure 2.13, and a similar plot for the second is shown in Figure 2.14. Again, the model did a pretty good job with the storm tracks. The first simulation track took the storm a bit too far west over the tip of the Yucatan Peninsula. It correctly turned the storm almost 90° northeast as it entered the Gulf of Mexico. The passage in the Gulf of Mexico was shifted too far north, but otherwise the track is very similar to the actual track. The second simulation was very slightly slow in turning the storm as it moved off the Yucatan Peninsula. Otherwise, the track is nearly spot on until the very end of the simulation when the storm curves too far eastward.

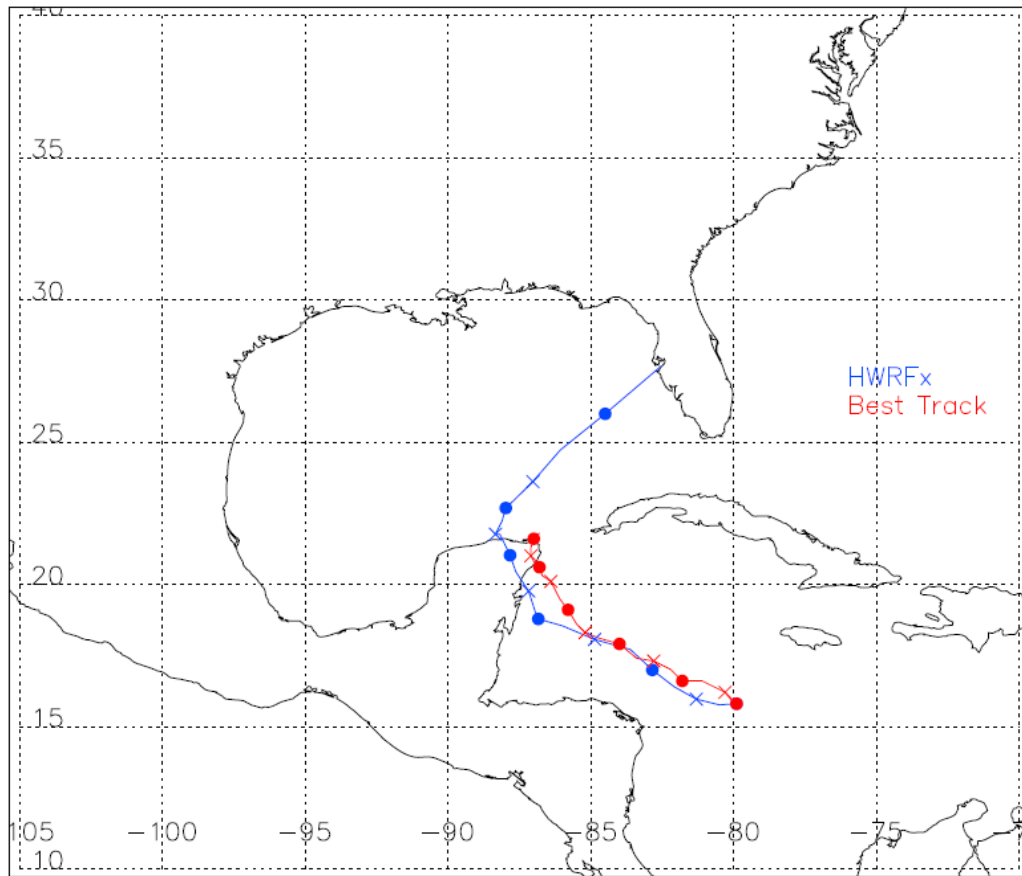


Figure 2.13: Track positions for the 18 October 2005 HWRFx simulation (blue) of Hurricane Wilma along with the matching best track positions (red) of the actual storm. The solid dots indicate the 00Z positions, and the 'X' marks indicate the 12Z positions.

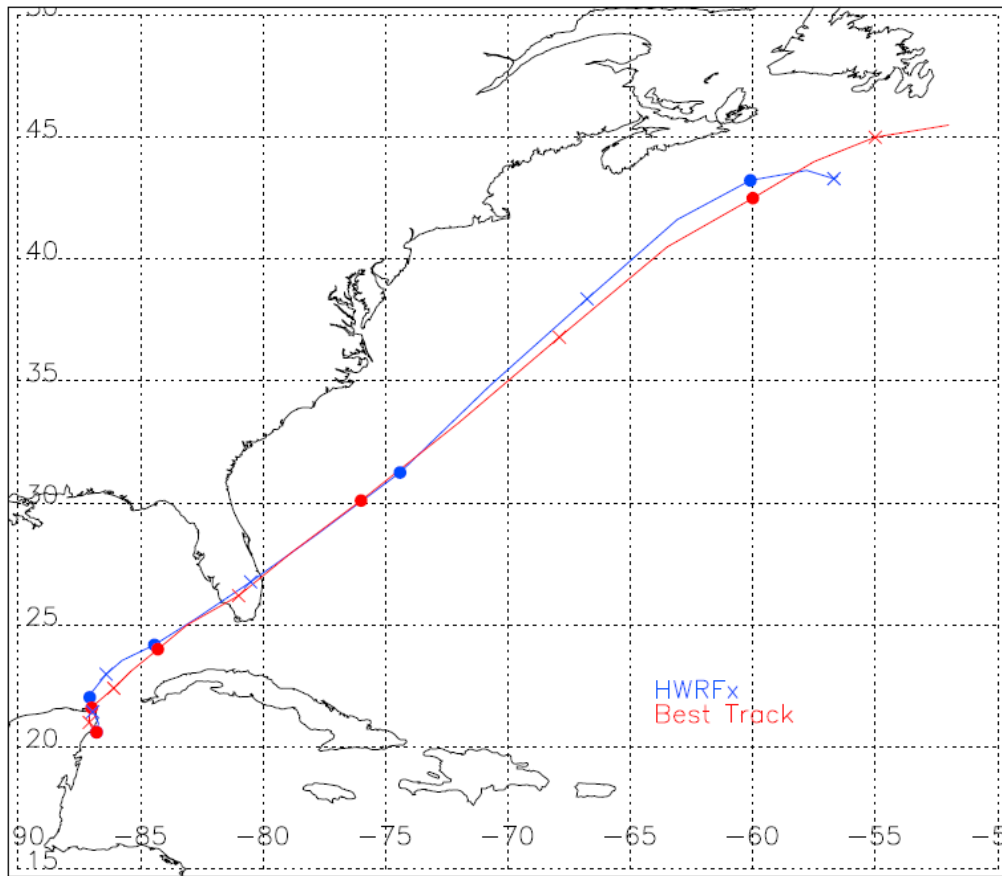


Figure 2.14: Track positions for the 22 October 2005 HWRFX simulation (blue) of Hurricane Wilma along with the matching best track positions (red) of the actual storm. The solid dots indicate the 00Z positions, and the ‘X’ marks indicate the 12Z positions.

The model intensities and the best track intensities for each simulation of Hurricane Wilma are shown in Figures 2.15 and 2.16. The 18 October 2005 simulation intensity evolution is quite different than that of the real storm (Figure 2.15). This is due to a couple of factors, which when taken into account make the intensity forecast not necessarily so bad. Firstly, the model, even with its 9 km inner nest grid resolution, is still too coarse to adequately resolve the storm’s early tiny eye and the eyewall replacement cycle which took place shortly after the storm reached its peak intensity. Secondly, while the placement of the track compares well with the actual storm the timing is off. The simulated storm ends with the cyclone on the western coast of Florida,

but at the equivalent time the actual storm was only just off of the coast of the Yucatan peninsula. With these factors in mind, the intensity evolution of the simulated storm does take the storm from tropical storm strength up to a major hurricane (Category 3) within the first 48 h. Then the simulated storm weakens through the passage over the Yucatan peninsula and then reintensifies as it crosses the Gulf of Mexico. The actual storm at this time (the end of the storm simulation) had yet to make its way across the Gulf of Mexico where it reintensified. So, that part of the storm forecast is actually fairly good.

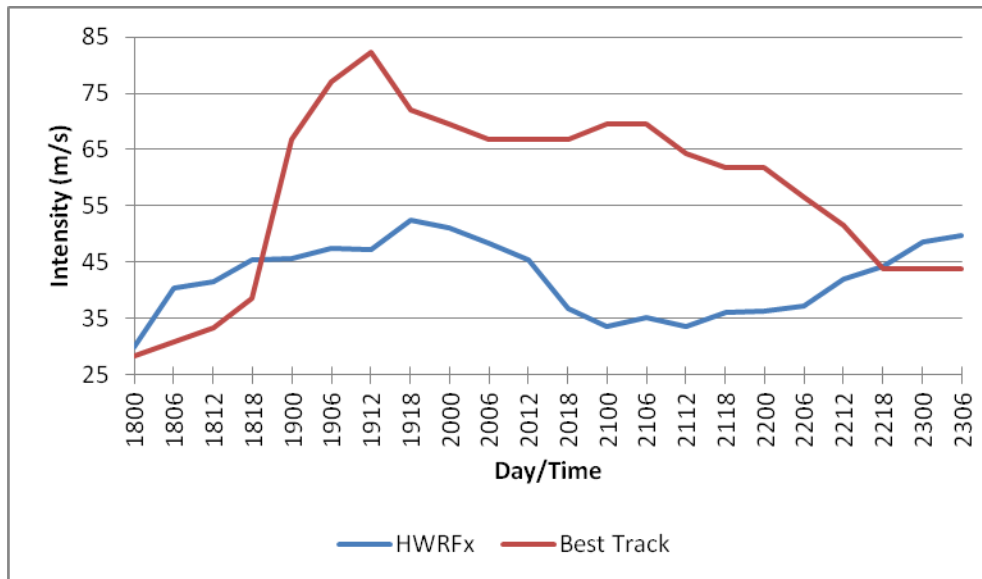


Figure 2.15: Surface intensity comparison between the 18 October 2005 HWRfX simulation of Hurricane Wilma (blue) and the NHC best track intensity (red).

The 22 October 2005 simulation of Hurricane Wilma intensity evolution, despite an approximate 5 m/s weaker initial intensity, compares reasonably well to that of the actual storm (Figure 2.16). The early weakening as the storm moves off of the Yucatan followed by intensification over the Gulf of Mexico and then a weakening pattern as the storm travels over the Atlantic and begins experiencing extratropical transition is all evident in both the actual and the simulated storm intensity evolutions.

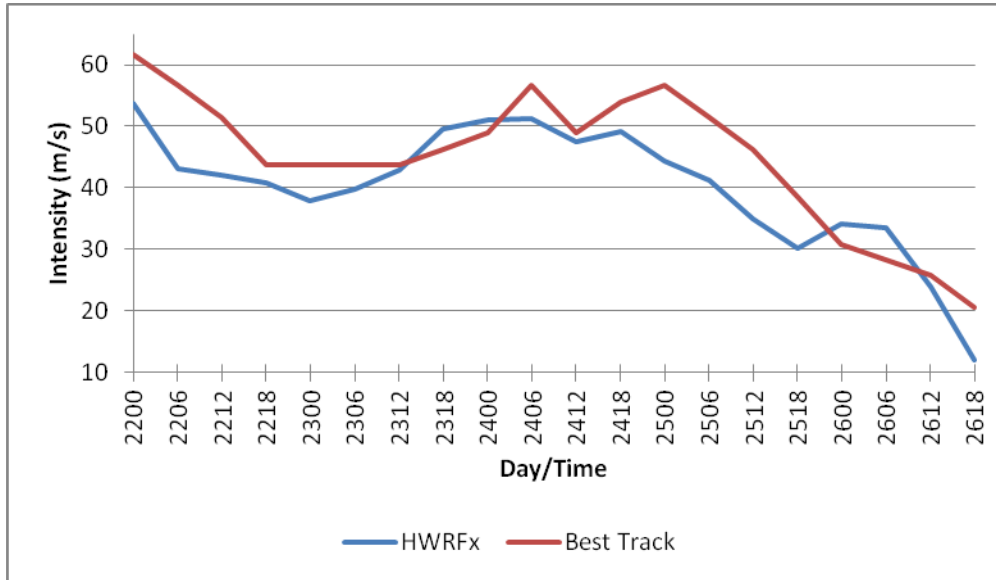


Figure 2.16: Surface intensity comparison between the 22 October 2005 HWRFX simulation of Hurricane Wilma (blue) and the NHC best track intensity (red).

2.3 Intensity and Kinetic Energy

Now that the model tracks have been reviewed, the next thing to look at is some measure of the structure. Maclay et al. (2008) demonstrated that the area integrated kinetic energy (KE), which depends both on the intensity and the wind structure, can be used as a rough measure of structure. The kinetic energy calculations are fairly straight forward, though slightly different, for both the real storm data and for the model data. The differences simply result from the data that is available for the real storm versus what is available for the model storm.

Consider first the real storm data. The kinetic energy calculations for the real storm data are identical to those used in Maclay et al. (2008), and are described by:

$$KE = \frac{\rho_o \Delta z}{2} \int_0^{2\pi R} \int_0^R (u^2 + v^2) r dr d\theta \quad (2.1)$$

where u is radial wind, v is tangential wind, ρ_o is a constant air density (0.9 kg m^{-3} , a typical air density at 700 hPa), r is radius, θ is azimuth, and z is height. The wind data is from the aircraft reconnaissance flight-level data for the storm, and note here that the standard flight-level is approximately 700 hPa. The winds are assumed to be representative of the storm structure of a 1 kilometer depth, so Δz is 1000 m. The radial increment of the aircraft reconnaissance reanalysis data (Mueller et al. 2006) is 4 km, and the azimuthal increment is 22.5° . The radial domain is from the storm center out to 200 km.

The model data kinetic energy calculations use the following equation:

$$KE = \frac{1}{2} \int_{z_1}^{z_2} \int_0^{2\pi R} \int_0^R \rho(u^2 + v^2 + w^2) r dr d\theta dz \quad (2.2)$$

where u is radial wind, v is tangential wind, w is vertical wind, ρ is air density, r is radius, θ is azimuth, and z is height. Notice the addition of the vertical wind and the air density is no longer assigned a constant value. These additions/alterations are made because the data is available in the model, and it is the more accurate calculation. So as to be consistent with the real-data calculations, the “flight-level” winds are assumed to be representative of the storm structure of a 1 km depth. As previously mentioned, flight-level is approximately 700 hPa, and this roughly corresponds to 3000 m height in the model data.

$$KE = \frac{\Delta z_{3000}}{2} \int_0^{2\pi R} \int_0^R \rho(u^2 + v^2 + w^2) r dr d\theta \quad (2.3)$$

In the model the radial increment is 2 km and the azimuthal increment is 1°. The radial domain is from the center of the grid out to 200 km.

To compare the model to the real data in terms of the storm intensity and structure the approximate 700 hPa 0-200 km integrated kinetic energy is plotted versus the intensity. The intensity used here for the real data is the maximum wind from the flight-level data. The intensity used here for the model data is the maximum wind from the 3000 m height level within the 200 km radial domain. For the model data the KE and intensity both have a modified “121” time filter applied ten times to them. This is done because the model data is in 1 h increments, whereas the reanalysis data is, at best, in 6 h increments. The model data, therefore, is fairly noisy in time. Applying the “121” filter ten times effectively smoothes out the model data fields so that they are more comparable to the reanalysis data. This modified “121” filter can be described by the following equation, where x is the variable being filtered.

$$x(t) = \begin{cases} 0.25[x(t-1) + x(t+1)] + 0.5[x(t)] & \text{for } 0 < t < 126 \\ 0.25[x(t+1)] + 0.75[x(t)] & \text{for } t = 0 \\ 0.25[x(t-1)] + 0.75[x(t)] & \text{for } t = 126 \end{cases} \quad (2.4)$$

In the KE versus intensity plots the model data (“HWRFX Filtered”) time span has been selected to coincide most closely with the available aircraft reconnaissance data (“Recon”) time span for each storm. Also, in all of these figures, the large dot on each line represents the starting point in terms of time for the data. Figure 2.17 shows the KE versus intensity plot for the comparison between the aircraft reconnaissance and the 13 July 2005 simulation of Hurricane Emily. This comparison shows that while the model did not intensify the storm enough it did demonstrate roughly the pattern of

intensification and increase in the wind field (increasing KE) and then a weakening and a more modest decrease in the KE. The model, though, has an additional significant increase in the KE while maintaining or even increasing intensity that is not seen in the real data.

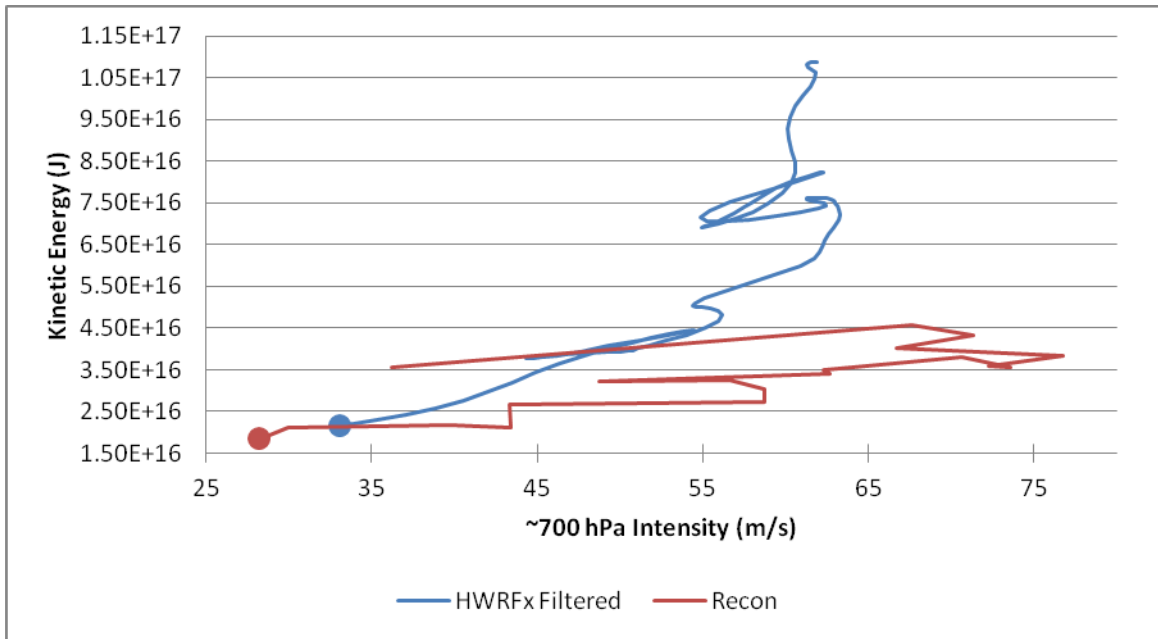


Figure 2.17: Kinetic energy versus intensity for Hurricane Emily (13 July 2005 HWRfX simulation). Recon time span: 13 July at 12Z to 18 July at 18Z; HWRfX time span: 13 July at 00Z to 18 July at 06Z. The solid dots indicate the first data point for each series.

Figure 2.18 shows the KE versus intensity plot for the comparison between the aircraft reconnaissance and the 15 July 2005 simulation of Hurricane Emily. This figure shows that the model wind field was poorly initialized for this simulation, because while the initial intensities are nearly the same between the model and the real data the kinetic energy is way too high in the model field as compared to the real storm data. The model corrects itself a bit as shown by the drop in the kinetic energy, and then assumes the more typical pattern of intensification with modest increase in the KE followed by an increase

in the KE with leveled out intensification and then a weakening and modest decrease in the KE, with the model failing to fully weaken the system as seen in the real storm.

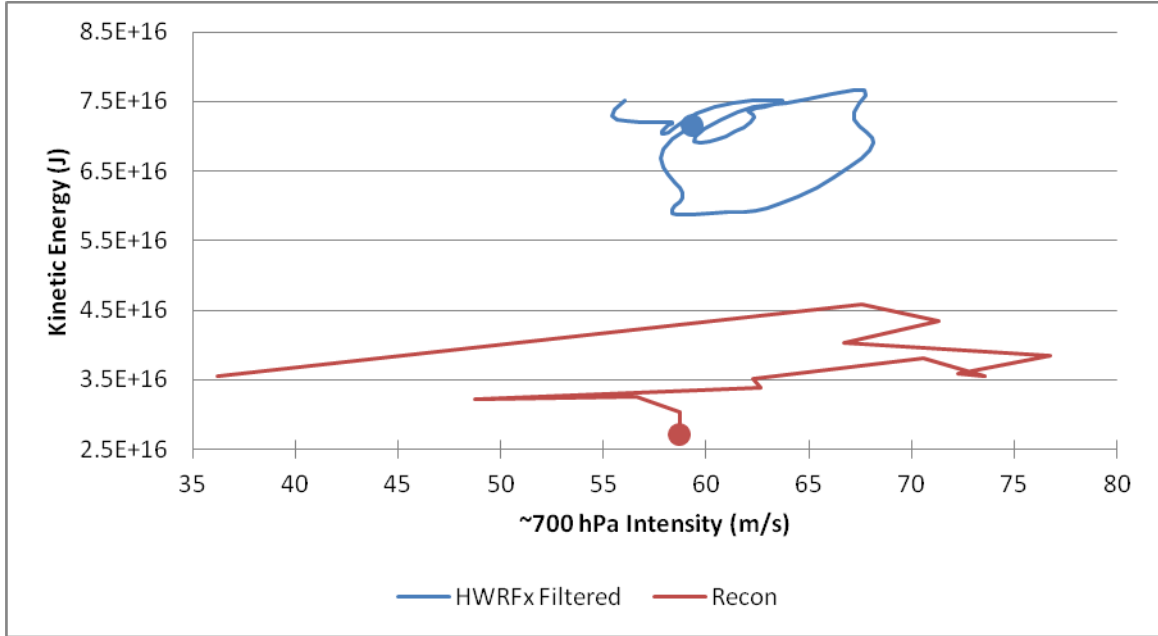


Figure 2.18: Kinetic energy versus intensity for Hurricane Emily (15 July 2005 HWRfX simulation). Recon time span: 15 July at 00Z to 18 July at 18Z; HWRfX time span: 15 July at 00Z to 18 July at 18Z. The solid dots indicate the first data point for each series.

Figure 2.19 shows the KE versus intensity plot for the comparison between the aircraft reconnaissance and 26 August 2005 simulation of Hurricane Katrina. For this case, the model does a good job with the initial intensification and increase in the kinetic energy, but then fails to really weaken the system as seen with the real storm. So the model storm ends up far more intense and with a much larger magnitude wind field (much larger KE) than the actual storm. As a note, the intensities in this figure show the model storm to be much more intense than shown in Figure 2.10. Figure 2.10 shows the surface level storm intensity and Figure 2.19 shows the model equivalent “flight-level” intensity. Therefore, the model storm is more intense at upper levels than the actual storm.

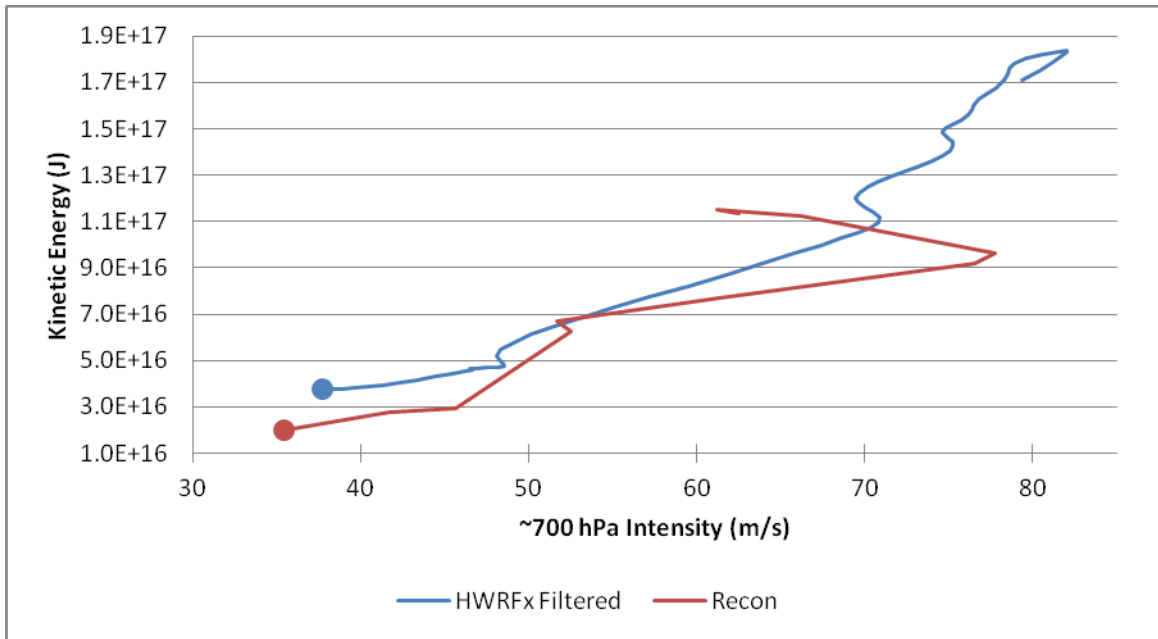


Figure 2.19: Kinetic energy versus intensity for Hurricane Katrina (26 August 2005 HWRFX simulation). Recon time span: 26 August at 00Z to 29 August at 18Z; HWRFX time span: 26 August at 00Z to 29 August at 08Z. The solid dots indicate the first data point for each series.

Figure 2.20 shows the KE versus intensity plot for the comparison between the aircraft reconnaissance and the 18 October 2005 simulation of Hurricane Wilma. Note that the real storm's dramatic eyewall replacement cycle that occurred early in its evolution is easily evident in this figure. There is first the strong intensification to the storm's peak intensity followed by a weakening as the pinhole eye breaks down and is replaced by the secondary eyewall forming a larger eye and then a reintensification to a second intensity peak before weakening again. Maclay et al. (2008) describes this evolution more thoroughly including microwave imagery to confirm the eyewall replacement cycle. Again, while the model is fairly high-resolution it is still not fine enough of a resolution to be able to properly reproduce the storm's remarkable pinhole eye or the structural details of the eyewall replacement cycle. So now consider the model's intensity and KE pattern. Firstly, the model's initial intensity is approximately

10 m/s too high. Secondly, while the model clearly does not capture the details of the pinhole eye, it is encouraging that the model does intensify and increase the KE, then weaken the storm and the KE, and then reintensify and increase the KE. This pattern is loosely similar to that of the real storm.

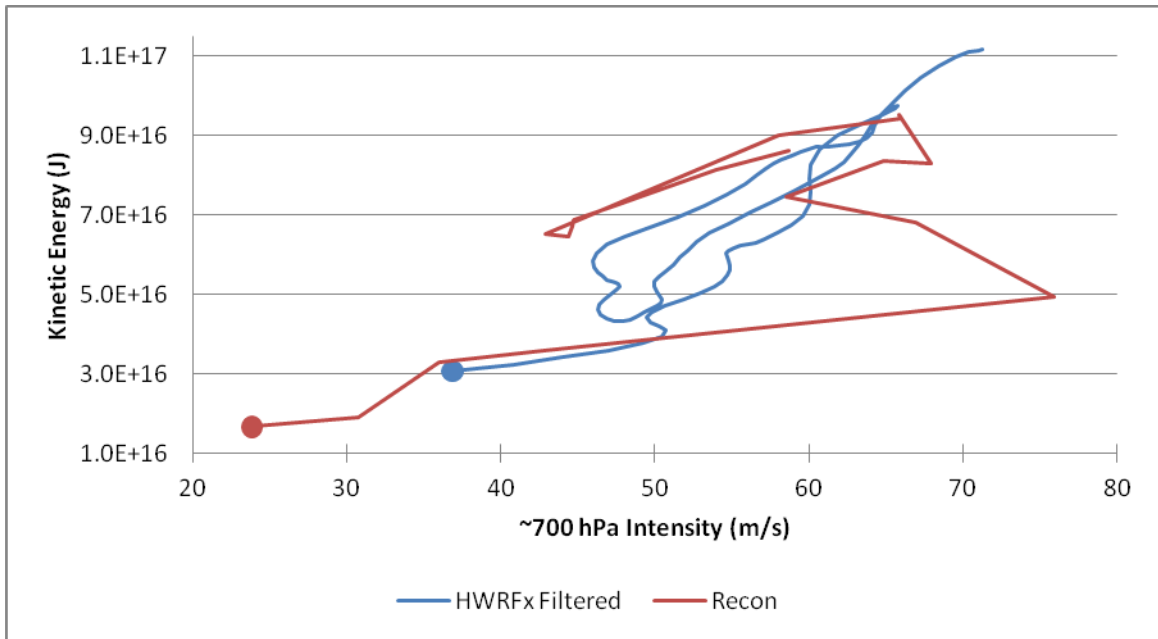


Figure 2.20: Kinetic energy versus intensity for Hurricane Wilma (18 October 2005 HWRFx simulation). Recon time span: 18 October at 00Z to 24 October at 06Z; HWRFx time span: 18 October at 00Z to 23 October at 06Z. The solid dots indicate the first data point for each series.

Figure 2.21 shows the KE versus intensity plot for the comparison between the aircraft reconnaissance and 22 October 2005 simulation of Hurricane Wilma. The model is initialized approximately 5 m/s greater intensity than the real storm and the model weakens for the passage of the storm over the Florida peninsula whereas the actual storm was barely affected as it quickly passed over Florida. Otherwise, the pattern of the two lines is really quite similar for this case. This indicates that the latter part of Hurricane Wilma's evolution, when it was in the Gulf of Mexico and then the Atlantic as it began

its extratropical transition is handled well by the model in terms of intensity and wind field structure.

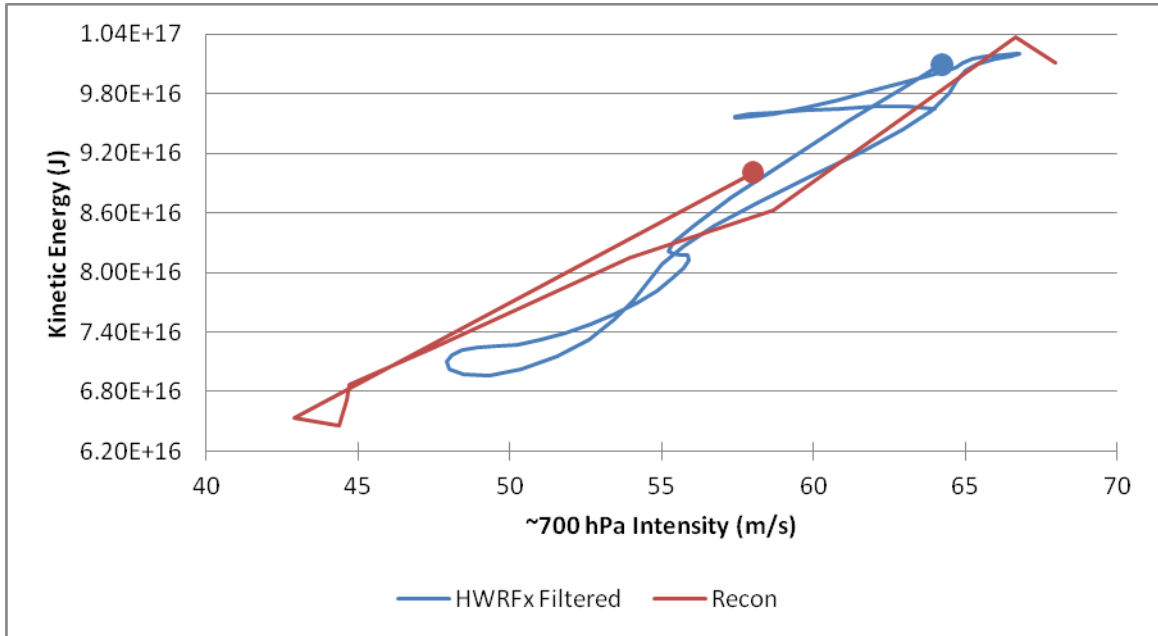


Figure 2.21: Kinetic energy versus intensity for Hurricane Wilma (22 October 2005 HWRFX simulation). Recon time span: 22 October at 00Z to 25 October at 00Z; HWRFX time span: 22 October at 00Z to 25 October at 00Z. The solid dots indicate the first data point for each series.

2.4 Tangential Wind Structure

A significant part of this study focuses on the vertical structure of the tangential winds. Therefore, it is important that the HWRFX model adequately simulates this structure. Example plots of the radial-height cross section of the azimuthal mean tangential winds from the first Emily simulation, the Katrina simulation, and the first Wilma simulation are shown in Figures 2.22, 2.23, and 2.24, respectively. Similar plots of the second Emily and Wilma simulations are not shown since they have very similar vertical structure to those shown here. Firstly, in terms of the low level radius of maximum wind (RMW): the Emily simulation shown (Fig. 2.22) has a RMW in the 45

km region; the Katrina simulation (Fig. 2.23) has a RMW in the 90 km region; and the Wilma simulation (Fig. 2.24) has a RMW in the 60 km region. Kimball and Mulekar (2004) studied the climatology of the size parameters of Atlantic tropical cyclones from 1988-2002. From their analysis the mean RMW was 64.6 km, the 25% quantile RMW was 46.2 km, and the 75% quantile RMW was 111 km. Thus, these storm simulations are within a reasonable range of tropical cyclone size and can be considered representative of small, average, and large tropical cyclones in terms of the RMW.

Frank (1977) analyzed tropical cyclone structure using composite analyses of northwest Pacific rawinsonde data from storms from 1961-1970. Figure 9 in the Frank (1977) paper shows a composite radial-pressure cross section of the tangential winds. Figure 2.22, 2.23, and 2.24 correspond roughly to the 0° - 2° radial portion of the Frank (1977) figure. The tangential wind structures compare well. The tangential wind maximum in the HWRFx simulations occur at the right region in the 1.5-2 km region near the center, compared to around 850 mb in Frank (1977). Also, while the radial range of the simulations is not large enough to really capture the anticyclonic flow in the upper levels that is evident in the Frank (1977) work, the cyclonic tangential winds in the simulations do gradually decrease to near zero values at the upper levels. Therefore, the HWRFx model adequately produces realistic vertical structure of the tangential winds for the simulations used in this study.

One may question how the horizontal model resolution might affect the ability to accurately simulate inner-core TC structure. Davis et al. (2008) used real-time forecasts of Hurricane Katrina with the Advanced Hurricane WRF (AHW) at different horizontal resolutions to study the sensitivity of storm structure to the model resolution. The 12 km

resolution simulation produced a RMW that was too large, but an accurate extent of the hurricane force winds; the 4 km resolution run produced a more accurate RMW size (although the storm intensity was too low), but underestimated the extent of the hurricane force winds; and the 1.33 km resolution simulation RMW and extent of the hurricane force winds were both too small. So, it is likely that the HWRFx simulations, with their 9 km grid spacing, will have RMW values that are generally larger than those of the actual storm.

To summarize, the HWRFx model performed reasonably well in the five simulations of the three tropical cyclones from the 2005 Atlantic hurricane season. The track forecasts were all good in that none were drastically inaccurate. The intensity and structure forecasts certainly had inaccuracies, but overall they were not terribly far from the observed intensity and structural evolution patterns. Lastly, the vertical structure of the tangential winds in the simulations compared well to the typical structure of tropical cyclones. For the purposes of this study it is not essential that the model forecasts have very accurate verifications, since the emphasis is on the model generated asymmetries and the relationships with the storm environment.

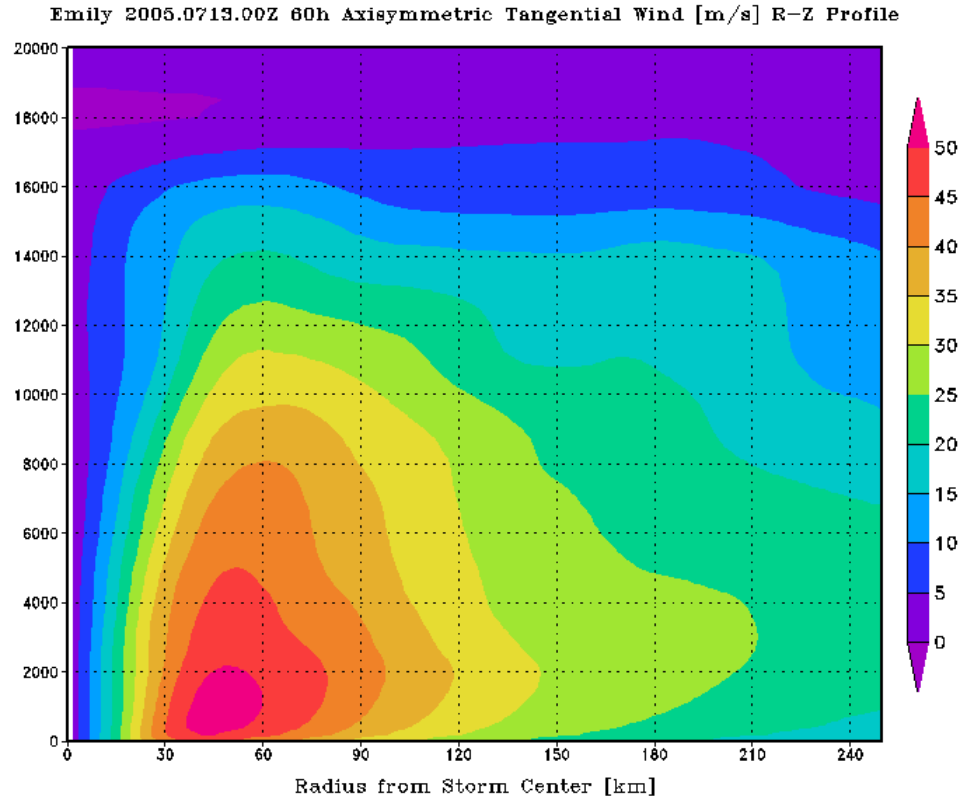


Figure 2.22: Radial-Height cross section of the azimuthal mean tangential winds (m/s) 13 July 2005 Hurricane Emily simulation at hour 60.

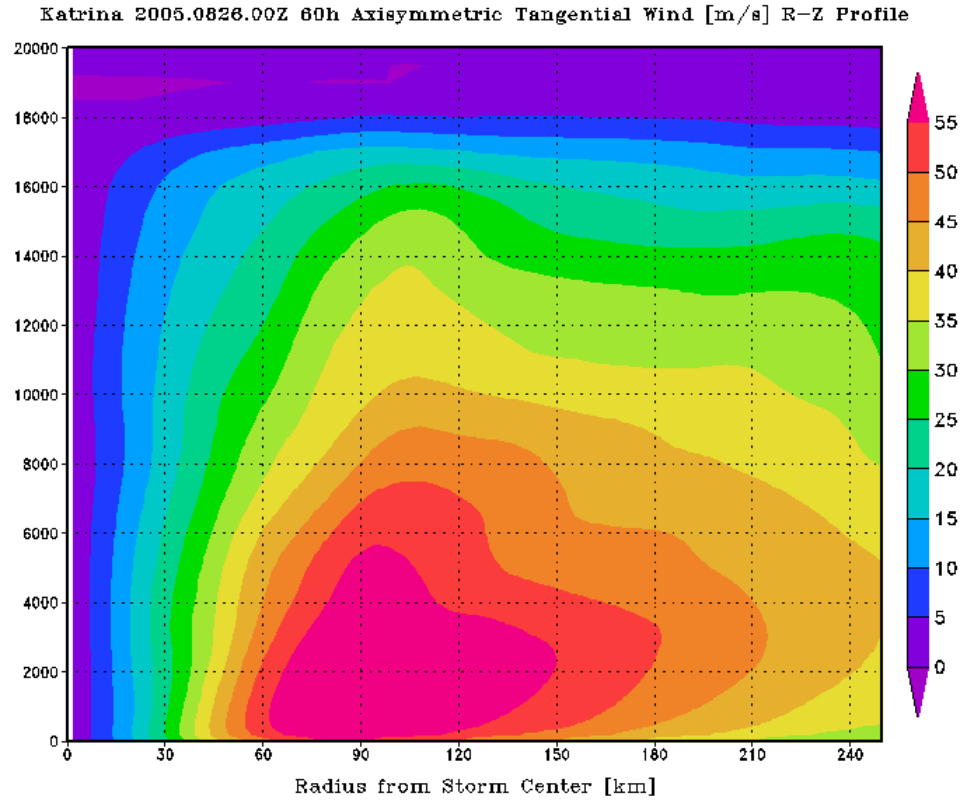


Figure 2.23: Radial-Height cross section of the azimuthal mean tangential winds (m/s) 26 August 2005 Hurricane Katrina simulation at hour 60.

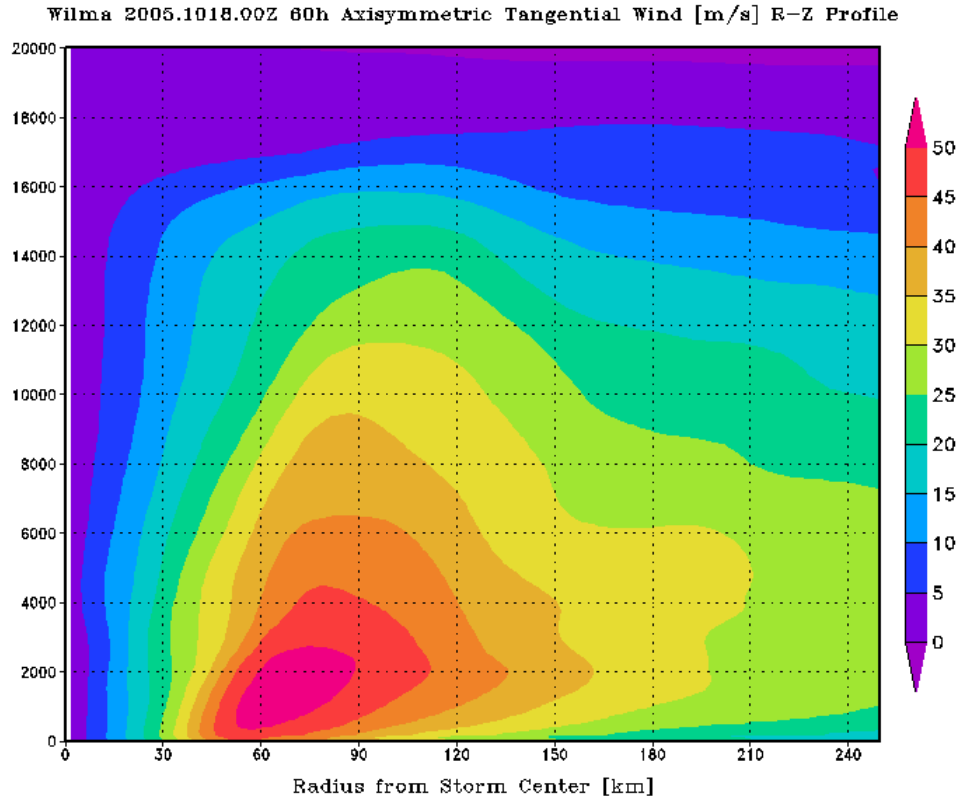


Figure 2.24: Radial-Height cross section of the azimuthal mean tangential winds (m/s) 18 October 2005 Hurricane Wilma simulation at hour 60.

CHAPTER 3 – METHODOLOGY

This chapter covers methodology used for portions of the analysis and results that will be reported and discussed in this study. The first section describes the details of the Fourier analysis which is used to decompose various variables into wavenumber space in both azimuth and time. A derivation of the double Fourier decomposition is presented, where a horizontal field at a given radius is first decomposed into azimuthal wavenumber space, and then these amplitudes are further decomposed via temporal Fourier analysis. The azimuthal decomposition is used to determine the wavenumber contributions to the asymmetries relative to the mean azimuthal flow. The combined azimuthal and temporal decomposition is used to determine if there is a signal in the asymmetries from vortex Rossby waves. The second section describes the calculations of the modeled storm motion and shear vectors and then reviews the magnitude and direction of each of these vectors for each simulation. The vector directional differences, which are an important part of a large portion of the results, are also shown.

3.1 Fourier Analysis (Wavenumber Decomposition)

For any given variable in cylindrical coordinates at any given radii, that variable can be thought of as a periodic function of azimuth with a period of 2π . One can use a Fourier series, then, to decompose that function into the sum of a set of sine and cosine (or complex exponentials) functions. The Fourier series for a function $f(x)$ on a periodic domain $x=0$ to $x=L$ is defined as:

$$f(x) = \frac{a_0}{2} + \sum_{n=1}^N (a_n \cos \frac{2\pi nx}{L} + b_n \sin \frac{2\pi nx}{L}) \quad (3.1)$$

where the amplitudes of the cosine and sine waves, a_n and b_n are:

$$a_n = \frac{2}{L} \int_0^L f(x) \cos \left(\frac{2\pi nx}{L} \right) dx \quad (3.2)$$

$$b_n = \frac{2}{L} \int_0^L f(x) \sin \left(\frac{2\pi nx}{L} \right) dx \quad (3.3)$$

and $n=0,1,2,\dots,N$.

At a given radii in a tropical cyclone, a defined variable is a function of azimuth where $L=2\pi$, the above Fourier series and associated amplitudes can be written as:

$$f(\theta) = \frac{a_0}{2} + \sum_{n=1}^N [a_n \cos(n\theta) + b_n \sin(n\theta)] \quad (3.4)$$

where the amplitudes of the cosine and sine waves, a_n and b_n are:

$$a_n = \frac{1}{\pi} \int_0^{2\pi} f(\theta) \cos(n\theta) d\theta \quad (3.5)$$

$$b_n = \frac{1}{\pi} \int_0^{2\pi} f(\theta) \sin(n\theta) d\theta. \quad (3.6)$$

Equations (3.4)-(3.6) are used to decompose the radial and tangential wind fields, and the vorticity fields into their wavenumber components in Chapter 4. The square of f , which is useful for decomposing the kinetic energy fields, can be determined using Parseval's identity:

$$\frac{1}{\pi} \int_0^{2\pi} \{f(\theta)\}^2 d\theta = \frac{a_0^2}{2} + \sum_{n=1}^N (a_n^2 + b_n^2). \quad (3.7)$$

The model kinetic energy is defined by (2.2). However, for the remainder of this paper, only the horizontal wind components (u and v) will be included. Neglecting the vertical component of the wind in the calculations does not make an appreciable change to the integrated kinetic energy. For example, the integrated kinetic energy was calculated with and without the vertical winds at the 3000 m level for each of the five simulations. The percent difference in the two values was calculated for each time step in each simulation and the results are shown in Table 3.1. The vertical velocity component accounts for well less than one percent of the integrated kinetic energy calculations at 3000 m, so using the simpler form with only the horizontal winds is acceptable.

Table 3.1: The maximum percent difference and average percent difference between the integrated kinetic energy at 3000 meters with and without the vertical winds.

HWRFx Simulation	Maximum % Difference	Average % Difference
Emily – 13 July 2005	0.16%	0.05%
Emily – 15 July 2005	0.19%	0.06%
Katrina – 26 August 2005	0.16%	0.04%
Wilma – 18 October 2005	0.19%	0.06%
Wilma – 22 October 2005	0.43%	0.10%

A second simplification is made to the integrated kinetic energy equation with respect to the density. The previous form (2.2) used the density at each grid point. However, for any given radius the azimuthal variations in the density are, at minimum, two orders of magnitude smaller than azimuthal mean density. Therefore, it is a reasonable approximation to use the azimuthal mean density at each radius. So, the integrated kinetic energy equation for this portion of the study is given by:

$$KE = \frac{\Delta z}{2} \int_0^{2\pi} \int_0^R \bar{\rho}(u^2 + v^2) r dr d\theta. \quad (3.8)$$

The form of the KE in (3.8) only includes the quadratic function of azimuth, so Parseval's relationship can be applied. The decomposed integrated kinetic energy for wavenumbers $n=0,1,2,3,4,\dots,N$ is then:

$$KE_n = \frac{\Delta z}{2} \int_0^R \bar{\rho} \left[\frac{1}{2}(a_n^2 + b_n^2) + \frac{1}{2}(c_n^2 + d_n^2) \right] r dr \quad (3.9)$$

where a and b are the amplitudes of the cosine and sine waves of the radial winds and c and d are the amplitudes of the cosine and sine waves of the tangential winds. To analyze the relative importance of the contribution to the integrated kinetic energy from each wavenumber, the KE percentage is calculated using

$$KE \text{ wave percentage} = \frac{KE_n}{KE_{total}} * 100. \quad (3.10)$$

For the vortex Rossby wave portion of the study it is useful to determine the temporal frequencies associated with each azimuthal wavenumber so that they can be compared with theoretical relationships. For this purpose, the vorticity field will be considered. The vorticity field must first be spatially decomposed through Fourier analysis into azimuthal wavenumber space. The amplitudes from this spatial decomposition can be put through a temporal Fourier decomposition. The equations for this analysis are derived here. For this analysis, the complex form of the Fourier series is used. Also, all functions in the cylindrical coordinate system are periodic in azimuth. However, they will almost never be periodic in time. To correct for this problem, the azimuthal wavenumber amplitudes will be detrended (Shumway and Stoffer 2000) prior to the temporal Fourier decomposition.

The complex form of the Fourier series is

$$f(x) = \sum_{n=-N}^{+N} c_n e^{\frac{2\pi n x}{L}} \quad (3.11)$$

where

$$c_n = \frac{1}{L} \int_0^L f(x) e^{-\frac{2\pi n x}{L}} dx \quad (3.12)$$

Using the identity $e^{i\theta} = \cos\theta + i\sin\theta$ (and $e^{-i\theta} = \cos\theta - i\sin\theta$), and letting

$c_n = c_{nr} + ic_{ni}$ where c_{nr} is the real part of c_n and c_{ni} is the imaginary part, (3.11) can

be written as:

$$f(x) = \sum_{n=-N}^{+N} (c_{nr} + ic_{ni}) \left(\cos \frac{2\pi n x}{L} - i \sin \frac{2\pi n x}{L} \right)$$

$$f(x) = \sum_{n=-N}^{+N} \left\{ [c_{nr} \cos \frac{2\pi n x}{L} + c_{ni} \sin \frac{2\pi n x}{L}] + i [c_{ni} \cos \frac{2\pi n x}{L} - c_{nr} \sin \frac{2\pi n x}{L}] \right\} \quad (3.13)$$

Dividing the summation in (3.13) into the negative, zero and positive values of n gives:

$$\begin{aligned} f(x) = & (c_{0r} + ic_{0i}) + \sum_{n=1}^{+N} \left\{ [c_{nr} \cos \frac{2\pi n x}{L} + c_{ni} \sin \frac{2\pi n x}{L}] + i [c_{ni} \cos \frac{2\pi n x}{L} \right. \\ & \left. - c_{nr} \sin \frac{2\pi n x}{L}] \right\} + \sum_{n=-N}^{-1} \left\{ [c_{nr} \cos \frac{2\pi n x}{L} + c_{ni} \sin \frac{2\pi n x}{L}] + i [c_{ni} \cos \frac{2\pi n x}{L} \right. \\ & \left. - c_{nr} \sin \frac{2\pi n x}{L}] \right\} \end{aligned}$$

The last two terms in the above equation can be combined using:

$$\begin{aligned} f(x) = & (c_{0r} + ic_{0i}) + \sum_{n=1}^{+N} \left\{ [c_{nr} \cos \frac{2\pi n x}{L} + c_{ni} \sin \frac{2\pi n x}{L}] + i [c_{ni} \cos \frac{2\pi n x}{L} \right. \\ & \left. - c_{nr} \sin \frac{2\pi n x}{L}] \right\} + \sum_{n=1}^{+N} \left\{ [c_{-nr} \cos \frac{2\pi n x}{L} - c_{-ni} \sin \frac{2\pi n x}{L}] \right. \\ & \left. + i [c_{-ni} \cos \frac{2\pi n x}{L} + c_{-nr} \sin \frac{2\pi n x}{L}] \right\} \end{aligned}$$

and thus

$$f(x) = (c_{0r} + ic_{0i}) + \sum_{n=1}^{+N} [(c_{nr} + c_{-nr}) \cos \frac{2\pi nx}{L} + (c_{ni} - c_{-ni}) \sin \frac{2\pi nx}{L}] + \sum_{n=1}^{+N} i [(c_{ni} + c_{-ni}) \cos \frac{2\pi nx}{L} - (c_{nr} - c_{-nr}) \sin \frac{2\pi nx}{L}] \quad (3.14)$$

If $f(x)$ is real, all the imaginary part of (3.14) must be zero. This will be true if:

$$c_{0i} = 0, c_{nr} = c_{-nr}, \text{ and } c_{ni} = c_{-ni} \quad (3.15)$$

Equation (3.15) is equivalent to:

$$c_{-n} = c_n^* \quad (3.15a)$$

where the * denotes the complex conjugate.

Comparing (3.14) and (3.1) for the real case and using (3.15) gives:

$$a_0 = 2c_{0r}, a_n = 2c_{nr}, \text{ and } b_n = 2c_{ni} \text{ for } n=1, 2, 3, \dots, N \quad (3.16)$$

For the general case where a field such as vorticity (ζ) is expanded in azimuthal and temporal Fourier series, let $\zeta(\theta, t)$ be vorticity at a given radius as a function of azimuth and time. First, expand in a complex Fourier series in azimuth, where $\theta \in [0, 2\pi]$ and $L = 2\pi$,

$$\zeta(\theta, t) = \sum_{m=-M}^{+M} \zeta_m(t) e^{-im\theta} \quad (3.17)$$

where

$$\zeta_m(t) = \frac{1}{2\pi} \int_0^{2\pi} \zeta(\theta, t) e^{im\theta} d\theta \quad (3.18)$$

Because ζ is real, ζ_m only needs to be calculated for $m \geq 0$. The ζ_m for $m < 0$ can be determined from (3.15a), so that

$$\zeta_{-m} = \zeta_m^*. \quad (3.19)$$

Now, expand $\zeta_m(t)$ in a timeseries where $t \in [0, T]$ so that:

$$\zeta_m = \sum_{n=-N}^{+N} \zeta_{mn} e^{-\frac{2\pi i n t}{T}} \quad (3.20)$$

where

$$\zeta_{mn} = \frac{1}{T} \int_0^T \zeta_m e^{\frac{2\pi i n t}{T}} dt. \quad (3.21)$$

Letting $\nu_n = \frac{2\pi n}{T}$, then (3.20) and (3.17) can be combined to give:

$$\zeta(\theta, t) = \sum_{m=-M}^{+M} \sum_{n=-N}^{+N} \zeta_{mn} e^{-i(m\theta + \nu_n t)}. \quad (3.22)$$

The magnitude of the vorticity coefficient ζ_{mn} is given by:

$$|\zeta_{mn}| = \sqrt{\zeta_{mn} \zeta_{mn}^*}. \quad (3.23)$$

ζ_{mn} in (3.23) can be calculated from the sine/cosine form of the Fourier series using (3.16) as follows. First consider ζ_m as defined in (3.17). Let ζ_{mr} be the real part of ζ_m and ζ_{mi} be the imaginary part. Then,

$$\zeta_m = \zeta_{mr} + i\zeta_{mi}. \quad (3.24)$$

From (3.16):

$$\zeta_{mr} = \frac{a_m}{2}, \zeta_{mi} = \frac{b_m}{2}, m = 0, 1, 2, \dots, N \quad (3.25)$$

where a_m and b_m are the coefficients of the sine/cosine Fourier series of $\zeta(\theta, t)$ as in (3.2)-(3.3).

Now, substituting (3.24) into (3.21):

$$\zeta_{mn} = \frac{1}{T} \int_0^T (\zeta_{mr} + i\zeta_{mi}) e^{i\omega_n t} dt$$

$$\zeta_{mn} = \frac{1}{T} \int_0^T \zeta_{mr} e^{i\omega_n t} dt + \frac{i}{T} \int_0^T \zeta_{mi} e^{i\omega_n t} dt. \quad (3.26)$$

Letting A_{mnr} and B_{mnr} be the cosine/sine Fourier coefficients of ζ_{mr} , ζ_{mnr} be the real part of the coefficients for ζ_{mr} and ζ_{mnr} be the imaginary part, then using (3.16) gives:

$$\left. \begin{aligned} \zeta_{mnr} &= \frac{A_{mnr}}{2} & \text{and} & & \zeta_{mnr} &= \frac{B_{mnr}}{2} & \text{for } n \geq 0 \\ \zeta_{m-nr} &= \frac{A_{mnr}}{2} & \text{and} & & \zeta_{m-nr} &= -\frac{B_{mnr}}{2} & \text{for } n < 0. \end{aligned} \right\} \quad (3.27)$$

Similarly, letting A_{mni} and B_{mni} be the coefficients of ζ_{mi} , ζ_{mni} be the real part of the coefficients for ζ_{mi} and ζ_{mni} be the imaginary part, then using (3.16) gives:

$$\left. \begin{aligned} \zeta_{mni} &= \frac{A_{mni}}{2} & \text{and} & & \zeta_{mni} &= \frac{B_{mni}}{2} & \text{for } n \geq 0 \\ \zeta_{m-ni} &= \frac{A_{mni}}{2} & \text{and} & & \zeta_{m-ni} &= -\frac{B_{mni}}{2} & \text{for } n < 0. \end{aligned} \right\} \quad (3.28)$$

Then from (3.26):

$$\begin{aligned} \zeta_{mn} &= \zeta_{mr} + i\zeta_{mi} = (\zeta_{mnr} + i\zeta_{mnr}) + i(\zeta_{mni} + i\zeta_{mni}) \\ &= (\zeta_{mnr} - \zeta_{mni}) + i(\zeta_{mnr} + \zeta_{mni}). \end{aligned} \quad (3.29)$$

$$\left. \begin{aligned}
\text{For } n \geq 0: \quad \zeta_{mn} &= \frac{1}{2}(A_{mnr} - B_{mni}) + \frac{i}{2}(A_{mni} + B_{mnr}) \\
\text{For } n < 0: \quad \zeta_{mn} &= \frac{1}{2}(A_{mnr} + B_{mni}) + \frac{i}{2}(A_{mni} - B_{mnr})
\end{aligned} \right\} \quad (3.30)$$

The complex conjugate, ζ_{mn}^* :

$$\zeta_{mn}^* = (\zeta_{mnr} - \zeta_{mni}) - i(\zeta_{mnr} + \zeta_{mni}) \quad (3.31)$$

$$\left. \begin{aligned}
\text{For } n \geq 0: \quad \zeta_{mn}^* &= \frac{1}{2}(A_{mnr} - B_{mni}) - \frac{i}{2}(A_{mni} + B_{mnr}) \\
\text{For } n < 0: \quad \zeta_{mn}^* &= \frac{1}{2}(A_{mnr} + B_{mni}) - \frac{i}{2}(A_{mni} - B_{mnr})
\end{aligned} \right\} \quad (3.32)$$

Recalling (3.23):

$$|\zeta_{mn}| = (\zeta_{mn} \zeta_{mn}^*)^{1/2} = [(\zeta_{mnr} - \zeta_{mni})^2 + (\zeta_{mnr} + \zeta_{mni})^2]^{1/2} \quad (3.33)$$

$$\left. \begin{aligned}
\text{For } n \geq 0: \quad |\zeta_{mn}| &= \left[\left(\frac{1}{2}A_{mnr} - \frac{1}{2}B_{mni} \right)^2 + \left(\frac{1}{2}B_{mnr} + \frac{1}{2}A_{mni} \right)^2 \right]^{1/2} \\
\text{For } n < 0: \quad |\zeta_{mn}| &= \left[\left(\frac{1}{2}A_{mnr} + \frac{1}{2}B_{mni} \right)^2 - \left(\frac{1}{2}B_{mnr} - \frac{1}{2}A_{mni} \right)^2 \right]^{1/2}
\end{aligned} \right\} \quad (3.34)$$

Theoretical relationships between frequency and azimuthal wavenumber for idealized tangential wind profiles (Kuo et al. 1999) will be compared to those from applying (3.34) to the vorticity from the model output. This will be covered in more detail in Chapter 4.

3.2 Shear, Storm Motion, and Directional Difference

An integral part of this study is an analysis of how the storm motion and environmental deep layer shear effect TC wind field structure. Presented here is an

overview of the magnitude and direction of the storm motion and shear vectors along with the vector directional differences (DD) for each storm simulation.

The storm motion vector was calculated using the latitude and longitude values of the storm center (i.e. the location of the minimum central pressure) at each forecast time, available at 1 h intervals. The latitudinal and longitudinal distances are calculated for each forecast time using centered differencing. The distances are then converted from degrees to meters. The total magnitude and direction of the storm motion is then easily determined from the zonal and meridional speeds.

The shear is calculated by area averaging the horizontal wind components at 12000 m (~200 hPa) and 1500 m (~850 hPa) over an annulus from 150 km to 250 km using (3.35). The annulus is used so that the value is more representative of the environment, and to minimize the influence of small differences in the center estimate. These area averaged wind components are then used to calculate the shear vector.

$$Shear = \frac{\sum_{r=150km}^{250km} \left\{ \frac{\sum_{\theta=0}^{2\pi} \vec{v}(r, \theta)}{2\pi} \right\} r}{\sum_{r=150km}^{250km} r} \quad (3.35)$$

Both the storm motion and shear vectors have been smoothed by running the hourly values through the modified “121” filter, previously described in Chapter 2, ten times. This procedure removed very high frequency variability (period less than 6 h) that is related to small scale oscillations of the storm center, which is not representative of the motion and shear due to the environmental forcing. Figures 3.1 and 3.2 show examples

of the raw and filtered storm motion and shear magnitudes, respectively, for the 13 July 2005 simulation of Hurricane Emily.

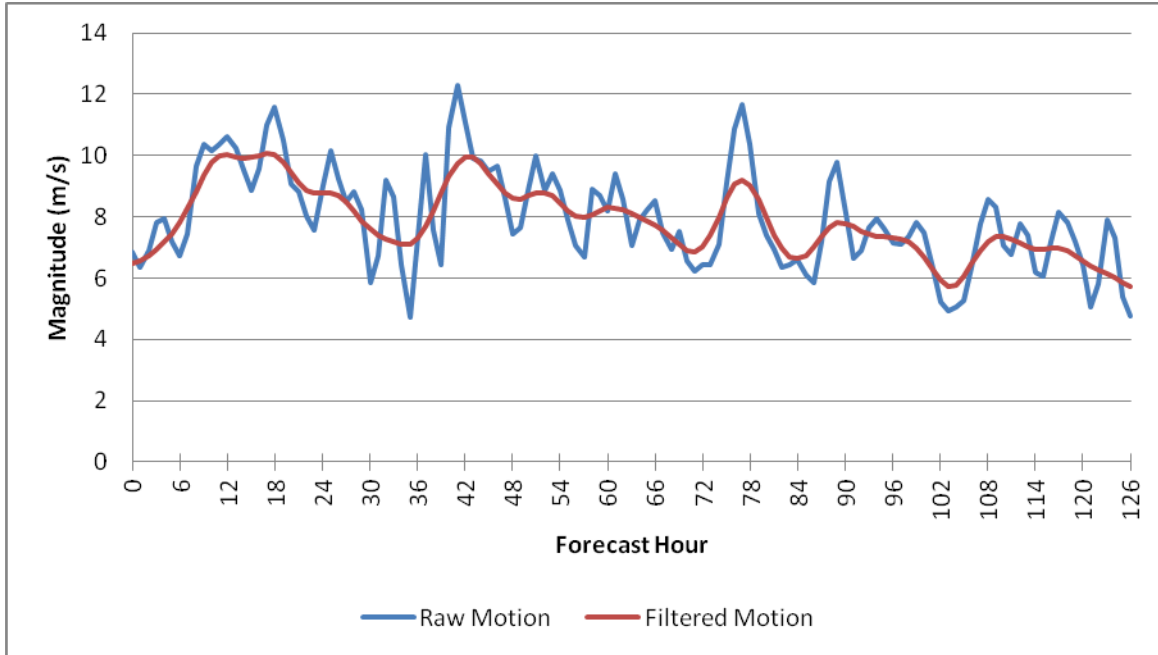


Figure 3.1: Magnitude of the raw and filtered storm motion vector for HWRFx simulation of Hurricane Emily initialized 13 July 2005.

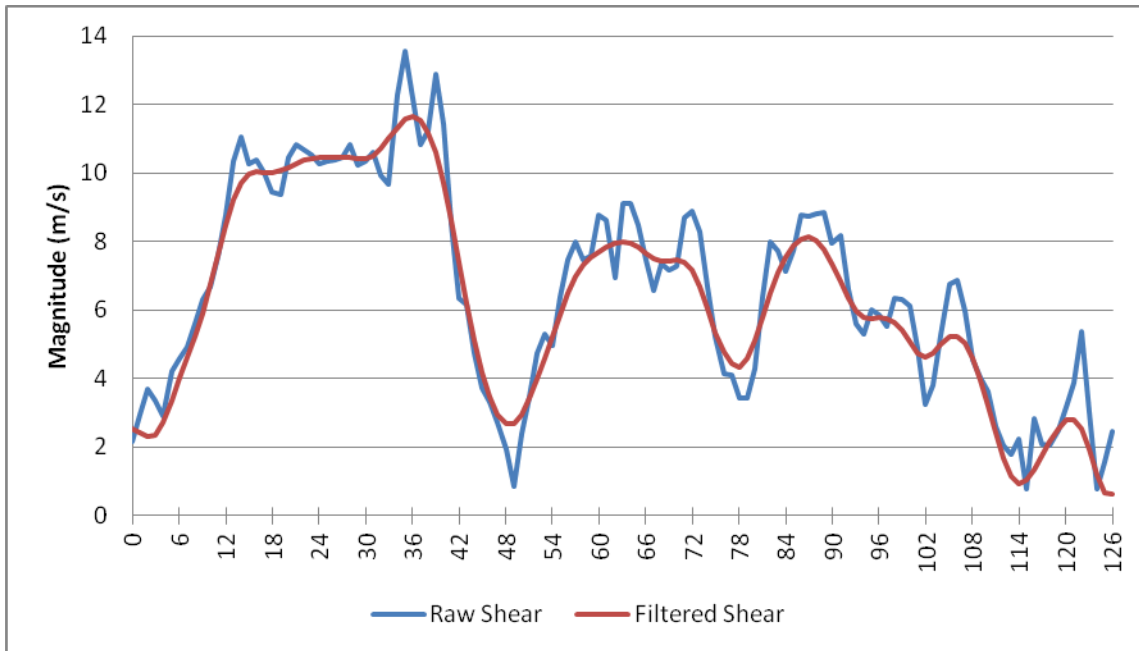


Figure 3.2: Magnitude of the raw and filtered shear vector for HWRFx simulation of Hurricane Emily initialized 13 July 2005.

The vector directional difference (DD) is the difference between the direction of the storm motion vector and the direction of the shear vector. If the DD is between 0° - 45° then the storm motion and shear vectors are considered approximately aligned. If the DD is between 135° - 180° then the vectors are considered approximately opposed. The DD values between 46° - 134° represent a perpendicular relationship between the vectors. These DD categories (aligned, opposed, and perpendicular) are used in the analysis of storm asymmetries in Chapter 4.

The filtered storm motion and shear magnitude, direction, and vector directional difference plots for each storm are shown in Figures 3.3-3.17. In these figures there is a vertical dotted line at the 24 h mark. The first 24 h of the simulations is influenced by the model initialization and storm spin-up. This portion of the simulations is removed from much of the analysis presented later in this study. Also note that the shear and storm motion figures for the second Emily simulation (at 117 h), the Katrina simulation (at 80 h), and the second Wilma simulation (at 98 h) contain a second vertical dotted line. This second vertical dotted line marks the forecast hour after which the data is not included either because the storm center is over land (Emily and Katrina cases) or the storm has become too disorganized due to extratropical transition (Wilma case).

The storm motion and shear magnitude, direction and the vector directional difference plots for the 13 July 2005 simulation of Hurricane Emily are shown below in Figures 3.3-3.5.

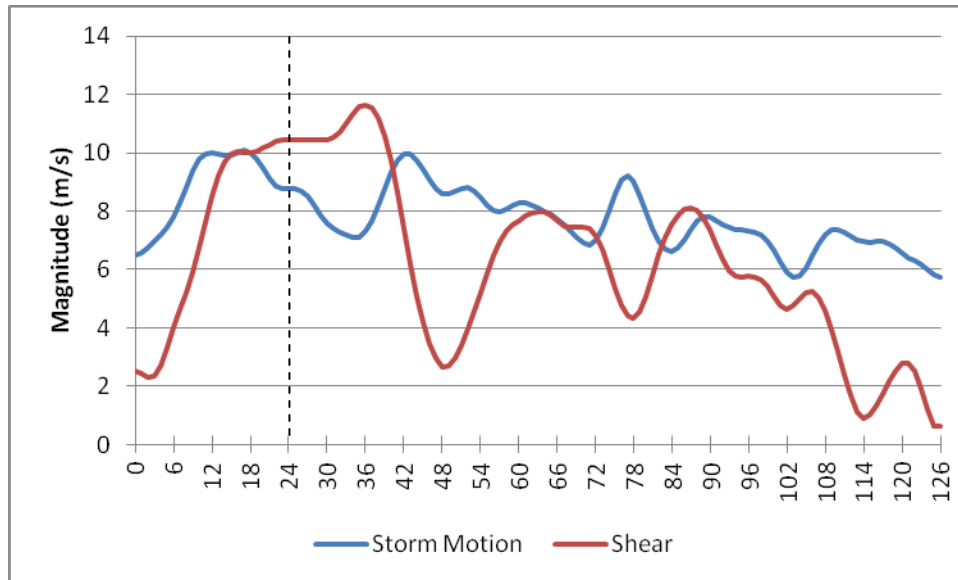


Figure 3.3: Magnitude of the storm motion and shear vectors for HWRFX simulation of Hurricane Emily initialized 13 July 2005.

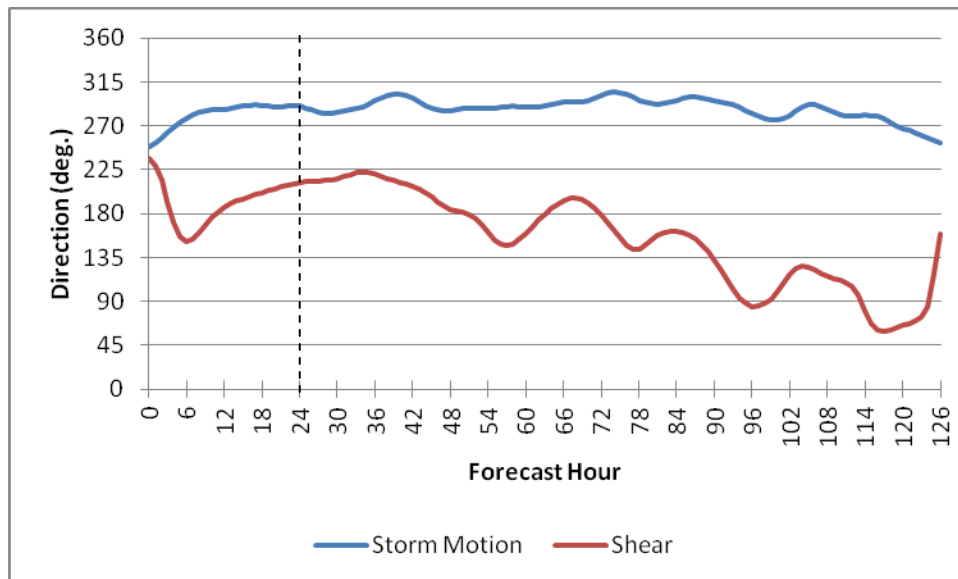


Figure 3.4: Direction of the storm motion and shear vectors for the HWRFX simulation of Hurricane Emily initialized 13 July 2005.

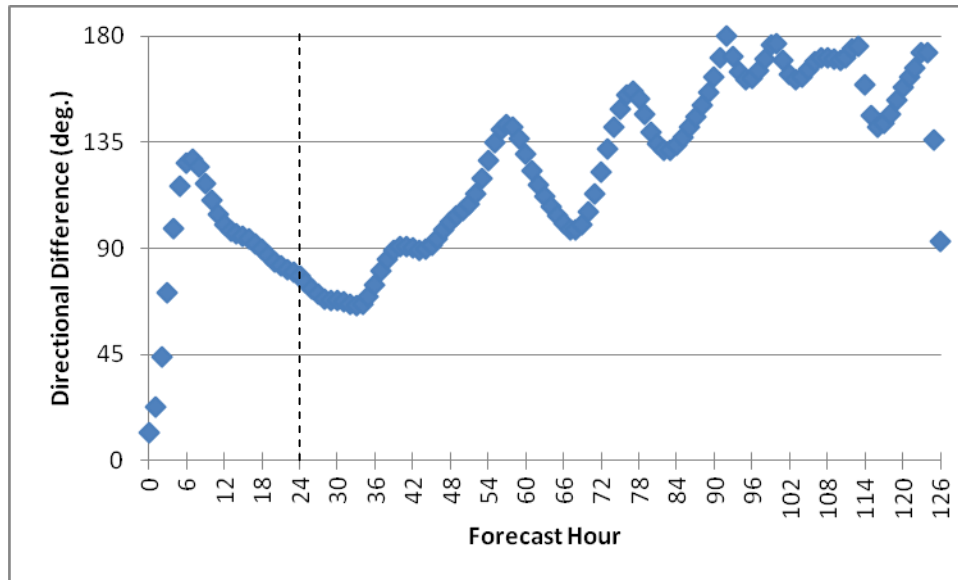


Figure 3.5: Vector directional difference between the storm motion and shear vectors for the HWRFx simulation of Hurricane Emily initialized 13 July 2005.

The storm motion and shear magnitude, direction and the vector directional difference plots for the 15 July 2005 simulation of Hurricane Emily are shown below in Figures 3.6-3.8.

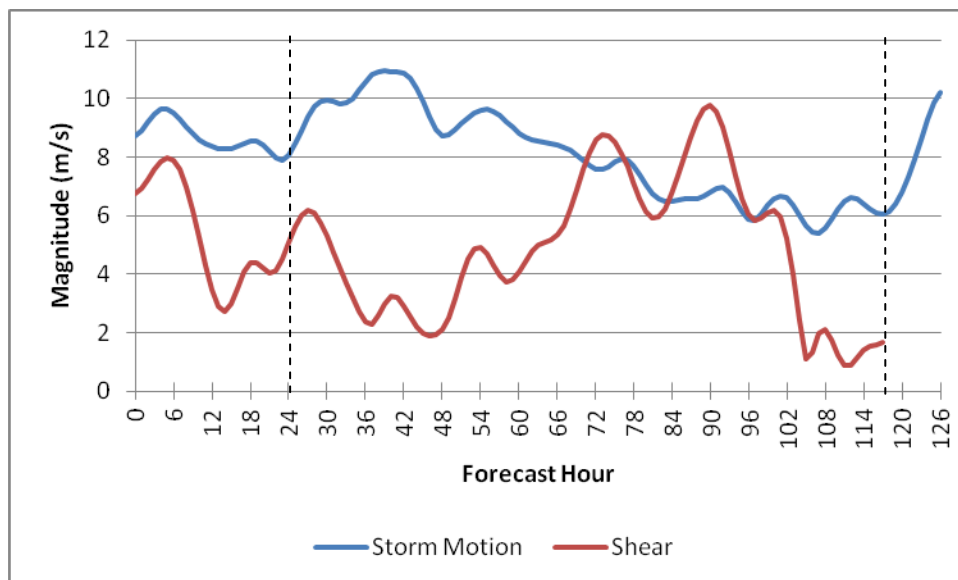


Figure 3.6: Magnitude of the storm motion and shear vectors for the HWRFx simulation of Hurricane Emily initialized 15 July 2005.

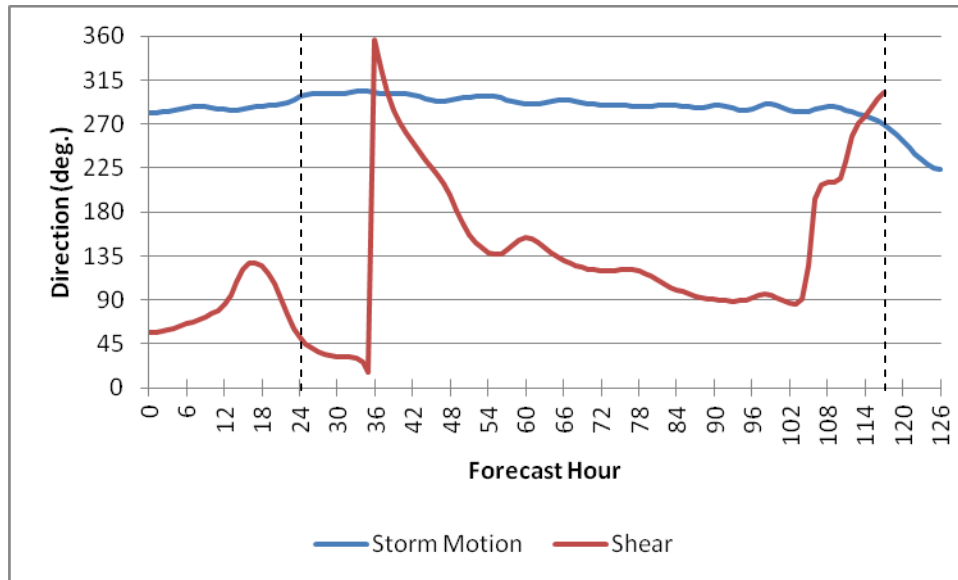


Figure 3.7: Direction of the storm motion and shear vectors for the HWRFX simulation of Hurricane Emily initialized 15 July 2005.

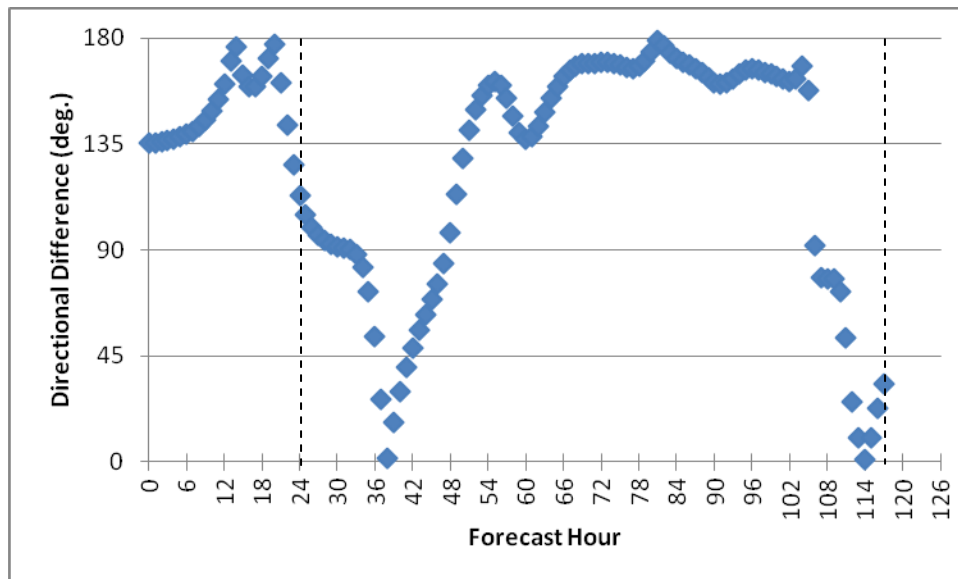


Figure 3.8: Vector directional difference between the storm motion and shear vectors for HWRFX simulation of Hurricane Emily initialized 15 July 2005.

The storm motion and shear magnitude, direction and the vector directional difference plots of the 26 August 2005 simulation of Hurricane Katrina are shown below in Figures 3.9-3.11.

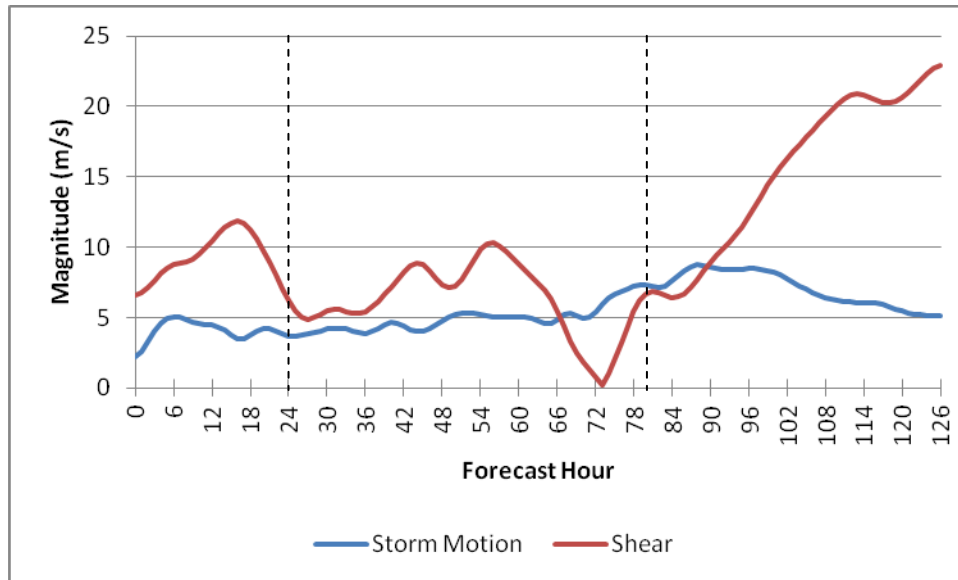


Figure 3.9: Magnitude of the storm motion and shear vectors for the HWRFX simulation of Hurricane Katrina initialized 26 August 2005.

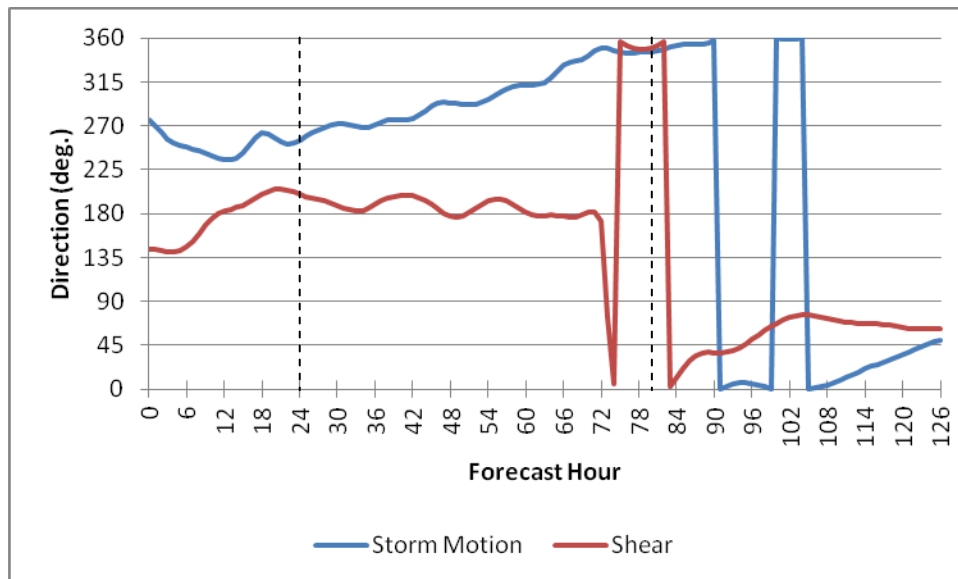


Figure 3.10: Direction of the storm motion and shear vectors for the HWRFX simulation of Hurricane Katrina initialized 26 August 2005.

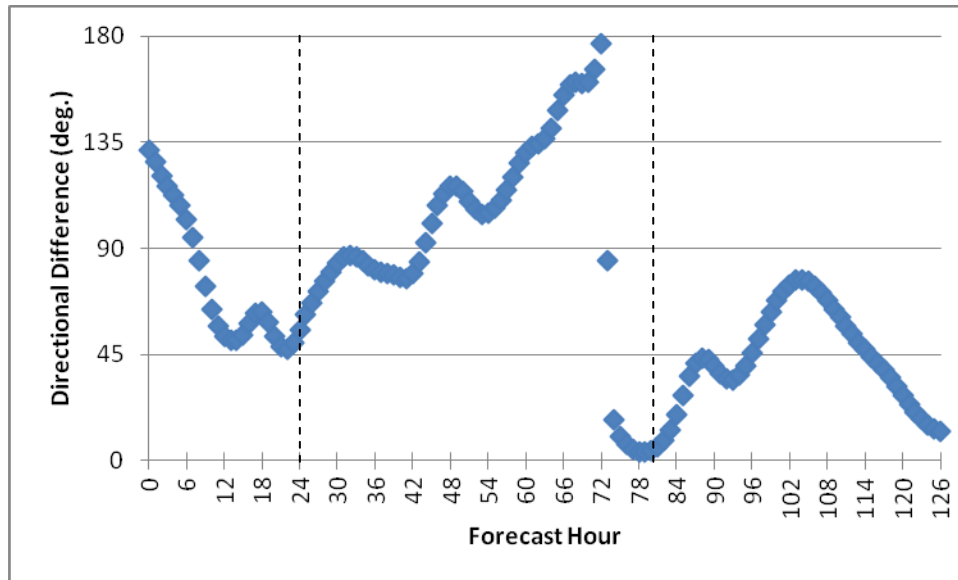


Figure 3.11: Vector directional difference between the storm motion and shear vectors for the HWRFX simulation of Hurricane Katrina initialized 26 August 2005.

The storm motion and shear magnitude, direction and the vector directional difference plots for the 18 October 2005 simulation of Hurricane Wilma are shown below in Figures 3.12-3.14.

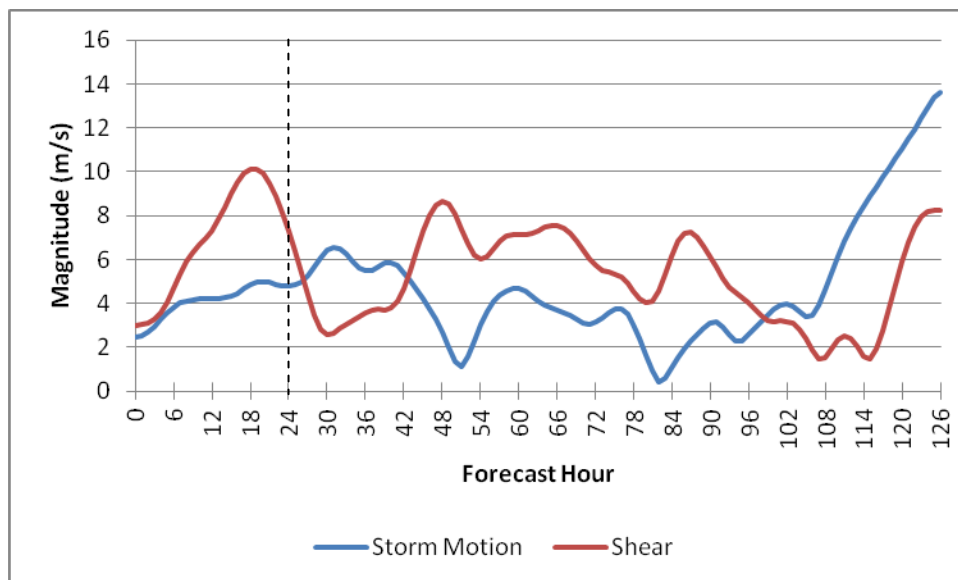


Figure 3.12: Magnitude of the storm motion and shear vectors for the HWRFX simulation of Hurricane Wilma initialized 18 October 2005.

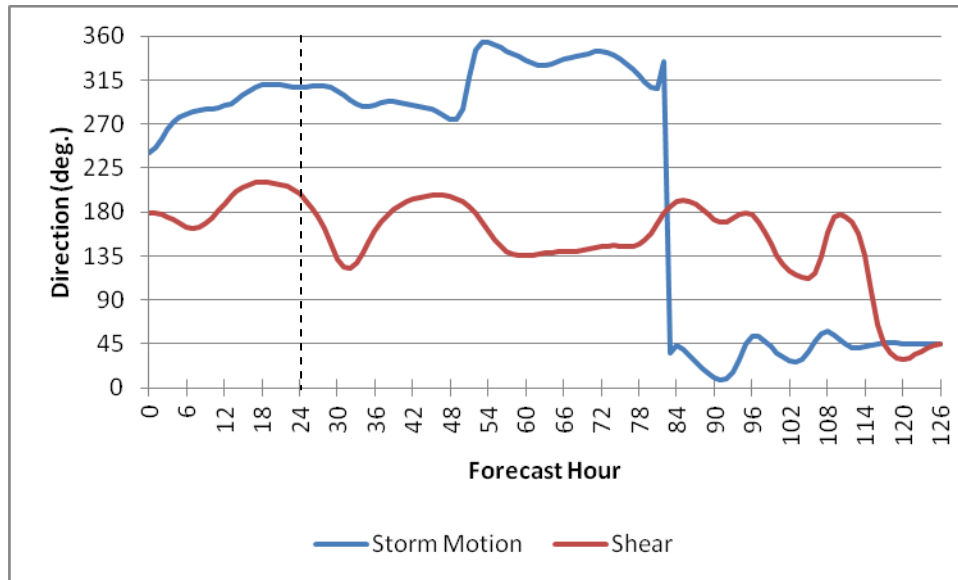


Figure 3.13: Direction of the storm motion and shear vectors for the HWRFX simulation of Hurricane Wilma initialized 18 October 2005.

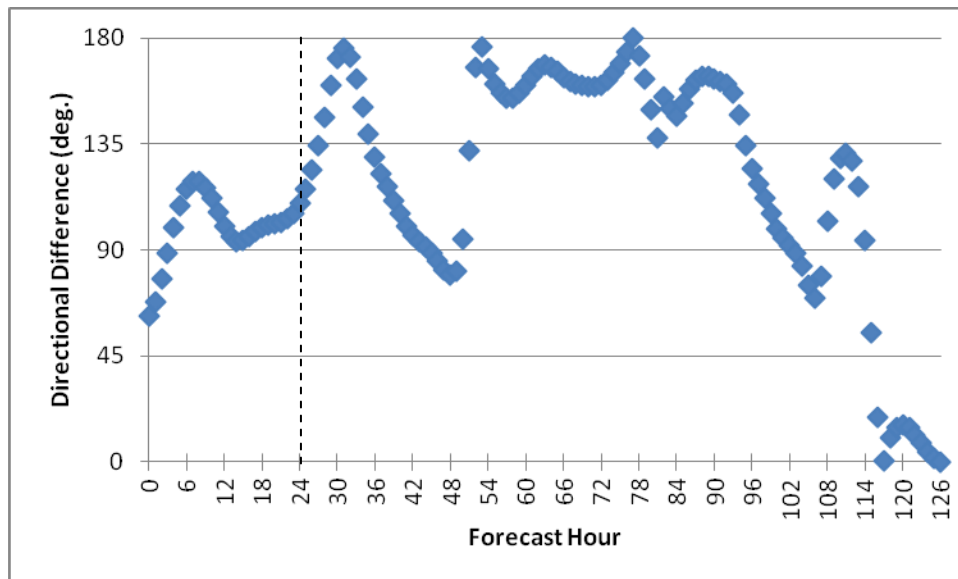


Figure 3.14: Vector directional difference between the storm motion and shear vectors for the HWRFX simulation of Hurricane Wilma initialized 18 October 2005.

The storm motion and shear magnitude, direction and the vector directional difference plots of the 22 October 2005 simulation of Hurricane Wilma are shown below in Figures 3.15-3.17.

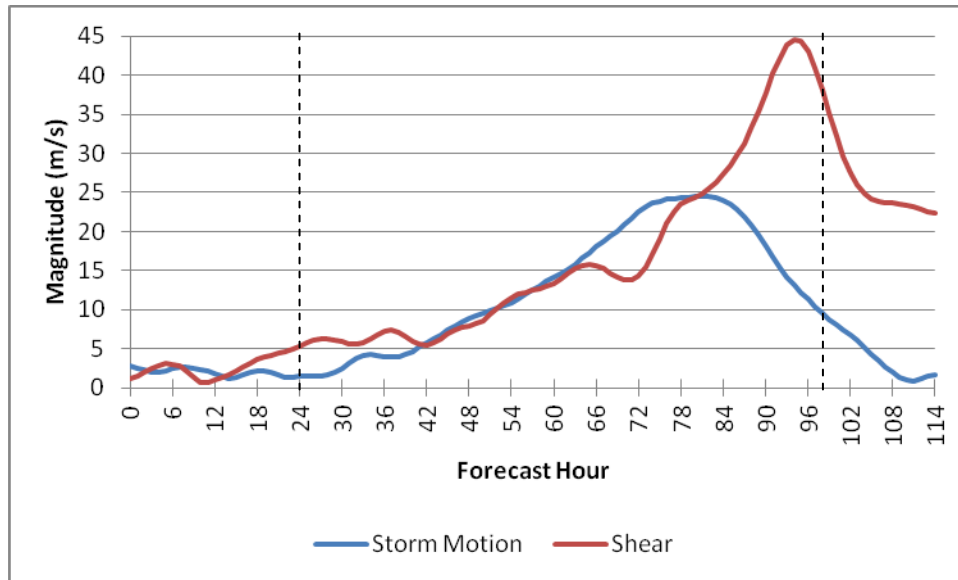


Figure 3.15: Magnitude of the storm motion and shear vectors for the HWRFX simulation of Hurricane Wilma initialized 22 October 2005.

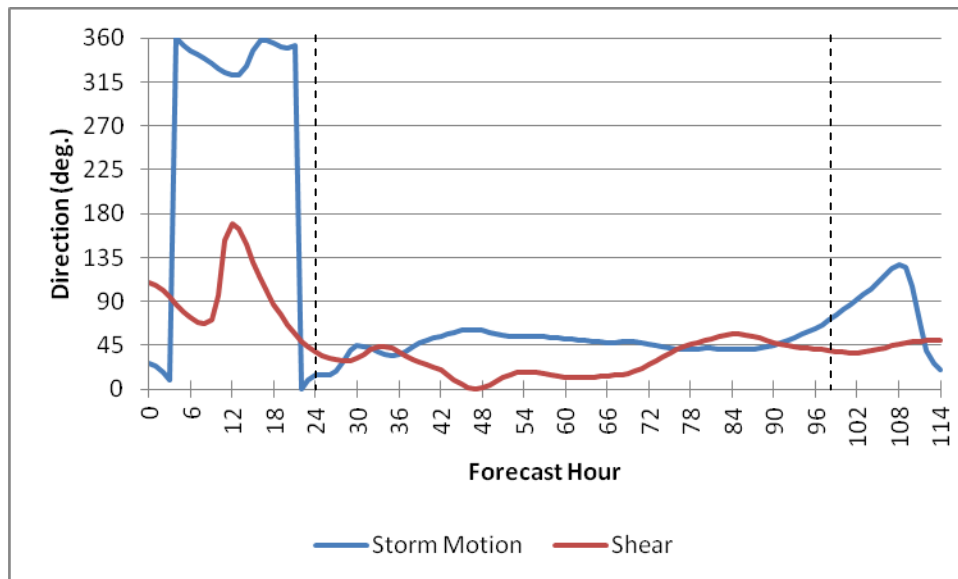


Figure 3.16: Direction of the storm motion and shear vectors for the HWRFX simulation of Hurricane Wilma initialized 22 October 2005.

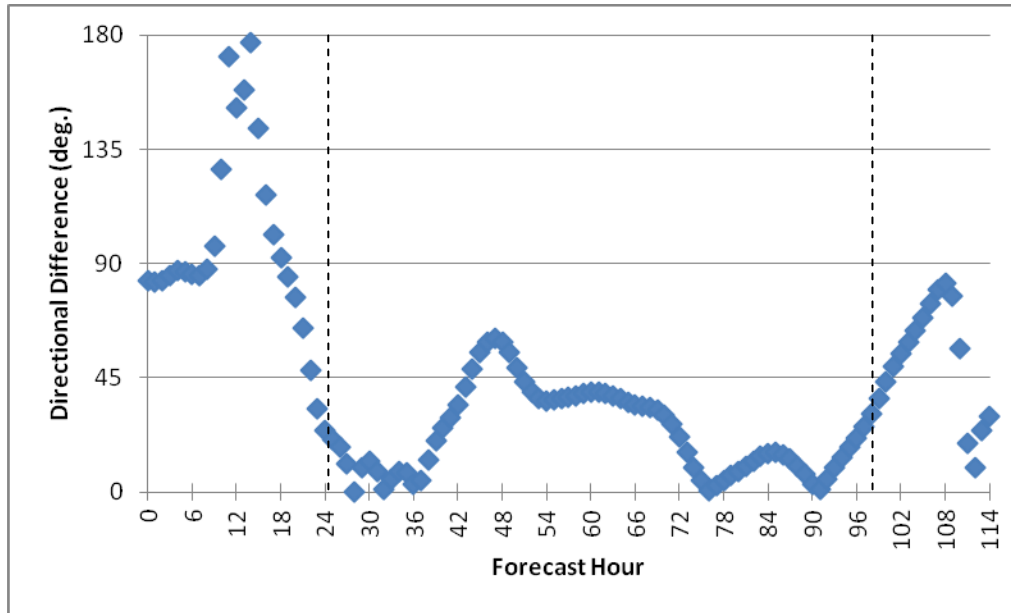


Figure 3.17: Vector directional difference between the storm motion and shear vectors for the HWRFx simulation of Hurricane Wilma initialized 22 October 2005.

As can be seen from the previous figures, these five simulations represent a spectrum of tropical cyclones experiencing low, medium, and high environmental shear. There is also a reasonable number of when the shear and storm motion vectors are aligned and times when they are opposed. This will be of good use for analyzing the relationship between structural asymmetries and storm motion and shear.

CHAPTER 4 – HORIZONTAL STRUCTURE

In this chapter the horizontal structure of the modeled tropical cyclones is addressed with an emphasis on the asymmetric structure in relation to the storm motion and environmental vertical shear. The horizontal structure is first investigated through the total integrated kinetic energy, including an azimuthal wavenumber analysis. Then a composite analysis of the wind fields is presented in order to demonstrate the predominant asymmetric features. The tangential wind field is then decomposed into its specific wavenumber asymmetry components to further illuminate the importance of each asymmetric feature. Finally, a more detailed analysis is performed of the wavenumber-2 fields to determine if these asymmetries contain a signal from vortex Rossby waves. The goal is to determine the relative importance of the asymmetries related to the slowly varying forcing due to storm motion and environmental shear and due to internal processes. The asymmetries will be examined at 10 m, 1500 m, 3000 m, 5000 m, and 12000 m, with an emphasis on the lower level asymmetries. The multiple heights are chosen to capture a representation of the vertical structure of the asymmetries, and correspond roughly to surface, 850 hPa, 700 hPa, 500 hPa, and 200 hPa levels. The low level field is emphasized because it is most related to the storm destructive potential.

4.1 Integrated Kinetic Energy Wavenumber Decomposition and Analysis

The integrated kinetic energy can be decomposed into wavenumber space as described in Chapter 3 using equations (3.7)-(3.9). To examine the relative contribution of the azimuthal mean flow (wavenumber-0) and the azimuthal asymmetric flow (wavenumbers 1, 2, 3 and 4), the kinetic energy wave percentage (3.10) is used. Figure 4.1 shows the time series plot for each storm simulation consecutively of the 1500 m height level KE wave percentage for wavenumbers 0-4. Note that the vertical axis uses a logarithmic scale, so that each KE wavenumber contribution is easily discernable. Also note that:

- ‘EMILY’ = the 13 July 2005 HWRFx simulation of Hurricane Emily
- ‘EMILY2’ = the 15 July 2005 HWRFx simulation of Hurricane Emily
- ‘KATRINA’ = the 26 August 2005 HWRFx simulation of Hurricane Katrina
- ‘WILMA’ = the 18 October 2005 HWRFx simulation of Hurricane Wilma
- ‘WILMA2’ = the 22 October 2005 HWRFx simulation of Hurricane Wilma.

The first 24 h of each simulation has been removed from the analysis (storm spin up), as well as some amount of the final portion of the second Emily and Wilma simulations and the Katrina simulation when the storm has made landfall (Emily and Katrina) or become too disorganized following extratropical transition (Wilma).

From Figure 4.1 it is clear that the total integrated kinetic energy is primarily dominated by the azimuthal mean flow (KE0 %). The wavenumber-1 asymmetries are the next most important contributor, generally speaking, though they are occasionally overcome by the wavenumber-2 asymmetric features (most notably in the case of the first

and second Wilma simulations). The wavenumber-3 asymmetries for the most part contribute to less than one percent of the total kinetic energy, although, the contribution creeps up to over one percent at a few times for both the Wilma simulations. The KE wave percentages have been examined at the additional heights of 3000 m, 5000 m (plots not shown), and 12000 m to determine how the patterns change with height. The most significant difference at increasing height in the storm is that the asymmetric contributions to the total integrated kinetic energy increase. Most notably, with greater heights the wavenumber-1 asymmetries occasionally exceed the wavenumber-0 (mean flow) contributions to the total kinetic energy field, as evident in Figure 4.2 which shows the time series plot of the 12000 m height level KE wave percentages. The increased asymmetric contributions at the 12000 m height are related to the fact that asymmetries are typically much larger in the outflow layer in a tropical cyclone than at lower levels (Black and Anthes 1971).

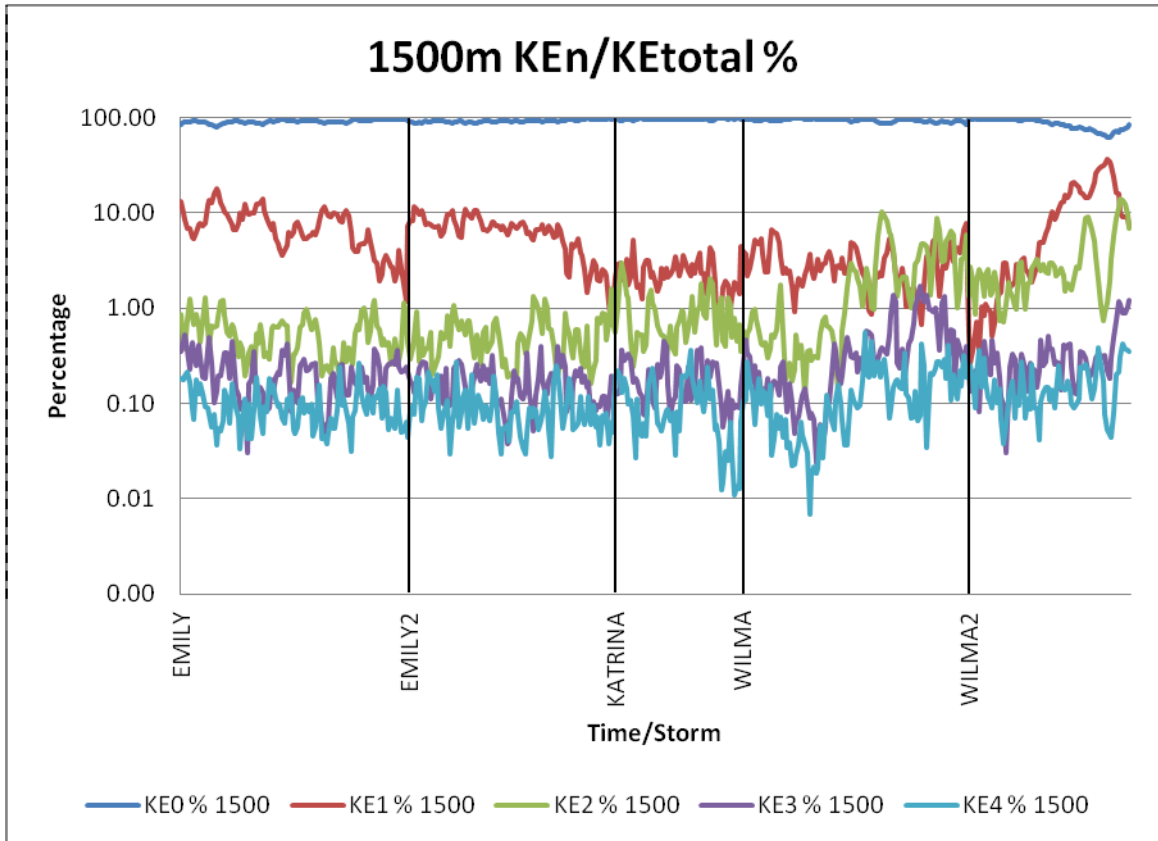


Figure 4.1: 1500 m vertical level percentages of the total KE that is created by the decomposed wave (0-4) KE for the five HWRFX simulations used in this study.

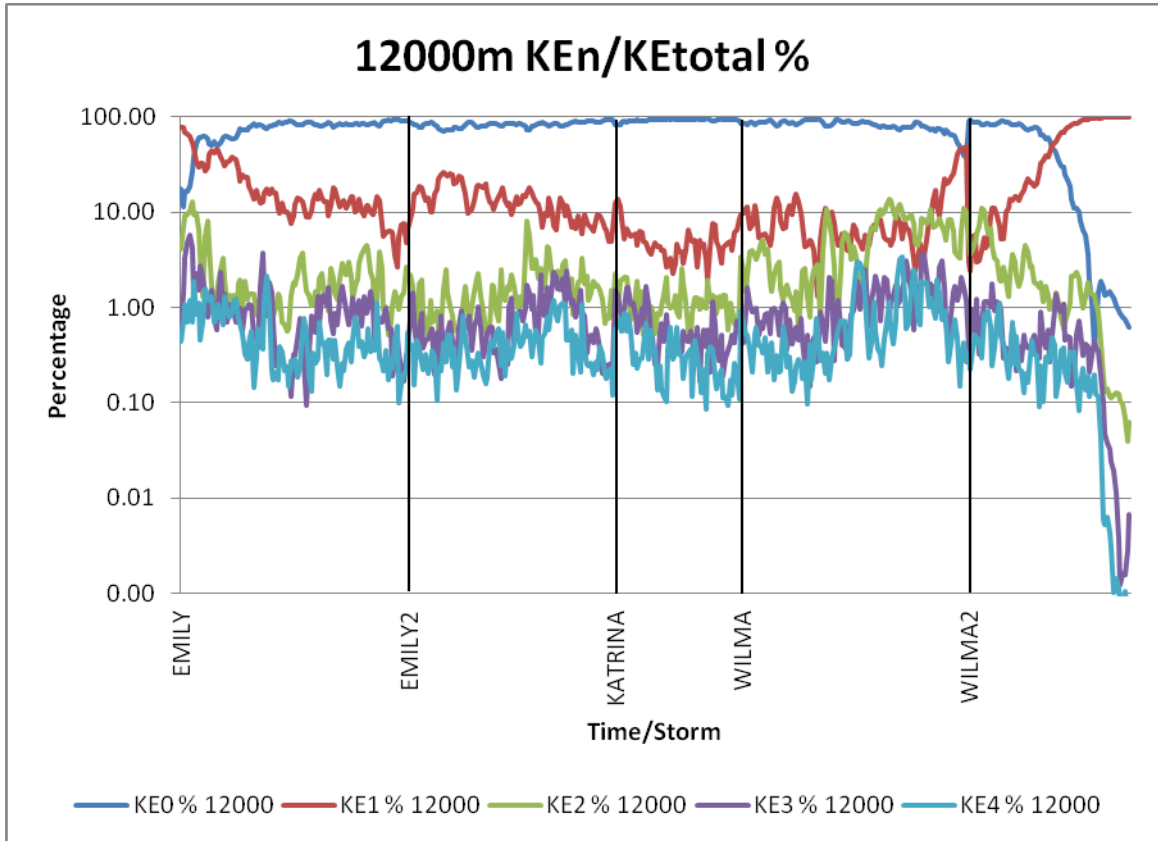


Figure 4.2: 12000 m vertical level percentages of the total KE that is created by the decomposed wave (0-4) KE for the five HWRFX simulations used in this study.

As discussed in Chapter 1, storm motion and shear have been shown to affect the asymmetric structure of tropical cyclones. These relationships should be evident in the KE wave percentages, such that greater shear and greater storm motion should each individually result in greater storm wavenumber-1 asymmetries. In other words, the KE wave percentages for the wavenumber-1 asymmetries should increase with increasing values of shear and storm motion. The trends of the higher wavenumber asymmetries in the KE wave percentages may also be of interest.

Consider first the effects of storm motion on the integrated kinetic energy field. Figure 4.3 shows a scatter plot of the 1500 m level wavenumbers 1, 2, 3 and 4 KE wave percentages versus the magnitude of the storm motion for all of the storm simulations

together. There appears to be a trend in the KE wavenumber-1 asymmetries, which look to increase with increased storm motion values. It is more difficult to see a specific trend in the KE wavenumber-2, 3 and 4 asymmetries. To elucidate any such trends, the linear correlations are calculated between the KE wave percentages and the storm motion magnitude for the heights of 1500 m, 3000 m, 5000 m, and 12000 m. These correlations are shown in Table 4.1. The cells in the table that are highlighted correspond to values that have met the criteria for 99% significance. The correlation significance is determined using the Pearson correlation critical values for 99% significance, which means that there is a one percent chance that the correlation is coincidental. For a sample size of $N = 431$, which is the case here, the critical correlation threshold for 99% significance is $R=0.129$.

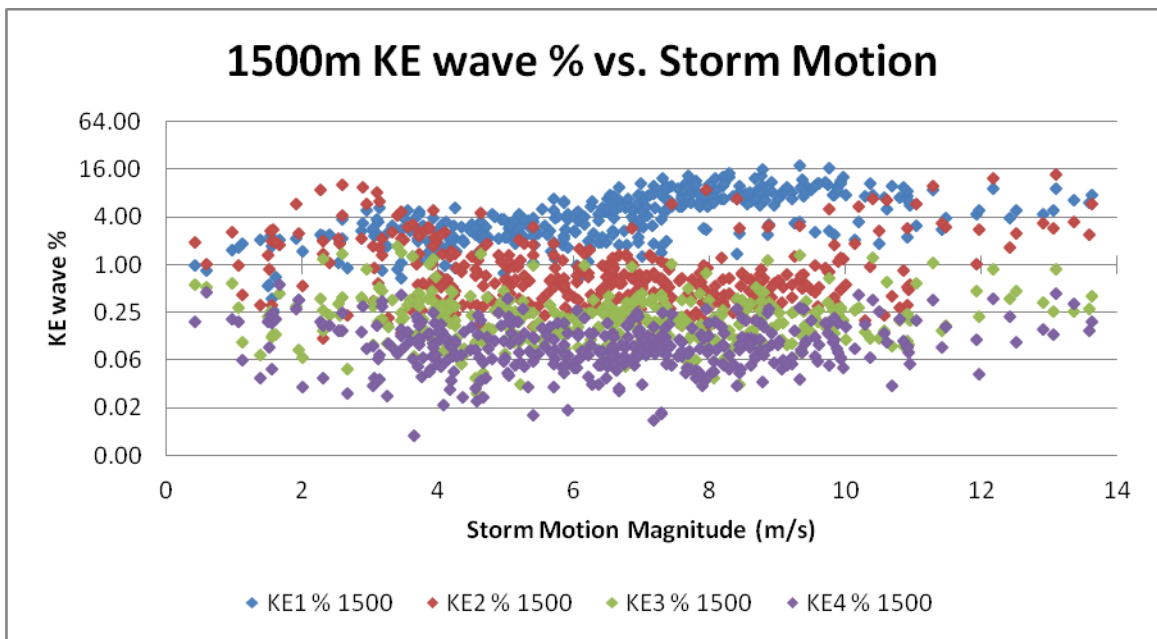


Figure 4.3: 1500 m vertical level decomposed wave KE percentage versus the magnitude of the storm motion vector for all the simulations

The correlations in Table 4.1 show that by far the strongest correlation at all of the selected height levels are for the wavenumber-1 KE percentages. It is a positive

correlation, which means that as the storm motion magnitude increases the wavenumber-1 asymmetries increase and contribute more to the integrated kinetic energy field. This is the expected relationship based on the theory and observations described previously. The other highlighted correlations for the wavenumbers 2, 3 and 4 asymmetries are much smaller in comparison to those for the wavenumber-1 asymmetries, and, aside from the KE wavenumber-2 correlation, are negative. The negative correlation means that as the storm motion magnitudes increase these asymmetries make less of a contribution to the total kinetic energy field.

Table 4.1: Storm motion magnitude correlations with the KE wave percentages

	KE1 %	KE2 %	KE3 %	KE4 %
1500 m	0.812	0.295	0.036	0.127
3000 m	0.821	0.041	-0.001	-0.047
5000 m	0.779	0.001	-0.060	-0.155
12000 m	0.860	-0.279	-0.206	-0.274

Consider now the effects of environmental vertical shear on the integrated kinetic energy field. Figure 4.4 shows a scatter plot of the 1500 m level wavenumbers 1, 2, 3 and 4 KE wave percentages versus the magnitude of the shear for all of the storm simulations together. This plot shows a bit more scatter than the previous one for storm motion (Fig. 4.3), but there appears to be more of a trend across all of the KE wave asymmetries for increasing values of shear.

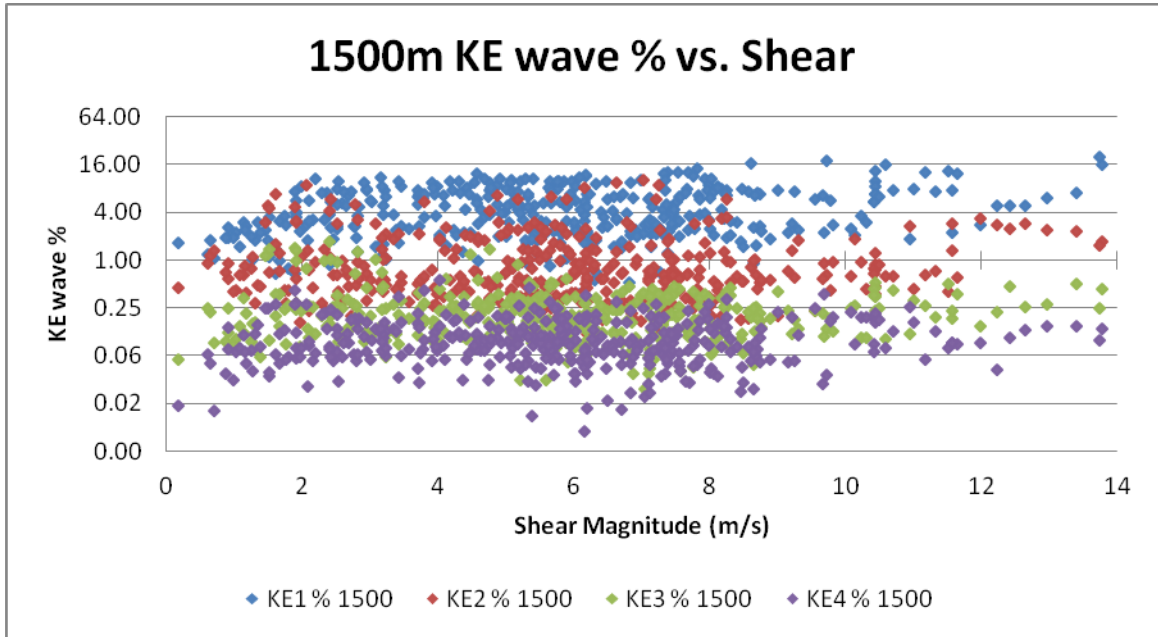


Figure 4.4: 1500 m vertical level decomposed wave KE percentage versus the magnitude of the environmental vertical shear vector for all the simulations.

To determine whether there is evidence of any such trends, the linear correlations between the KE wavenumber percentages and the shear are shown in Table 4.2. The KE wavenumber-1 asymmetries again show up with strong correlations at every level indicating that increased shear coincides with increased contribution of wavenumber-1 asymmetries to the total kinetic energy field. Interestingly, however, the higher wavenumber asymmetries also show significant correlations. At the 1500 m height the wavenumber-2 asymmetries correlate almost as strongly as the wavenumber-1 asymmetries. For the 1500 m and 3000 m heights all of the higher wavenumber asymmetries show positive correlations. At the 12000 m height, however, the wavenumber-2, 3, and 4 asymmetries display a negative correlation, which is the same as for storm motion.

Table 4.2: Shear magnitude correlations with the KE wave percentages.

	KE1 %	KE2 %	KE3 %	KE4 %
1500 m	0.620	0.564	0.239	0.290
3000 m	0.853	0.293	0.219	0.148
5000 m	0.897	0.149	-0.007	-0.007
12000 m	0.826	-0.185	-0.182	-0.228

The work of Ueno and Kunii (2009) and Ueno and Bessho (2011), as discussed in Chapter 1, present the theory that the relative orientation of the storm motion and shear vectors are related to the magnitude and organization of the structural asymmetries in a tropical cyclone. To determine whether the vector direction difference (DD) is associated with a predominance of storm asymmetries the KE wave percentages have been sorted by the DD value. Then the average KE wave percentage is calculated for each wavenumber at each of the four selected height levels for the cases where the storm motion and shear vectors are approximately aligned (DD1) and for cases where they are approximately opposed (DD2). The results of these calculations are shown in Table 4.3. The salient feature to take from these results is that nearly across the board the asymmetries (wavenumber-1 to 4) have a greater presence in the total KE field for the cases where the storm motion and shear are aligned (DD1) than for the cases where they are opposed (DD2). When the shear is opposed to the storm motion vector the total KE field is more symmetric in nature (the KE0 percentage is larger and the KE1-4 percentages are smaller). The next section of this chapter more thoroughly explores the details of the wind field structure.

Table 4.3: Average KE wave percentage for vector directional differences: DD1 (aligned) and DD2 (opposed).

1500 m	DD1	DD2	3000 m	DD1	DD2
Avg KE0 %	87.64	93.36	Avg KE0 %	80.14	91.76
Avg KE1 %	8.68	5.14	Avg KE1 %	17.73	6.72
Avg KE2 %	3.04	1.00	Avg KE2 %	1.51	0.88
Avg KE3 %	0.32	0.22	Avg KE3 %	0.29	0.23
Avg KE4 %	0.15	0.10	Avg KE4 %	0.13	0.13
5000 m	DD1	DD2	12000 m	DD1	DD2
Avg KE0 %	71.51	92.28	Avg KE0 %	52.67	85.02
Avg KE1 %	26.64	6.01	Avg KE1 %	43.41	9.64
Avg KE2 %	1.11	0.81	Avg KE2 %	2.49	2.89
Avg KE3 %	0.33	0.32	Avg KE3 %	0.58	0.88
Avg KE4 %	0.15	0.18	Avg KE4 %	0.28	0.50

4.2 Composite Wind Field Analysis and Decomposition

In this section, a composite analysis of the tropical cyclone wind field is presented. The objective is to determine how the storm wind structure is influenced by the combination of storm translation and environmental shear. First the composite storm motion relative wind field and then the shear relative composite wind field is shown. Then the data is stratified by the vector directional difference (DD) and composite wind fields are created for the two following cases: DD1 = vectors aligned, DD2 = vectors opposed. The figures shown are at the 10 m height, but discussion is included concerning how the composite wind fields change with height.

Consider first the storm motion relative and shear relative wind field composites. This is for all five of the simulations (minus the 24 h spin up, landfall, and post extratropical cases). Figure 4.5 shows the storm motion relative 10 m composite wind field. The storm motion direction is directly northward. As expected, the 10 m wind field displays a distinct wavenumber-1 asymmetry with a maximum to the right of the

motion vector. Figure 4.6 shows the shear relative 10 m composite wind field, where the shear direction is now directly northward. Again consistent with expectations based on previous theory and observation, the wind field has a well-defined wavenumber-1 asymmetry maximized to the left of the shear vector.

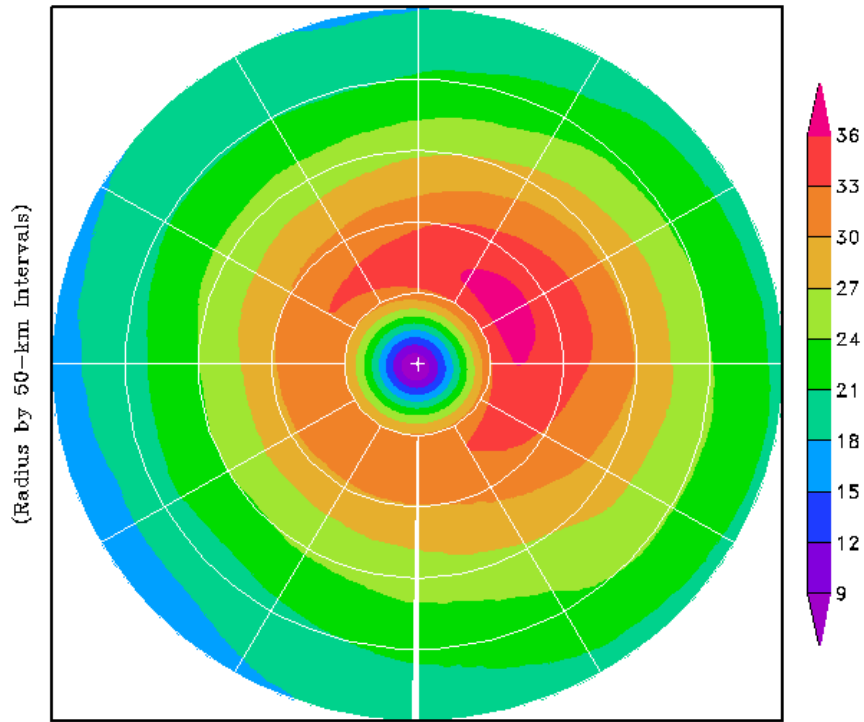


Figure 4.5: Storm motion relative 10 m composite wind field of all storm data (N = 431). Storm motion direction is directly northward.

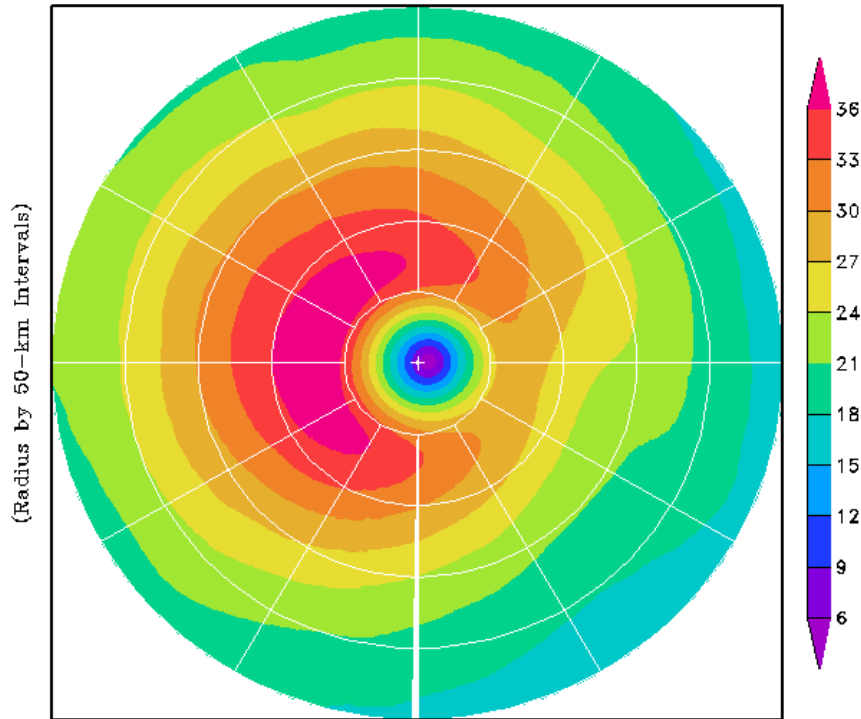


Figure 4.6: Shear relative 10 m composite wind field of all storm data (N = 431). Shear direction is directly northward.

The composite wind field displays structural variations with height. Analogous plots were created for the 1500 m, 3000 m, 5000 m, and 12000 m heights, but are not shown here. Within the frictional boundary layer, the winds aloft in a tropical cyclone are stronger than at the surface. The magnitude of the winds in the composite plots seems to maximize around the 1500 m level, and this is consistent for both the storm motion relative and shear relative composites. Also seen consistently for both the storm motion and shear relative composites, starting at 5000 m the azimuthal location of the asymmetric maximum begins to rotate cyclonically. At the 12000 m height the cyclonic shift is most pronounced. In the storm motion relative composite the 12000 m height cyclonic shift is large enough that the asymmetric maximum is now located to the left of the storm motion direction. Also, there is a shift in the radial location of the asymmetric

maximum to slightly larger radii. Again, this is consistent for both the storm motion and shear relative composites.

The next step in the composite analysis is to stratify the data by the relative orientation of the storm motion and shear vectors. Table 4.4 summarizes the number of cases included in each compositing group as well as the average maximum wind speed, storm motion magnitude, and shear magnitude for each group. All of the vector directional difference composite plots are storm motion relative, so the storm motion is directly northward. Figure 4.7 shows the 10 m composite wind field for the case where the vectors are approximately aligned (DD1). The maximum occurs to the left of the storm motion, but there is a clear wavenumber-2 pattern in the asymmetries. This is consistent with the findings of Ueno and Bessho (2011) from their QuikSCAT study of western Pacific typhoons (previously discussed in Chapter 1). They found this wavenumber-2 asymmetry when they isolated their composite analysis for the storm motion and shear vectors aligned cases to include only the strong shear data (i.e. shear magnitude exceeding 7 m/s). Interestingly, for this study, the wavenumber-2 asymmetry is seen even without having to isolate the strong shear cases, although this may be because the average shear for the DD1 group in this study is 13.6 m/s which is even larger than the average shear for Ueno and Bessho's (2011) strong shear group (their average shear was 11.9 m/s). Also of note, the maximum magnitude asymmetry in the Ueno and Bessho (2011) strong shear composite occurs to the right of the storm motion unlike what is shown here.

The wavenumber-2 asymmetry is less evident in the composite 1500 m wind field (not shown), and the asymmetric structure is distinctly more wavenumber-1 in nature at

the 3000 m, 5000 m and 12000 m heights (not shown) with the maximum located to the left of the storm motion vector. This suggests that the asymmetries forced by interaction with vertical shear extend through a deeper layer than those from the storm motion. At increasing height, the wavenumber-1 asymmetry maxima are broader than at the surface level. At the 12000 m height the asymmetric maxima is shifted marginally cyclonically.

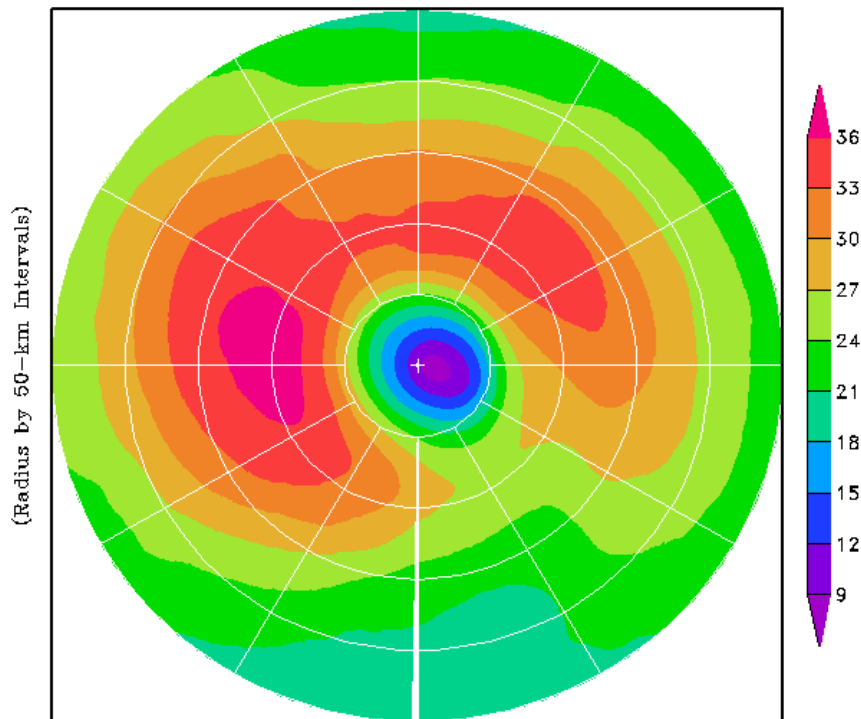


Figure 4.7: 10 m composite wind field of DD1 data (N = 96) where the storm motion and shear direction are approximately aligned. Storm motion direction is directly northward and shear direction is within $\pm 45^\circ$ of the direction of storm motion.

The 10 m composite wind field for the DD2 group where the storm motion and shear vectors are approximately opposed is shown in Figure 4.8. The plot shows a large wavenumber-1 asymmetry with the maximum wind located to the right of the storm motion vector. This is consistent with the findings of Ueno and Bessho (2011) for their equivalent group ('S1'). This was the expected result because if the maximum winds are generally found to the right of the storm motion vector, and to the left of the shear vector,

then if the two vectors are opposed the predicted locations for the maximum winds are both to the right of the storm motion vector. This should result in a strong wavenumber-1 asymmetry, which is what is seen here. The composite wind field for the DD2 group variations with height primarily in the form of the wind field spreading out. The wavenumber-1 asymmetry is consistent through all heights and the maximum winds remain located to the right of the storm motion vector. Only at the 12000 m height is there a small cyclonic shift in the location of the maximum winds.

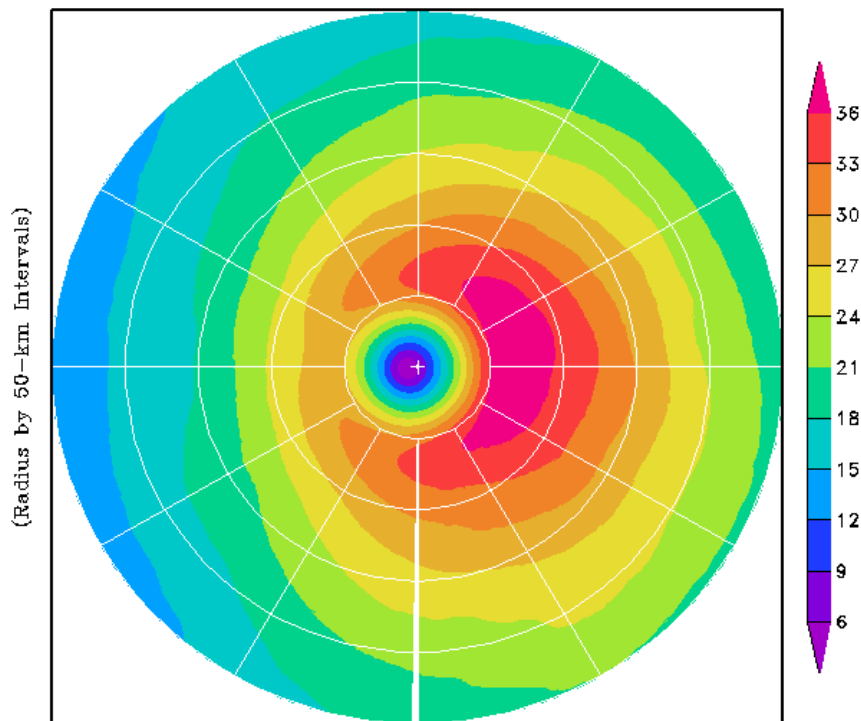


Figure 4.8: 10 m composite wind field of DD2 data (N = 171) where the storm motion and shear direction are approximately opposed. Storm motion direction is directly northward and shear direction is greater than $\pm 135^\circ$ of the direction of storm motion.

Table 4.4: List of groups formed for the composite analyses. The last three columns indicate the group average of the respective parameters.

Group ID	Number of Cases	Maximum Wind (m/s)	Storm Motion (m/s)	Shear (m/s)
DD1	96	33.7	12.35	13.56
DD2	171	35.2	6.05	5.45

In order to isolate the individual wavenumber components of the wind field, the tangential winds are decomposed using the Fourier analysis techniques described in Chapter 3 ((3.4)-(3.6)). The total wind field is well approximated by the tangential winds since they dominate over the radial winds in tropical cyclones. A composite wind field is created for each wavenumber from 0-4 for all storm motion relative and shear relative data, and for both the aligned (DD1) and opposed (DD2) groups. Figures 4.9-4.18 show a selection of these composites for the 10 m height.

Consider first the composites of all of the data for the storm motion relative and shear relative scenarios. Recall that the wavenumber-0 field simply describes the azimuthal mean flow. Because it describes the mean flow, it is the same for both the storm motion relative and shear relative composites of all data. The mean tangential wind field values range from 0 m/s to greater than 30 m/s. The magnitudes of the asymmetric features in the wavenumber-1 to 4 fields are much smaller, which means that the azimuthal mean field is the dominant feature in the tropical cyclone wind fields. Figure 4.9 shows the wavenumber-1 tangential wind field for all the data composited in storm motion relative coordinates. Figure 4.10 shows the same figure, but for the shear relative composite. For the storm motion relative composite the maximum tangential wind is located in the right front quadrant of the storm. For the shear relative composite the maximum is located approximately 90° to the left of the storm motion vector. Also, note the relative magnitudes of the maxima. The wavenumber-1 asymmetric maximum for the shear relative composite is more than twice the magnitude for the storm motion relative composite. This suggests that not only is the shear important in determining the location of storm asymmetries, but also in determining their magnitude.

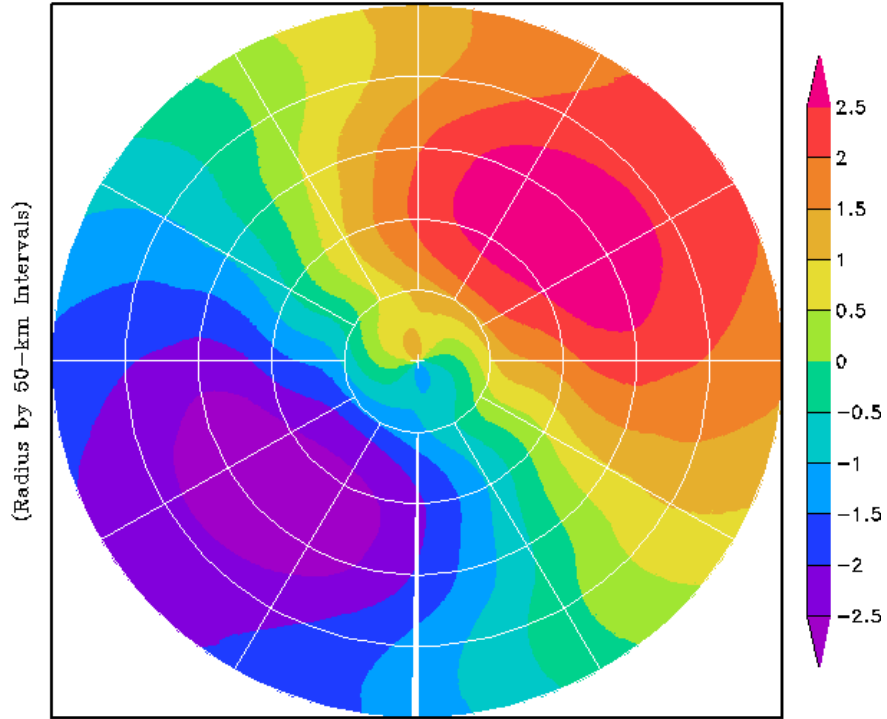


Figure 4.9: Storm motion relative 10 m composite plot of the wavenumber-1 tangential wind field of all data. Storm motion direction is directly northward.

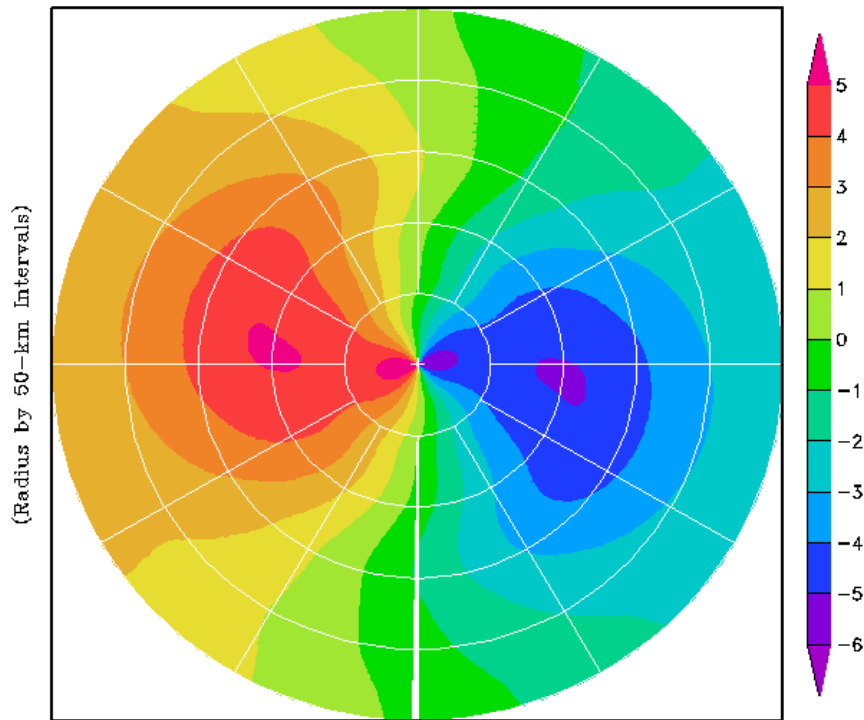


Figure 4.10: Shear relative 10 m composite plot of the wavenumber-1 tangential wind field of all data. Shear direction is directly northward.

Figure 4.11 shows the storm motion relative composite of the wavenumber-2 tangential wind field for all the data. Figure 4.12 shows the same plot for the shear relative composite. Notice first that the scale of these asymmetries is much smaller (contours ranging from -0.6 to 0.6 m/s) than that of the wavenumber-1 features. For the storm motion relative composite the locations of the maxima are approximately 90° to the left and right of the storm motion vector. For the shear relative composite the maxima are located in the right front and left rear quadrants of the storm. The magnitude of the asymmetries is about the same between the storm motion and shear relative composites. The wavenumber-3 and 4 asymmetries are increasingly small compared to the wavenumber-0, 1, and 2 features, and therefore are most likely less important.

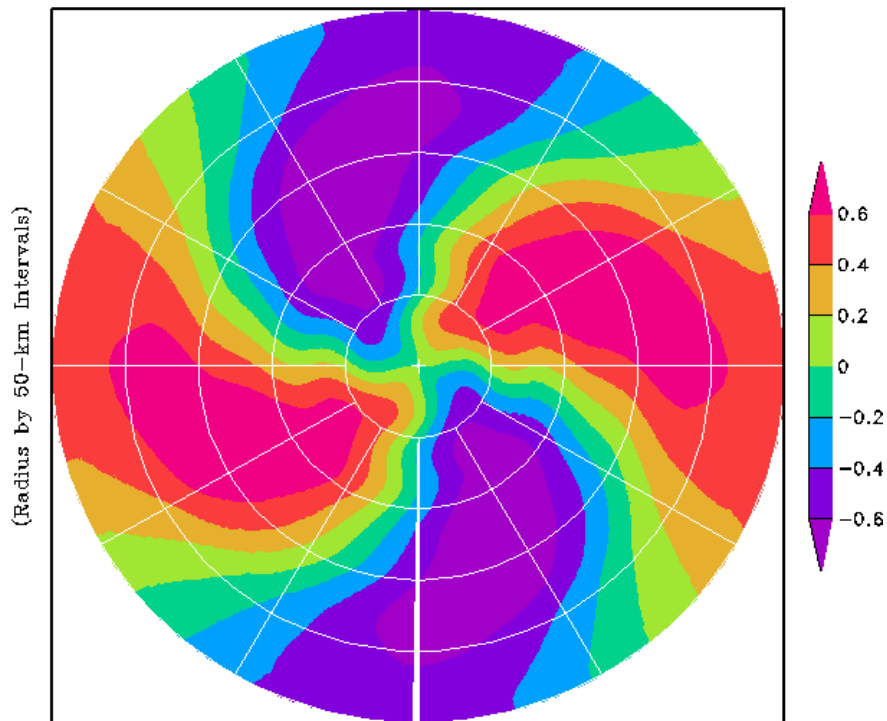


Figure 4.11: Storm motion relative 10 m composite plot of the wavenumber-2 tangential wind field of all data. Storm motion direction is directly northward.

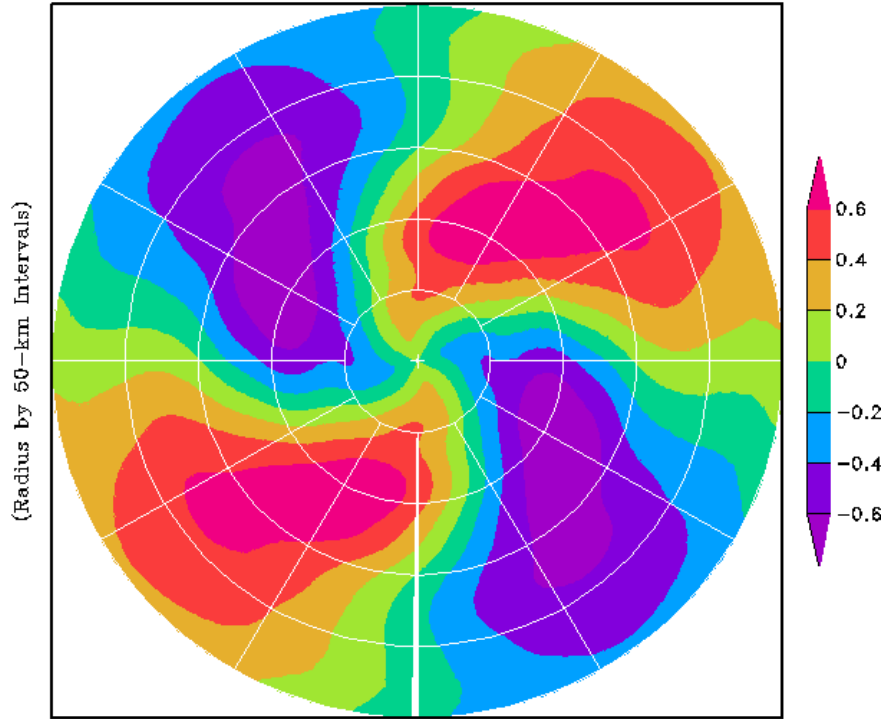


Figure 4.12: Shear relative 10 m composite plot of the wavenumber-2 tangential wind field of all data. Shear direction is directly northward.

The 10 m composite wavenumber-0 tangential winds for the DD1 group (aligned) are shown in Figure 4.13 and for the DD2 group (opposed) are shown in Figure 4.14. For the DD1 group (aligned) the azimuthal mean flow is much broader and larger magnitude than the azimuthal mean flow pattern of the DD2 group (opposed). For the DD2 group the strongest azimuthal mean flow is concentrated at smaller radii. These results are a consequence of the fact that the largest contributor to the aligned (DD1) group is the 22 October 2005 Wilma simulation during its extratropical transition when the wind field is relatively large.

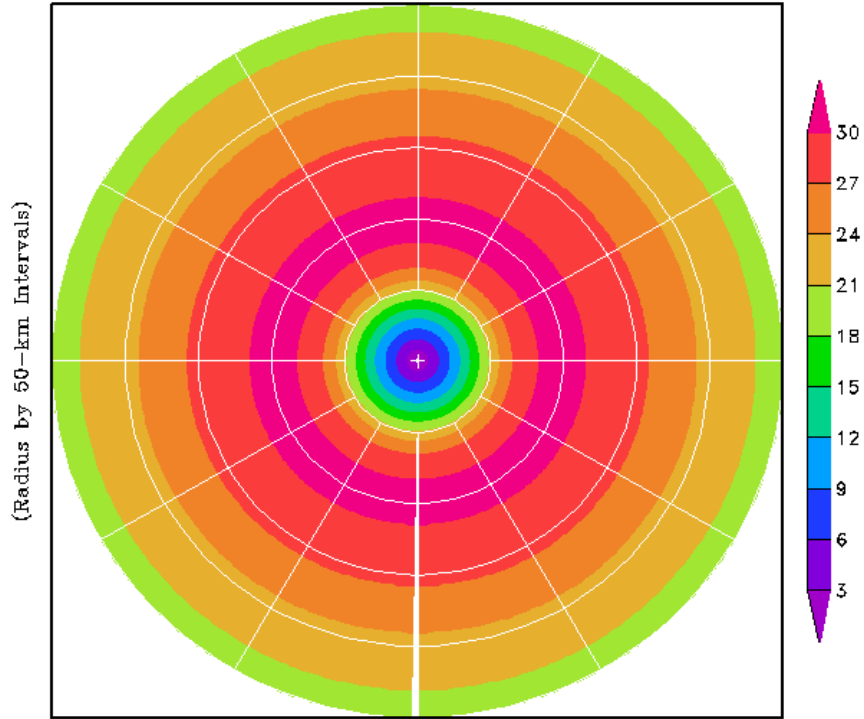


Figure 4.13: 10 m composite of the wavenumber-0 tangential wind field of DD1 data.

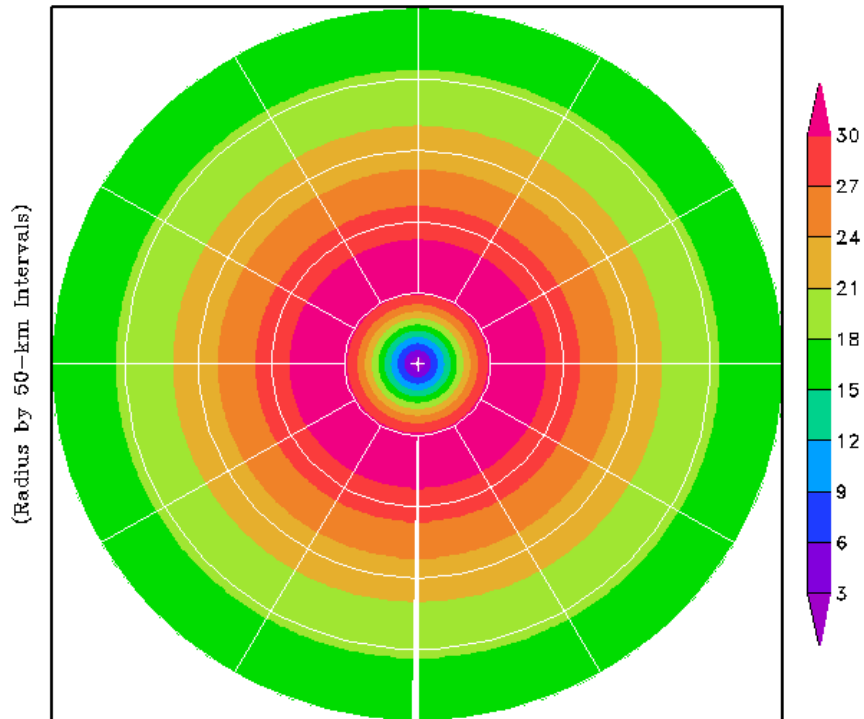


Figure 4.14: 10 m composite of the wavenumber-0 tangential wind field of DD2 data.

The wavenumber-1 composite structure is shown in Figure 4.15 for the DD1 group, and is shown in Figure 4.16 for the DD2 group. Firstly, is it best to disregard the asymmetric structures near the storm center (approximately inside of 50 km radius) because these features are influenced by small differences in the identification of the storm center in the pressure field and wind field. Willoughby (1992) referred to these apparent asymmetries related to the dislocation of the vortex center from the grid center as “alpha gyres.” For the DD1 group (aligned) the maximum tangential wind is located in the left front quadrant. For the DD2 group (opposed) the maximum tangential wind is located nearly 90° to the right of the storm motion vector. The magnitudes of the wavenumber-1 maxima for the DD1 and DD2 groups are about the same.

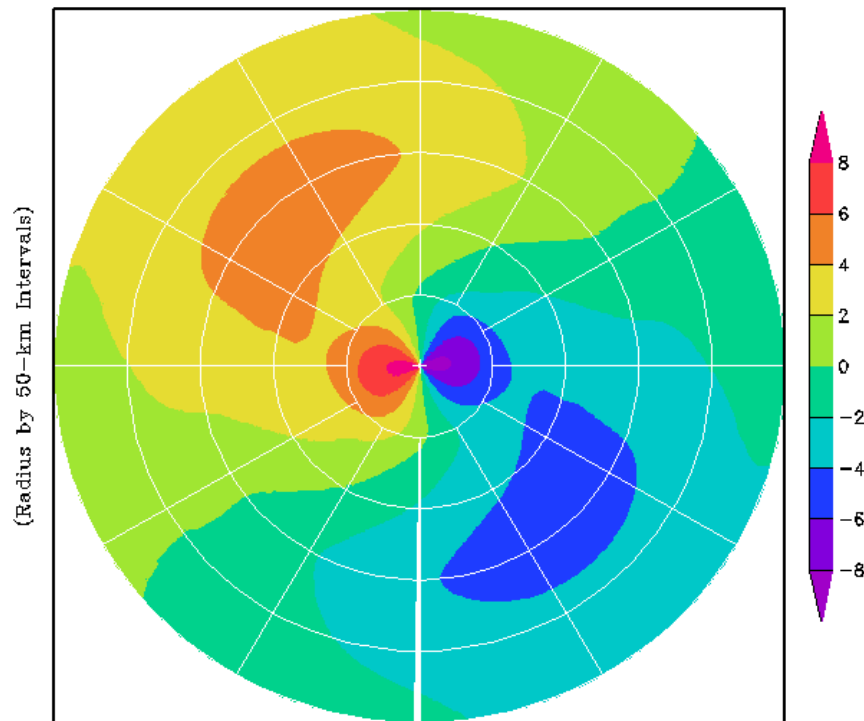


Figure 4.15: 10 m composite of the wavenumber-1 tangential wind field of DD1 data.

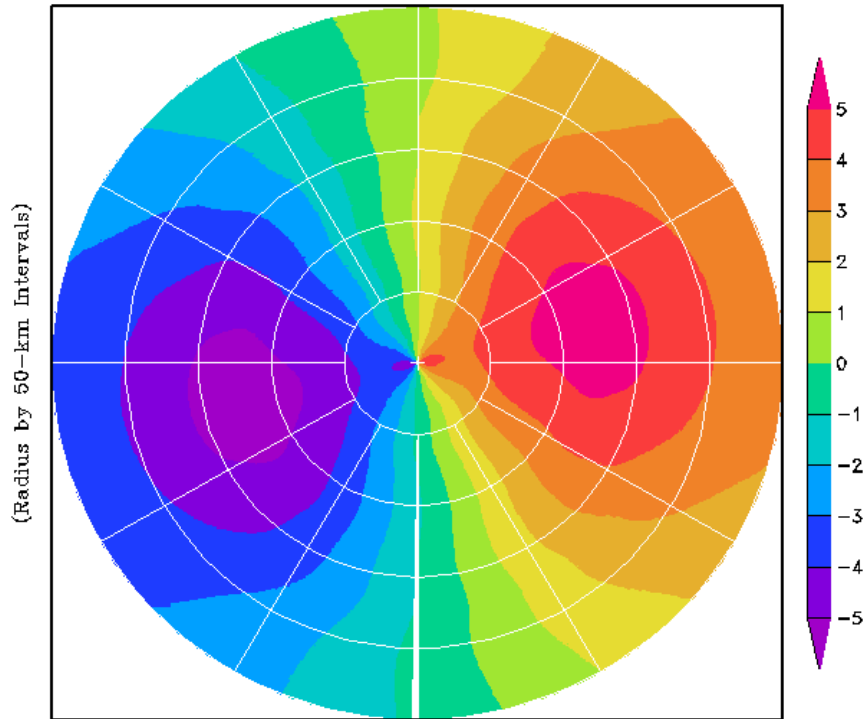


Figure 4.16: 10 m composite of the wavenumber-1 tangential wind field of DD2 data.

The 10 m height wavenumber-2 tangential wind field composite for the DD1 group (aligned) is shown in Figure 4.17, and the composite for the DD2 group (opposed) is shown in Figure 4.18. Firstly, the relative magnitude of the wavenumber-2 features for the two groups is significantly different. The DD1 group wavenumber-2 asymmetries maximize in the range of 3.0 m/s whereas the DD2 group asymmetries maximize around 0.5 m/s. Not only are the asymmetries much smaller for the DD2 group, but there isn't as well defined a structure to the field. The DD1 group composite wavenumber-2 asymmetries have well-defined maxima in the tangential winds to the right (front quadrant) and the left (rear quadrant) of the storm motion vector. This structure and relative larger magnitude to the asymmetries suggests that the wavenumber-2 asymmetries are a more important component of the wind field structure when the storm motion and shear vectors are aligned.

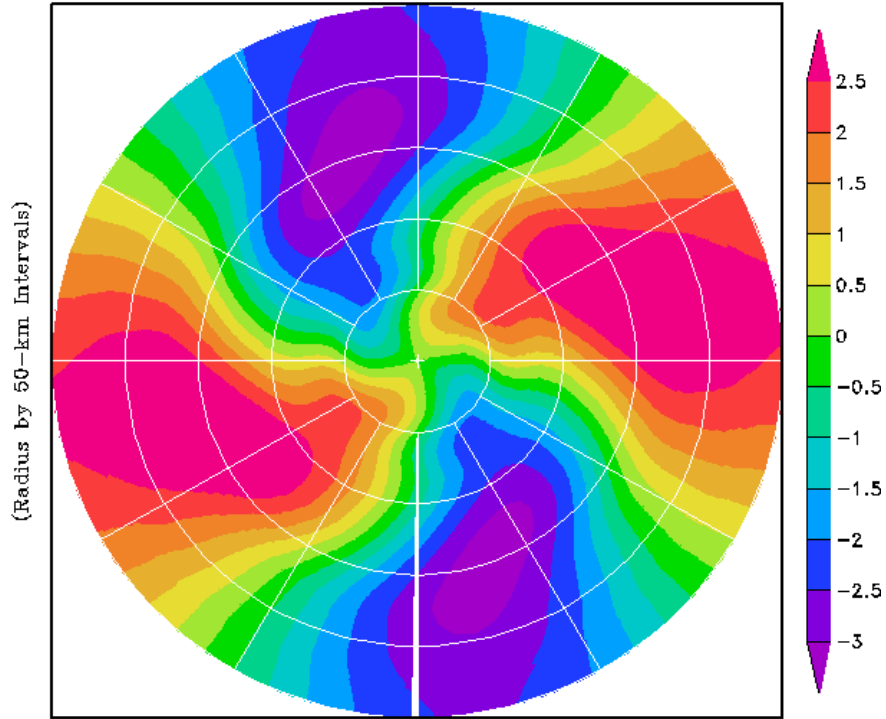


Figure 4.17: 10 m composite of the wavenumber-2 tangential wind field of DD1 data.

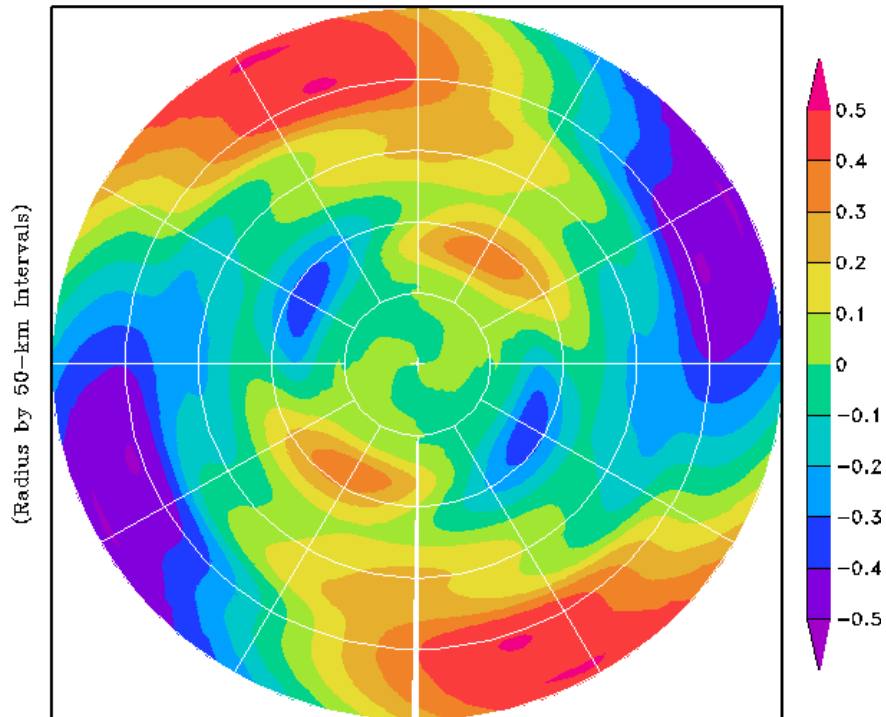


Figure 4.18: 10 m composite of the wavenumber-2 tangential wind field of DD2 data.

The wavenumber-3 and 4 composite fields are not shown. This is because the magnitude of these asymmetries are quite small for both the DD1 (aligned) and DD2 (opposed) groups compared to the magnitudes of the wavenumbers 0, 1, and 2 fields. It is interesting to note, however, that the magnitudes of the wavenumber-3 and 4 asymmetries is greater for the DD1 group than for the DD2 group which indicates that there is a stronger high wavenumber asymmetry presence for the cases where the storm motion and shear vectors are aligned compared to when they are opposed.

4.3 Vortex Rossby Wave Analysis

The above results show that the low level wind asymmetries are strongly related to environmental shear forcing and storm motion. Vortex Rossby waves have also been theorized to play a role in the asymmetric structure of tropical cyclones. Wavenumber-2 vortex Rossby waves have been investigated in tropical cyclone vorticity fields by Kuo et al. (1999), who were looking into the elliptical eye structure of Typhoon Herb (1996), and by Reasor et al. (2000), who examined the asymmetric structure in Hurricane Olivia (1994). Wang (2001) also looked at wavenumber-2 vortex Rossby waves in the vorticity field and its contributions to the asymmetries in the tropical cyclone inner core in a numerical modeling study.

The phase speed of the vortex Rossby wave from the linear wave theory of Lamb (1932) is given by:

$$c = V_{\max} \left(1 - \frac{1}{m}\right) \quad (4.1)$$

where V_{max} is the maximum tangential wind speed, and m is the azimuthal wavenumber.

This predicted propagation speed assumes a Rankine vortex. For azimuthal wavenumber-2, the phase speed is half the speed of the maximum tangential wind.

Wavenumber-2 vortex Rossby waves near the eye edge should propagate to the left of the vorticity gradient, and therefore asymmetries should move upstream with respect to the mean flow. However, in a tropical cyclone the cyclonic tangential mean flow is significant and is far greater than that of the proposed vortex Rossby wave propagation speed. Thus, the vortex Rossby waves will still rotate cyclonically around the storm center, but with a speed slower than the advective speed.

To determine if there is evidence to warrant a vortex Rossby wave analysis, the 1500 m vorticity fields were first examined. Within the five simulations used in this study, there are certainly indications from the vorticity fields that there may be some vortex Rossby wave type features. Figure 4.19 shows an example from the Hurricane Katrina simulation. The panels labeled a-f are snapshots of the 1500 m vorticity field over a 6 h time span (the panels are 1 h apart). In these figures there appears to be a persistent wavenumber-2 asymmetry in the vorticity that moves cyclonically around the storm. This encourages further investigation to try to ascertain whether this kind of feature is in part due to vortex Rossby waves. Time series analysis of the model vorticity fields will be performed to compare the spectra to those expected from the vortex Rossby wave theory, as described below.

For the time series analysis, the five simulations are divided into 48 h temporal sections. There are a total of eight 48 h sections for examination as shown in Table 4.5. This table also shows the average maximum tangential wind at the 1500 m height (from

the average tangential wind profile), the radius which is used for evaluation, and the predicted vortex Rossby wave temporal wavenumber, n_{VRW} (the calculation of this will be explained shortly). The radius for each 48 h section is chosen to be twice the radius of the maximum azimuthal mean vorticity. Twice the radius of maximum vorticity is roughly in the region of the radius of maximum tangential wind, which is where the asymmetric signal is more likely to be strongest.

Table 4.5: The 48 h temporal sections used in the vortex Rossby wave analysis.

HWRFX Simulation	Forecast Hour Time Span	Average Maximum Tangential Wind (m/s)	Radius (km) of evaluation	n_{VRW}
Emily, 13 July	24-71	46.4	32	40
Emily, 13 July	72-119	50.1	52	27
Emily, 15 July	22-69	52.8	68	21
Emily, 15 July	70-117	51.9	100	14
Katrina, 26 August	24-71	61.4	88	19
Wilma, 18 October	24-71	51.2	72	20
Wilma, 18 October	72-119	40.2	132	8
Wilma, 22 October	24-71	49.9	92	15

These 48 h sections of the 1500 m vorticity are first decomposed via Fourier analysis into spatial wavenumber space. The amplitudes from this spatial analysis are then fed into a temporal Fourier decomposition (recall the methodology description in Chapter 3). The magnitudes of the 1500 m vorticity azimuthal wavenumber-2 coefficients (from equation (3.34)) can be plotted as a function of the temporal wavenumber, n (or frequency). The task now is to find the temporal frequency that corresponds to azimuthal wavenumber-2 vortex Rossby waves. Equation (4.1) gave the phase speed for wavenumber-2 vortex Rossby waves at any given time. A more general definition of phase speed is:

$$c = \frac{v}{k}$$

where v is frequency, and k is the azimuthal wavenumber, and

$$v = \frac{2\pi n}{T}$$

where n is the temporal wavenumber, and T is the period (48 h = 172800 sec), and

$$k = \frac{2\pi m}{L} = \frac{2\pi m}{2\pi r} = \frac{m}{r}$$

where L is the length which for any given radius and is equal to $2\pi r$ (the circumference of the radial circle). Therefore, the phase speed can be written as:

$$c = \frac{2\pi nr}{Tm}$$

and using equation (4.1), and solving for n :

$$n_{\text{vrw}} = \frac{V_{\text{max}} T}{2\pi r}. \quad (4.2)$$

This is the predictive equation for the temporal wavenumber corresponding to azimuthal wavenumber-2 vortex Rossby waves.

One of the assumptions in the derivation of (4.2) is that the simulated tropical cyclone symmetric tangential wind is well approximated by a Rankine vortex. A Rankine vortex is defined by axisymmetric flow where the tangential wind profile is defined by:

$$v = V_{\text{max}} \frac{r}{R} \text{ if } 0 \leq r < R \quad \text{and} \quad v = V_{\text{max}} \frac{R}{r} \text{ if } R \leq r$$

where R is the radius of maximum wind. The vorticity profile in a Rankine vortex is a constant value inside the radius of maximum wind and then drops to zero outside the radius of maximum wind and is described by the following:

$$\nabla_{xv} = k \begin{cases} 2 \frac{V_{max}}{R}, & \text{if } 0 \leq r < R \\ 0, & \text{if } R \leq r \end{cases} .$$

Figure 4.20 shows a sample comparison of the radial profiles of the 1500 m mean tangential wind (solid black) and mean vorticity (solid blue) for the 24-71 h time span of the 26 August 2005 HWRFx simulation of Hurricane Katrina. The dotted black line is the tangential wind profile for a Rankine vortex, and the dotted blue line is the vorticity profile for a Rankine vortex. The left hand vertical axis is for the tangential wind, and the right hand vertical axis is for the vorticity. The simulated storm is not an exact fit to a Rankine vortex. The tangential winds do not drop off as quickly outside the radius of maximum wind as the Rankine vortex tangential winds, and the vorticity profile is far more complex than the Rankine ‘box car’ function. However, the vorticity does drop off dramatically in the region where the Rankine vorticity goes to zero, so the maximum vorticity gradient from the model is in the same region as the vorticity discontinuity of the Rankine vortex. Thus, equation (4.2) is still applicable, although some variability in the location of the maxima in the model frequency spectra relative to that from the theory is expected.

The magnitudes of the 1500 m vorticity azimuthal wavenumber-2 coefficients are calculated for temporal wavenumbers ranging from -24 to 24 (temporal wavenumbers greater than 24 cannot be resolved for the 48 h time spans). Then the temporal wavenumber corresponding to the vortex Rossby wave is calculated using equation (4.2).

The predicted vortex Rossby wave temporal wavenumber (n_{VRW}) is displayed in the last column of Table 4.5. The coefficient magnitudes are then plotted versus the temporal wavenumber (n) for each of the 48 h sections. The predicted vortex Rossby wave temporal wavenumber is highlighted on each plot by an asterisk (*), as well as the surrounding $n\pm 1$ temporal wavenumbers which are highlighted by a triangle (Δ). Figures 4.21-4.26 show the resulting plots. Note that the two plots for the 13 July 2005 Emily simulation are not shown. This is because the predicted vortex Rossby wave temporal wavenumber was too large to be resolved (i.e. greater than $n=24$). Of the six remaining figures presented here, the predicted vortex Rossby wave temporal wavenumber occurs either at or within an n -point or two of a peak in the azimuthal wavenumber-2 vorticity coefficients. This suggests that there is indeed a vortex Rossby wave contribution to the wavenumber-2 asymmetries in the simulated tropical cyclones. The positive n values indicate that the waves propagate upstream relative to the mean flow, which matches the vortex Rossby wave theory.

4.4 Summary and Discussion of Results

In this chapter a variety of parameters connected to the horizontal structure of tropical cyclones have been investigated. Special focus was put on the asymmetric structures associated with the relative orientation of the storm motion and shear vectors. First the integrated kinetic energy was evaluated including a dissection to wavenumber space. Then a composite analysis of the wind fields was done with a further break down of the tangential wind field using Fourier analysis. Then a more precise study was done to determine whether there is a vortex Rossby wave influence in the wavenumber-2 asymmetric structures.

The integrated kinetic energy field analysis showed that the mean flow is the dominant contributor to the total kinetic energy, but there are non-trivial contributions from some of the low wavenumber asymmetries, particularly for wavenumber-1 asymmetries. The kinetic energy field storm motion related asymmetries are dominated by wavenumber-1 contributions, but the shear related asymmetries have larger contributions from more of the low wavenumber asymmetries. When the storm motion and shear vectors are aligned the integrated kinetic energy field has large contributions from the wavenumber-1 to 4 asymmetries in comparison to the scenario where the storm motion and shear vectors are opposed.

The wind field composites showed that the storm motion relative field has a wavenumber-1 wind maxima to the right of the storm motion vector, and the shear relative field has a wavenumber-1 wind maxima to the left of the shear vector. The scenario where the storm motion and shear vectors are approximately opposed display a composite wind structure with a solid wavenumber-1 asymmetry with the maximum located to the right of the storm motion vector. This result agrees with the previous results of Ueno and Bessho (2011). However, when the storm motion and shear vectors are approximately aligned the composite surface wind structure displays a wavenumber-2 asymmetric pattern. Additionally, the wavenumber-1 maximum within this field is located to the left of the storm motion vector. The wavenumber-2 pattern is consistent with the previous findings of Ueno and Bessho (2011), but the relative location of the wavenumber-1 maximum within the field is different than was seen in Ueno and Bessho's (2011) work. This may be a result of the fact that the simulations used in this study include some far more highly sheared storms. The 22 October 2005 Hurricane

Wilma simulation is the dominant contributor to the compositing group where the storm motion and shear vectors are aligned. This simulation is the one where the storm is beginning to experience extratropical transition and is quite highly sheared. With a case where the shear is such a dominant force it may overcome the storm motion force asymmetries resulting in a stronger maxima to the left of the storm motion vector when the shear vector is roughly aligned.

Finally, the analysis to determine whether there is evidence that vortex Rossby waves have a role in the wavenumber-2 asymmetries revealed that there is, in fact, evidence that they are present in the simulated storms. These vortex Rossby waves act to slow the overall propagation of the wavenumber-2 asymmetries, such that they move more slowly than is predicted by pure advective velocity.

The asymmetries due to environmental shear and motion have fairly long time scales (~12 h), since they are related to the larger spatial scale forcing of the storm environment. The time scales of the vortex Rossby waves are much shorter. Thus, the asymmetries are due to a combination of factors varying over a variety of time scales. To get a rough idea of the magnitude of each, the amplitudes of the spectral peaks associated with vortex Rossby wave frequencies in Figures 4.21-4.26 are 1 to $2 \times 10^{-5} \text{ s}^{-1}$. If the waves are confined to the region within the vorticity gradient, the spatial scale would be about 100 km, so a tangential wind magnitude would be about 1 to 2 m/s. This is about the same magnitude as the asymmetries due to the shear and motion.

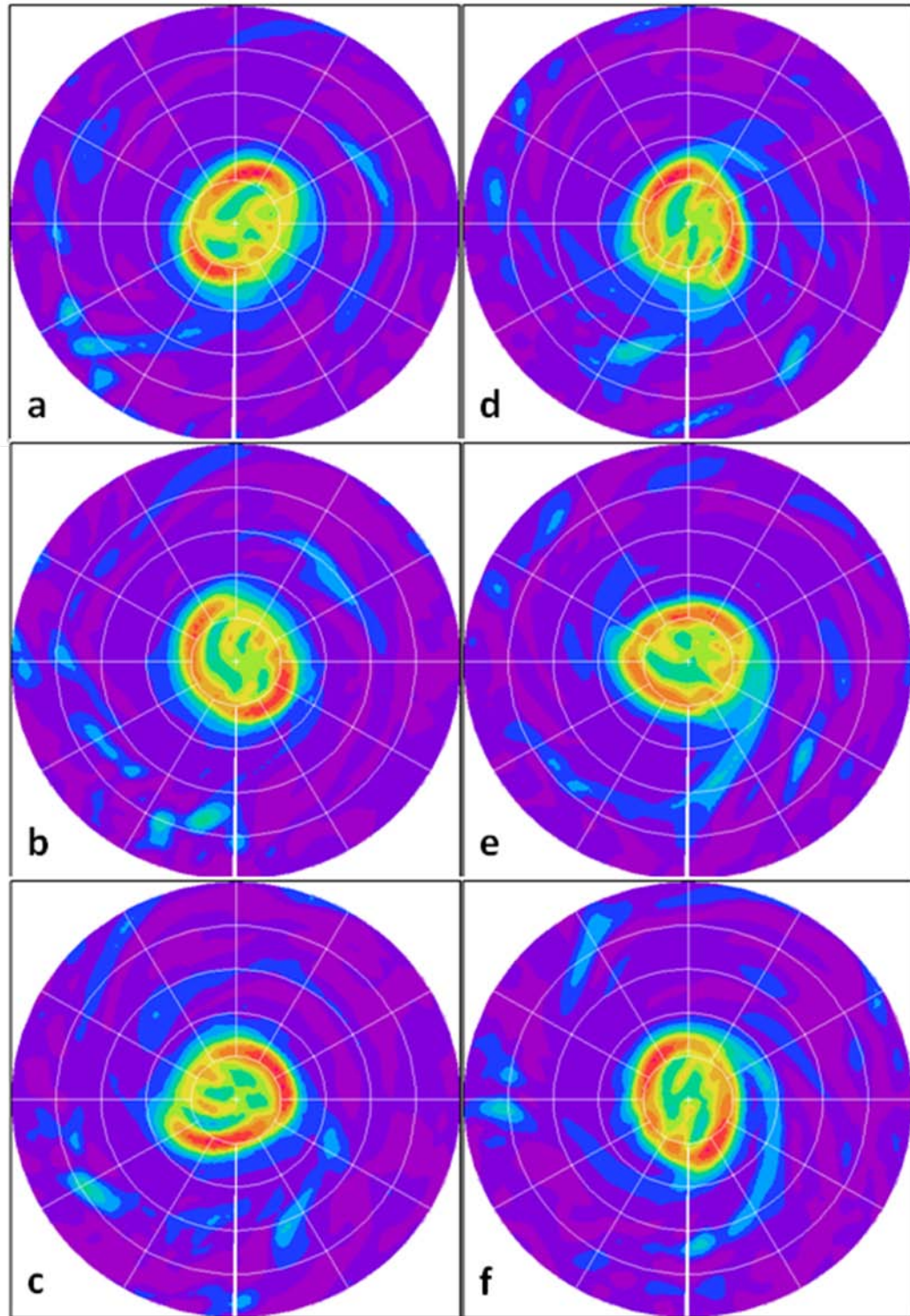


Figure 4.19: 1500 m vorticity field from the 26 August 2005 Hurricane Katrina simulation. Panel's a-f sequentially increment by 1 h.

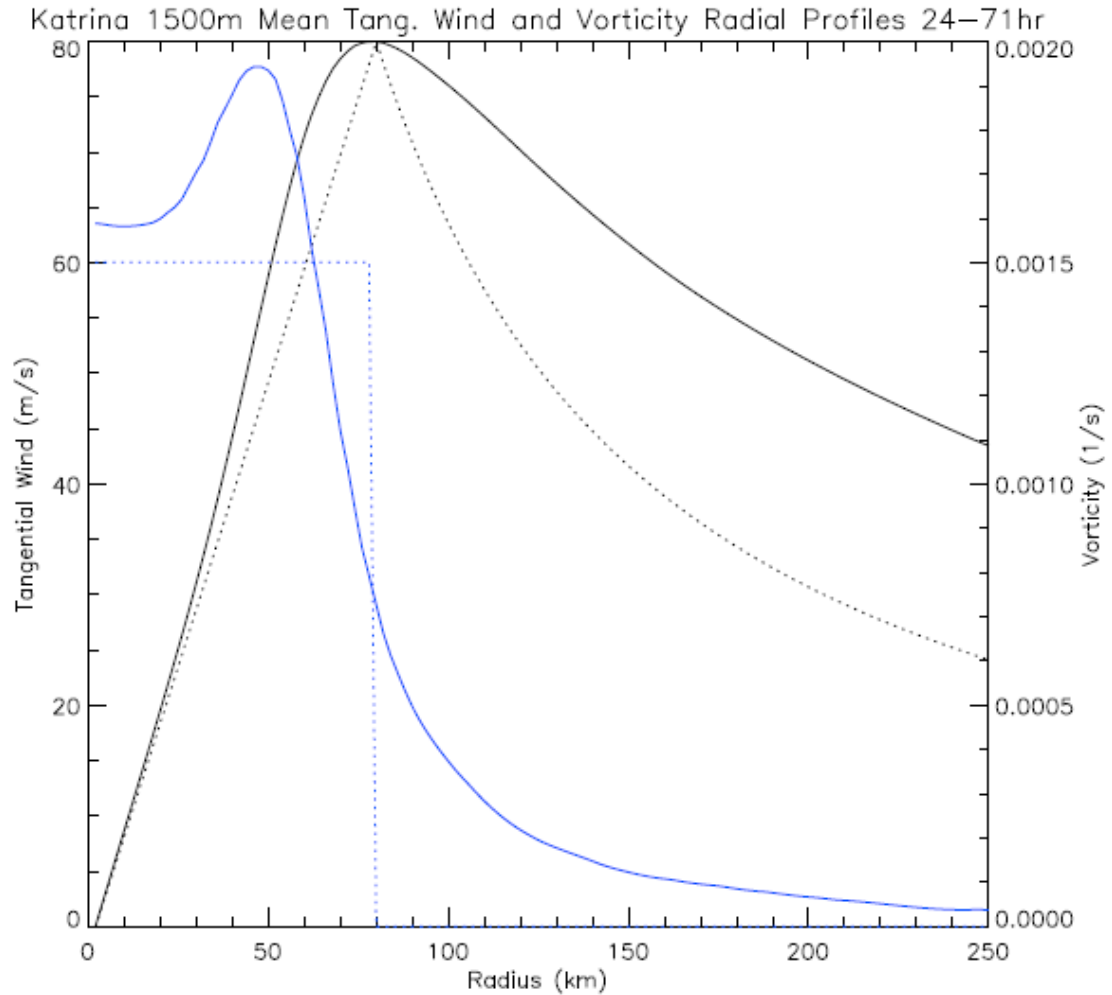


Figure 4.20: Radial profiles of the 1500 m mean tangential wind (solid black) and mean vorticity (solid blue) for the 24-71 h time span of the 26 August 2005 HWRFx simulation of Hurricane Katrina. The dotted black line is the tangential wind profile for a Rankine vortex, and the dotted blue line is the vorticity profile for a Rankine vortex. The left hand vertical axis is for the tangential wind, and the right hand vertical axis is for the vorticity.

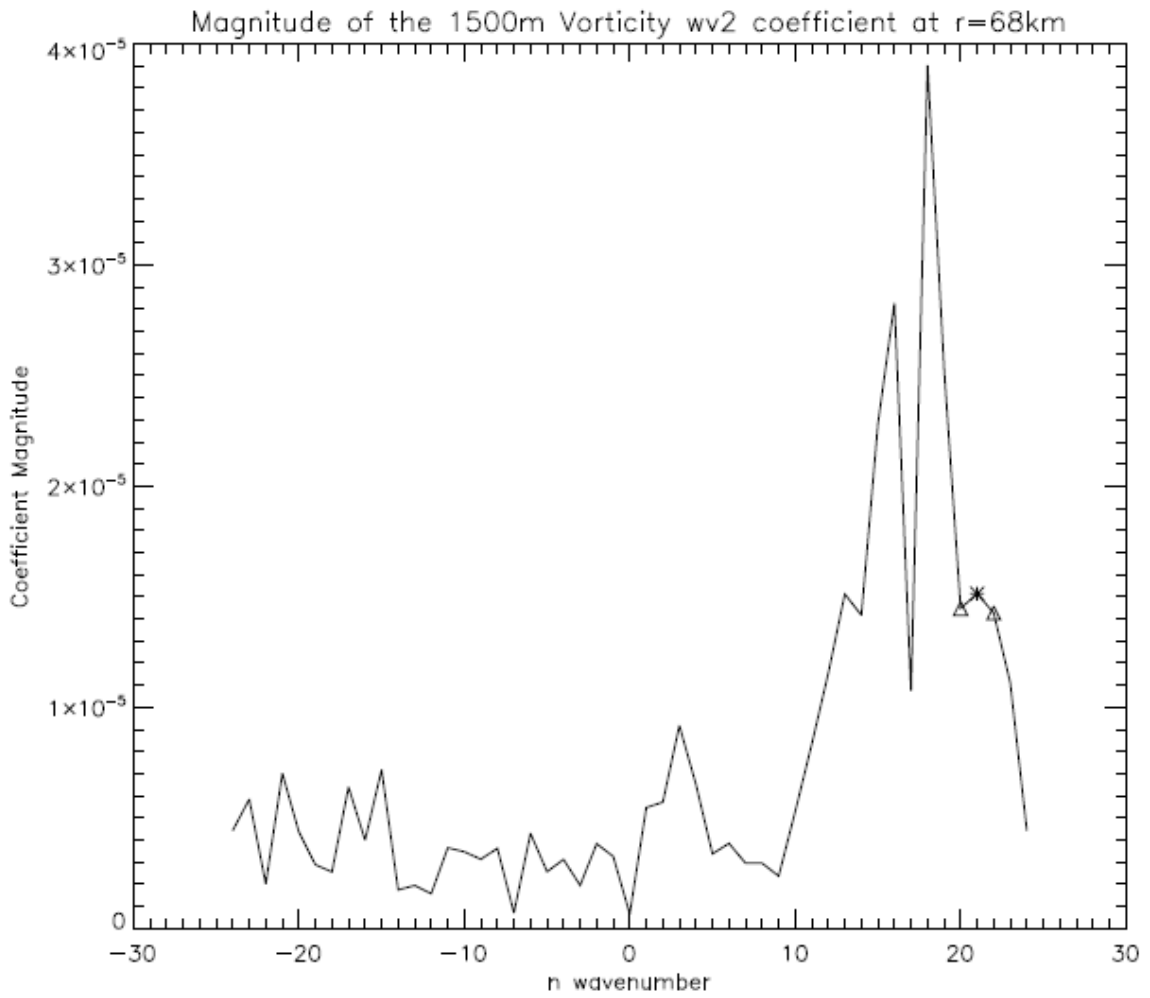


Figure 4.21: Magnitude of the 1500 m vorticity wavenumber-2 coefficient at a radius of 68 km for the 22-69 h time span of the 15 July 2005 HWRFx simulation of Hurricane Emily.

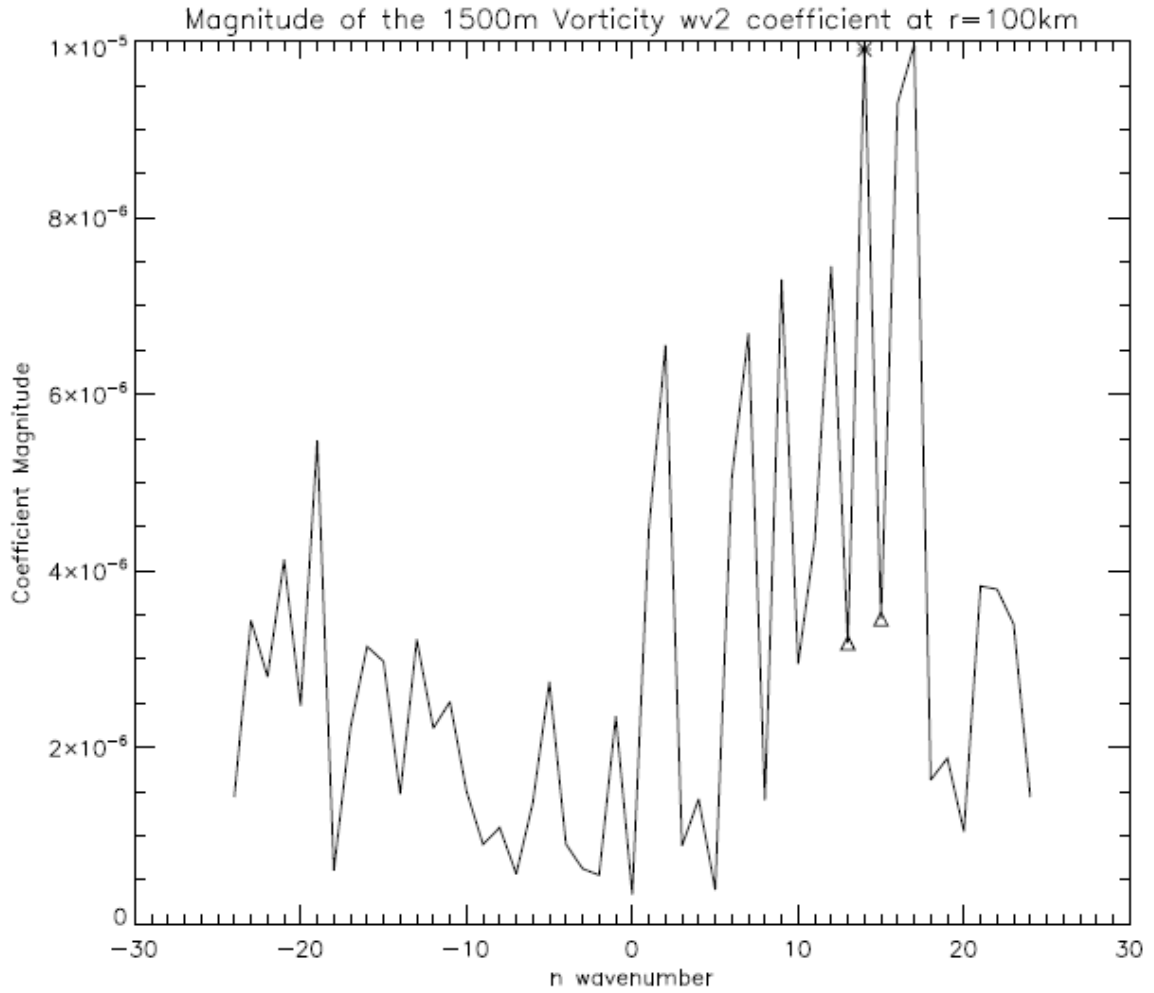


Figure 4.22: Magnitude of the 1500 m vorticity wavenumber-2 coefficient at a radius of 100 km for the 70-117 h time span of the 15 July 2005 HWRFx simulation of Hurricane Emily.

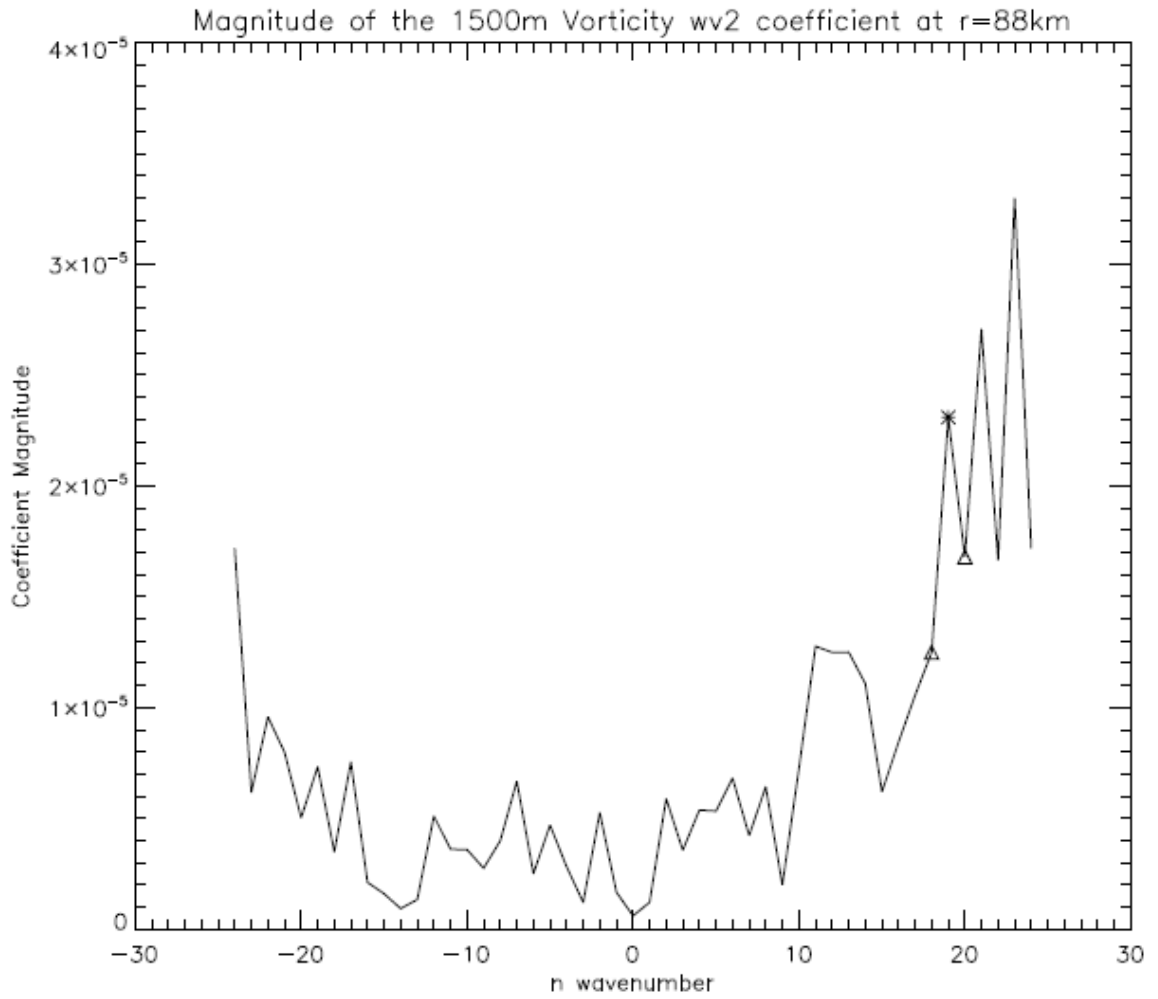


Figure 4.23: Magnitude of the 1500 m vorticity wavenumber-2 coefficient at a radius of 88 km for the 24-71 h time span of the 26 August 2005 HWRFx simulation of Hurricane Katrina.

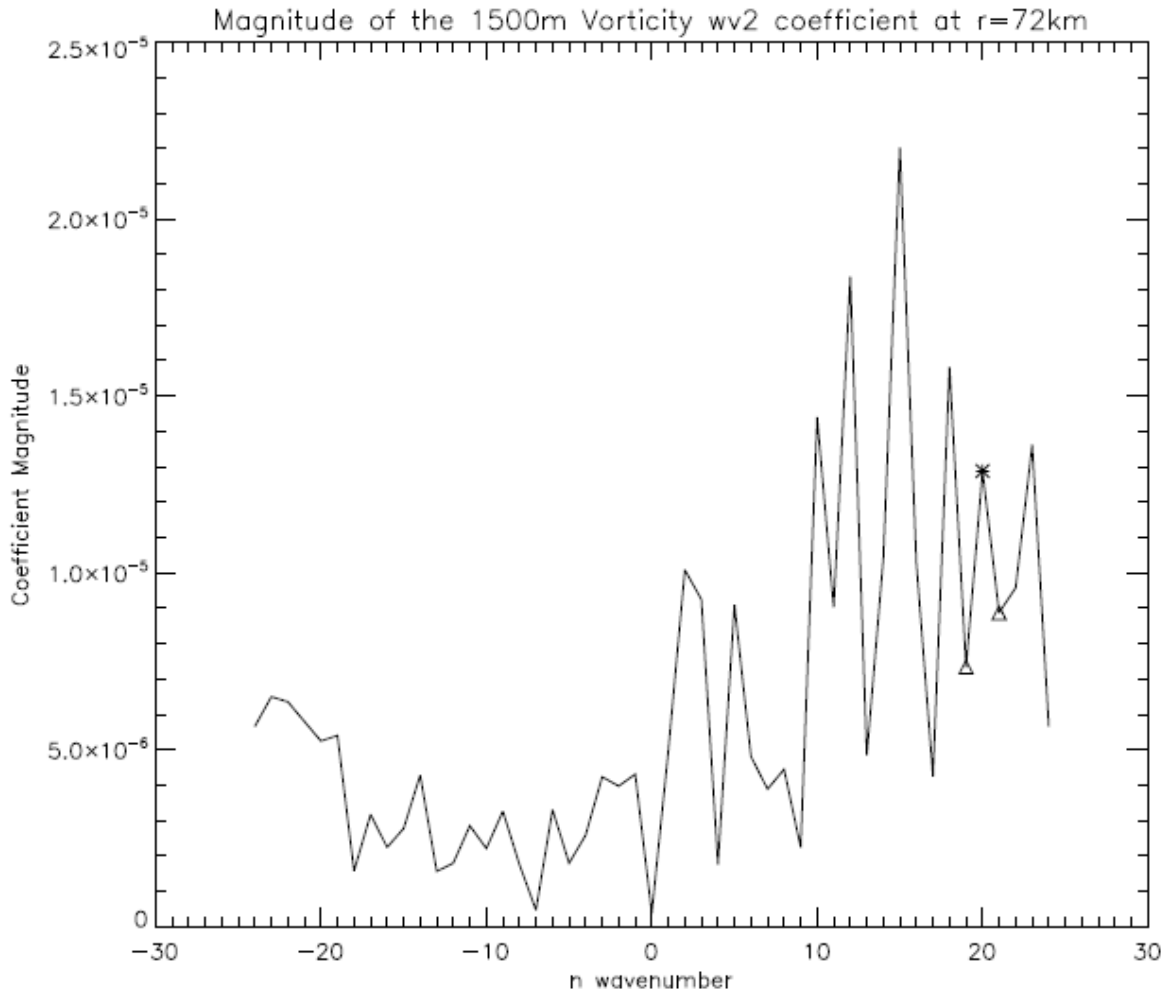


Figure 4.24: Magnitude of the 1500 m vorticity wavenumber-2 coefficient at a radius of 72 km for the 24-71 h time span of the 18 October 2005 HWRFx simulation of Hurricane Wilma.

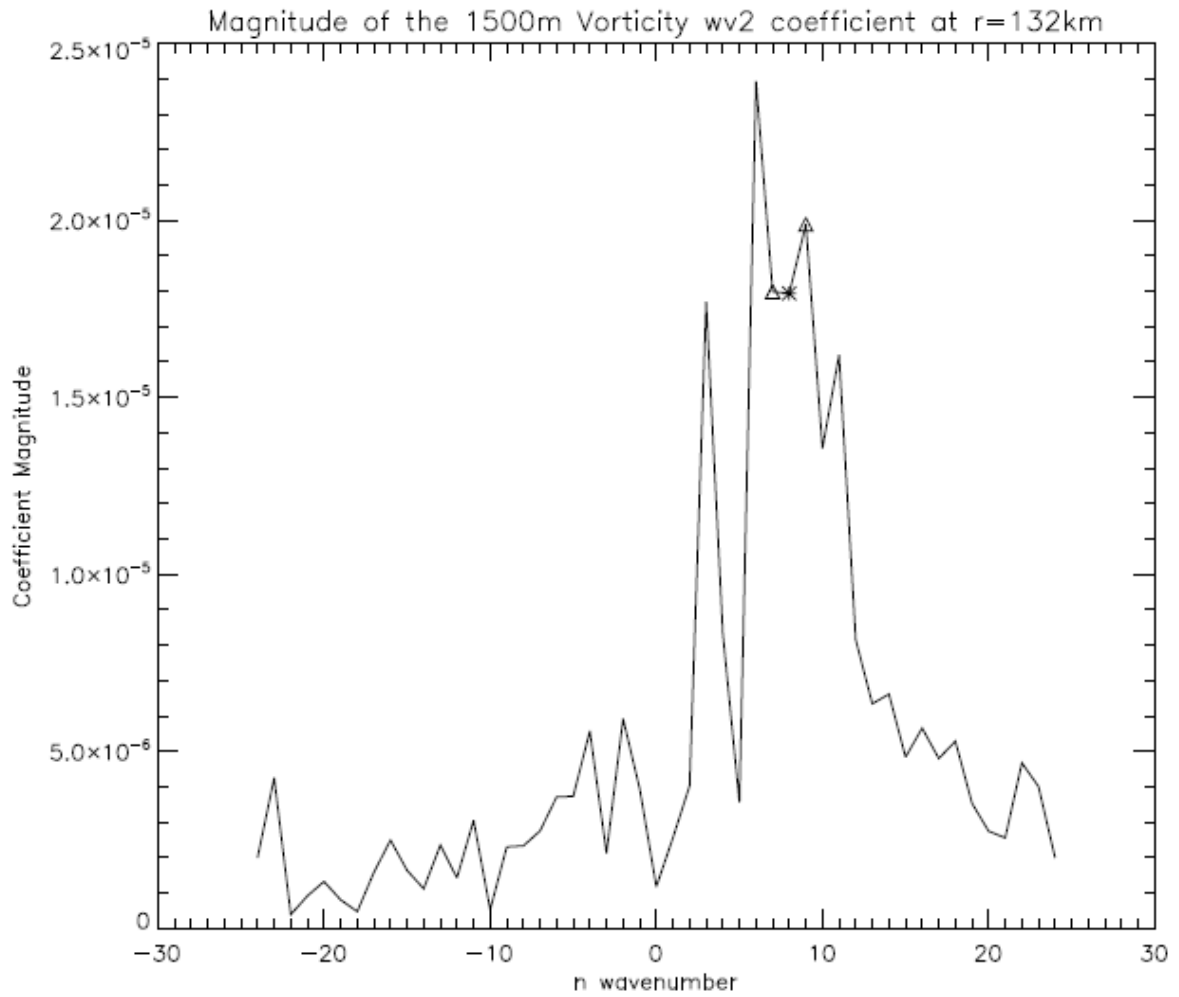


Figure 4.25: Magnitude of the 1500 m vorticity wavenumber-2 coefficient at a radius of 132 km for the 72-119 h time span of the 18 October 2005 HWRFx simulation of Hurricane Wilma.

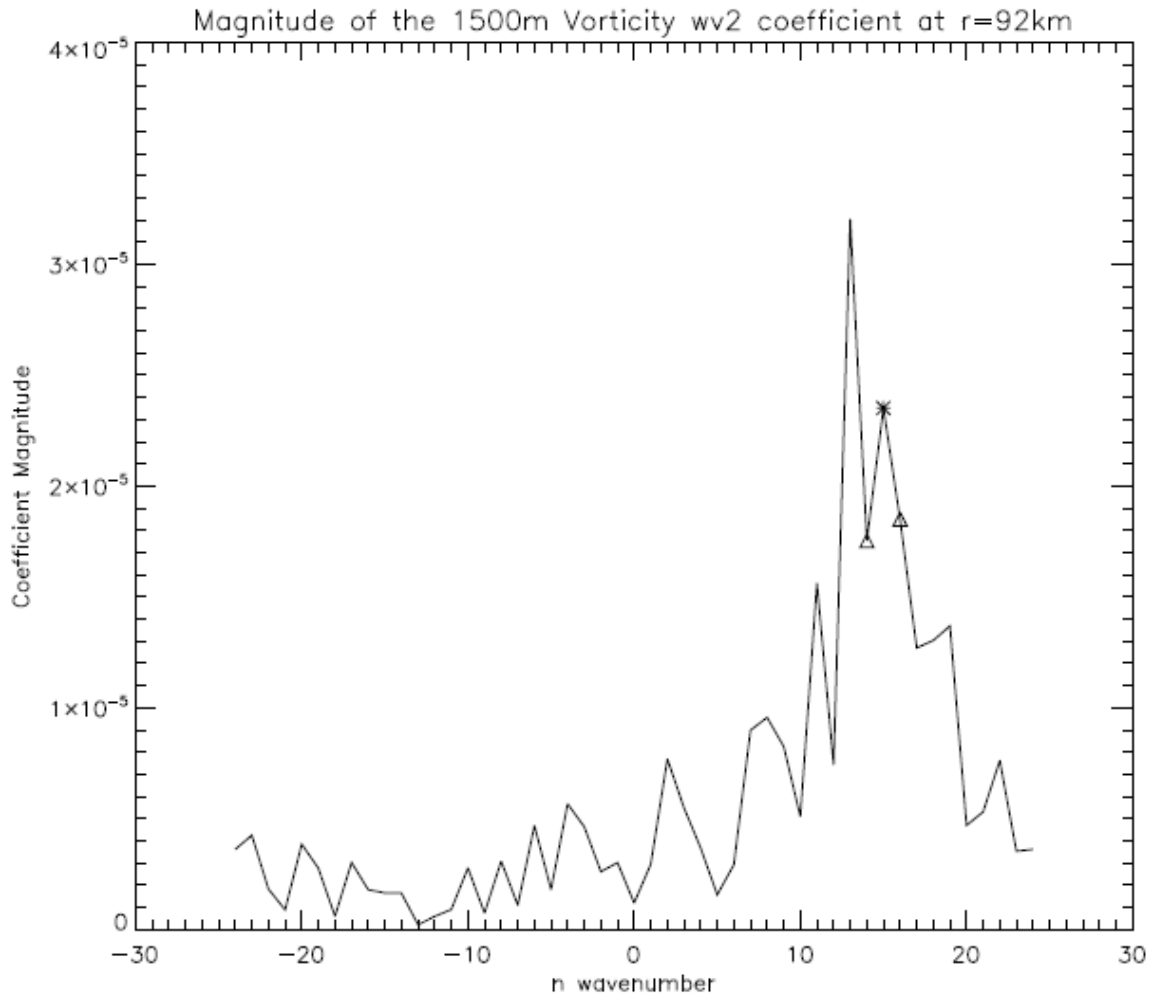


Figure 4.26: Magnitude of the 1500 m vorticity wavenumber-2 coefficient at a radius of 92 km for the 24-71 h time span of the 22 October 2005 HWRFx simulation of Hurricane Wilma.

CHAPTER 5 – VERTICAL STRUCTURE

While the previous chapter dealt entirely with aspects of the horizontal wind structure, this chapter will address several characteristics of the vertical structure of tropical cyclones. This includes an analysis of: 1) the slope of the radius of maximum winds and its relation to the radius of maximum wind; 2) the relation of the slope of the radius of maximum wind to the maximum azimuthal mean tangential wind (a proxy for storm intensity); and 3) whether the vertical slope of the radius of maximum wind is well approximated by a surface of constant angular momentum. As described in the Introduction, a number of recent papers have focused on this topic using aircraft observations and numerical simulations. In this study, the structure is examined in cases where there is a wide range of environmental shear. The next part of the chapter then explores the vertical warm core structure of a tropical cyclone. This investigation focuses on the height and magnitude of the warm core, and whether they are associated with storm intensity change or shear.

5.1 Vertical Structure of the RMW and AAM

The following analysis of the vertical structure of the HWRFx simulated tropical cyclones uses the same methods as those of Stern and Nolan (2009) (hereafter SN09) for the purpose of comparison. The first step will be to apply the analysis to all of the

simulated storm data used in this study to see if the same kind of results as those of SN09 are found. The next step then stratifies the data by the shear magnitude into three groups: low shear, medium shear, and high shear.

As was done in the previous chapter, the first 24 h of data from each simulation has been removed as well as the portions of data where the storm is over land or the storm's circulation has become too disorganized. Also, since the focus is now on the vertical structure of the storm, if the vertical profile of the radius of maximum wind exceeds the limits of the nested grid domain (250 km) then that data is removed from this portion of the study. All of the vertical profiles are limited to the 1.8 km to 8 km region. These levels are chosen because they most closely match the vertical limits used by SN09 (2 km-8 km). SN09 chose the 2 km lower limit because this level is above the boundary layer, where frictional processes play a dominant role, and the Doppler derived winds are thought to be reliable at this level. The two vertical levels in the HWRFx data closest to 2 km are 1.8 km and 2.1 km. Since this study is not limited by data reliability the lower height was chosen.

There is a large variety in both the radius of maximum wind and its vertical profile from one storm to the next and even within the evolution of a single storm. The profiles of the RMW for all the data used for this analysis are shown in Figure 5.1. The profiles are color coded by storm simulation, such that:

- Black = 13 July 2005 Hurricane Emily data
- Blue = 15 July 2005 Hurricane Emily data
- Green = 26 August 2005 Hurricane Katrina data

- Yellow = 18 October 2005 Hurricane Wilma data
- Red = 22 October 2005 Hurricane Wilma data.

There are a number of the RMW vertical profiles that exhibit large jumps in radius from one vertical level to the next. This can occur when there is an upper-level tangential wind feature building in, but has not yet reached lower levels in the simulated storm. Also, in the analysis following the slopes of the RMW are examined. Some of these slopes are negative. While not a common occurrence in tropical cyclones it is not unheard of, and in the SN09 observational study, which is used for comparison in this study, two of their 17 cases have negative RMW slopes. Therefore, it is not unrealistic that the model simulations have produced some negatively sloped RMWs.

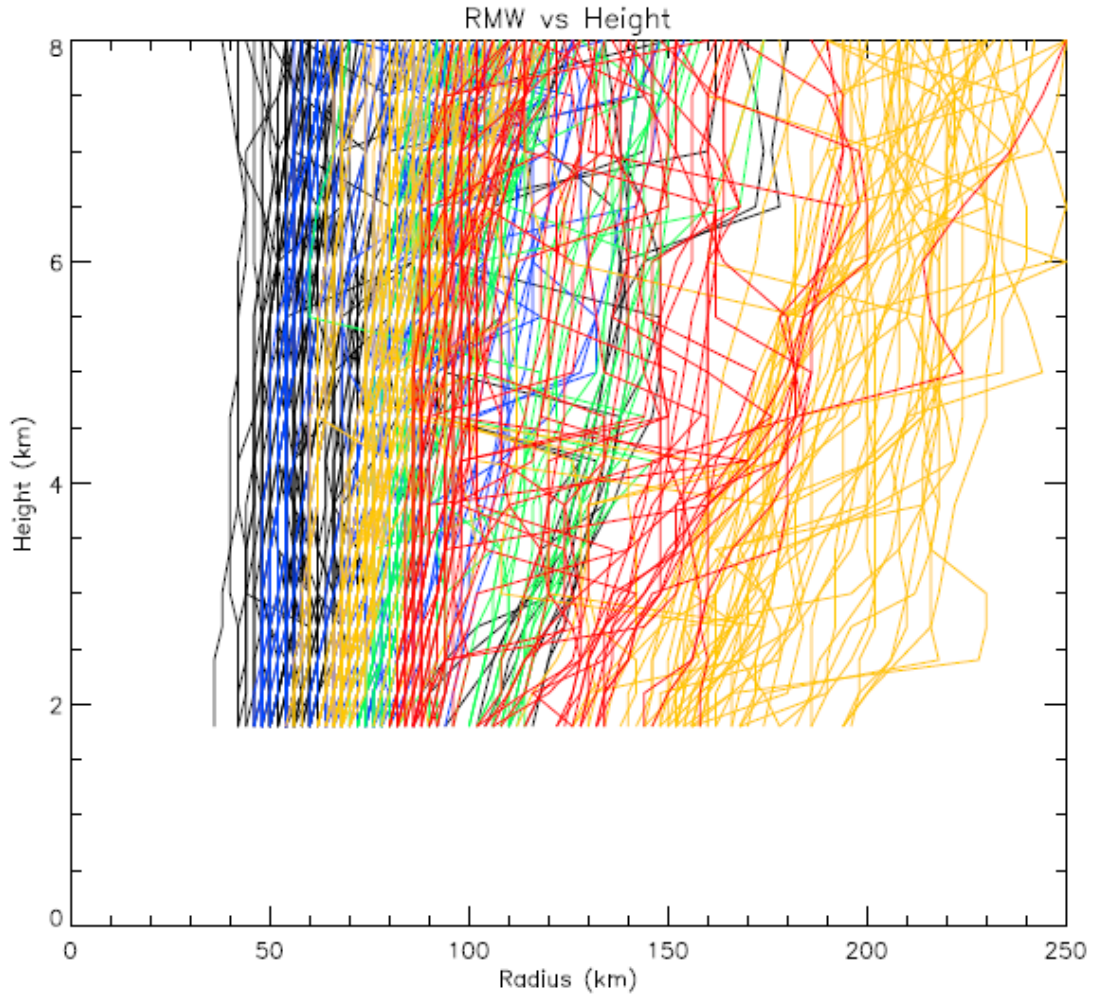


Figure 5.1: Radius of maximum wind versus height from 1.8 km to 8 km (black = Emily 13 July; blue = Emily 15 July; green = Katrina 26 August; yellow = Wilma 18 October; red = Wilma 22 October).

A constant absolute angular momentum surface is a principle part of the following study of tropical cyclone structure. Namely, that the vertical profile of the radius of maximum wind corresponds to a constant absolute angular momentum surface. Absolute angular momentum (AAM) is defined as:

$$M = rv + \frac{1}{2}fr^2 \quad (5.1)$$

where r is the radius, v is the tangential wind, and f is the Coriolis parameter. The Coriolis parameter is defined as $f = 2\Omega \sin\phi$ where $\Omega = 7.2921 \times 10^{-5} \text{ rad/sec}$ is the

earth rotation rate, and ϕ is the latitude. The constant AAM surface is chosen to be the AAM value at the 1.8 km radius of maximum wind. This AAM value is then traced through the vertical levels, which gives a vertical AAM profile. Figure 5.2 shows the vertical profiles of the radius of constant AAM for all of the data.

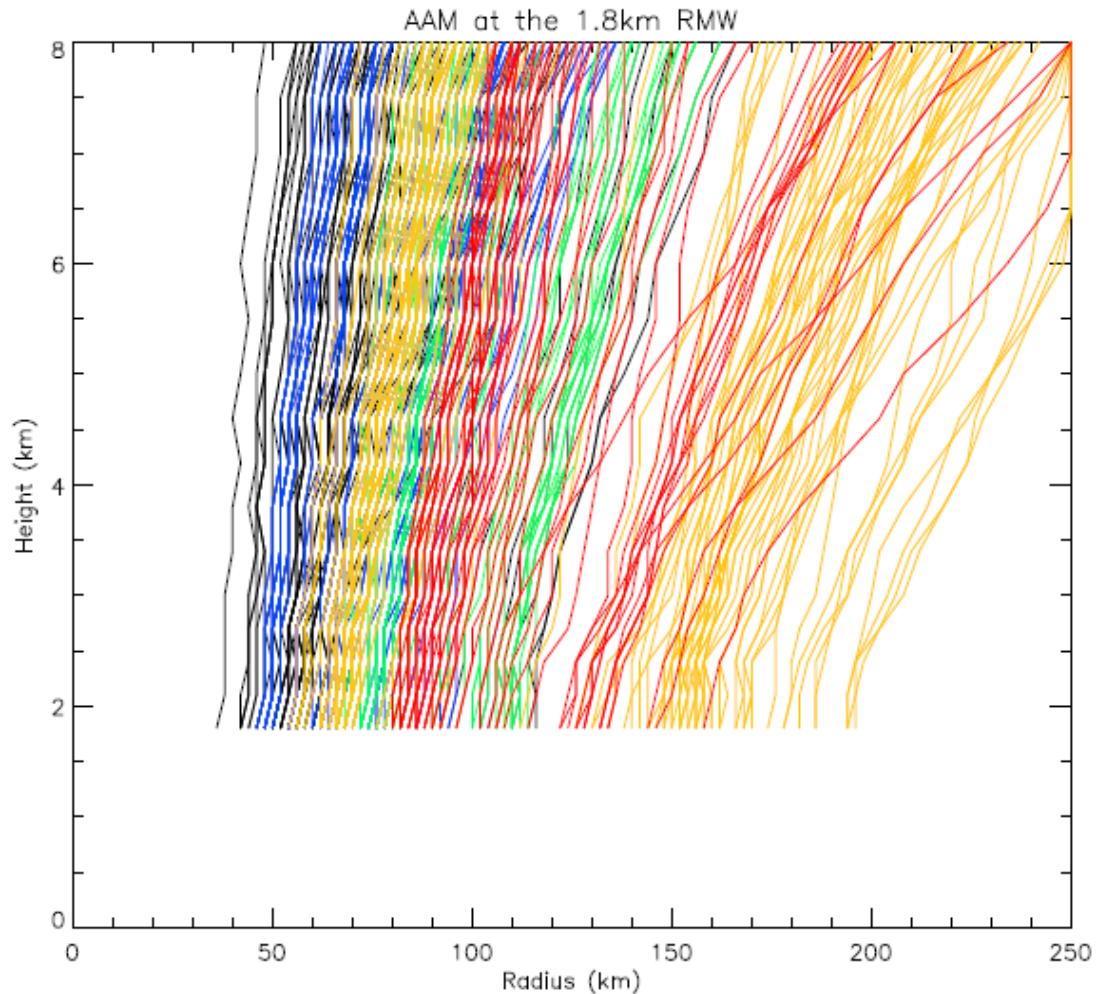


Figure 5.2: Radius of constant absolute angular momentum surface (value at 1.8 km radius of maximum wind) versus height from 1.8 km to 8 km (black = Emily 13 July; blue = Emily 15 July; green = Katrina 26 August; yellow = Wilma 18 October; red = Wilma 22 October).

The slopes of the RMW and constant AAM surfaces are used in the following investigations. The slope is simply determined from the linear best-fit line for each

vertical profile. The slope of this best-fit line will then be used to represent the overall slope of the RMW or constant AAM surface profile.

An important portion of this study hinges on isolating the effects of shear on the vertical structure. Figure 5.3 illustrates the shear distribution for all the data and the thresholds for the low, medium, and high shear categorizations. Low shear is shear less than 5 m/s, medium is shear greater than or equal to 5 m/s, but less than 10 m/s, and high is shear equal to or exceeding 10 m/s.

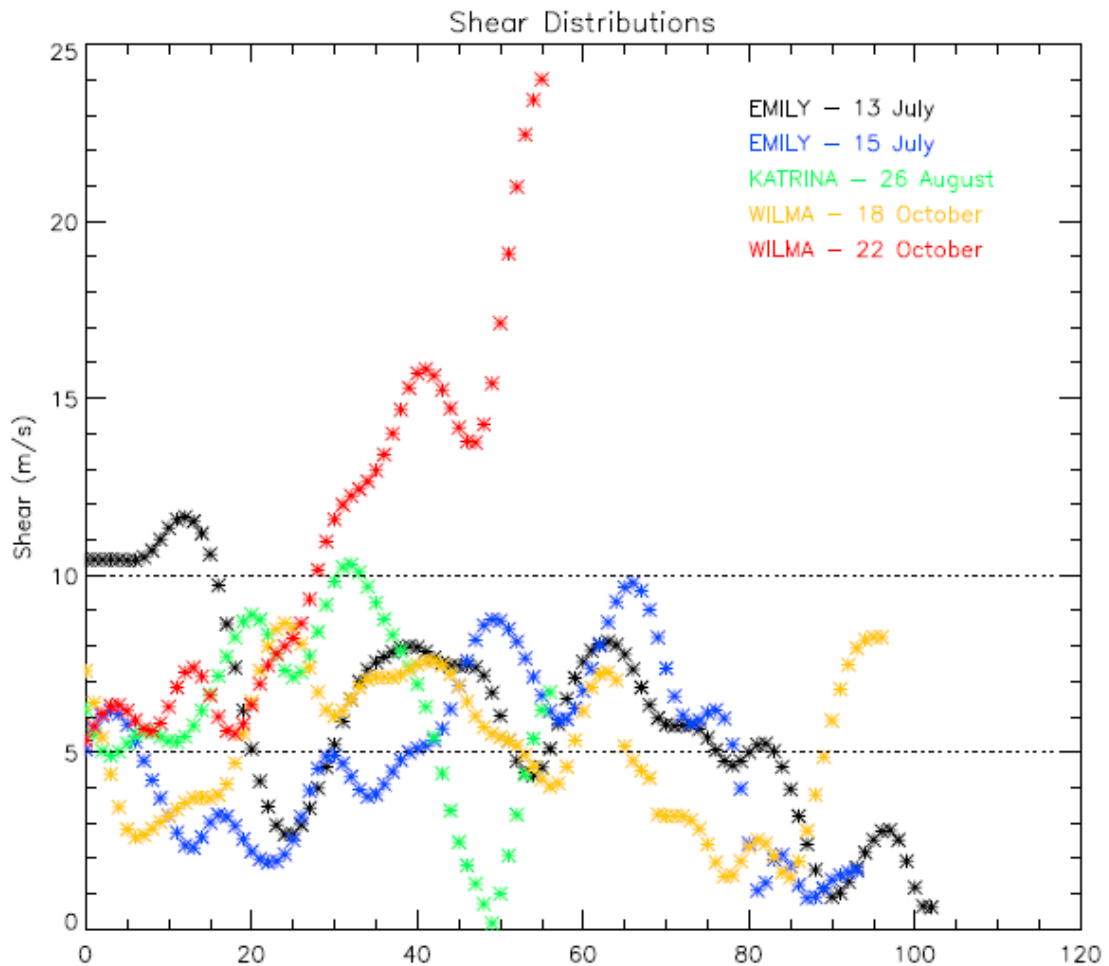


Figure 5.3: The shear distributions from the five simulated storms.

Before delving into the specifics of various aspects of the vertical structure of the simulated storms some average profiles can be considered. Firstly, the average azimuthal mean tangential wind profile normalized by the value of the average azimuthal mean tangential wind at the 1.8 km RMW is shown in Figure 5.4. The black line corresponds to the average across all of the data used in the analysis, and the three colored lines correspond to the averages for the low, medium, and high shear cases (blue = low shear; green = medium shear; red = high shear). The overall structure shows that the intensity (approximated by the azimuthal mean tangential winds) decays with height above the boundary layer, and this decay is enhanced for the highly sheared storms. The intensity profiles of the low and medium shear storms are not largely different than the overall average profile. Interestingly, the medium shear storms maintain the intensity slightly better with height than the other cases.

The other average profiles to look at are the average radius of maximum wind and average constant AAM surface both normalized by the value at the 1.8 km RMW. These profiles are shown in Figures 5.5 and 5.6, respectively. The overall structure is that the RMW and AAM surfaces slope outward with height. The more highly sheared cases are least outwardly sloped for the RMW and most outwardly sloped for the AAM surface. Again an interesting feature, though not statistically significant, is that the medium shear cases show a slight tendency to have a more vertical AAM surface than the low and high shear cases. This, along with the intensity profile, suggests that moderate shear may actually have a constructive influence on the vertical TC structure.

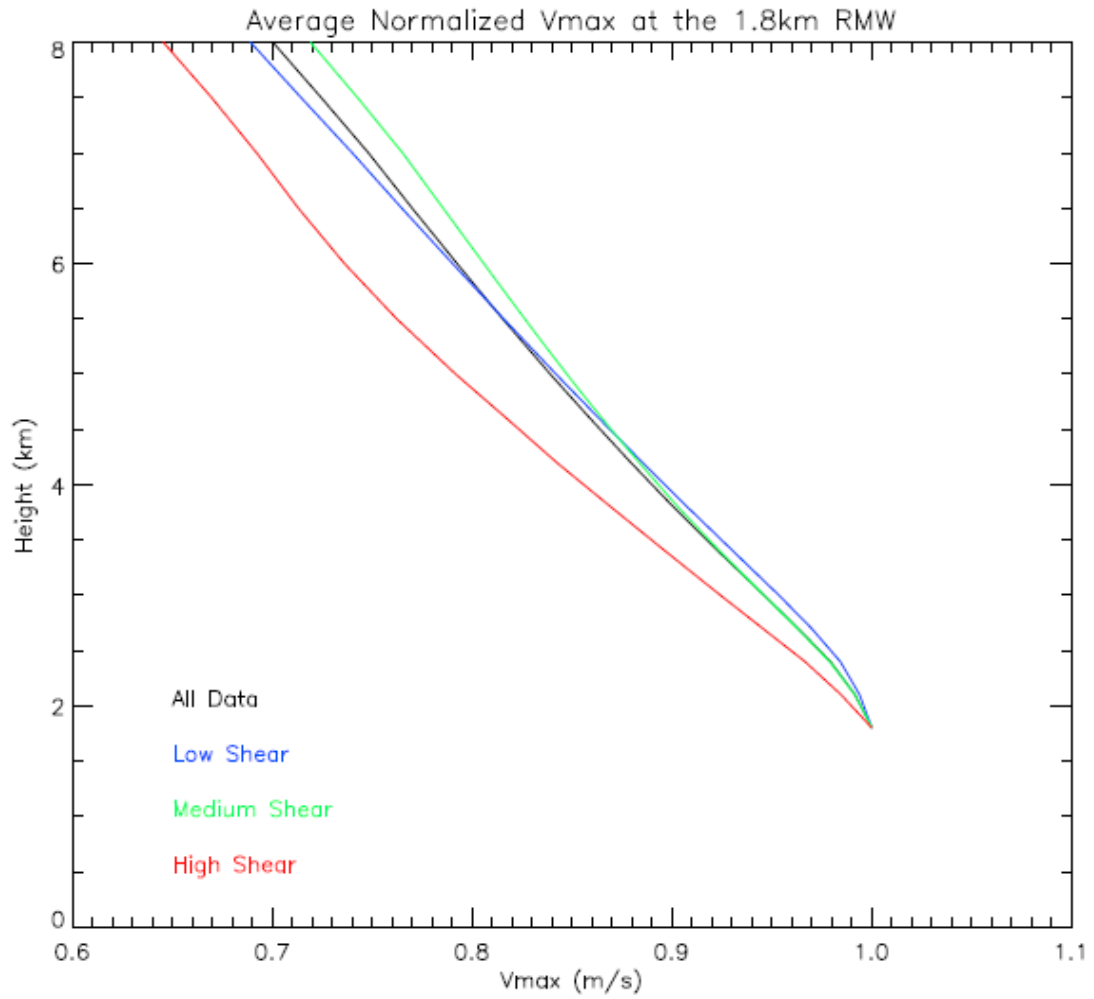


Figure 5.4: Average normalized tangential wind along the radius of maximum wind for all data, and then the low, medium and high shear cases.

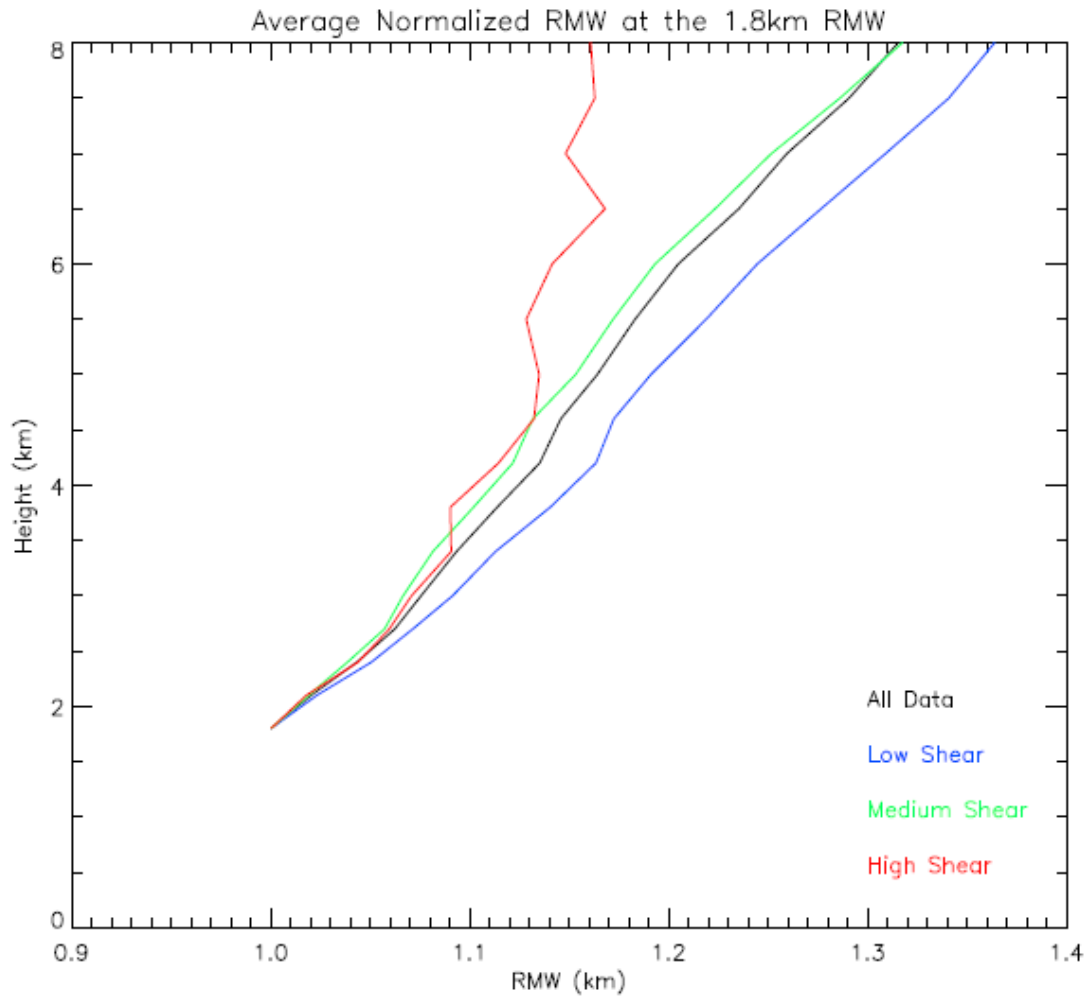


Figure 5.5: Average normalized profile of the radius of maximum wind for all data, and then the low, medium and high shear cases.

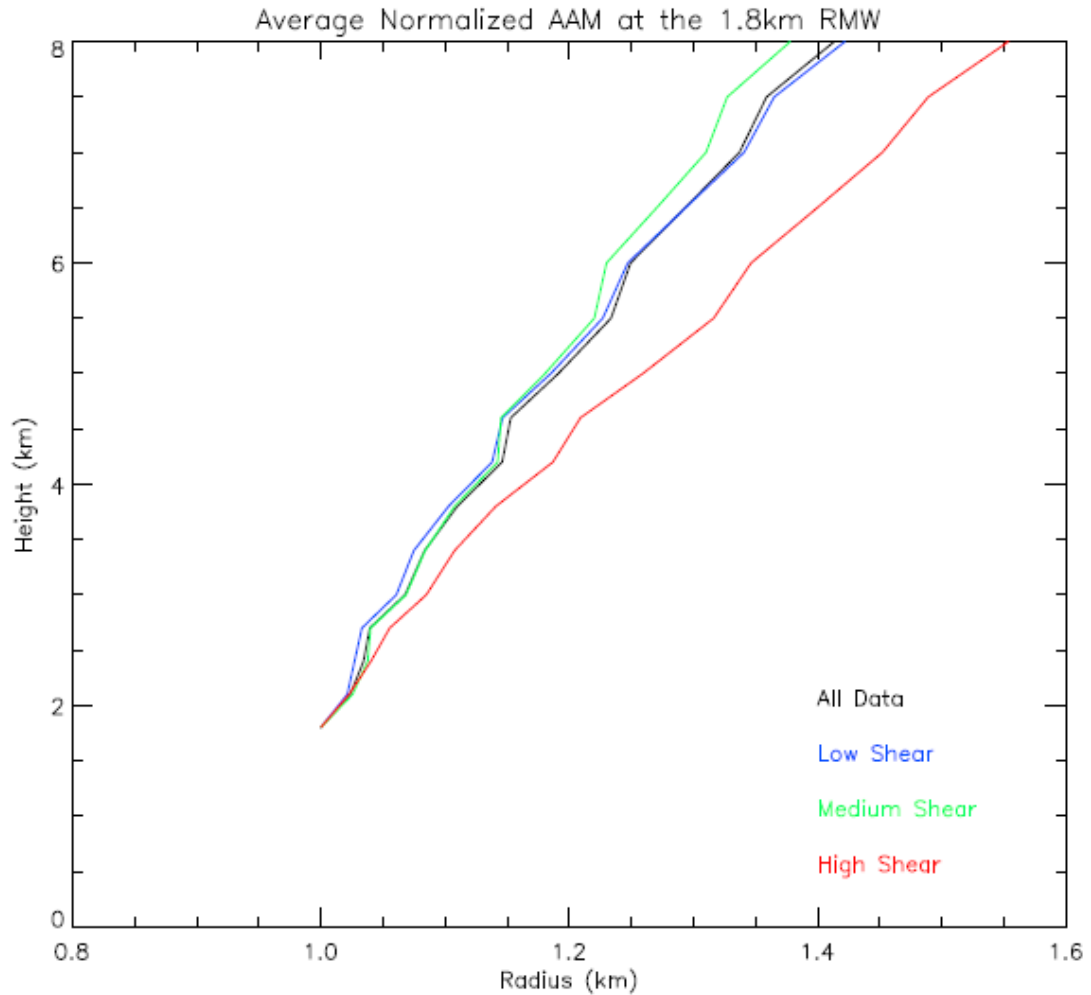


Figure 5.6: Average normalized absolute angular momentum at the 1.8 km radius of maximum wind for all data, and then the low, medium and high shear cases.

5.1.1 Slope of the RMW and Intensity

The first relationship that will be explored is whether the storm intensity is instrumental in determining the slope of the RMW. SN09 cast doubt on the theory that the more intense the storm the more vertical (or less outwardly sloped) the RMW, and their analysis showed little to no relationship between the two. Figure 5.7 shows the plot of the slope of the RMW versus the maximum azimuthal mean tangential wind at 1.8 km. The coefficient of determination, or R^2 (the square of the correlation coefficient), is 0.0001. Such a low value indicates that the slope of the RMW is not dependent upon the

storm intensity. To test whether the results are skewed by highly sheared cases, the results are divided by the low, medium, and high shear. Figure 5.8 shows the low shear cases, which have an R^2 of 0.015. Figure 5.9 shows the medium shear cases, which have an R^2 of 0.001. Figure 5.10 shows the high shear cases, which have an R^2 of 0.003. While the correlation is better for each shear case than for all of the data together, the relationship remains insignificant. It is clear that the intensity of a storm has little to no effect on the slope of the RMW no matter the shear scenario. These results agree with those of SN09.

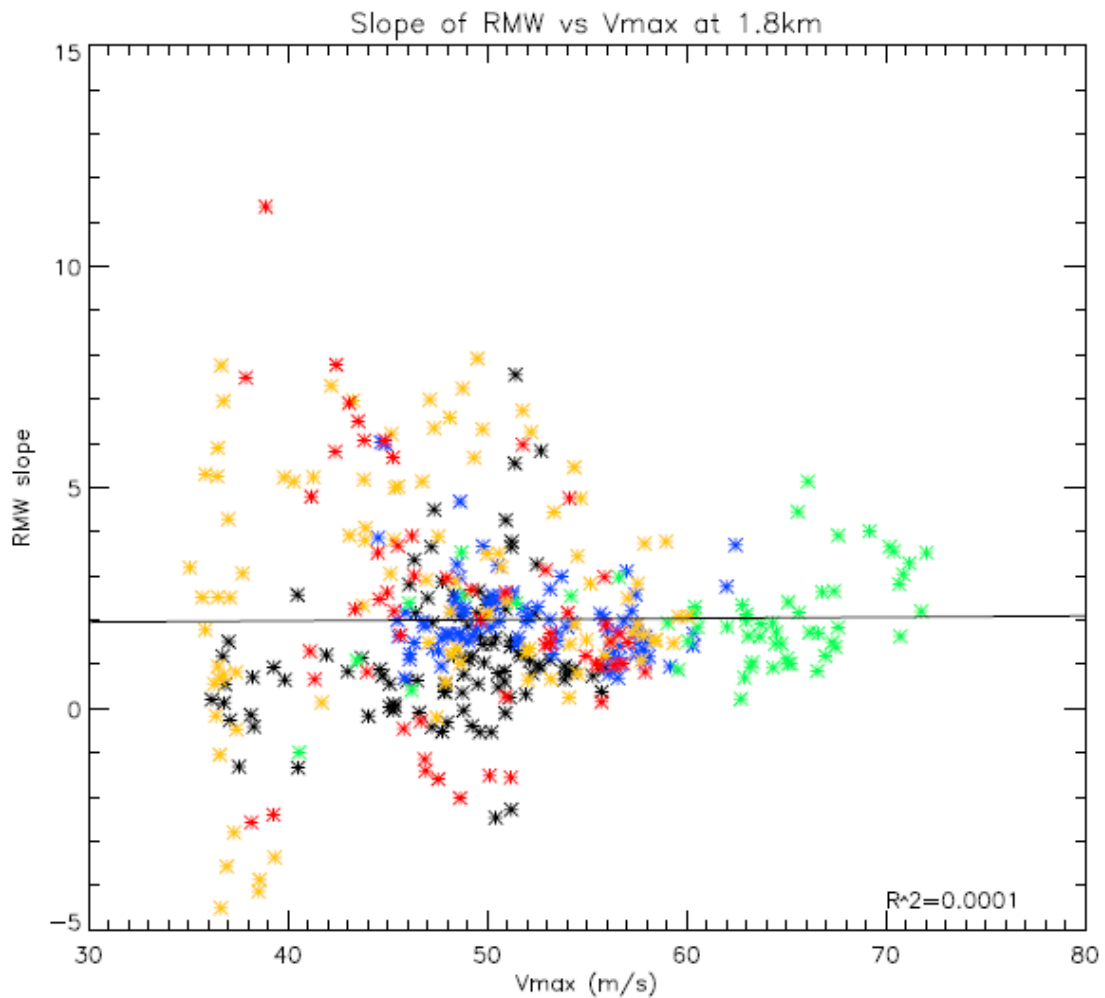


Figure 5.7: Slope of radius of maximum wind versus the maximum azimuthal mean tangential wind at 1.8 km for all the data. The solid black line is the linear best-fit line.

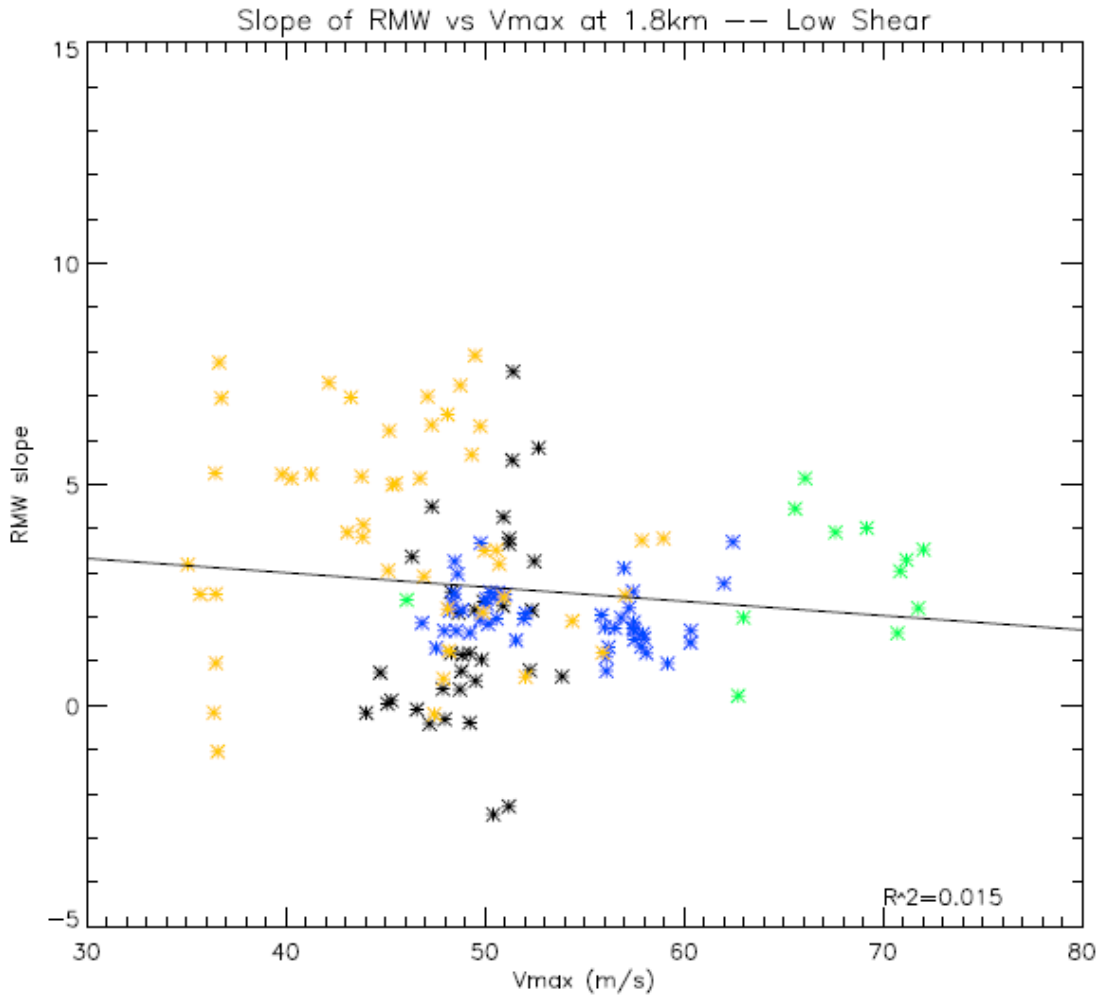


Figure 5.8: Slope of radius of maximum wind versus the maximum azimuthal mean tangential wind at 1.8 km for the low shear cases. The solid black line is the linear best-fit line.

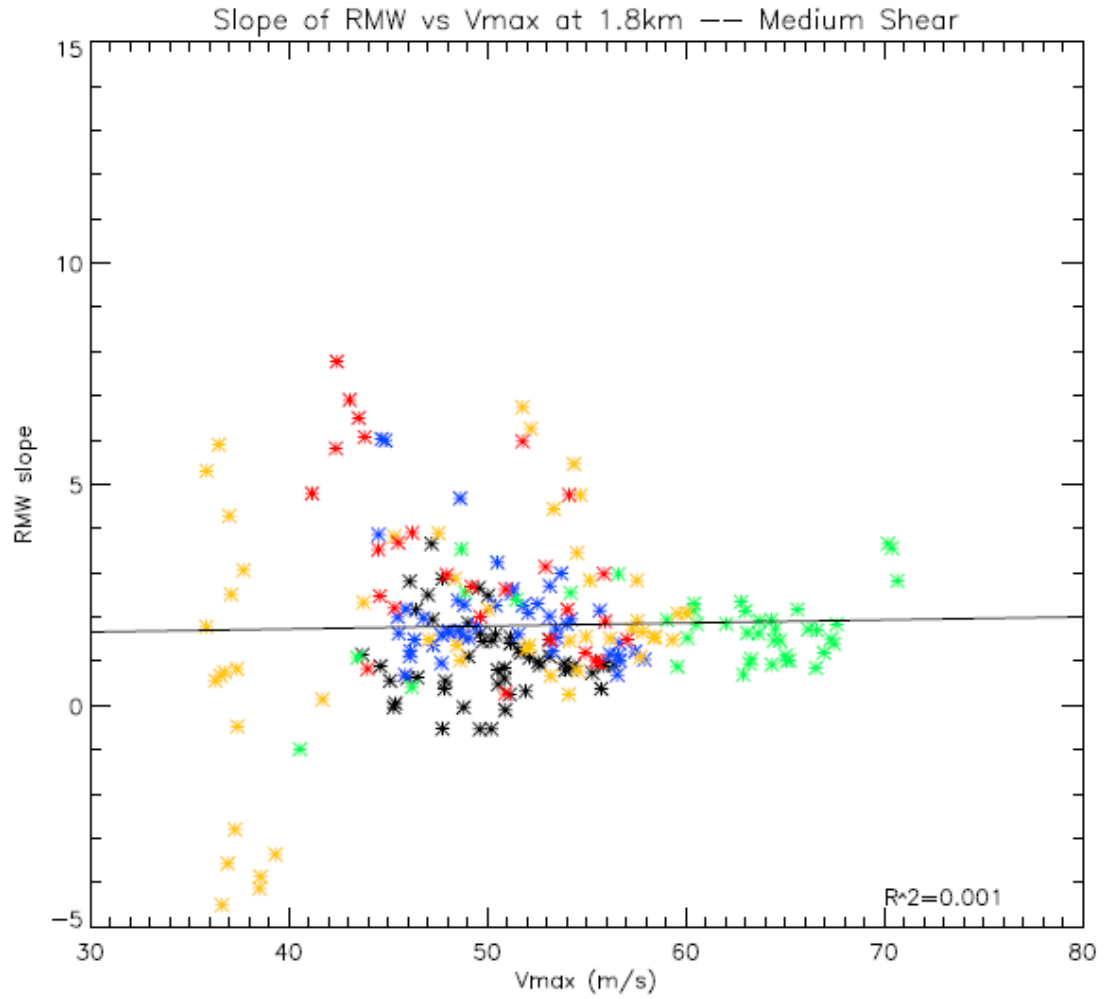


Figure 5.9: Slope of radius of maximum wind versus the maximum azimuthal mean tangential wind at 1.8 km for the medium shear cases. The solid black line is the linear best-fit line.

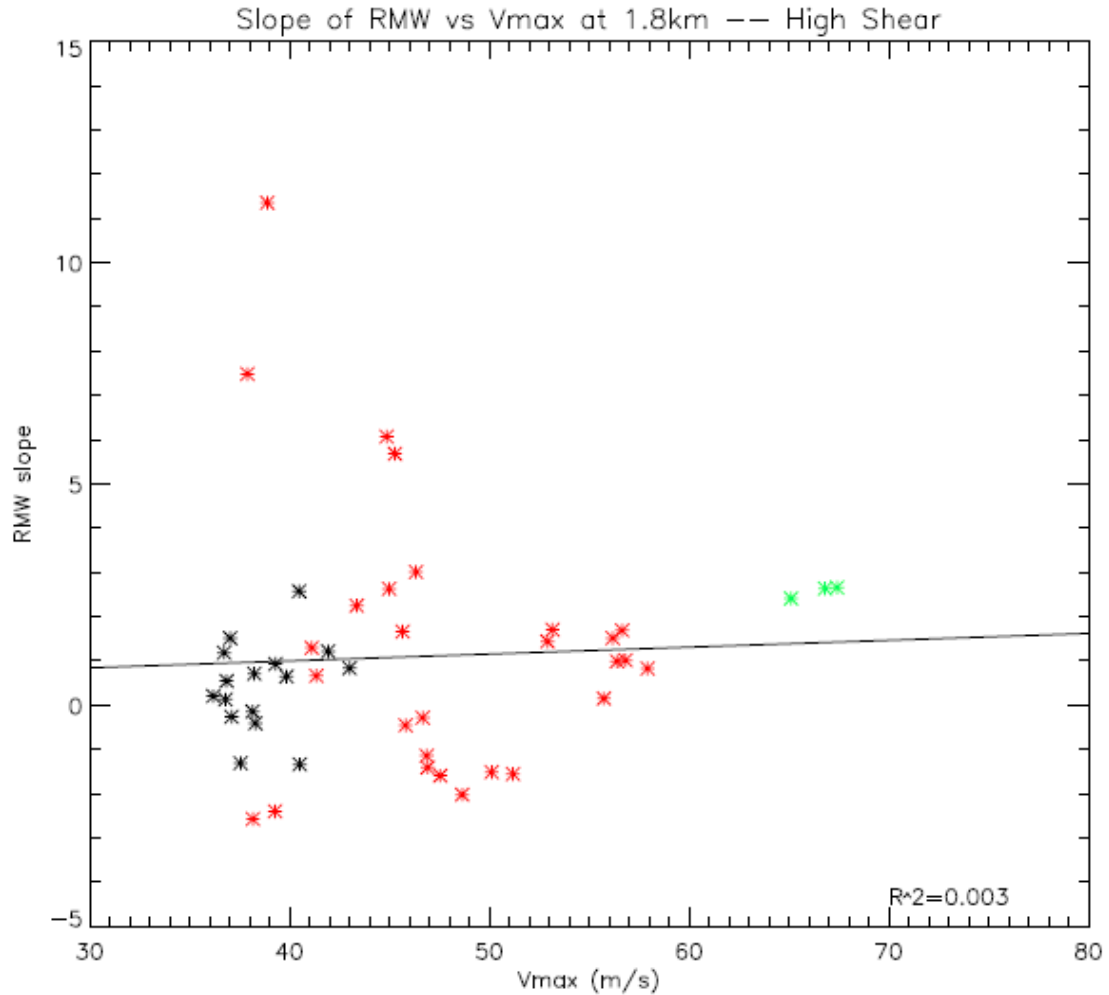


Figure 5.10: Slope of radius of maximum wind versus the maximum azimuthal mean tangential wind at 1.8 km for the high shear cases. The solid black line is the linear best-fit line.

5.1.2 Slope of the RMW and Size of the RMW

Now the slope of the RMW and its relationship to the size of the RMW (i.e. the 1.8 km RMW value) is considered, the theory in question is whether the RMW slopes more outwardly with larger RMW. A cursory look at the vertical profiles of the RMW in Figure 5.1 may give one the impression that, very generally, the profiles with a smaller base RMW are more vertical in structure than those with a larger base RMW. SN09's observationally based study demonstrated results that suggested a nearly linear

relationship between the base RMW and the slope of the RMW such that larger base RMW had a more outwardly sloped RMW vertical profile. Figure 5.11 shows the slopes of the RMW versus the RMW at 1.8 km for all of the data. There is a lot of scatter to the data and it certainly does not show a well-defined linear type relationship like that shown in SN09's study. However, there is a correlation between the RMW slope and the RMW that does meet the threshold for the 99% significance. The R^2 value is 0.093, which is small, but again, it meets the significance criteria.

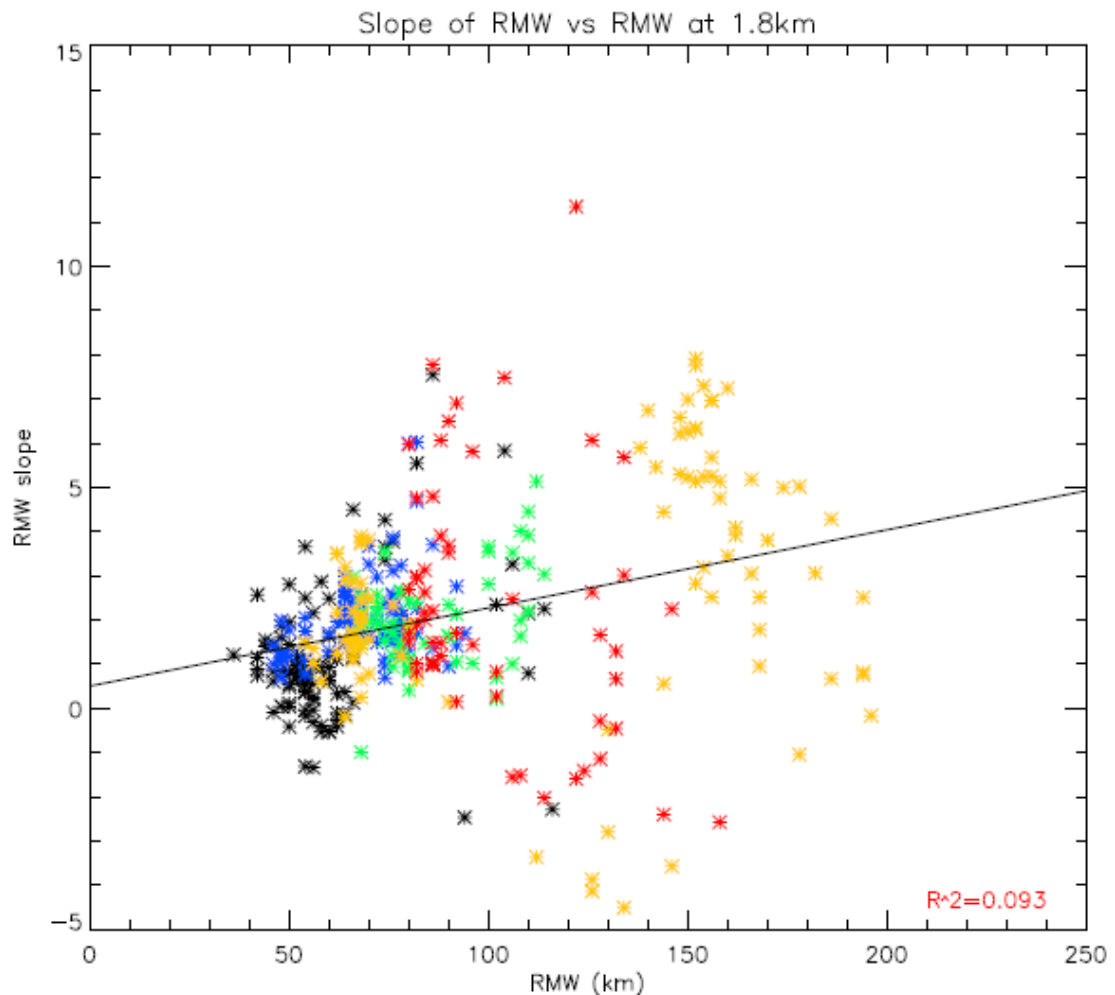


Figure 5.11: Slope of the radius of maximum wind versus the radius of maximum wind at 1.8 km for all of the data. The solid black line is the linear best-fit line.

It may be that environmental vertical shear influences the slope of the radius of maximum wind and therefore affects the relationship between the RMW and its slope. So consider the slope of the RMW versus the 1.8 km RMW for each shear case now. Figure 5.12 shows the low shear case results. For the low shear cases there is a marked improvement in the strength of the relationship. The R^2 value is 0.300, which is a much better correlation than was seen for all of the data together (Figure 5.11). There is still more scatter than SN09's results. Figure 5.13 shows the medium shear case results, and there is clearly a decline in the correlation between the RMW and the slope of the RMW. The R^2 for this case is 0.02, and this value does not meet the criteria for 99% significance. Finally, figure 5.14 shows the high shear case results. The correlation has declined further still from the medium shear to the high shear cases. Here the R^2 value has fallen to 0.006, and does not meet the 99% significance criteria. The conclusion that can be drawn from this is that shear has a negative influence on the relationship between the RMW and its slope. So, for a storm experiencing very little shear the slope of the RMW can be expected to relate to the RMW in that the larger the RMW the more outwardly sloped it will be. However, for storms under the influence of moderate to high shear it is not necessarily accurate to make assumptions about the slope of the RMW based on the lower level RMW value.

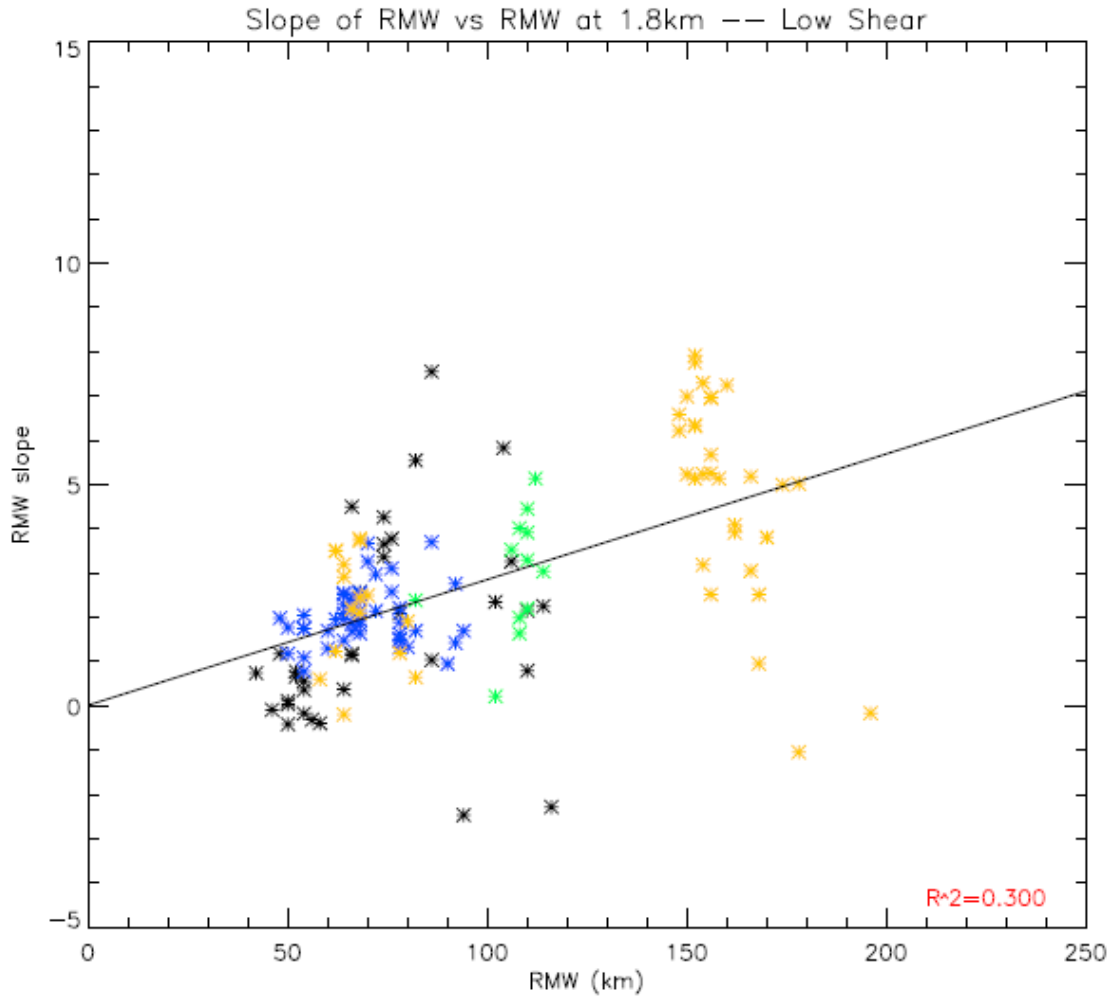


Figure 5.12: Slope of the radius of maximum wind versus the radius of maximum wind at 1.8 km for the low shear cases. The solid black line is the linear best-fit line.

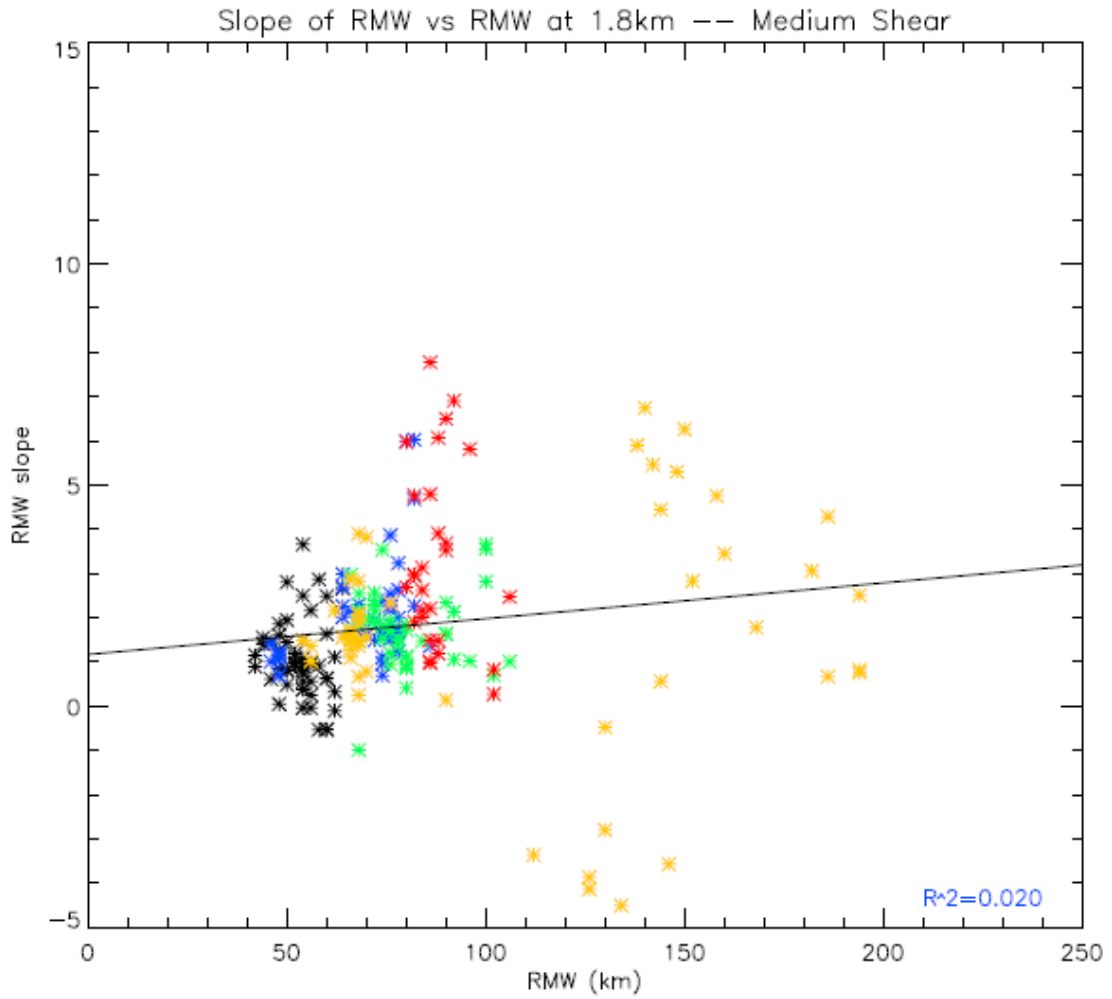


Figure 5.13: Slope of the radius of maximum wind versus the radius of maximum wind at 1.8 km for the medium shear cases. The solid black line is the linear best-fit line.

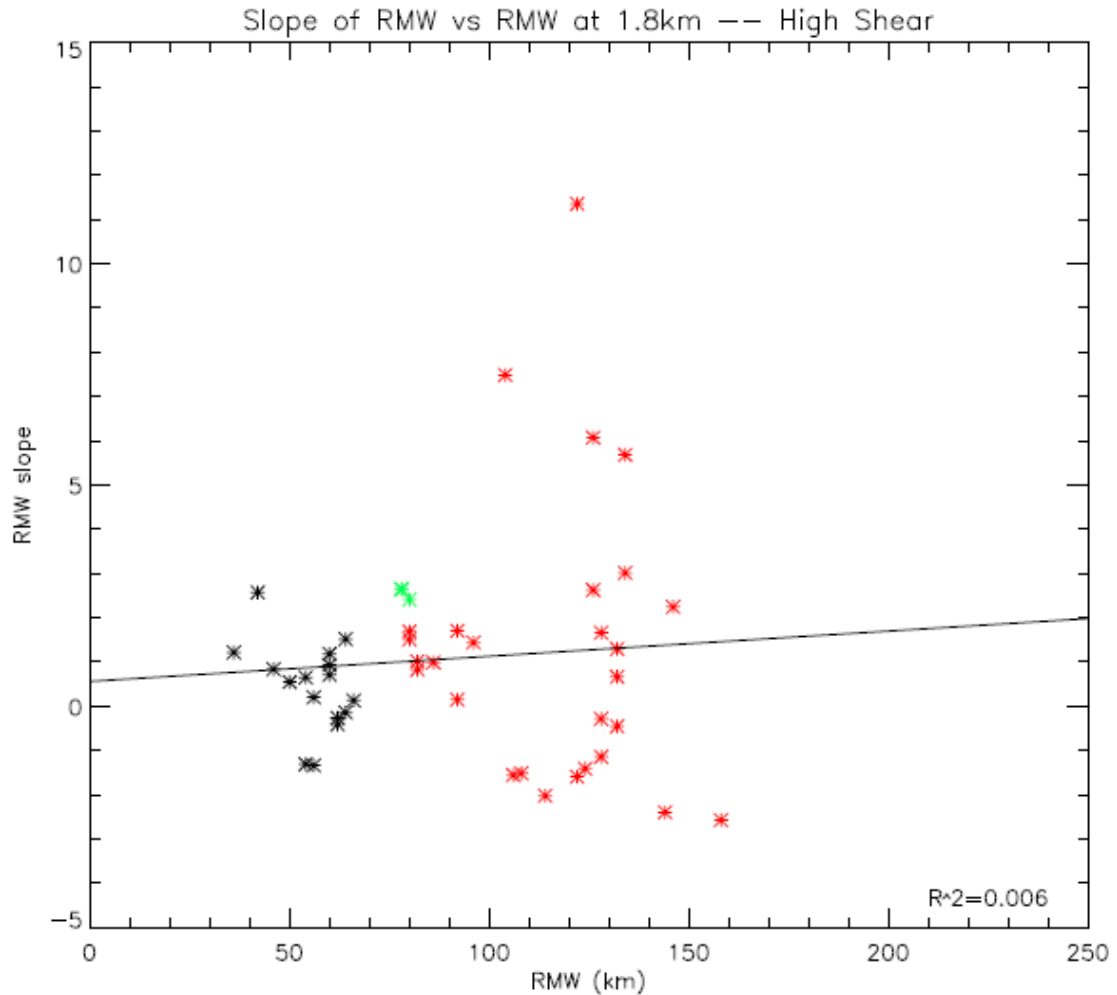


Figure 5.14: Slope of the radius of maximum wind versus the radius of maximum wind at 1.8 km for the high shear cases. The solid black line is the linear best-fit line.

SN09 also looked briefly at the slope of the constant absolute angular momentum surface versus the 2 km RMW and noted that there was an even better relationship for this data than for the slope of the RMW versus the 2 km RMW. So, for comparison the same analysis will be done here. Figure 5.15 shows the slope of the constant AAM surface versus the 1.8 km RMW for all of the data. There is a far better relationship between the slope of the constant AAM surface and the 1.8 km RMW than was seen for the slope of the RMW and the 1.8 km RMW. The data shows a much higher correlation with an R^2 value of 0.616. To see how shear affects the relationship, Figure 5.16 shows

the low shear cases, Figure 5.17 shows the medium shear cases, and Figure 5.18 shows the high shear cases. The low shear cases have an R^2 value of 0.812; the medium shear cases have an R^2 value of 0.728; and the high shear cases have an R^2 value of 0.422. All of the shear cases have correlations that meet the 99% significance criteria. The low and medium shear cases show high correlations between the slope of the AAM surface and the 1.8 km RMW. The high shear has the lowest correlation, but the relationship is still easily evident.

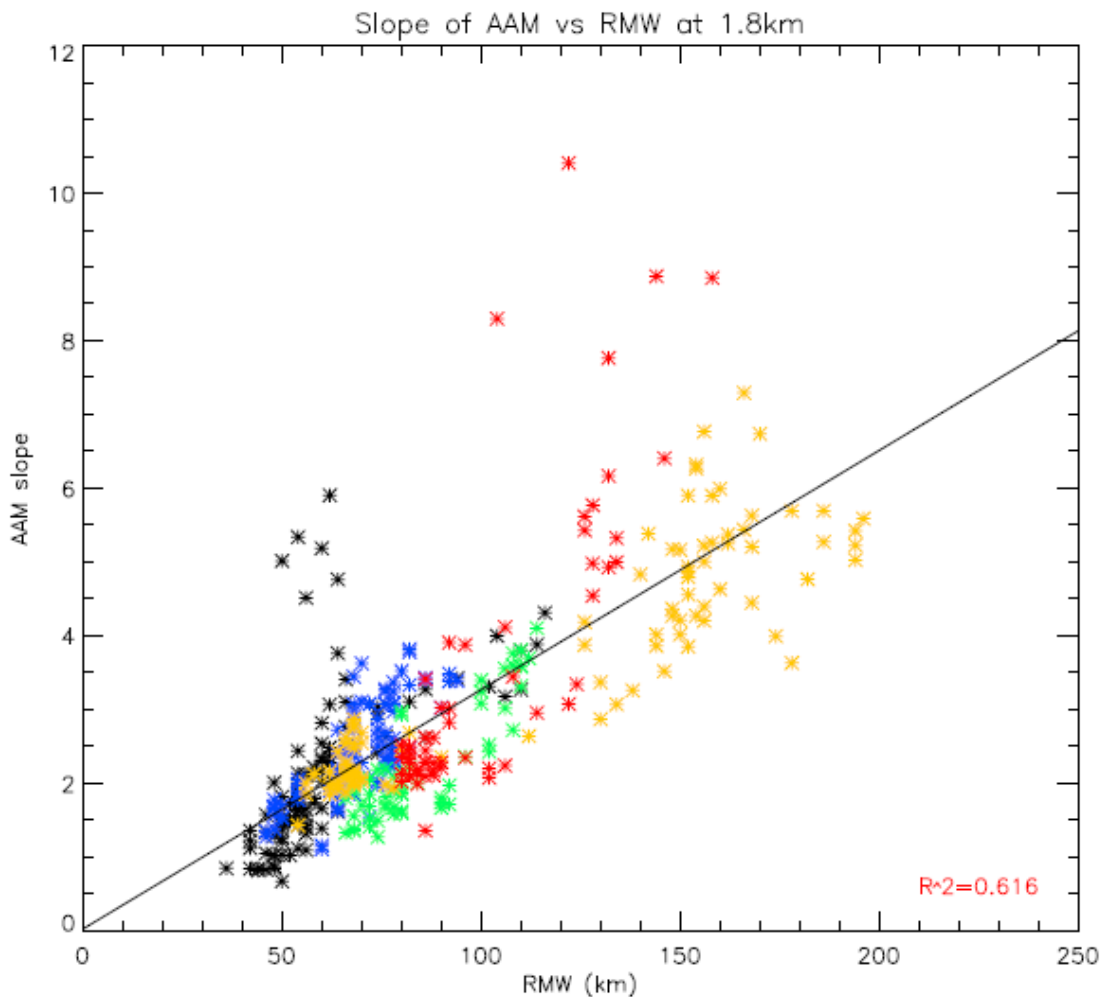


Figure 5.15: Slope of the absolute angular momentum versus the radius of maximum wind at 1.8 km for all of the data. The solid black line is the linear best-fit line.

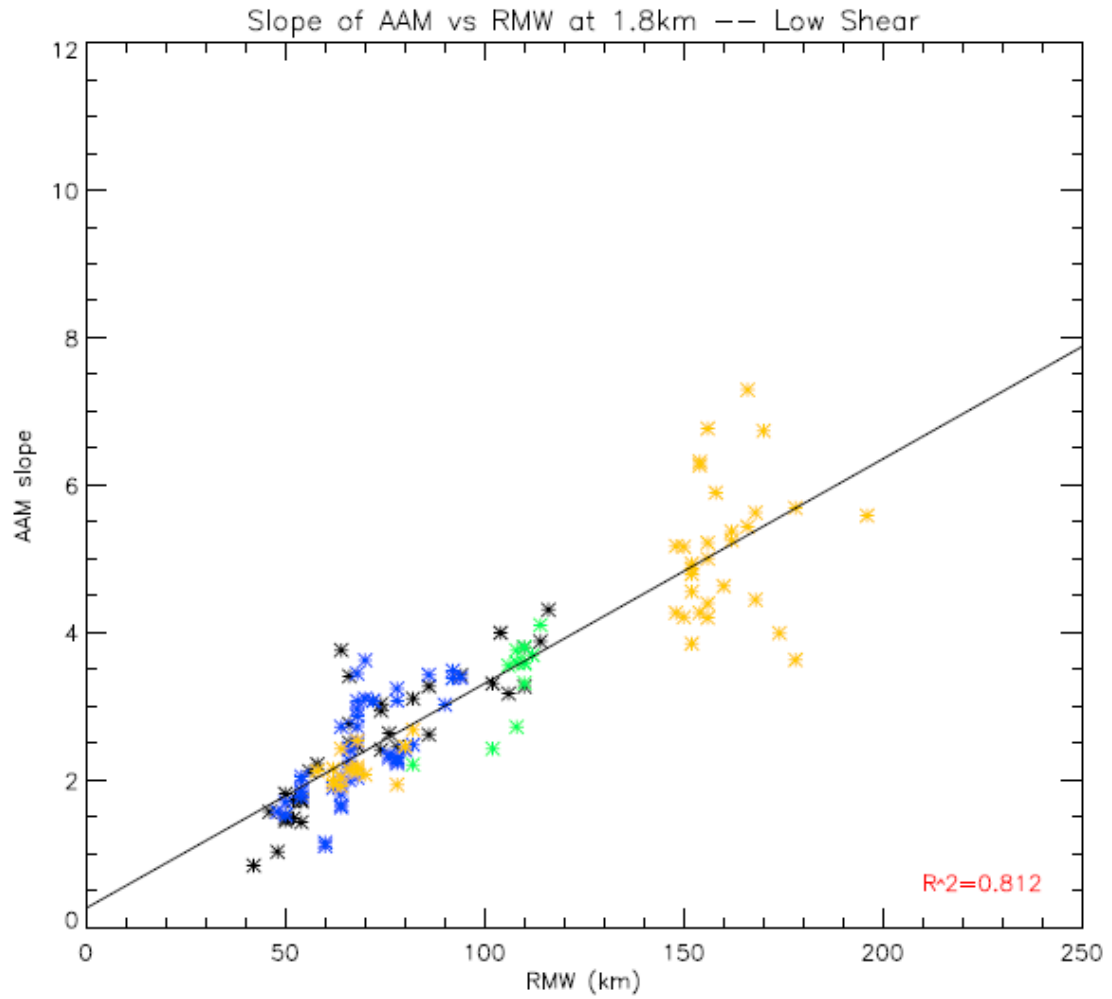


Figure 5.16: Slope of the absolute angular momentum versus the radius of maximum wind at 1.8 km for the low shear cases. The solid black line is the linear best-fit line.

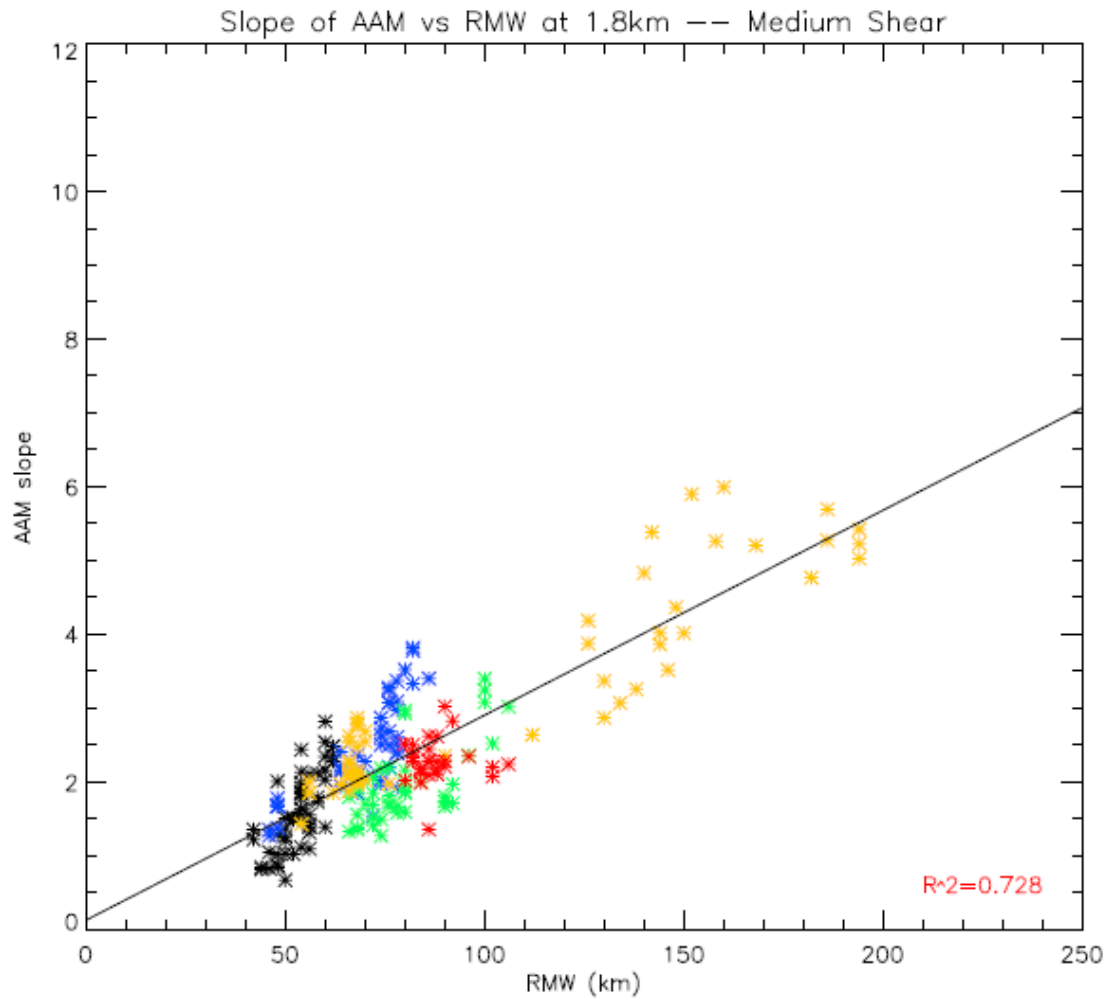


Figure 5.17: Slope of the absolute angular momentum versus the radius of maximum wind at 1.8 km for the medium shear cases. The solid black line is the linear best-fit line.

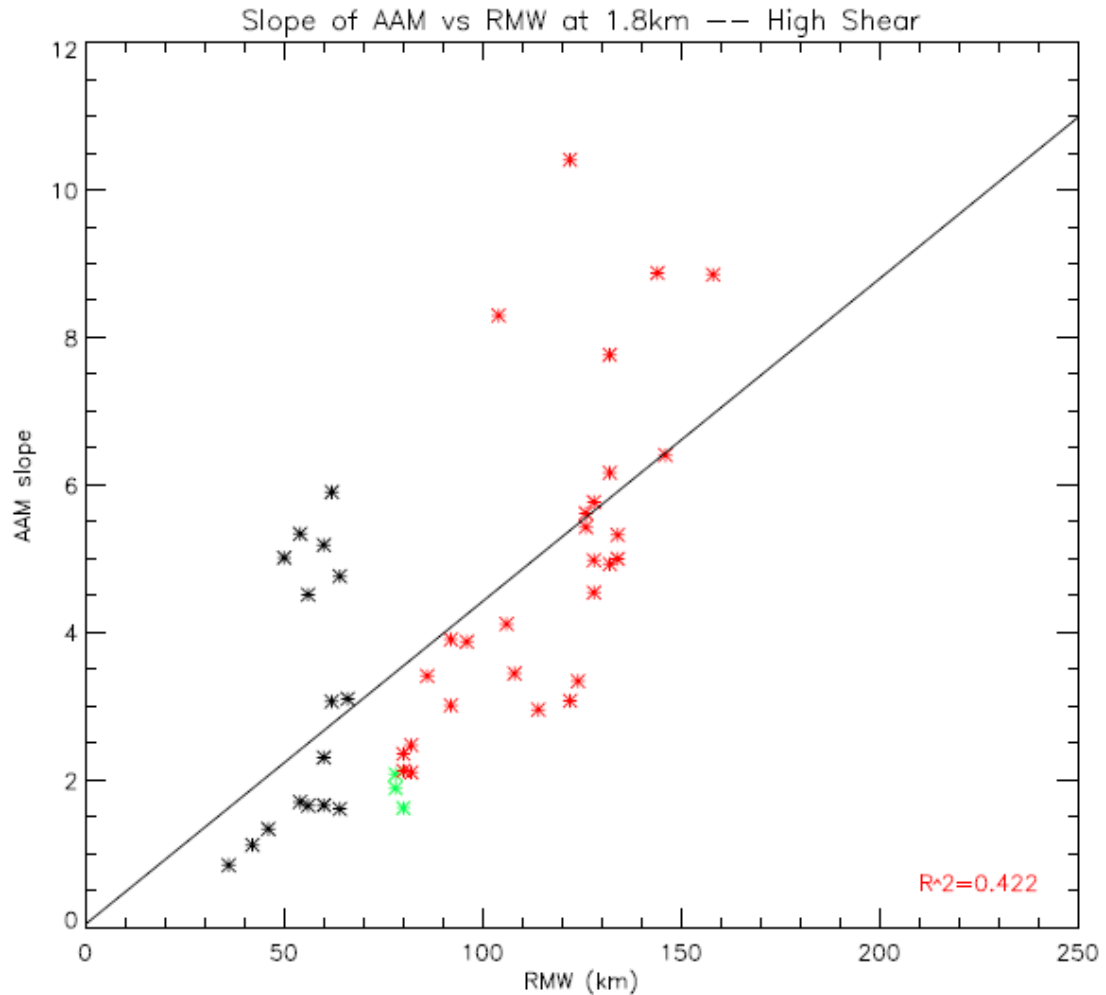


Figure 5.18: Slope of the absolute angular momentum versus the radius of maximum wind at 1.8 km for the high shear cases. The solid black line is the linear best-fit line.

5.1.3 RMW and Absolute Angular Momentum Surface

The theory that the RMW is approximately a surface of constant absolute angular momentum can be tested by plotting the slopes of the RMW versus the slopes of the constant AAM. This theory was first proposed by Jorgensen (1984b) in an observational study of Hurricane Allen, and there have been a number of other observational studies showing this relationship. SN09 revealed the theoretical reasoning behind this theory to be problematic, and sought to develop a better explanation using Emanuel’s MPI theory (Emanuel 1995). It is of interest to determine whether the HWRFx model simulations

exhibit this relationship. Figure 5.19 shows the distribution of the RMW slopes versus the AAM slopes for all of the data. The theory is verified if the points lie approximately along the 1:1 line (the dashed black line). However, not only is there a broad spread in the data, which does not lie along the 1:1 line, but the linear best-fit trend line (solid black) is quite different than that of the 1:1 line. The correlation is fairly low, the R^2 value is 0.09, but does meet the 99% critical significance criteria. It may be that the more highly sheared cases are negatively influencing the correlation, so the individual low, medium and high shear cases are now considered separately. Figure 5.20 shows the low shear cases, Figure 5.21 shows the medium shear cases, and Figure 5.22 shows the high shear cases. The low shear cases exhibit the highest correlation with an R^2 value of 0.292, which exceeds the 99% significance threshold. The medium and high shear cases are more poorly correlated with R^2 values of 0.049 and 0.079 respectively. The medium shear case correlation meets the 99% significance threshold, but the high shear case correlation does not. None of the slopes for any of the shear cases congregate along the 1:1 line, which does not bode well for the theory that the RMW is a surface of constant AAM.

SN09's analysis of a comparison between the slopes of the RMW and the slopes of the AAM surface found a relationship closer to that described by the 1:1 line, although their data showed a systematic tendency for the AAM to decrease upward along the RMW. This tendency is not evident in the results presented here. There does not appear to be an inclination for the AAM slope to be greater or lesser than the slope of the RMW. As previously mentioned, the study by SN09 is observationally based, whereas this study uses model based analysis. This difference raises the question of whether there is a

deficiency in the model, or if the greater detail in the model analysis (i.e. hourly analysis capturing the full evolution of each modeled storm) are revealing attributes that have just not been highlighted by previous studies.

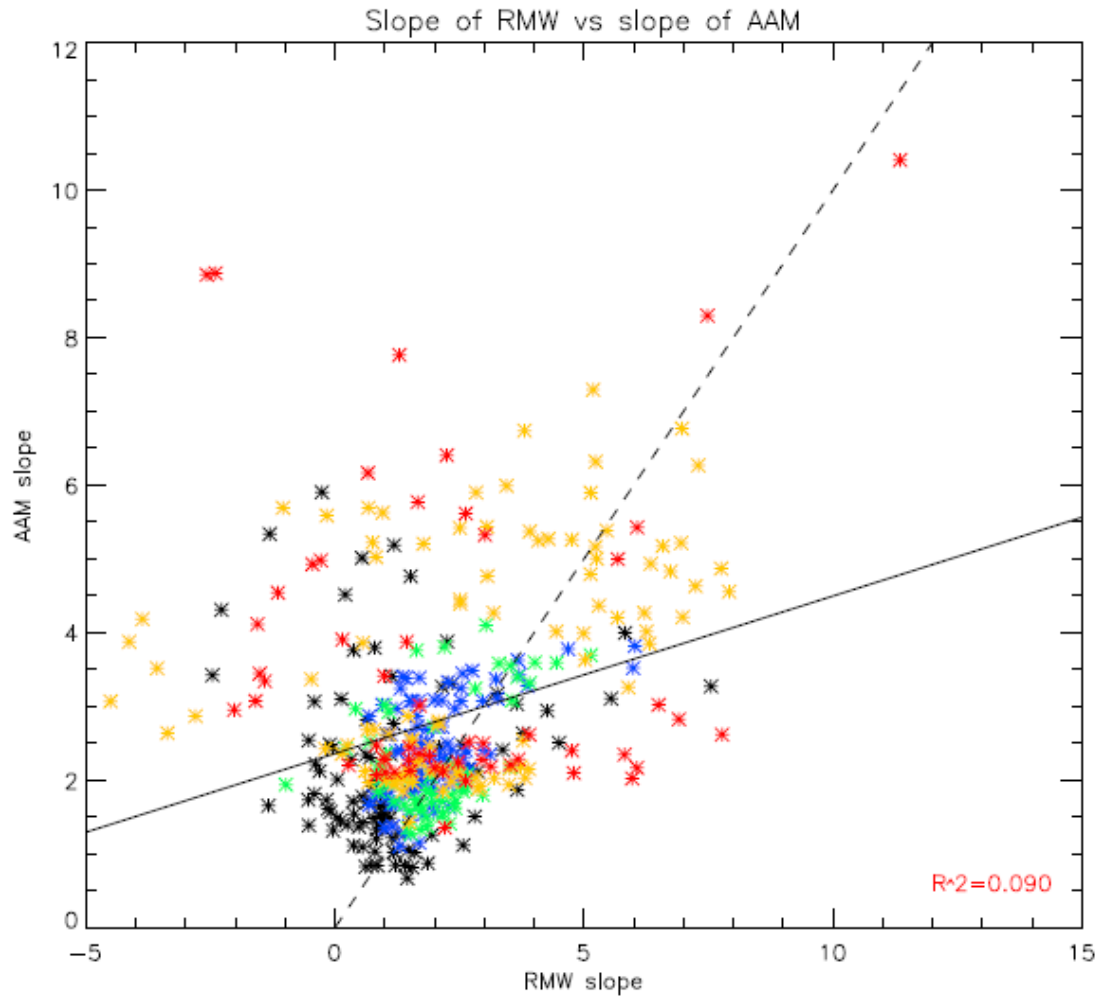


Figure 5.19: Slope of radius of maximum wind versus the slope of the absolute angular momentum for all the data. The solid black line is the linear best-fit line, and the dashed black line is the 1:1 line.

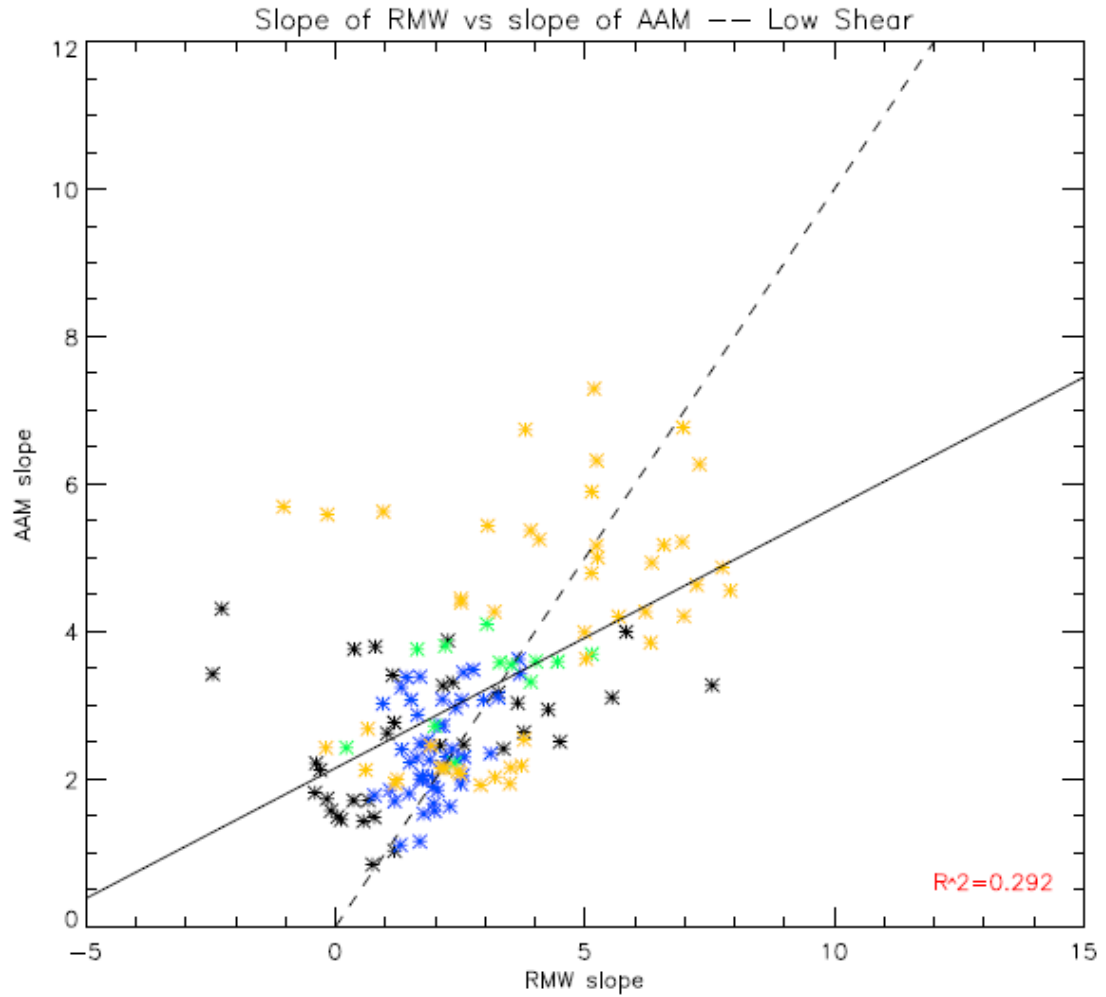


Figure 5.20: Slope of radius of maximum wind versus the slope of the absolute angular momentum for the low shear cases. The solid black line is the linear best-fit line, and the dashed black line is the 1:1 line.

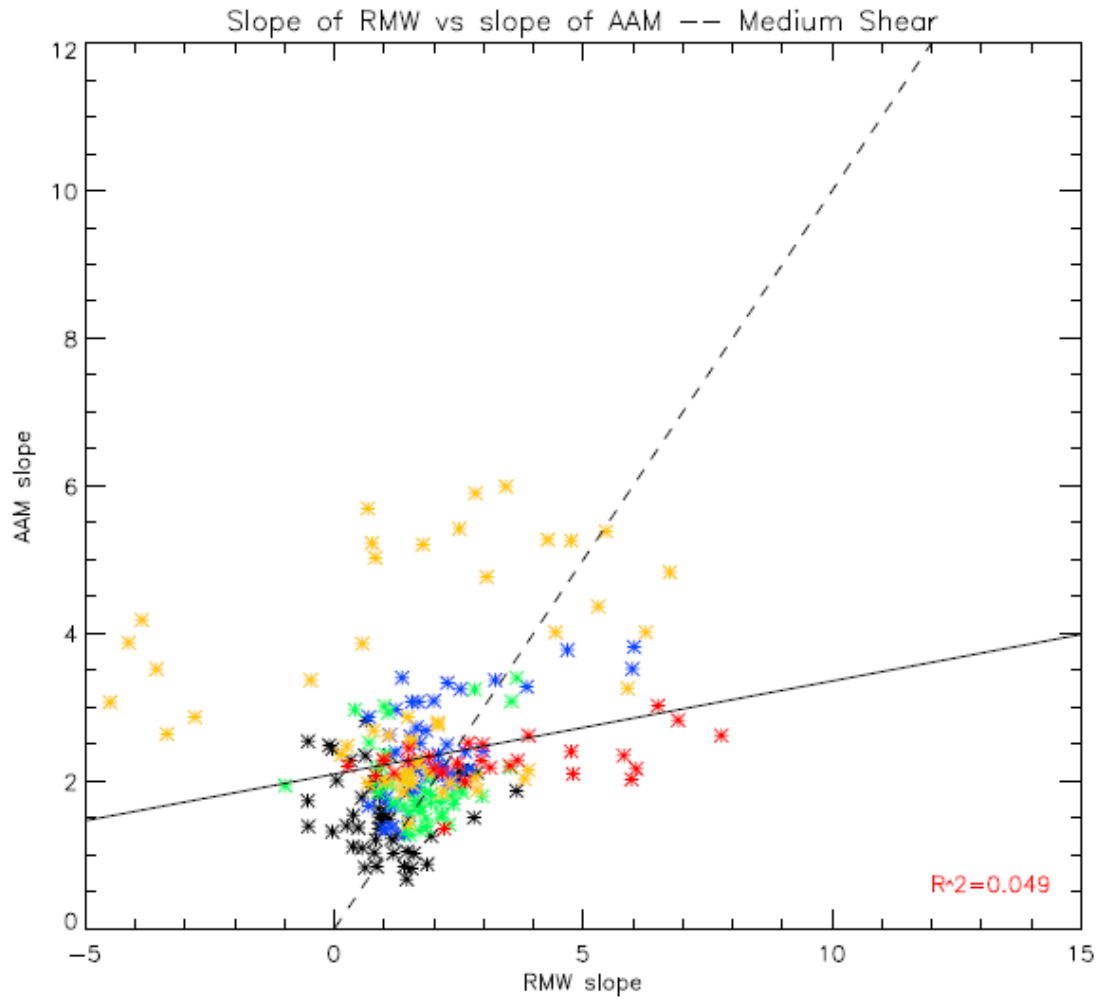


Figure 5.21: Slope of radius of maximum wind versus the slope of the absolute angular momentum for the medium shear cases. The solid black line is the linear best-fit line, and the dashed black line is the 1:1 line.

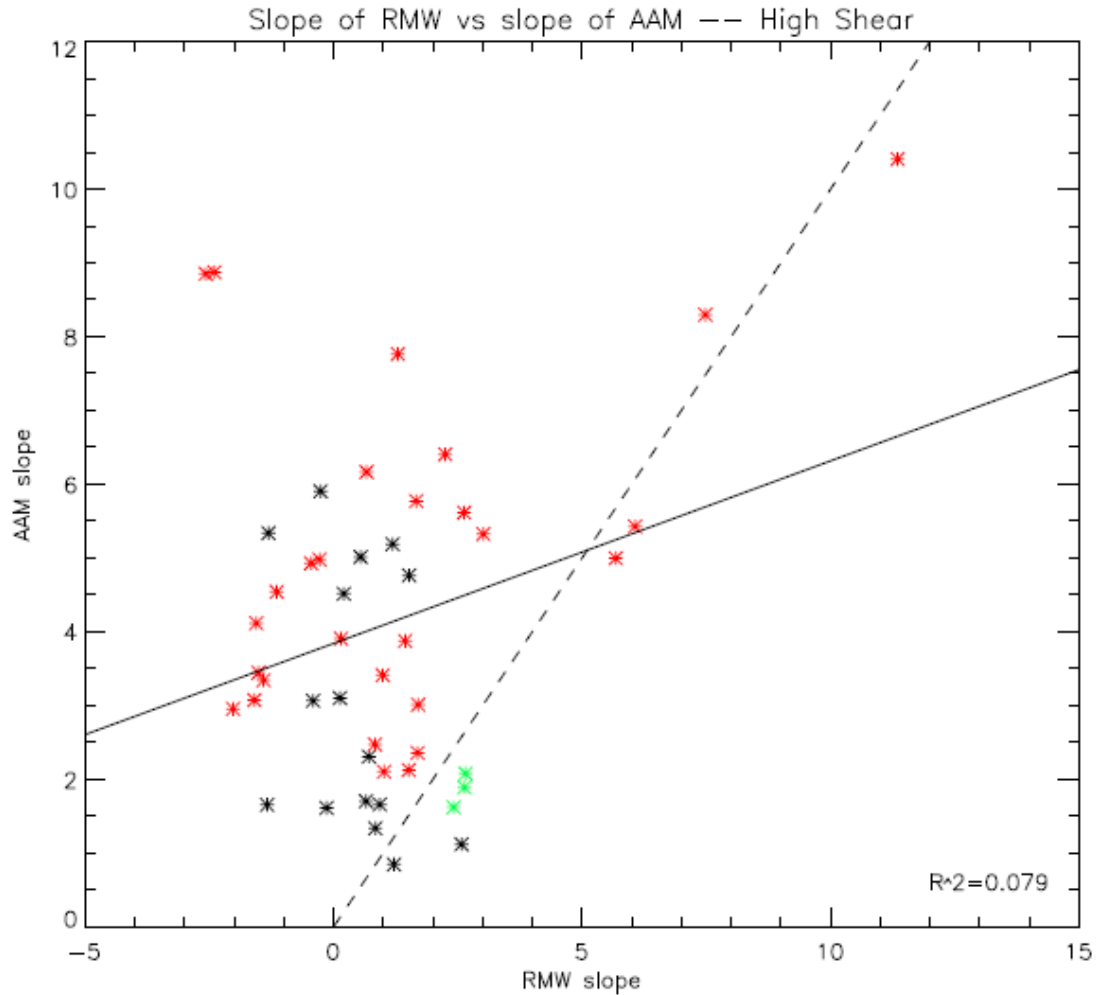


Figure 5.22: Slope of radius of maximum wind versus the slope of the absolute angular momentum for the high shear cases. The solid black line is the linear best-fit line, and the dashed black line is the 1:1 line.

5.2 Warm Core Structure

Tropical cyclones are warm core systems such that the warmest temperatures occur at their center. The study will now turn its focus to the vertical structure of the warm core. The warm core can be defined by the strength and the height. The strength is characterized by the magnitude of the temperature anomaly at the center of the storm (or the 2 km radius). The temperature anomaly is the temperature deviation from some environmental temperature. For this study, the environmental temperature profile is the

azimuthal mean temperature profile at the outer limit of the nested grid (i.e., the 250 km radius). So the temperature anomaly is the azimuthal mean temperature deviations from the environmental temperature profile. The height of the warm core is the height at which the 2 km radius temperature anomaly magnitude is maximized.

There is a great deal of ambiguity concerning the typical height of the warm core in a tropical cyclone, as was discussed in Chapter 1. A cursory look at the warm core structure of the simulated storms used in this study reveals a significant diversity. Figures 5.23-5.25 provide an example of the range. In these figures the solid black contours show the azimuthal mean tangential winds, and the large red arrow is positioned at the height of the environmental tropopause. Figure 5.23 shows the 24 h average profile of the azimuthal mean temperature anomalies for the 73-96 h forecast times of the 13 July 2005 Hurricane Emily simulation. This average profile shows a warm core height located near 9 km with a magnitude of approximately 7K. Figure 5.24 shows the 24 h average mean temperature anomaly profile for the 49-72 h forecast times of the 26 August 2005 Hurricane Katrina simulation. This plot clearly shows at least two well defined maxima. The primary warm core maximizes around 6 km with a magnitude exceeding 9K, and the secondary warm core is located at the 17 km height with a magnitude of approximately 8K. Finally, Figure 5.25 shows the 24 h average mean temperature anomaly profile for the 73-96 h forecast times of the 22 October 2005 Hurricane Wilma simulation. This plot again shows a double maximum structure, but at much lower heights. The primary warm core is located near 1.5 km with a magnitude in the 7K range, and the secondary warm core is located in the 4-5 km region with a

magnitude of approximately 6K. So there is clearly a good deal of variability in the warm core structure.

Generally, the temperature and tangential wind fields in a tropical cyclone are related via thermal wind balance, such that where there is a large radial temperature gradient the vertical gradient of the tangential winds is small. This is evident in Figures 5.23, 5.24, and 5.25 where the azimuthal mean tangential wind contours near the center of the storms are more vertical which is where the radial temperature gradients are largest.

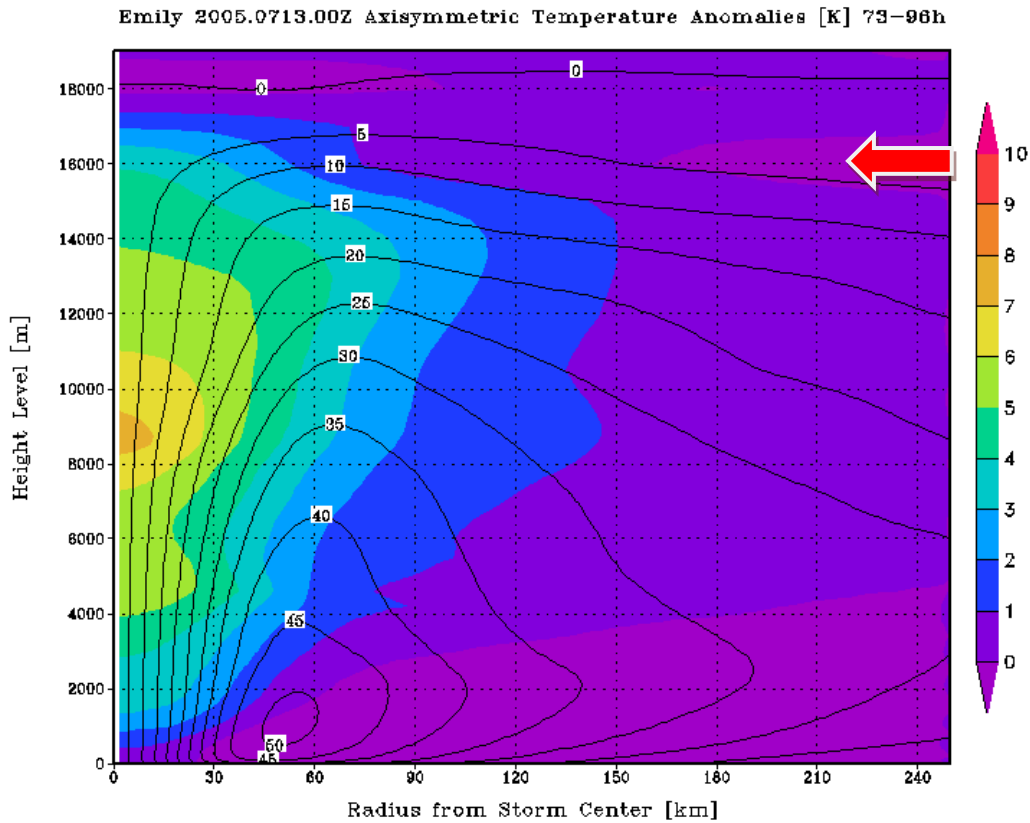


Figure 5.23: Vertical profile of the azimuthal mean temperature anomalies (color contours) averaged over the 73-96 h forecast times for the 13 July 2005 HWRFX simulation of Hurricane Emily. Solid black contours are the azimuthal mean tangential winds. The red arrow indicates the environmental tropopause height (16 km).

Katrina 2005.0826.00Z Axisymmetric Temperature Anomalies [K] 49-72h

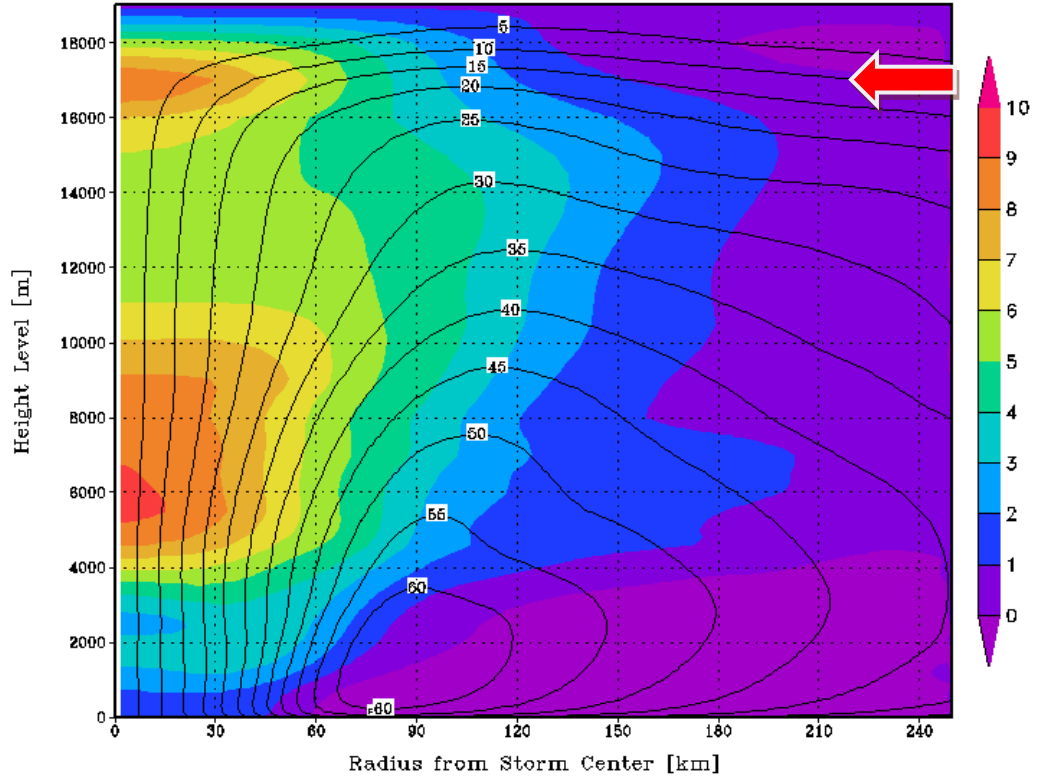


Figure 5.24: Vertical profile of the azimuthal mean temperature anomalies (color contours) averaged over the 49-72 h forecast times for the 26 August 2005 HWRFX simulation of Hurricane Katrina. Solid black contours are the azimuthal mean tangential winds. The red arrow indicates the environmental tropopause height (17 km).

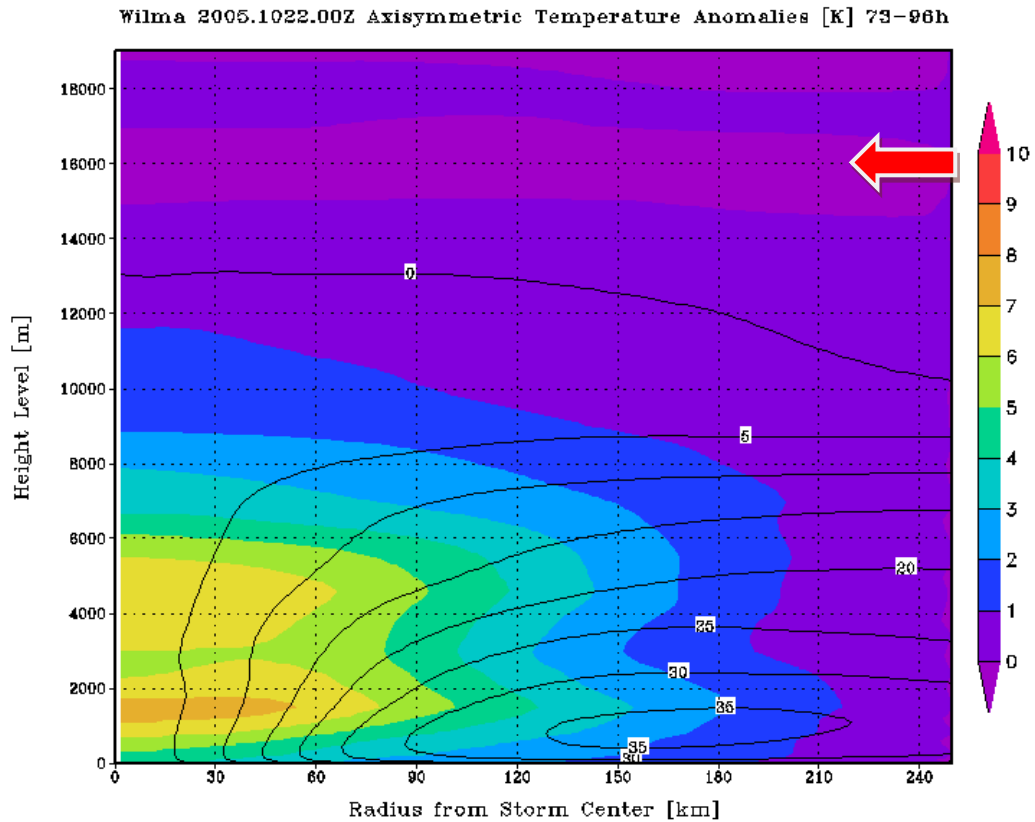


Figure 5.25: Vertical profile of the azimuthal mean temperature anomalies (color contours) averaged over the 73-96 h forecast times for the 22 October 2005 HWRFX simulation of Hurricane Wilma. Solid black contours are the azimuthal mean tangential winds. The red arrow indicates the environmental tropopause height (16 km).

In order to study the characteristics of the warm core structure, the locations and magnitudes of the primary and any possible secondary maximums in the temperature anomalies at the center of the storms must be determined. The primary maxima are defined initially as the height where the temperature anomaly is greatest. The secondary maxima are defined as the height where there is a secondary peak in the temperature anomaly, but the temperatures between this height and the primary maxima height must drop by at least 0.75K below this secondary maximum before rising to the second maxima. There is always a primary warm core, but there isn't always a secondary one. Furthermore, the magnitude of the secondary warm core can occasionally be greater than

that of the primary because of a time continuity constraint used in the analysis. This is accomplished by testing at each forecast time where there is a secondary maximum whether the height of the secondary is closer to the previous primary maxima height than the current primary maxima, and if it is, then the values are switched for that time.

The warm core heights for the 13 July 2005 simulation of Hurricane Emily are shown in Figure 5.26, and the magnitudes of the warm core(s) are shown in Figure 5.27. The primary warm core height starts out with some large fluctuations early in the simulation, but then settles to a height in the region of 9 km with some tendency towards the end of the simulation towards lower heights between 5 km and 8 km. The secondary warm core heights are largely either at very high levels in the region of 16-19 km, or are scattered at lower heights between 1-10 km. The magnitude of the primary warm core increases from around 2K at the start of the simulation up to 7-8K by around 40 h into the simulation, and this magnitude is roughly maintained for the rest of the simulation.

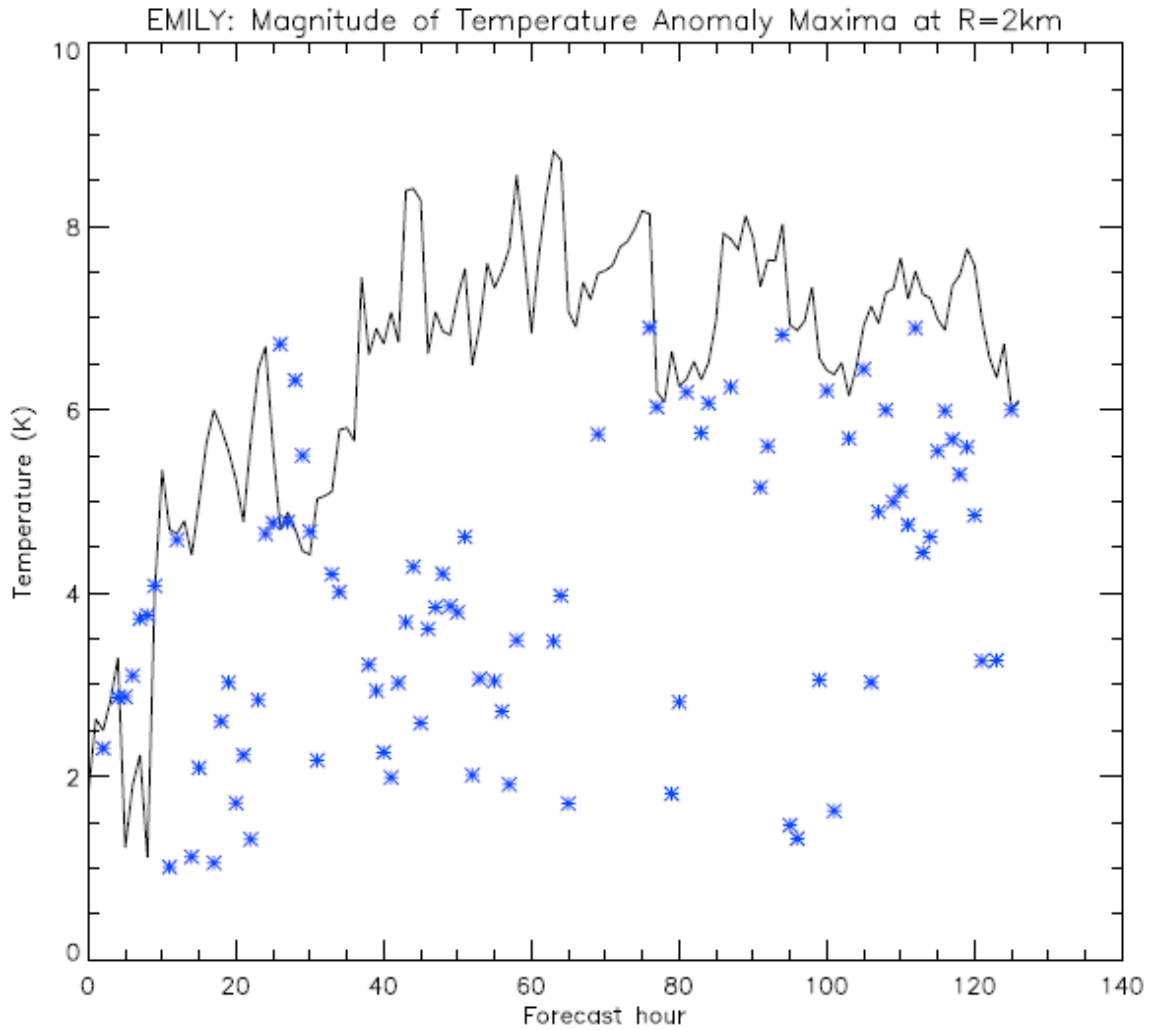


Figure 5.27: Time series of the magnitudes of the primary warm core at the 2 km radius (black line) for the 13 July 2005 HWRFx simulation of Hurricane Emily. The magnitudes of the secondary warm core are shown by the blue stars.

The warm core heights for the 15 July 2005 simulation of Hurricane Emily are shown in Figure 5.28, and the corresponding magnitudes are shown in Figure 5.29. The heights of the primary warm core roughly start out in the 9-10 km region and then gradually lower to around 5 km through the progression of the simulation. The secondary warm core height are generally located either very high (near the 15-19 km heights) or very low (near the 1-3 km heights). The magnitudes of the primary warm core fluctuations in the 7-9K range throughout the simulation.

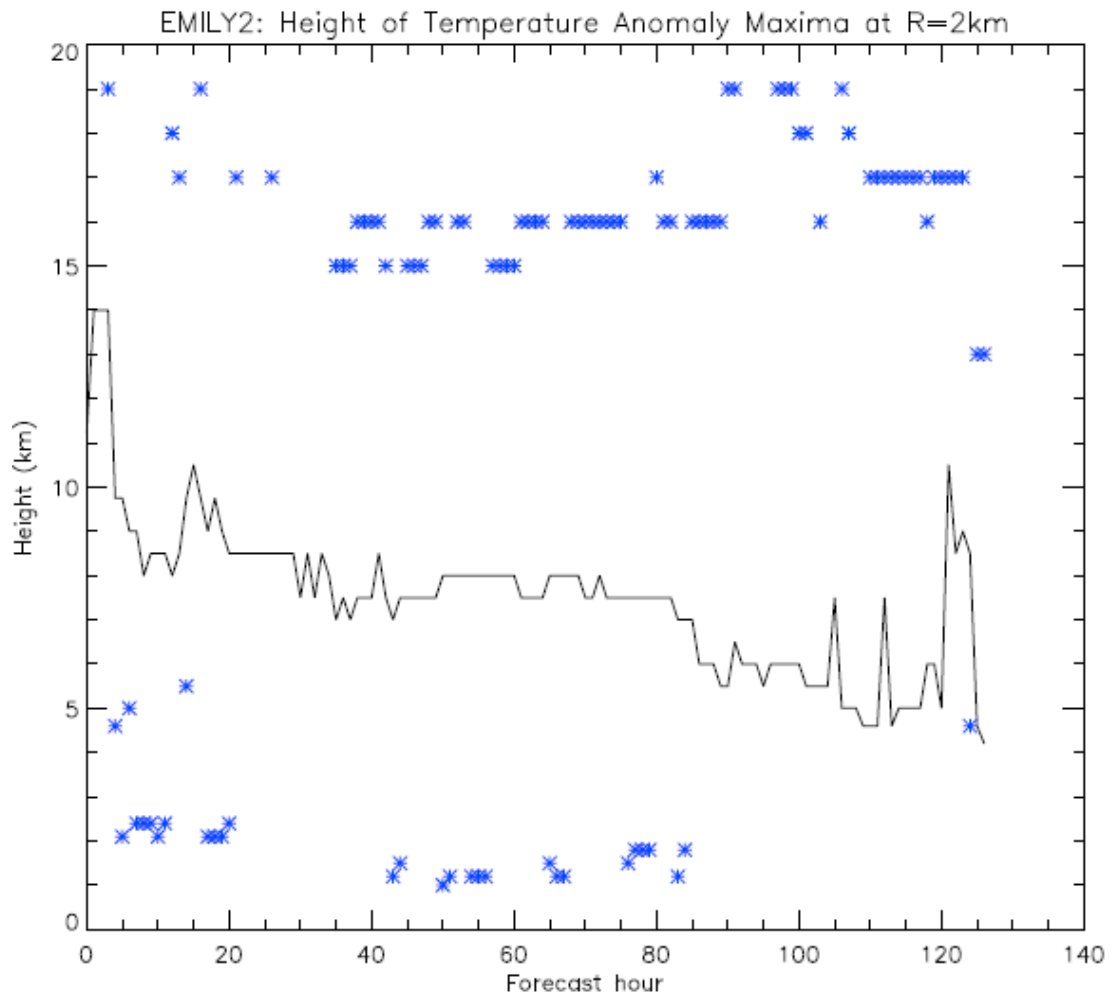


Figure 5.28: Time series of the heights of the primary warm core at the 2 km radius (black line) for the 15 July 2005 HWRFx simulation of Hurricane Emily. The heights of the secondary warm core are shown by the blue stars.

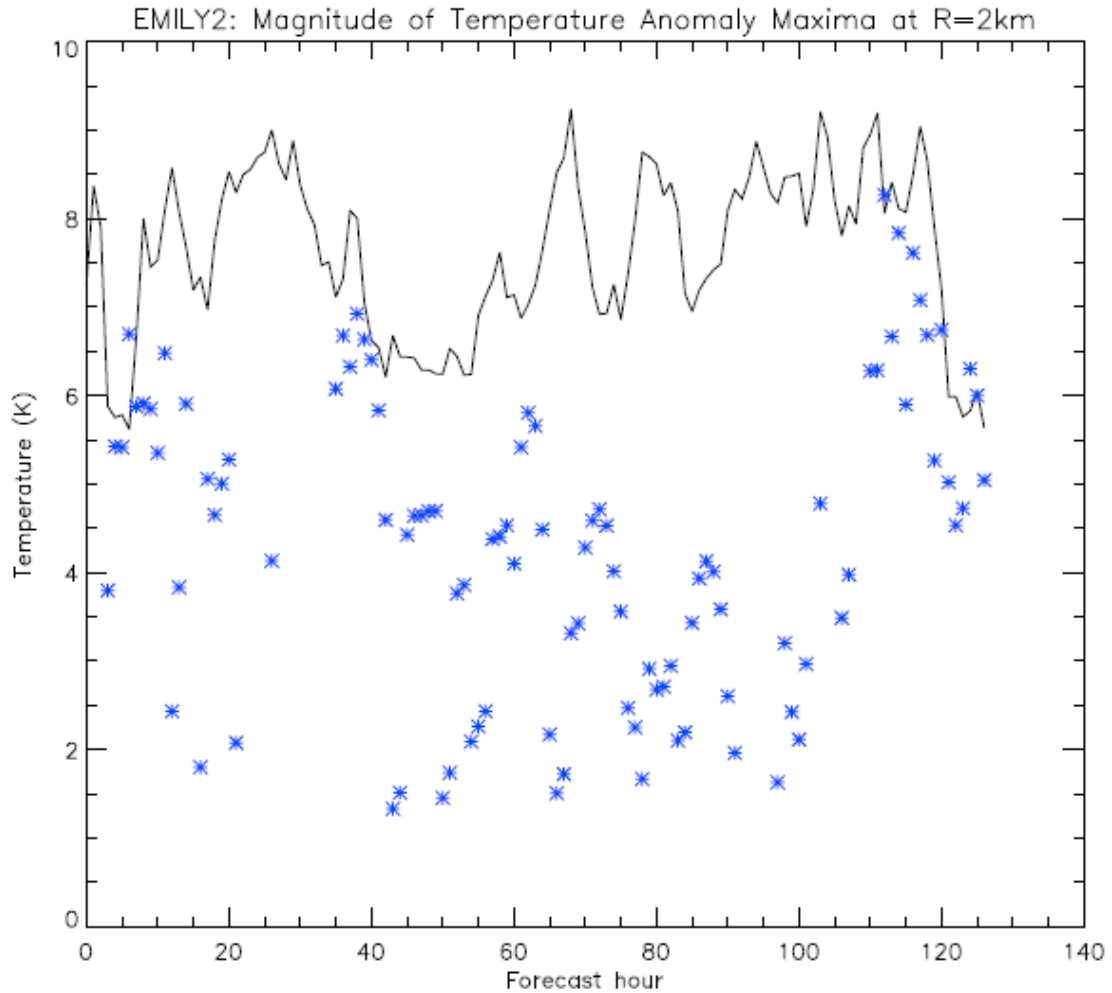


Figure 5.29: Time series of the magnitudes of the primary warm core at the 2 km radius (black line) for the 15 July 2005 HWRFx simulation of Hurricane Emily. The magnitudes of the secondary warm core are shown by the blue stars.

The warm core heights for the 26 August 2005 simulation of Hurricane Katrina are shown in Figure 5.30, and the corresponding magnitudes are shown in Figure 5.31. The heights of the primary warm core once past the initial variations settle into the 6-8 km region. Then just past the 80 h forecast time there is a large jump to around the 12 km height and then a drop down to around 8 km. This jump in the warm core height coincides with the simulated storm making landfall. The secondary warm core heights are again either located in the upper regions around 16-19 km or are at heights below 5

km. The magnitudes of the primary warm core rise from around 5K up to 10K temperatures before dropping significantly off with the landfall of the storm.

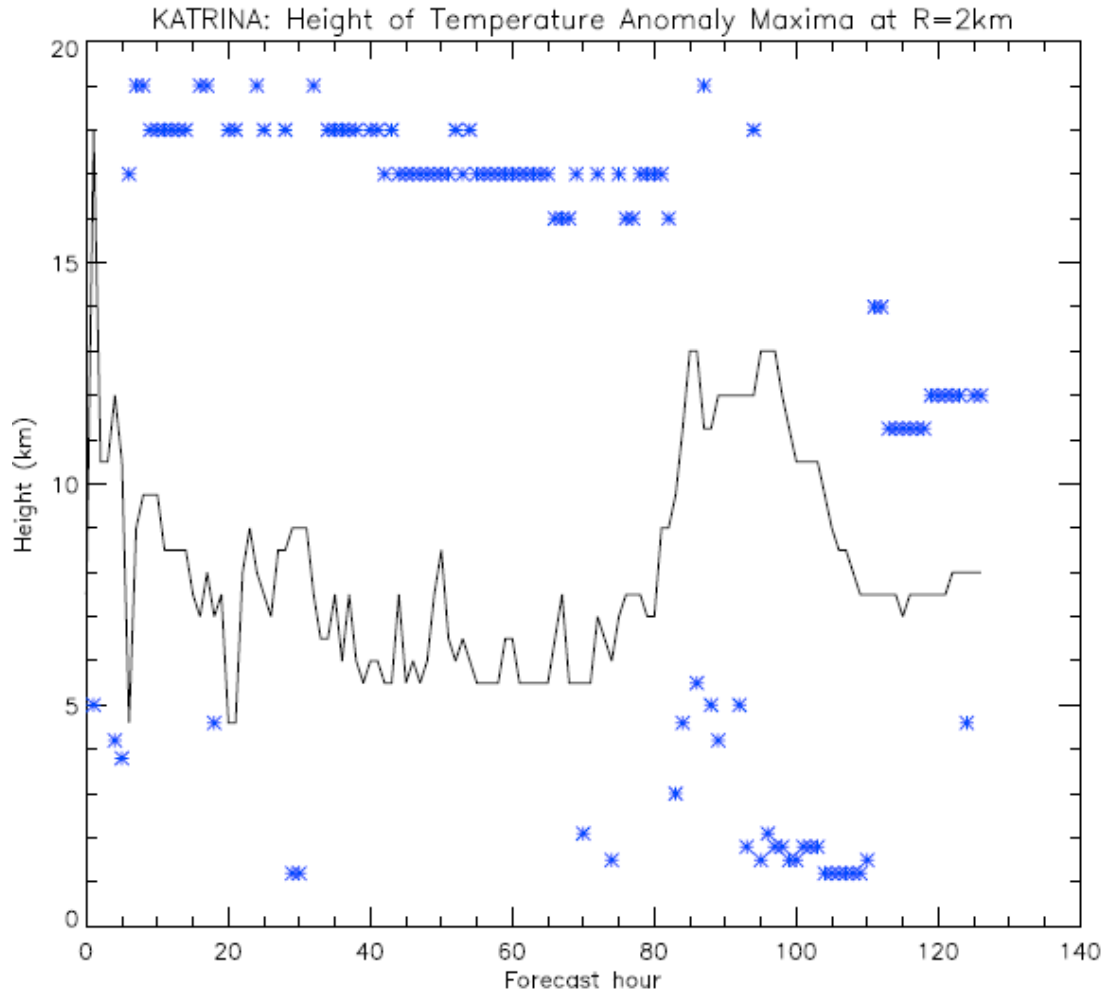


Figure 5.30: Time series of the heights of the primary warm core at the 2 km radius (black line) for the 26 August 2005 HWRFX simulation of Hurricane Katrina. The heights of the secondary warm core are shown by the blue stars.

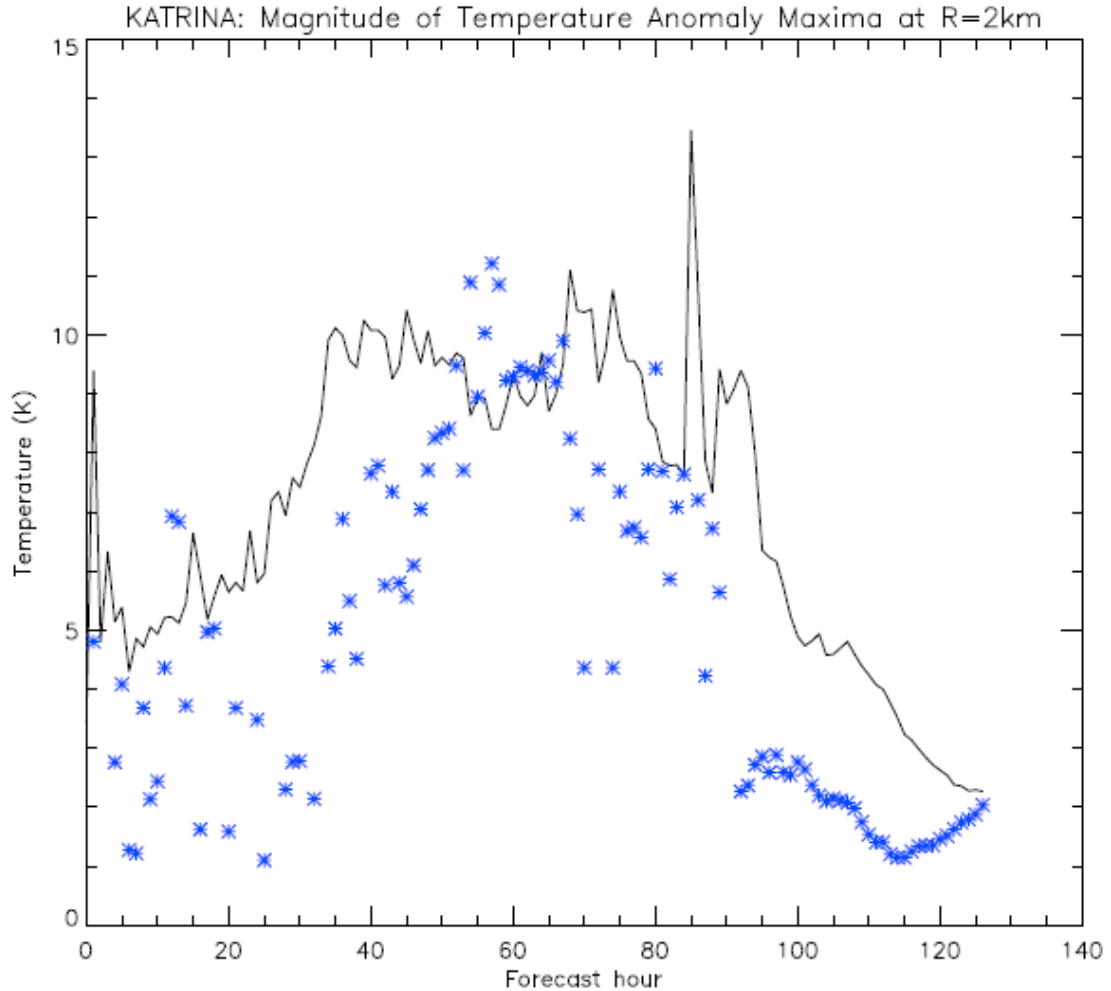


Figure 5.31: Time series of the magnitudes of the primary warm core at the 2 km radius (black line) for the 26 August 2005 HWRFx simulation of Hurricane Katrina. The magnitudes of the secondary warm core are shown by the blue stars.

The warm core heights for the 18 October 2005 simulation of Hurricane Wilma are shown in Figure 5.32, and the corresponding magnitudes are shown in Figure 5.33. The heights of the primary warm core are largely in the 5-8 km region, and they exhibit a slight overall drop in height through the evolution of the simulation. The secondary warm core heights are mostly located in the 16-19 km region, but there are a few low level secondary warm core heights below 5 km. The magnitudes of the primary warm core rises from 4K up to around 8K, then drops fairly dramatically to almost 2K before rising back up to around 7K values.

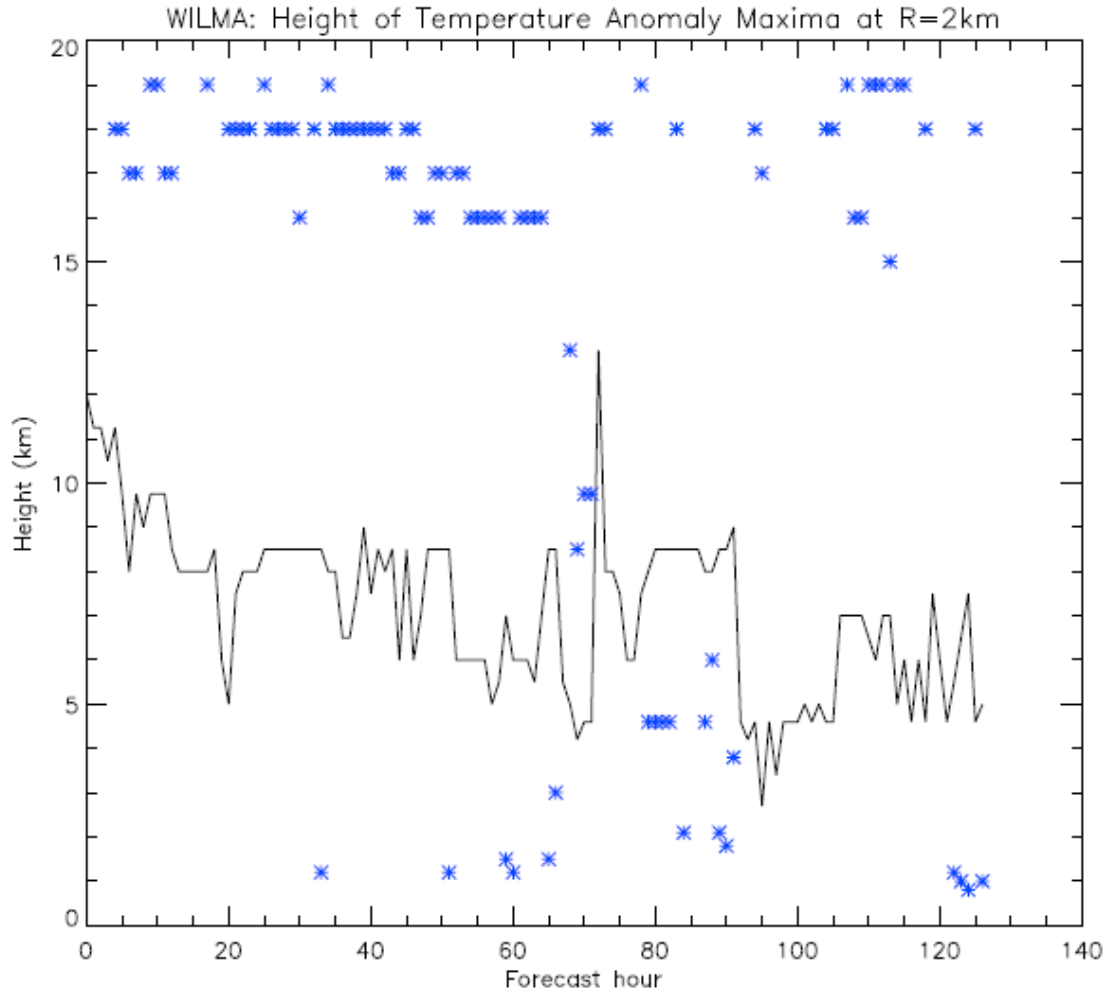


Figure 5.32: Time series of the heights of the primary warm core at the 2 km radius (black line) for the 18 October 2005 HWRFx simulation of Hurricane Wilma. The heights of the secondary warm core are shown by the blue stars.

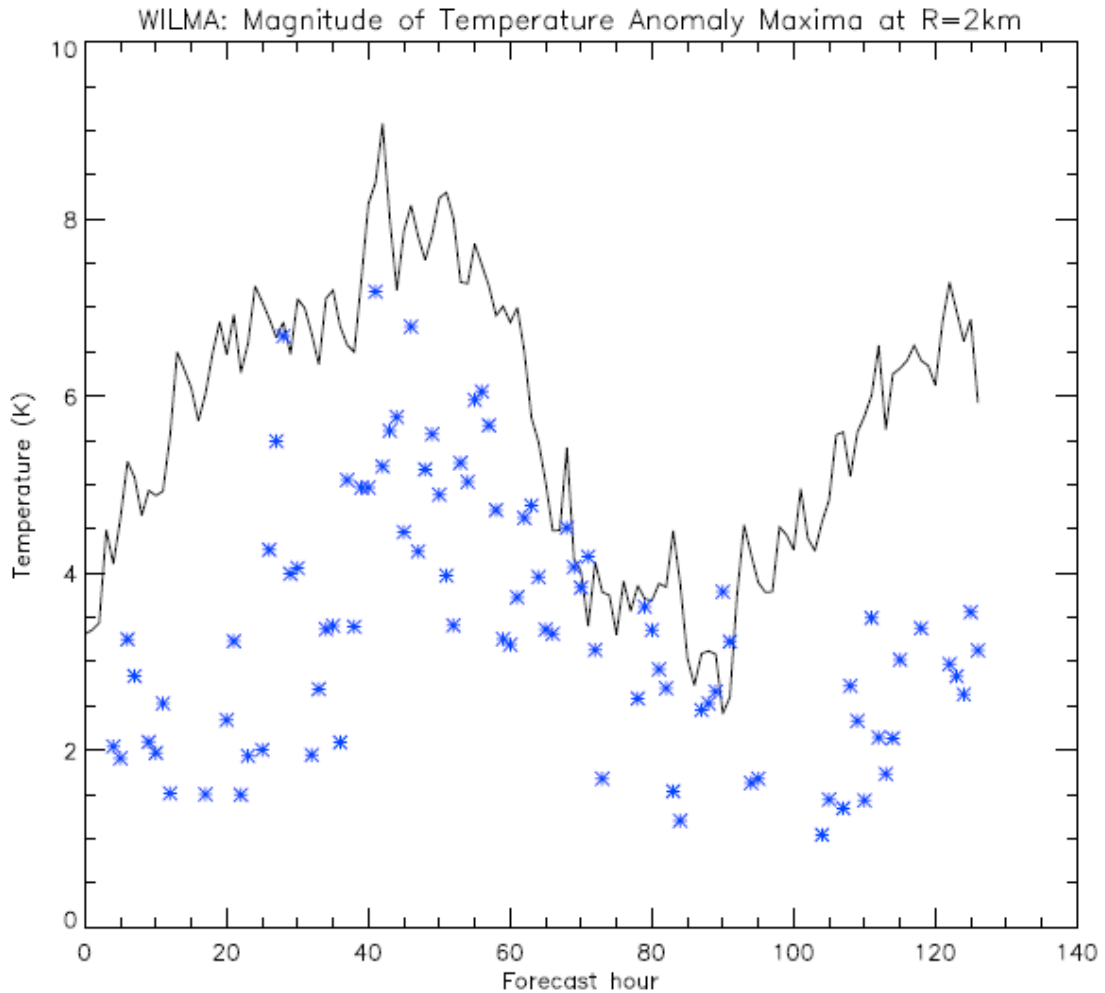


Figure 5.33: Time series of the magnitudes of the primary warm core at the 2 km radius (black line) for the 18 October 2005 HWRFx simulation of Hurricane Wilma. The magnitudes of the secondary warm core are shown by the blue stars.

The warm core heights for the 22 October 2005 simulation of Hurricane Wilma are shown in Figure 5.34, and the corresponding magnitudes are shown in Figure 5.35. The primary warm core heights, after some initial spikes, are located in the 10 km region and exhibit a gradual drop to around 8 km, then spike up to around 13 km and finally drop to 5 km and end up around 1.5 km at the end of the simulation. This dramatic drop to such low heights is concurrent with the simulated storm experiencing some effects of extratropical transition. The secondary warm core heights are either located high up at the 17-19 km heights or quite low in the 1.5-2 km region. The magnitudes of the primary

warm core are in the 5-10K range, but then warm considerably to more than 15K before cooling way down. This large increase and then decrease occurs during the extratropical transition influenced portion of the simulation.

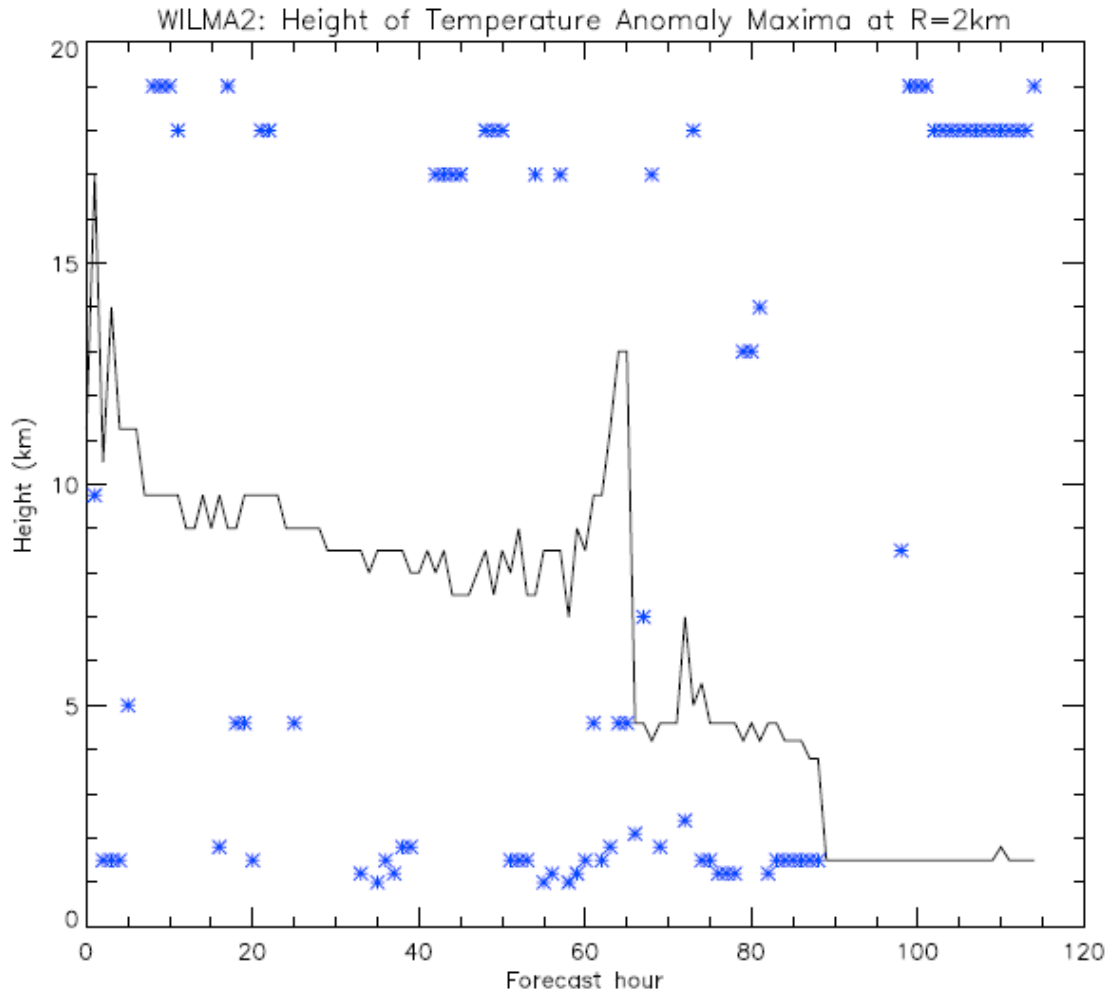


Figure 5.34: Time series of the heights of the primary warm core at the 2 km radius (black line) for the 22 October 2005 HWRFX simulation of Hurricane Wilma. The heights of the secondary warm core are shown by the blue stars.

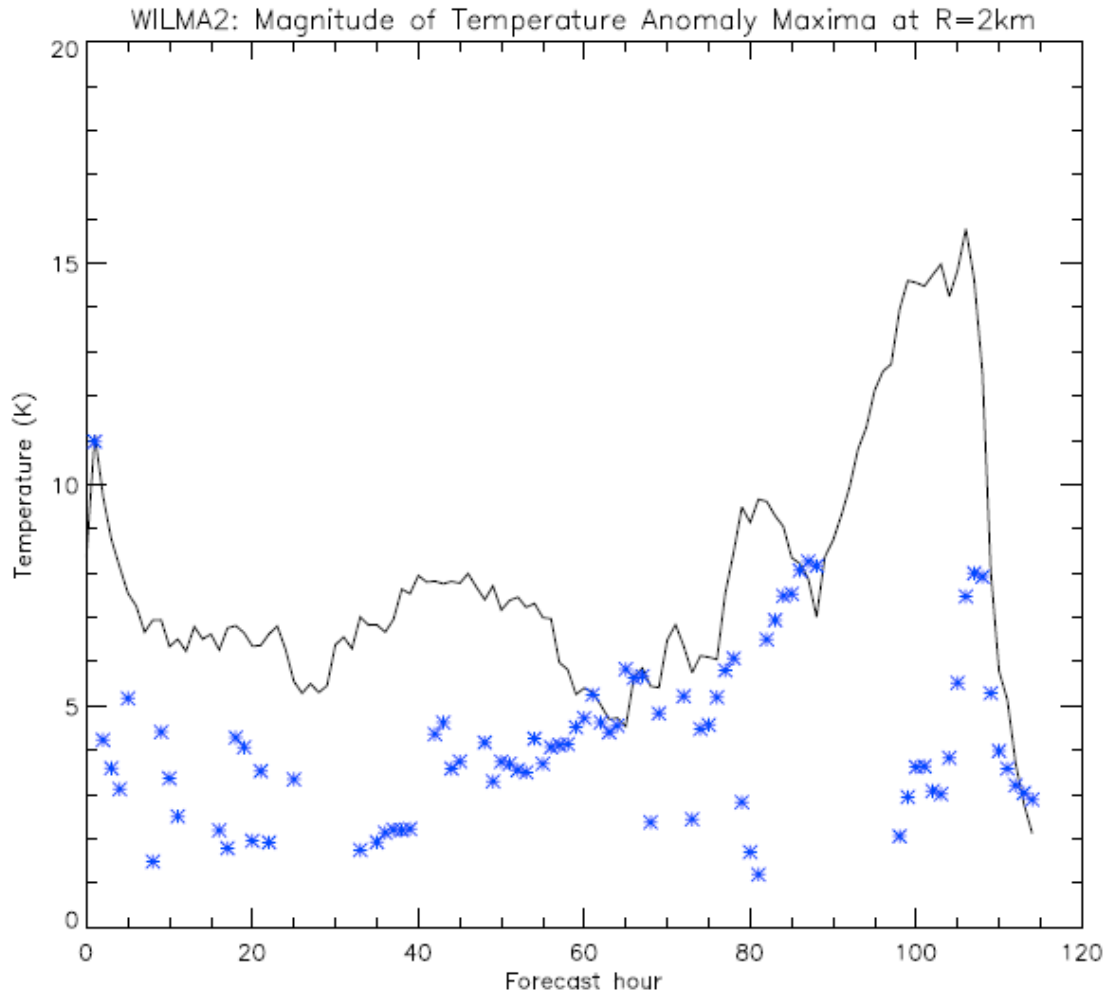


Figure 5.35: Time series of the magnitudes of the primary warm core at the 2 km radius (black line) for the 22 October 2005 HWRFX simulation of Hurricane Wilma. The magnitudes of the secondary warm core are shown by the blue stars.

Now the question of whether the height and magnitude of the warm core are affected by the environmental vertical wind shear and storm intensity changes will be addressed. This can simply be done by calculating the correlation between the primary warm core features (height and magnitude) and the magnitude of the shear and then the magnitude of the storm intensity change. The storm intensity change is represented by the average six hour intensity change. This is calculated by finding the average intensity change at each forecast time and then taking a six hour average centered about each forecast hour. The correlations are done across all five of the simulations in order to

capture the general nature of the relationships. The correlation coefficients for these relationships are shown in Table 5.1. The light blue highlighting indicates that the 95% significance criteria have been met for the warm core height versus intensity change relationship. The yellow highlighting indicates that the 99% significance criteria have been met for the warm core magnitude versus intensity change relationship. The actual values of the correlation are quite low however which suggests that relationship is weak.

Table 5.1: Correlation coefficients for the primary warm core height and magnitude and the environmental vertical shear and the 6 h averaged intensity change for all five of the simulations together. The light blue highlighting indicates the 95% significance criteria have been met, and the yellow highlighting indicates that the 99% significance criteria have been met.

	Environmental Vertical Shear	6 h Averaged Intensity Change
Warm Core Height	-0.049	0.096
Warm Core Strength (Magnitude)	-0.010	-0.196

5.2.1 Discussion of Warm Core Results

The results shown here overall suggest a number of features related to the warm core. Firstly, it is quite common to find multiple warm core features within the vertical structure of the inner core of the tropical cyclone. Generally there is a dominant primary warm core, and then a weaker secondary warm core. The strength of the secondary warm core is often a good amount cooler than the primary warm core, but not always.

Occasionally the secondary warm core feature can rival the primary warm core in strength. The existence of multiple warm core features within the vertical inner core structure is not a new concept. Stern and Nolan (2011) found this primary and secondary warm core structure in their modeling study, as did the modeling study of Rotunno and

Emanuel (1987), and Hawkins and Imbembo (1976) found a dual warm core feature in their study of Hurricane Inez (1966).

The heights of the primary warm core features in the study were, very generally speaking, in the 5-10 km height range. The secondary warm core features were commonly found either in the 16-19 km region, or were located below 5 km. By comparison, Stern and Nolan (2011) found the primary warm core height to be approximately 4-8 km, and the secondary warm core height to be around 13-14 km. So the secondary warm core heights in this study differ most greatly from those of Stern and Nolan (2011). Rotunno and Emmanuel (1987) did have their secondary warm core features at higher levels that are more consistent with the high level ones found in this study.

The previously implied relationship between the height and magnitude of the warm core and either storm intensity or shear was described above. There was little evidence found here to support the theory that shear affects either the height or magnitude of the warm core. As for the intensity change, there was weak evidence (i.e. low correlations) for a relationship between both the warm core characteristics and the 6 h average intensity change. The correlation was stronger for the magnitude of the warm core, but it is a negative correlation which suggests that the warm core is stronger when the storm is not experiencing as much of a change in intensity.

One may have some skepticism as to whether the environmental temperature profile that was used to calculate the temperature anomalies within the simulated storms well represents the environment. The magnitudes of the radial temperature gradient were

examined and it was found that the temperature gradients well within the radial storm core were far larger than at the outer radial limits for all of the simulations, but with one exception. Towards the later portions of the second Wilma simulation (after 72 h), the extratropical transitioning case, the radial temperature gradients across the whole domain were generally smaller, and the values well within the domain compared to those at the radial edge were not as significantly different. This is suggestive of storm contamination of the environment, and future analysis of this storm would be improved by using an environmental temperature profile at larger radii, if possible.

5.2.2 Cold Pool Analysis

The cold temperature anomalies will now be investigated. While tropical cyclones are warm core systems, there are some subtle cold pockets, in relative terms. One would think that these cold pockets would be more prominent with a storm that is beginning the extratropical transition process. Since the 22 October 2005 Hurricane Wilma simulation qualifies as a storm case that is beginning an extratropical transition, this is a good opportunity to investigate the cold temperature anomaly structure in the model.

The cold temperature anomalies are isolated simply by altering the plotting contours to show only the negative values. In order to show the general cold structures the 24 h average radius-height profiles are calculated. Figure 5.36 shows the first four 24 h average cold temperature anomaly profiles for the 15 July 2005 Hurricane Emily simulation. Figure 5.37 shows similar profiles for the 22 October 2005 Hurricane Wilma simulation. The contours range from -2.5K to 0K in 0.25K increments. The blue arrows

indicate the height of the average environmental tropopause height. Similar figures for the 13 July 2005 Hurricane Emily, 26 August 2005 Hurricane Katrina, and 18 October 2005 Hurricane Wilma simulations were created, but are not shown here. They display similar types of trends to those shown below.

The notable features in the plots are a cold pocket that persists in the lower levels (mostly below approximately 4-4.5 km). It is stronger in the Hurricane Emily simulation (Figure 5.36) than in the Hurricane Wilma simulation (5.37). In fact, the Wilma figure shows a very weak to nonexistent cold pool structure at the low levels. In panel D of Figure 5.37, which corresponds to the 73-96 h average, when the simulation is furthest into the extratropical transition processes there is a distant lack of a cold pool structure. This is interesting and not necessarily what was expected, although this analysis may be hampered by the previously discussed issue of the environmental temperature profile in this later portion of this Wilma simulation being affected by the expanding storm. The lower level cold pool structures are likely caused by processes associated with the evaporation of rain.

The other cold pool structure to note is the upper level features that show up in some of the figures. These features are located very near or above the height of the environmental tropopause and are thus likely related to overshooting tops and/or vertical displacements of the tropopause within the storm. Recall that similar secondary warm core features were found at the upper levels as well, and these may also be related to the vertical displacements of the tropopause within the storm.

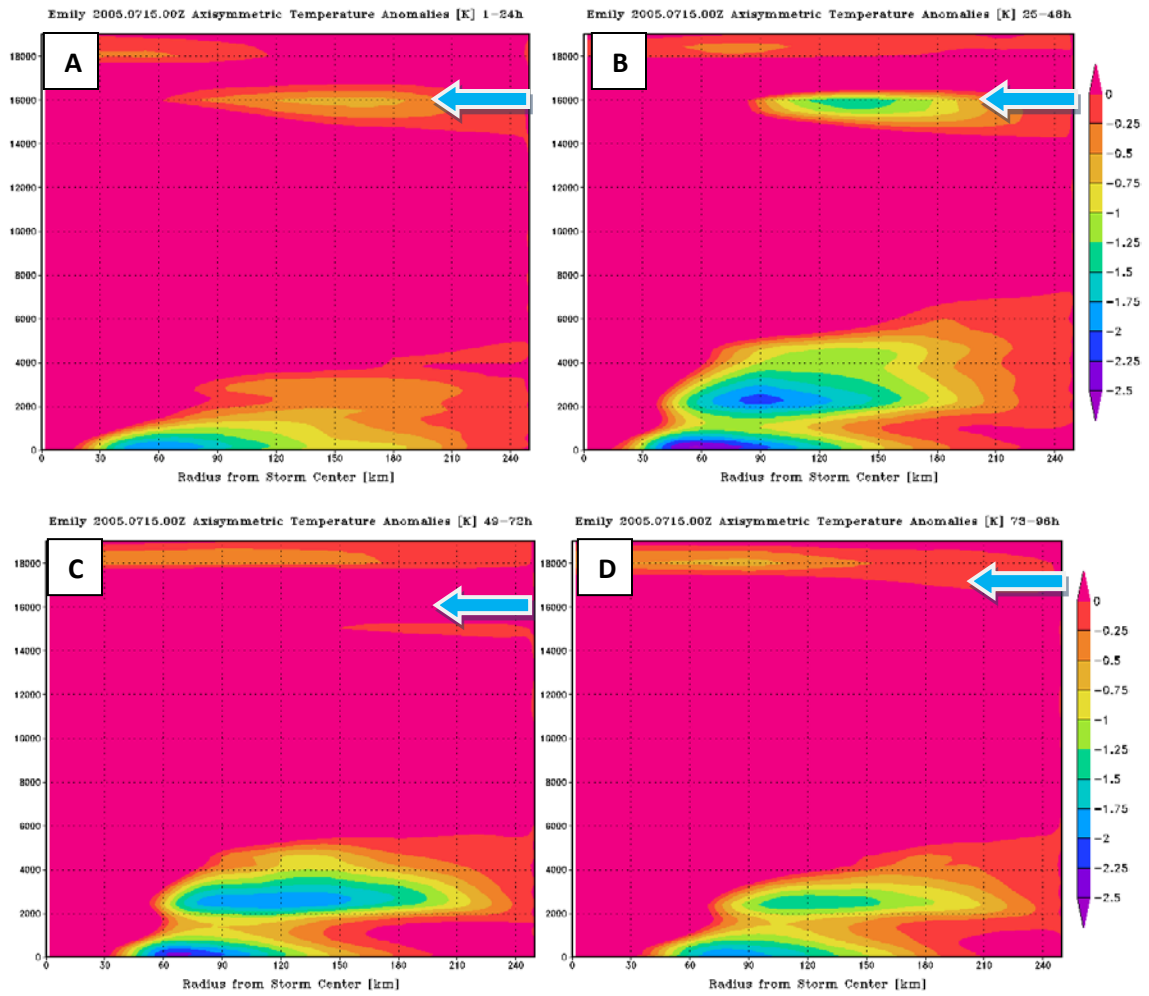


Figure 5.36: Cold contours of the 24 h average temperature anomalies for the 15 July 2005 HWRfX simulation of Hurricane Emily. A. 1-24 h average; B. 25-48 h average; C. 49-72 h average; D. 73-96 h average. Contours range from -2.5K to 0K. The blue arrows indicate the height of the environmental tropopause.

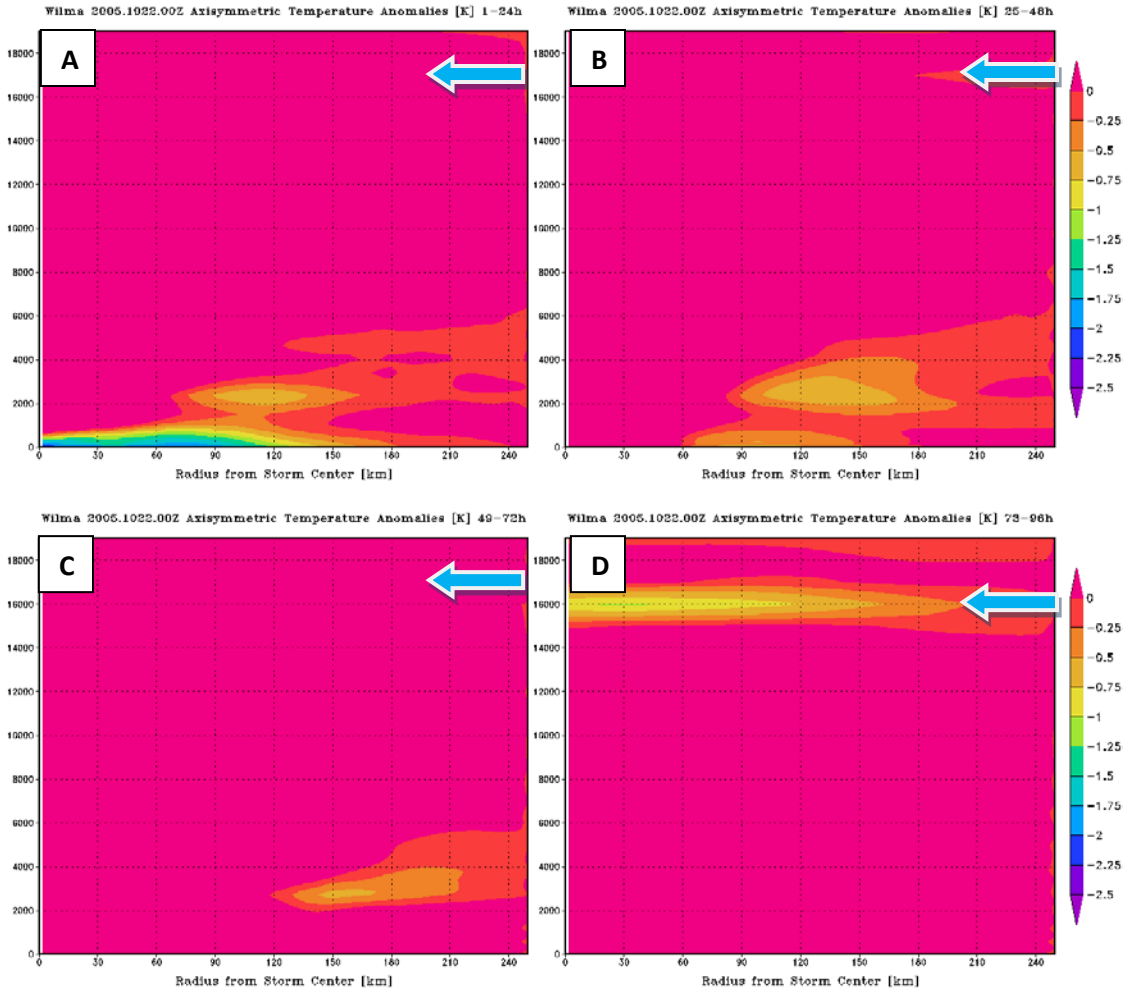


Figure 5.37: Cold contours of the 24 h average temperature anomalies for the 22 October 2005 HWRFX simulation of Hurricane Wilma. A. 1-24 h average; B. 25-48 h average; C. 49-72 h average; D. 73-96 h average. Contours range from -2.5K to 0K. The blue arrows indicate the height of the environmental tropopause.

CHAPTER 6 – CONCLUSIONS

This chapter provides a summary of the results from this study along with some concluding remarks. Additionally, some ideas and topics for future work are discussed.

6.1 Summary and Conclusions

The focus of this study was on the horizontal and vertical structure of tropical cyclones. The study was conducted using five real data simulated tropical cyclones from the 2005 Atlantic tropical cyclone season using the HWRFx model. Of the five simulations two were of Hurricane Emily, one was of Hurricane Katrina, and two were of Hurricane Wilma. These simulations were chosen because they provide a more varied dataset than a single storm case, and represent a spectrum of storms in different environments and undergoing a variety of structure changes.

The horizontal structural analysis concentrated on the integrated kinetic energy field and wind field asymmetries and how they are affected by storm motion, environmental shear, and the directional difference between the storm motion and environmental shear vectors. The study of the integrated kinetic energy field involved a wavenumber decomposition of the field and then a calculation of the percentage of the total field that each wavenumber makes up. Overall the largest contributor to the integrated kinetic energy field is the wavenumber-0, or azimuthal mean flow, kinetic energy. The wavenumber-1 asymmetries are the next largest contributor, and subsequent

wavenumbers make decreasingly significant contributions. Also, at greater heights in the storm the role of asymmetry becomes larger. Specifically, Table 6.1 shows the average symmetric (wavenumber-0) contributions and the average asymmetric (wavenumber-1 to 4) contributions to the kinetic energy field. The increased asymmetries at upper levels were an expected result based on many previous studies. The correlation of the kinetic energy wavenumber percentages with the storm motion revealed that the wavenumber-1 asymmetries for increased values of storm motion make up a larger portion of the total kinetic energy field than the higher wavenumber asymmetries. A similar correlation with the environmental shear showed that, while the wavenumber-1 asymmetries have the highest correlation, the higher wavenumber asymmetric contributions are also larger for greater shear. This suggests that the shear effect on storm asymmetric structure is not so simple. Storm motion and shear are potentially competing forces behind storm asymmetries, so the vector directional difference between the storm motion and environmental shear vectors was calculated. Focusing on the scenarios where the vectors are approximately aligned and approximately opposed, the average integrated kinetic energy wavenumber percentages were calculated. These showed that when the vectors are aligned the asymmetries play a much larger role in total integrated kinetic energy field than when the vectors are opposed.

Table 6.1: Average symmetric (wavenumber-0) and asymmetric (wavenumber-1 to 4) contributions to the kinetic energy field at the 1500 m, 3000 m, 5000 m, and 12000 m heights.

	1500 m	3000 m	5000 m	12000 m
Avg. Symm. KE_n/KE_{total} %	92.0%	89.3%	87.4%	75.4%
Avg. Asymm. KE_n/KE_{total} %	7.8%	10.4%	12.2%	23.5%

To better understand the details of the wind field asymmetries, a composite analysis of the wind field was completed followed by a wavenumber decomposition of the tangential wind field. A composite of all of the data in storm motion relative coordinates showed a clear wavenumber-1 asymmetry with a maximum to the right of the storm motion vector, which is consistent with numerous previous observations and studies. A similar composite in shear relative coordinates showed a wavenumber-1 asymmetry with a maximum located to the left of the shear vector, which is also consistent with previous observations and studies. A wind field composite in storm motion relative coordinates of the cases where the storm motion and shear vectors are approximately aligned revealed first a wavenumber-1 maximum to the left of the storm motion vector, but perhaps more notably a wavenumber-2 asymmetry with maxima to the left and right of the storm motion. In contrast, the composite for the cases where the storm motion and shear vectors are approximately opposed showed simply a wavenumber-1 asymmetry with its maximum located to the right of the storm motion vector. The wavenumber decomposition of the tangential wind field confirmed the above results and was also supportive of the integrated kinetic energy wavenumber decomposition analysis. That is, higher wavenumber asymmetries are more prevalent when the storm motion and environmental shear vectors are aligned than when they are opposed. These results are consistent with those of Ueno and Bessho (2011), however, these results showed a greater effect from the shear, but that may be because the data used for this study had some more highly sheared cases. These results also showed that the shear asymmetries extended more deeply through the troposphere than those related to the motion.

An additional analysis of the vorticity field was performed to determine if there is a vortex Rossby wave signal within the storm asymmetries. This analysis entailed an azimuthal wavenumber decomposition of the vorticity followed by a temporal wavenumber decomposition. The vortex Rossby wave influenced azimuthal wavenumber-2 vorticity asymmetries, according to theory, should propagate cyclonically at approximately half the velocity of the maximum wind. This translates to a frequency in the temporal analysis at which a peak should be evident if vortex Rossby waves are present. The results of this analysis in Chapter 4 suggested that there is a contribution to the wavenumber-2 asymmetries in the simulations. The vorticity spectra showed that the vortex Rossby wave amplitudes were comparable to those from the shear and motion induced asymmetries. However, because these rotate around the storm center, they would be much harder to detect with real data compared to the shear and motion asymmetries that are tied to the slowly varying storm environment.

The fact that at least part of the asymmetric structure is tied to the storm environment suggests that it might be possible to diagnose the asymmetric storm structure given information about the large scale analysis for cases where no in situ observations are available. A simple version of the parameterization of the asymmetric flow was described by Mueller et al. (2006) where the low level wind field of tropical cyclones is estimated from satellite observations. In that case, the asymmetries are determined from only the storm motion. The results of this study suggest that the method can be improved by also including information about the environmental wind shear.

The vertical structure analysis in Chapter 5 gave specific emphasis to understanding the impacts of a sheared environment on the structure. The vertical

structure of the tangential wind field was studied in terms of the RMW and its slope and how it relates to the storm intensity and a constant AAM surface, and then how these relationships change in an increasingly sheared environment. Firstly, the maximum tangential winds were found to decrease more steeply with height for the highly sheared cases, and the moderately sheared cases showed slightly better maintenance of the maximum tangential winds with height than for the low shear cases. Additionally, the constant AAM surface slopes outward more greatly with the high shear cases, and the medium shear cases have an AAM slope that is slightly more vertical than the low shear cases. This suggests that moderate shear may have a positive effect on the storm, while high shear is definitely more disruptive to the vertical structure.

The slope of the RMW was found to not be related to the intensity of the storm, which is consistent with the findings of Stern and Nolan (2009). However, the relationship between the low level RMW and the slope of the RMW was most strongly defined for the low shear cases ($R^2=0.3$), the relationship being that the RMW slopes outward more greatly with larger RMW values. The relationship declined greatly for the moderately ($R^2=0.02$) and highly ($R^2=0.006$) sheared cases. Stern and Nolan (2009) found a nearly linear relationship between the RMW and the slope of the RMW, but these results suggest that this connection breaks down with increasingly sheared cases. The slopes of the constant AAM surface versus the RMW showed a much better relationship ($R^2=0.6$), which is consistent with the results of Stern and Nolan (2009), and is best for the low ($R^2=0.8$) and medium ($R^2=0.7$) sheared cases. Finally, the theory that the RMW is well approximated by a constant AAM surface was tested. The results showed that the correlation between the RMW and AAM slopes was best for the low shear ($R^2=0.3$), and

declined greatly for the medium ($R^2=0.05$) and high ($R^2=0.08$) shear cases. However, for the theory to verify the slopes would need to display a 1:1 relationship, which was not the case.

The warm core vertical structure was then analyzed in order to better understand the characteristics of the primary and possible secondary warm anomalies. The main objective was to determine the height and magnitude of the warm core structure for the simulations and establish whether there are any significant trends with respect to storm evolution, environmental shear, and/or intensity change. The results showed that the vertical structure of the warm core often consists of a primary warm core and a secondary warm core. The primary warm core occurs usually in the 5-10 km region and the secondary warm core is located either below 5 km or in the 16-19 km region. The height of the primary warm core seemed to exhibit a tendency to decrease slightly over the evolution of the simulated storms. The height and magnitude of the primary warm core were not found to be linked to the environmental shear. The height of the primary warm core was shown to very weakly correlate ($R=0.1$) to the 6 h averaged intensity change, and the strength of the primary warm core was found to correlate a bit more significantly to the intensity change ($R=-0.2$). The correlation indicated that the magnitude of the warm core decreases when the storm is experiencing larger intensity changes. These results compare fairly well with that of previous studies, although the low level secondary warm core features seem somewhat unique.

Finally, a brief examination of the cold pool features within the simulations was completed to find out if there were any salient features. These results showed that there are persistent relative cold pockets at low levels in the simulated storms that are likely to

have formed due to evaporation of rain. There also were cold anomalies at high vertical levels that are likely associated either with overshooting tops or are due to a radial slope of the tropopause height within the storm core. Interestingly, there was a noticeable lack of cold anomalies for the storm simulation that was experiencing effects of an extratropical transition.

6.2 Future Work

There are a number of things that can be pursued in future work from this study. The analysis can be extended to include more HWRFx storm simulations. This would help to determine the robustness of the present findings. In addition to the 27:9 km resolution version of the HWRFx model, there is also a 9:3 km resolution version. Recreating all of the analysis using the higher resolution version of the HWRFx model may be quite enlightening. The particular benefit of using a higher resolution is that this version may be able to more accurately resolve structural features of the storms, and the convection is much better resolved. Specifically, features such as eyewall replacement cycles may be resolvable, which is a feature that simply cannot be captured with the 27:9 km version. Also, further study can be done on the cold pool structures in the simulations such as determining the characteristics in terms of height, magnitude, and radius; and can it be connected to specific mechanisms such as evaporative cooling.

An interesting scientific question is why there is commonly a dual warm core structure. Balance model theory (e.g. Schubert and Hack, 1983) indicates that changes in the tangential wind and the corresponding thermal structure required to maintain gradient balance are due to the horizontal and vertical structure of the heating, and the vortex

structure. Applying the balance model to the output from the HWRFx model may help to better understand the physical processes associated with the dual warm core structure.

Another scientific issue raised by this study is the relationship between vertical shear and vertical structure of the storm. The vertical shear impacted the slope of the absolute angular momentum surfaces, and the radius of maximum wind deviated further from a constant angular momentum surface in higher shear. The modification of the symmetric structure and related warm core may be another mechanism by which vertical shear can impact a tropical cyclone.

Finally, and perhaps most importantly, the results presented in this study might be used to improve real-time tropical cyclone structural forecasting. The fairly robust relationships between the wind field asymmetries and storm motion and shear suggest that it might be able to parameterize these effects when no in situ observations are available. These relationships with the large scale also suggest that at least part of the asymmetric flow may be predictable. The more rapidly varying asymmetries due to the vortex Rossby waves are probably much less predictable. Because there can be feedback between the asymmetric wind structure and convective evolution (Braun, 2002), the vortex Rossby waves are an additional source of forecast uncertainty.

REFERENCES

- AMS, 1993: Policy Statement: Hurricane detection, tracking, and forecasting. *Bull. Amer. Meteor. Soc.*, **74**, 1377-1380.
- Bender, M. A., R. E. Tuleya, and Y. Kurihara, 1987: A numerical study of the effect of island terrain on tropical cyclones. *Mon. Wea. Rev.*, **115**, 130-155.
- Black, P. G., and R. A. Anthes, 1971: On the asymmetric structure of the tropical cyclone outflow layer. *J. Atmos. Sci.*, **28**, 1348-1366.
- Braun, S. A., 2002: A cloud-resolving simulation of hurricane Bob (1991): Storm structure and eyewall buoyancy. *Mon. Wea. Rev.*, **130**, 1573-1592.
- Cecil, D.J., 2007: Satellite-derived rain rates in vertically sheared tropical cyclones. *Geophys. Res. Lett.*, **34**, L02811, doi:10.1029/2006GL027942.
- Chang, S. W.-J., 1982: The orographic effects induced by an island mountain range on propagating tropical cyclones. *Mon. Wea. Rev.*, **110**, 1255-1270.
- Chen, S.S., J.A. Knaff, and F.D. Marks, 2006: Effects of vertical wind shear and storm motion on tropical cyclone rainfall asymmetries deduced from TRMM. *Mon. Wea. Rev.*, **134**, 3190-3208.
- Corbosiero, K.L., and J. Molinari, 2002: The effects of vertical wind shear on the distribution of convection in tropical cyclones. *Mon. Wea. Rev.*, **130**, 2110-2123.
- Corbosiero, K.L., and J. Molinari, 2003: The relationship between storm motion, vertical wind shear, and convective asymmetries in tropical cyclones. *J. Atmos. Sci.*, **60**, 366-376.
- Davis, C.A., and Coauthors, 2008: Prediction of landfalling hurricanes with the advanced hurricane WRF model. *Mon. Wea. Rev.*, **136**, 1990-2005.
- Dudhia, J., 1989: Numerical study of convection observed during the winter monsoon experiment using a mesoscale two-dimensional model. *J. Atmos. Sci.*, **46**, 3077-3107.
- Ek, M. B., K. E. Mitchell, Y. Lin, E. Rogers, P. Grunmann, V. Koren, G. Gayno, J. D. Tarpley, 2003: Implementation of Noah land surface model advances in the NCEP operational mesoscale Eta model. *J. Geophys. Res.*, **108(D22)**, 8851, doi:10.1029/2002JD003296.
- Emanuel, K. A., 1995: The behavior of a simple hurricane model using a convective scheme based on subcloud-layer entropy equilibrium. *J. Atmos. Sci.*, **52**, 3960-3968.

- Farfan, L. M., and J. A. Zehnder, 2001: An analysis of the landfall of hurricane Nora (1997). *Mon. Wea. Rev.*, **129**, 2073-2088.
- Ferrier, B.S., Y. Lin, T. Black, E. Rogers, G. DiMego, 2002: Implementation of a new grid-scale cloud and precipitation scheme in thence Eta model. Preprints, 15th conference on numerical weather prediction, San Antonio, TX, American Meteorological Society, pp 280-283.
- Frank, W. M., 1977: The structure and energetics of the tropical cyclone I. Storm structure. *Mon. Wea. Rev.*, **105**, 1119-1135.
- Franklin, J.L., S.J. Lord, S.E. Feuer, and F.D. Marks, 1993: The kinematic structure of hurricane Gloria (1985) determined from nested analyses of dropwindsonde and doppler radar data. *Mon. Wea. Rev.*, **121**, 2433-2451.
- Franklin, J.L., and D.P. Brown, cited 2006: Tropical cyclone report: Hurricane Emily, 18pp. [Available online at http://www.nhc.noaa.gov/pdf/TCR-AL052005_Emilypdf.pdf.]
- Gopalakrishnan, S. G., F. Marks, X. Zhang, J. Bao, K. Yeh, R. Atlas, 2011: The experimental HWRF system: A study on the influence of horizontal resolution on the structure and intensity changes in tropical cyclones using an idealized framework. *Mon. Wea. Rev.*, **139**, 1762–1784.
- Gopalakrishnana, S. G., and Coauthors, 2011: Hurricane weather research and forecasting (HWRF) model: 2011 scientific documentation, 82pp. [Available online at <http://www.emc.ncep.noaa.gov/HWRF/HWRFScientificDocumentation2011.pdf>.]
- Guinn, T.A., and W.H. Schubert, 1993: Hurricane spiral bands. *J. Atmos. Sci.*, **50**, 3380-3403.
- Hong, S.-Y., H.-L. Pan, 1996: Nonlocal boundary layer vertical diffusion in a medium-range forecast model. *Mon. Wea. Rev.*, **124**, 2322-2339.
- Hong, S.-Y., H.-L. Pan, 1998: Convective trigger function for a mass-flux cumulus parameterization scheme. *Mon. Wea. Rev.*, **129**, 1164-1178.
- Janjic, Z. I., J.P. Gerrity Jr., and S. Nickovic, 2001: An alternative approach to non-hydrostatic modeling. *Mon. Wea. Rev.*, **129**(5), 1164-1178.
- Janjic, Z. I., 2003: A non-hydrostatic model based on a new approach. *Meteor. Atmos. Physics*, **82**, 271-285.
- Jones, S.C., and Coauthors, 2003: The extratropical transition of tropical cyclones: Forecasting challenges, current understanding, and future directions. *Wea. Forecasting*, **18**, 1052-1092.
- Jorgensen, D. P., 1984b: Mesoscale and convective-scale characteristics of mature hurricanes. Part II: inner core structure of Hurricane Allen (1980). *J. Atmos. Sci.*, **41**, 1287-1311.

- Kepert, J., 2001: The dynamics of boundary layer jets within the tropical cyclone core. Part I: Linear theory. *J. Atmos. Sci.*, **58**, 2469-2484.
- Kepert, J., and Y. Wang, 2001: The dynamics of boundary layer jets within the tropical cyclone core. Part II: Nonlinear enhancements. *J. Atmos. Sci.*, **58**, 2485-2501.
- Kepert, J., 2006: Observed boundary layer wind structure and balance in the hurricane core. Part II: Hurricane Mitch. *J. Atmos. Sci.*, **63**, 2194-2211.
- Kimball, S. K., and M. S. Mulekar, 2004: A 15-year climatology of North Atlantic tropical cyclones. Part I: Size parameters. *J. Climate*, **17**, 3555-3575.
- Knabb, R.D., J.R. Rhome, and D.P. Brown, cited 2006: Tropical cyclone report: Hurricane Katrina, 43pp. [Available online at http://www.nhc.noaa.gov/pdf/TCR-AL122005_Katrina.pdf.]
- Knaff, J. A., S. A. Seseske, M. DeMaria, and J. L. Demuth, 2004: On the influences of vertical wind shear on symmetric tropical cyclone structure derived from AMSU. *Mon. Wea. Rev.*, **132**, 2503-2510.
- Kuo, H.-C., R.T. Williams, and J.-H. Chen, 1999: A possible mechanism for the eye rotation of Typhoon Herb. *J. Atmos. Sci.*, **56**, 1659-1673.
- Kurihara, Y., 1975: Budget analysis of a tropical cyclone simulated in an axisymmetric numerical model. *J. Atmos. Sci.*, **32**, 25-59.
- Lamb, H., 1932: *Hydrodynamics*. 6th ed. Dover, 732 pp.
- Liu, Y., D.-L. Zhang, and M. K. Yau, 1997: A multiscale numerical study of hurricane Andrew (1992). Part I: Explicit simulation and verification. *Mon. Wea. Rev.*, **125**, 3073-3093.
- Liu, Y., D.-L. Zhang, and M. K. Yau, 1999: A multiscale numerical study of hurricane Andrew (1992). Part II: Kinematics and inner-core structures. *Mon. Wea. Rev.*, **127**, 2597-2616.
- Maclay, K.S., M. DeMaria, and T.H. Vonder Haar, 2008: Tropical cyclone inner-core kinetic energy evolution. *Mon. Wea. Rev.*, **136**, 4882-4898.
- Marks, F.D., R.A. Houze, and J.F. Gamache, 1992: Dual-aircraft investigation of the inner core of hurricane Norbert. Part I: Kinematic structure. *J. Atmos. Sci.*, **49**, 919-942.
- Mlawer, E. J., S. J. Taubman, P. D. Brown, M. J. Iacono, S. A. Clough, 1997: Radiative transfer for inhomogeneous atmosphere: RRTM, a validated correlated-k model for the long-wave. *J. Geophys. Res.*, **102(D14)**, 16663-16682.
- Montgomery, M.T., R.J. Kallenbach, 1997: A theory for vortex Rossby-waves and its application to spiral bands and intensity changes in hurricanes. *Quart. J. Roy. Meteor. Soc.*, **123**, 435-465.

- Moon, I., I. Ginis, T. Hara, B. Thomas, 2007: Physics-based parameterization of air sea momentum flux at high wind speeds and its impact on hurricane intensity predictions. *Mon. Wea. Rev.*, **135**, 2869-2878.
- Mueller, K., M. DeMaria, J. Knaff, and T.H. Vonder Haar, 2006: Objective estimation of tropical cyclone wind structure from infrared satellite data. *Wea. Forecasting*, **21**, 990-1005.
- Pasch, R.J., E.S. Blake, H.D. Cobb III, and D.P. Roberts, cited 2006: Tropical cyclone report: Hurricane Wilma, 27pp. [Available online at http://www.nhc.noaa.gov/pdf/TCR-AL252005_Wilma.pdf.]
- Pendergrass, A. G., and H. E. Willoughby, 2009: Diabatically induced secondary flows in tropical cyclones. Part I: Quasi-steady forcing. *Mon. Wea. Rev.*, **137**, 805-821.
- Powell, M., and T. Reinhold, 2007: Tropical cyclone destructive potential by integrated kinetic energy. *Bull. Amer. Meteor. Soc.*, **88**, 513-526.
- Reasor, P.D., M.T. Montgomery, F.D. Marks, and J.F. Gamache, 2000: Low-wavenumber structure and evolution of the hurricane inner core observed by airborne dual-Doppler radar. *Mon. Wea. Rev.*, **128**, 1653-1680.
- Rotunno, R., and K. A. Emanuel, 1987: An air-sea interaction theory for tropical cyclones. Part II: Evolutionary study using a nonhydrostatic axisymmetric numerical model. *J. Atmos. Sci.*, **44**, 542-561.
- Schubert, W. H., and J. J. Hack, 1983: Transformed Eliassen balanced vortex model. *J. Atmos. Sci.*, **40**, 1571-1583.
- Schwendike, J., and J. D. Kepert, 2008: The boundary layer winds in Hurricanes Danielle (1998) and Isabel (2003). *Mon. Wea. Rev.*, **136**, 3168-3192.
- Shapiro, L. J., 1983: The asymmetric boundary layer flow under a translating hurricane. *J. Atmos. Sci.*, **40**, 1984-1998.
- Shapiro, L. J., 1996: The motion of Hurricane Gloria: A potential vorticity diagnosis. *Mon. Wea. Rev.*, **124**, 2497-2508.
- Shea, D. J., and W. M. Gray, 1973: The hurricane's inner core region. I. Symmetric and asymmetric structure. *J. Atmos. Sci.*, **30**, 1544-1564.
- Shumway, R. H., and D. S. Stoffer, 2000: Time series analysis and its applications. Springer, 549.
- Stern, D. P., and D. S. Nolan, 2009: Reexamining the vertical structure of tangential winds in tropical cyclones: Observations and theory. *J. Atmos. Sci.*, **66**, 3579-3600.
- Stern, D. P., and D. S. Nolan, 2011: On the height of the warm core in tropical cyclones. *J. Atmos. Sci.*, in review.

- Ueno, M., 2007: Observational analysis and numerical evaluation of the effects of vertical wind shear on the rainfall asymmetry in the typhoon inner-core region. *J. Meteor. Soc. Japan*, **85**, 115-136.
- Ueno, M., 2008: Effects of ambient vertical wind shear on the inner-core asymmetries and vertical tilt of a simulated tropical cyclone. *J. Meteor. Soc. Japan*, **86**, 531-555.
- Ueno, M., and M. Kunii, 2009: Some aspects of azimuthal wavenumber-one structure of typhoons represented in the JMA operational mesoscale analyses. *J. Meteor. Soc. Japan*, **87**, 615-633.
- Ueno, M., and K. Bessho, 2011: A statistical analysis of near-core surface wind asymmetries in typhoons obtained from QuikSCAT data. *J. Meteor. Soc. Japan*, **89**, 225-241.
- Wang, Y., 2001: An explicit simulation of tropical cyclones with a triply nested movable mesh primitive equation model: TCM3. Part I: Model description and control experiment. *Mon. Wea. Rev.*, **129**, 1370-1394.
- Wang, Y., 2002: Vortex Rossby waves in numerically simulated tropical cyclone. Part I: Overall structure, potential vorticity, and kinetic energy budgets. *J. Atmos. Sci.*, **59**, 1213-1238.
- Willoughby, H. E., 1992: Linear motion of a shallow-water barotropic vortex as an initial-value problem. *J. Atmos. Sci.*, **49**, 2015-2031.
- Yang, M.-J., D.-L. Zhang, and H.-L. Huang, 2008: A modeling study of typhoon Nari (2001) at landfall. Part I: Topographic effects. *J. Atmos. Sci.*, **65**, 3095-3115.